Doctoral Dissertation

博士論文

Study of the high-energy emission from the gamma-ray binary system LS 5039

(ガンマ線連星 LS 5039 の X 線ガンマ線放射の研究)

A Dissertation Submitted for the Degree of Doctor of Philosophy

December 2019

令和元年 12 月博士 (理学) 申請

Department of Physics, Graduate School of Science,
The University of Tokyo

東京大学大学院理学系研究科物理学専攻

Hiroki Yoneda

米田 浩基

Abstract

Gamma-ray binary systems are compact binary systems whose spectral energy distributions have peaks above ~ 1 MeV. Their non-thermal spectra are completely different from those of most of compact binary systems, which indicates that efficient particle acceleration occurs in these systems. However, the mechanism of the particle acceleration has been a long-standing problem until now. Furthermore, in most of gamma-ray binary systems, the nature of the compact objects is also still unclear. In order to solve these problems, in this thesis we studied the high-energy gamma-ray emission from the gamma-ray binary system LS 5039 which is the brightest source in this class.

By utilizing the *NuSTAR* observatory, we studied the hard X-ray spectrum of LS 5039 with unprecedented sensitivity. We found that it is well described by a single powerlaw component below 70 keV. Comparing with the previous observation, the flux in 3–10 keV varies by $\sim 10\%$ around the inferior conjunction (INFC) orbit-by-orbit. Furthermore, we did find a small spike in a light curve which was observed around the INFC previously. These results suggest that the emission mechanism varies slightly around the inferior conjunction orbit-by-orbit.

We also searched the hard X-ray observations for a pulsed signal for the first time. By mitigating the Doppler effect due to the orbital motion, the 10–30 keV *Suzaku* data revealed the periodic component of 8.960 ± 0.009 s with a chance probability of 1.1×10^{-3}. Furthermore, the *NuSTAR* data also showed a sign of the pulsation of 9.046 ± 0.009 s. Therefore, we found evidence: the compact object in LS 5039 is a neutron star with a spin period of ~ 9 s and a period derivative of $\dot{P} \sim 3 \times 10^{-10}$ s s^{-1}.

In order to study details of GeV emission, we analyzed 11 years of observations of *Fermi* LAT. We found that the spectrum around the INFC is well described by two components: a powerlaw with a photon index of ~ 3.6, and an exponential cutoff powerlaw with a photon index ~ 1.3 and a cutoff energy ~ 1.9 GeV. Furthermore, we found that the flux is nearly independent of the orbital phase from 1 GeV to 5 GeV. These results strongly indicate that there are two emission origins in the GeV band. In addition, the *Fermi* LAT observations revealed that the flux of LS 5039 is stable from 100 MeV to 10 GeV within $\sim 20\%$ in both 1-month and 1-year time scales.

In order to interpret the observed spectrum of LS 5039 from the X-ray to TeV band, we constructed a spectral model with minimizing assumptions. By comparing the model with the observations, the magnetic field in the X-ray emission region was constrained. Moreover, we revealed that the MeV gamma-ray emission has a different spectral origin from that of

the X-ray emission. The MeV gamma-ray spectral component is found to be explained only if it is the synchrotron spectrum hardened by both adiabatic losses and a very hard injection electron spectrum with a spectral index ~ 1. From this result, we conclude that a direct acceleration process takes place in LS 5039.

On the basis of the derived spin period and its derivative, we obtained a new possibility: the compact object in LS 5039 is a magnetar with a magnetic field of $\sim 10^{15}$ G and its magnetic energy is a dominant energy source for the high-energy emission of LS 5039. Finally, we propose a plausible scenario: magnetic reconnection takes place efficiently in LS 5039 at a certain region close to the magnetar where anti-parallel magnetic field lines are formed.

Contents

Chapter 1

Introduction

The X-ray source population in our Galaxy is dominated by binary systems that contain neutron stars or black holes (Fabbiano, 2006; Grimm et al., 2002). These systems are called compact binary systems. So far, hundreds of objects in this class have been discovered (Liu et al., 2006, 2007). From the beginning of X-ray astrophysics, they have been studied intensively, and currently a standard picture of their nature has been established: the gravitational energy of material from a mass donating star is efficiently transformed to radiation when it accretes onto the compact star. Then it results in bright thermal X-ray emission.

In the middle of the 2000s, a new class of compact binary systems called "gamma-ray binary systems" were discovered owing to the development of high energy gamma-ray observations. These objects emit gamma rays in the GeV and TeV band, and their spectral energy distributions are peaked beyond 1 MeV. These features which are completely different from those of the X-ray binary systems indicate that particle acceleration takes place in these systems. Currently, eight gamma-ray binary systems have been discovered. However, the nature of their compact objects and the mechanism of the high-energy emission in these systems remain unclear. Therefore, this new type of accelerators in the Universe is one of open problems in modern astrophysics.

The high energy emission from these gamma-ray binary systems indicates extensive particle acceleration. In order to understand their non-thermal activity, several theoretical models have been proposed so far. They are mainly divided into two scenarios. In the microquasar model, relativistic jets are launched from a stellar mass black hole, and non-thermal emission is produced by particles accelerated in the jets. On the other hand, the pulsar wind model predicts that the compact object is a neutron star with strong pulsar winds. Stellar winds from the mass donating star collide with the pulsar winds, which then forms a colliding shock.

The particles are then accelerated via shock acceleration, and emit the high energy gamma rays.

Recent observations revealed that some gamma-ray binary systems have spectral components that cannot be explained by these models. Collmar & Zhang (2014) re-analyzed the COMPTEL/CGRO data, and confirmed that the gamma-ray binary system LS 5039 has strong emissions in the 1–10 MeV range. All the spectral models proposed for this source fail to explain this MeV emission. Furthermore, Abdo et al. (2011) found that the gamma-ray luminosity of PSR B1259-63 becomes higher than the pulsar spin down luminosity near periastron, which is also difficult to explain in standard scenarios. These observations suggest that some of the gamma-ray binary systems have an acceleration/radiation process that is not considered in previous works.

LS 5039 is one of the best targets for investigating the mysterious nature of the gamma-ray binary systems, because it is the brightest object in this class. Furthermore, since its orbital period is relatively short ~ 3.9 days, it is possible to observe this source over its entire orbit. Although it has been observed in many wavelengths, its spectrum from 10 keV to $\sim$ 100 keV is poorly constrained. It is important to investigate details of the X-ray emission, because it provides essential information *e.g.* the highest electron energy, or the size of an acceleration region. Moreover, the GeV gamma-ray emission is also important for this source. Hadasch et al. (2012) reported that the spectrum in the GeV band indicates several spectral components. Considering these facts, the best way to study LS 5039 is to comprehensively analyze the spectrum of this source in hard X-rays and GeV gamma-rays.

The spectrum and stability of the emission of LS 5039 suggest the presence of a neutron star. In order to confirm this, the pulse detection provides definitive evidence. However, such attempts have not observed the presence of a neutron star using radio (Virginia McSwain et al., 2011) to soft X-rays (Rea et al., 2011). It can be argued that the pulsed emission is strongly absorbed by stellar winds of the O star. In this sense, higher energy photons, *i.e.* hard X-rays, can be better probes for the pulsation since they penetrate stellar winds without the absorption.

In this thesis, we analyze the spectrum of LS 5039 from hard X-rays to GeV gamma-rays using *NuSTAR*, *Suzaku* and *Fermi*. The study includes the orbital dependence of the flux, and time variability of the emission on different time scales. Moreover, we search for the pulsation using hard X-ray observations. Finally, we develop a spectral model for LS 5039, and compare it with the observed spectrum in order to constrain the physical parameters of the acceleration region.

This thesis is organized as follows. In Chapter 2, we review current understanding of the gamma-ray binary systems and physical processes related to them. In Chapter 3, we briefly describe the *Suzaku*, *NuSTAR* and *Fermi* observatories. The results of the spectral and timing analysis of the hard X-ray observations are presented in Chapter 4 and 5, respectively. Chapter 6 gives the spectral analysis of *Fermi*. In Chapter 7, we describe the spectral model and the results of the comparison of it with the observed spectrum. Combining the obtained results, we discuss the nature of the compact object and the particle acceleration mechanism in LS 5039 in Chapter 8. Finally, a summary of this thesis is given in Chapter 9.

Chapter 2

Review

In this thesis, we observationally study the high-energy emission of the gamma-ray binary system LS 5039. Here, we review the current understanding of gamma-ray binary systems and explain the importance of multi-wave length analysis for this class. The basics of the particle acceleration and non-thermal radiation processes are also described.

2.1   Compact Binary Systems

A Compact binary system is a binary system that contains a neutron star or a black hole. It is known that the compact binary system is a major class of X-ray sources in the Galaxy. In the ASM catalog, about 70% of the X-ray sources are compact binary systems (Grimm et al., 2002). It is widely accepted that the gravitational energy is converted to radiation energy via the accretion process in a majority of compact binary systems. In the accretion process, hot plasma is formed with a temperature of a few keV, and it produces bright thermal X-ray emission.

The compact binary systems are mainly divided into two subclasses. If the companion star has a spectral type later than A, it is classified into a low mass X-ray binary (LMXB). In the LMXBs, the companion star fills its Roche-lobe, and the materials of the companion star flow onto the compact object through the Lagrangian point L_1. Then, they form an accretion disk around the compact star (Shakura & Sunyaev, 1973). Their luminosity ranges from $\sim 10^{36}$ to several 10^{38} erg s^{-1} (Church et al., 2014). Another subclass of the compact binary systems is a high mass X-ray binary (HMXB), in which a companion star is an OB star with few tens of the solar mass. The massive stars have strong stellar winds of ~ 2000 km s^{-1} with a mass loss rate of $\sim 10^{-6}$ M$_\odot$ yr^{-1} (Lamers, 1981; Lamers & Leitherer, 1993), which

surround the compact object. A fraction of the stellar winds are captured by the gravity of the compact object, and the accreting material emits thermal X rays.

If the compact object in the binary system is a neutron star, its magnetic field determines the behavior of the binary system. The neutron stars in HMXBs usually have a magnetic field of $\sim 10^{12}$ G. Such a strong magnetic field channels the accretion flow into a columnar geometry as shown in Figure 2.1. The thermal X-ray photons are produced in the column near the magnetic pole (Becker & Wolff, 2007). The neutron star spins up because the accretion flow transfers its angular momentum to it. However, if the neutron star is spinning much faster than the Keplerian frequency at the Alfvén radius, the centrifugal force prevents the in-falling matters from reaching the magnetic poles. Note that the Alfvén radius is the distance at which the magnetic pressure becomes comparable to the ram pressure of the in-falling matter. This phenomenon is called "the propeller effect". In this case, the spin-down takes place because the angular momentum of the neutron star is carried out by the material which is blown away. Several accreting neutron stars show both intrinsic spin-up and spin-down (Chakrabarty et al., 1993; Yatabe et al., 2018). If the magnetic field is weak $\sim 10^{10}$ G, which is a typical value in LMXBs, the columnar flow is not formed. Instead, the in-falling material accretes onto the neutron star as an accretion disk.
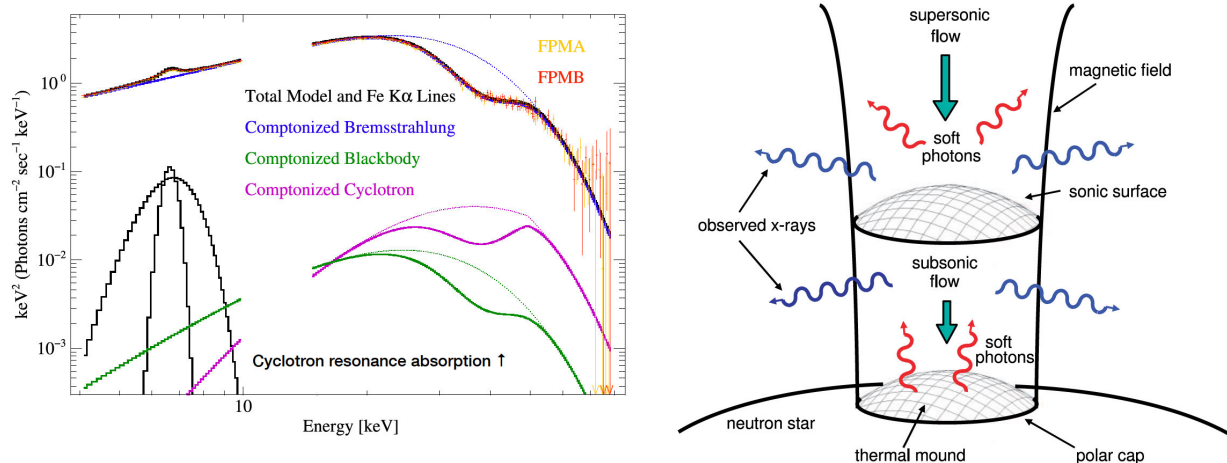
Figure 2.1: The spectrum of the accreting neutron star Her X-1 (Wolff et al., 2016). The right figure is a schematic of the accretion column on the magnetic pole of a neutron star, taken from Becker & Wolff (2007).

The accretion disk is also formed if the compact star is a black hole. Typically, the spectrum from the accretion disk is classified into two states, soft/high state and hard/low state. Figure 2.2 shows typical spectra for these two states. In the soft/high state, the

spectrum is dominated by the strong blackbody component. It is widely accepted that the blackbody spectrum is generated from the standard accretion disk (Shakura & Sunyaev, 1973). In the hard/low state, the dominant spectral component appears around a few hundred keV, which is explained by the Comptonization on the disk of blackbody photons by thermal electrons with a temperature of 50–100 keV. It is thought that the hot electrons are produced in hot accretion flows at inner regions of the accretion disk (Narayan & Yi, 1995; Yuan & Narayan, 2014).
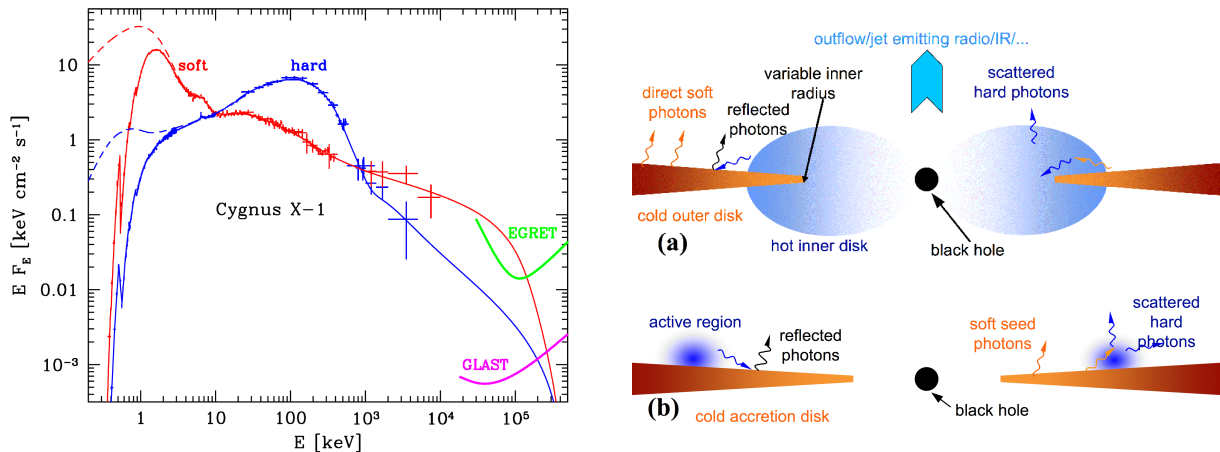
Figure 2.2: The spectra of the black hole binary Cyg X-1. The right figure is a schematic of the geometry in both hard/low state (a) and soft/high state (b). These figures are taken from Zdziarski & Gierliński (2004).

2.2 Gamma-ray Binary Systems

Gamma-ray binary systems are a subclass of compact binary systems established in the middle of 2000s. The development of GeV and TeV gamma-ray observations revealed high-energy gamma-ray emissions from several binary systems. Their spectral energy distributions peak beyond 1MeV. Although the companion stars in the gamma-ray binary systems are OB stars, their non-thermal emissions are completely different from the typical thermal emissions of the HMXBs. What makes the gamma-ray binary systems unusual is an unsolved problem in modern astrophysics. There is currently no scenario that reproduces their observational properties.

The gamma-ray emission from a binary system was detected in the late 1970s for the first time (Gregory & Taylor, 1978). The Cos-B was the first ESA mission to study gamma-ray

sources (Bignami et al., 1975; Scarsi et al., 1977), and it found a gamma-ray source which is possibly associated with the binary system LS I+61°303 which contains a Be star. In 1990s, CGRO/EGRET found several gamma-ray sources possibly associated with the binary systems (Hartman et al., 1999). However, it was difficult to confirm these associations because of the limited angular resolutions of these instruments. A significant progress in this field was made in the middle of 2000s by the developments of the imaging arrays of Cherenkov telescopes, H.E.S.S., MAGIC and VERITAS. For example, in 2004, H.E.S.S. detected the gamma-ray binary system PSR B1259-63 above 0.1 TeV (Aharonian et al., 2005a). It was the first binary system that was detected in the TeV band. Furthermore, the successors of EGRET, namely, *AGILE* and *Fermi* improved the angular resolution and the sensitivity of the GeV observations, resulting in the discovery of binary systems in the GeV band.

The development of gamma-ray observations enabled the study of the gamma-ray binary systems from the X-ray to the TeV gamma-ray band. As an example, we show the spectral energy distributions (SEDs) of the gamma-ray binary systems LS I+61°303 and PSR B1259-63 in Figure 2.3. While these SEDs peak around 1–100 MeV, there are considerable contributions from the X-ray, GeV and TeV band. Thus, the multi-band observations are essential for studying this class. Furthermore, the bright TeV emissions and the non-thermal spectra imply that electrons are accelerated to the TeV energies. Therefore, it is widely accepted that efficient particle acceleration takes place in the gamma-ray binary systems.
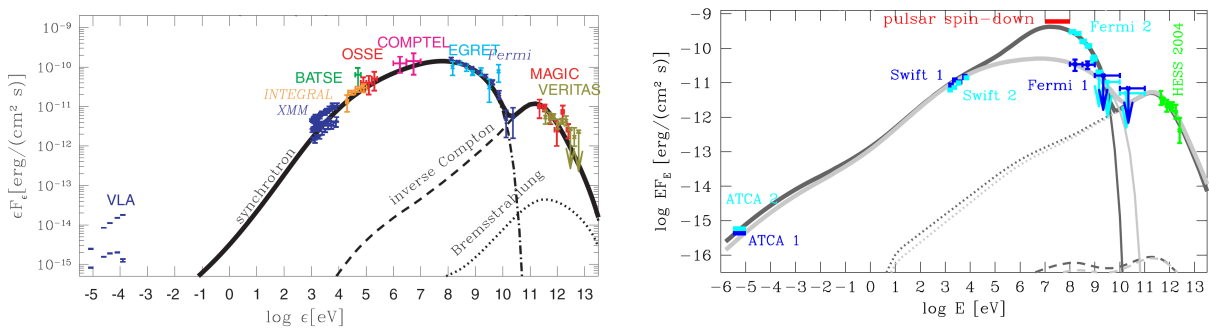
Figure 2.3: The spectral energy distributions (SEDs) of the gamma-ray binary systems. The left figure is the SED of LS I+61°303 (Zdziarski et al., 2010), and the right figure is the SED of PSR B1259-63 around periastron (Abdo et al., 2011).

Until now, eight gamma-ray binary systems have been discovered. Seven systems are in our Galaxy, and the other is the Large Magellanic Cloud. Table 2.1 shows all of the gamma-ray binary systems. The optical companion stars are found to be massive OB stars. PSR B1259-63 and PSR J2032+4127 are known to contain millisecond pulsars. It is considered

that the particle acceleration takes place via interaction between the pulsars and the outflows from the Be stars. On the other hand, what kinds of compact objects are in the other six gamma-ray binary systems is still unclear. Consequently, the mechanism of the particle acceleration in these systems remains a long-standing problem. To reveal the nature of the compact objects is key for understanding these gamma-ray binary systems.

Table 2.1: List of known gamma-ray binary systems.

Object Name	Orbital Period	Optical Star	Compact Star	D (kpc)	Ref.
LS 5039	3.90608(10) days	O6.5 V(f)	unknown	2.5 ± 0.1	(1,2,3)
1FGL J1018.6-5856	16.58(2) days	O6 V(f)	unknown	$5.4^{+4.6}_{-2.1}$	(4,5)
LMC P3	10.301(2) days	O5 III(f)	unknown	~ 50	(6,7)
4FGL J1405.1-6119	13.7135(19) days	O6.5 III	unknown	7.7	(8)
LS I+61°303	26.4960(28) days	B0 Ve	unknown	2.0 ± 0.2	(9,10)
HESS J0632+057	313^{+11}_{-8} days	B0 Vpe	unknown	1.1–1.7	(11,12,13)
PSR B1259-63	3.38603953(2) year	O9.5Ve	pulsar	$2.6^{+0.4}_{-0.3}$	(14,15,16)
PSR J2032+4127	45–50 years	B0 Vp	pulsar	1.3 ± 0.1	(17,18,19,20)

(1): McSwain et al. (2001) (2): Casares et al. (2005) (3): Aragona et al. (2009). (4): Fermi LAT Collaboration et al. (2012). (5): Napoli et al. (2011). (6): Corbet et al. (2016). (7): van Soelen et al. (2019). (8): Gregory (2002). (9): Frail & Hjellming (1991). (10): Moritani et al. (2018). (11): Napoli et al. (2011). (12): Casares et al. (2012). (13): Corbet et al. (2019). (14): Johnston et al. (1994). (15): Negueruela et al. (2011). (16): Miller-Jones et al. (2018). (17): Massey & Thompson (1991). (18): Camilo et al. (2009). (19): Kiminki et al. (2015). (20): Ho et al. (2017).

2.3 Particle Accelerations in Gamma-ray Systems

In order to explain the particle acceleration in the gamma-ray binary systems, several models have been proposed so far. These are mainly divided into three scenarios. Figure 2.4 shows schematic representations of these scenarios.

In the first model shown in Figure 2.4 (A), particles are accelerated via interaction between the outflowing disk from a Be star and pulsar winds. This model is accepted to explain the gamma-ray emission from PSR B1259-63 and PSR J2032+4127. The compact objects in

these systems are millisecond pulsars. Around the periastron passage, the pulsar penetrates the dense environment formed by the outflowing material in the Be disk. The pulsar winds interact with the ions and electrons in the massive outflows. Since their orbits have large eccentricities of ~ 0.9 with an orbital period longer than a year, the gamma-ray emissions take place only near periastron.

Figure 2.4 (B) shows the microquasar model. In this model, the compact object is assumed to be a stellar mass black hole. The accretion onto the black hole produces relativistic jets. In analogy with the quasars, the particles are accelerated by the jet. In some of the gamma-ray binary systems, the extended structures are observed in the radio band (Paredes et al., 2000), which can be interpreted as the radio emission caused by the jets. Furthermore, it is proposed that gamma-ray binary systems are a potential source of TeV neutrinos in the microquasar model (Aharonian et al., 2006a). If the hadronic processes take place in the jet, then high-energy neutrinos emerge from the decays of $\pi^\pm$ mesons produced by proton-proton and/or proton-gamma interactions.

The last scenario is the pulsar wind model as shown in Figure 2.4 (C). Here, the compact object is assumed to be a rotation-powered pulsar with strong pulsar winds. The compact object is surrounded by a dense environment since the massive star emits strong stellar wind and UV photons. Relativistic electrons in the pulsar winds interact with the surrounding materials. As a result, relativistic shocks are formed, and particles are accelerated via the shock acceleration.

2.4   The Gamma-ray Binary System LS 5039

LS 5039 is the brightest gamma-ray binary in the Galaxy with a bolometric luminosity of $\sim 10^{36}$ erg s^{-1} (Collmar & Zhang, 2014). It contains a massive O6.5 V(f) star with a mass of ~ 23 M$_\odot$ (Casares et al., 2005). From optical observations, the orbital period is found to be ~ 3.9 days with an eccentricity of ~ 0.3. Table 2.2 describes the orbital parameters of LS 5039. Figure 2.5 shows the orbit of LS 5039 based on the obtained orbital parameters. Because of its brightness and its relatively short orbital period, LS 5039 has been so far studied intensively from the radio to TeV energy range.

Initially, LS 5039 was discovered as a luminous star in the Galaxy (Stephenson & Sanduleak, 1971). Motch et al. (1997) identified it as a high mass X-ray binary from a cross correlation of the ROSAT galactic sources with OB star catalogs. Soon thereafter, the possible association of LS 5039 with the EGRET source 3EG 1824-1314 was reported by Paredes
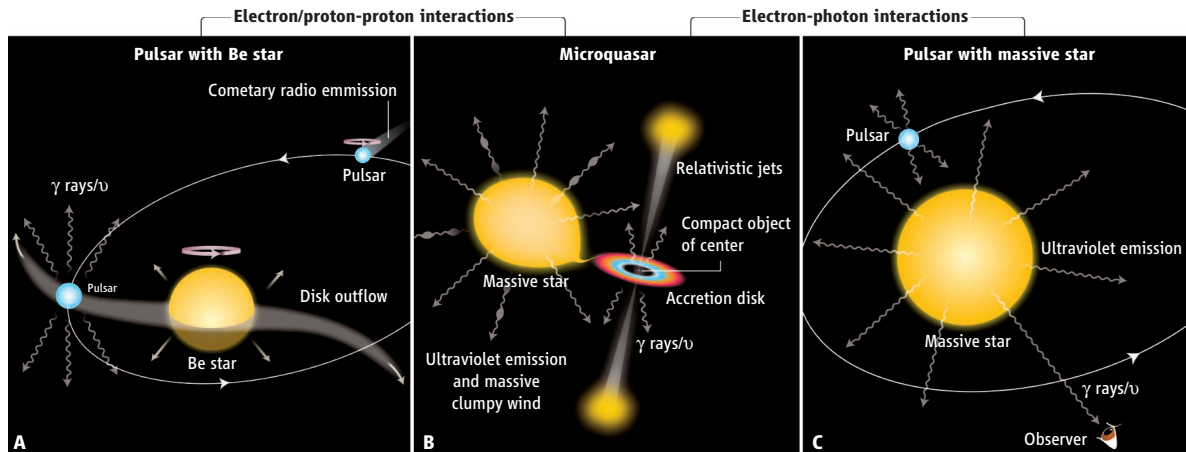
Figure 2.4: Several scenarios of gamma-ray binary systems (taken from Mirabel 2012). (A) The pulsar wind interacts with the outflowing particle in the disk of a Be star. (B) The mass accretion onto a stellar mass black hole powers the relativistic jet. The particles are accelerated in the jet. (C) The pulsar wind interacts with the stellar wind and UV photons from the companion star.

et al. (2000). Gamma rays from LS 5039 were detected by H.E.S.S. for the first time (Aharonian et al., 2005b). Surprisingly, Aharonian et al. (2006b) revealed that the gamma-ray flux depends on the orbital period. This was the first time in gamma-ray astronomy of the detection of orbital modulation. Following this discovery, the orbital modulation has also been confirmed in the X-ray, MeV and GeV band (Takahashi et al., 2009; Kishishita et al., 2009; Hoffmann et al., 2009; Chang et al., 2016; Collmar & Zhang, 2014; The Fermi LAT collaboration, 2009). Figure 2.6 shows the orbital modulation from the X-ray to TeV band. By combining the spectral analysis in different energy bands, Collmar & Zhang (2014) derived the spectral energy distribution of LS 5039, as shown in Figure 2.7. Note that so far only 32 sources have been detected between 0.75–30 MeV due to low sensitivity of the MeV observations (Schönfelder et al., 2000). Therefore, LS 5039 is one of the brightest MeV gamma-ray sources in the Galaxy.

2.5 Previous Observations of LS 5039

LS 5039 has been observed extensively over a long period of time. Here, we describe important results of previous observations from radio to TeV gamma rays.
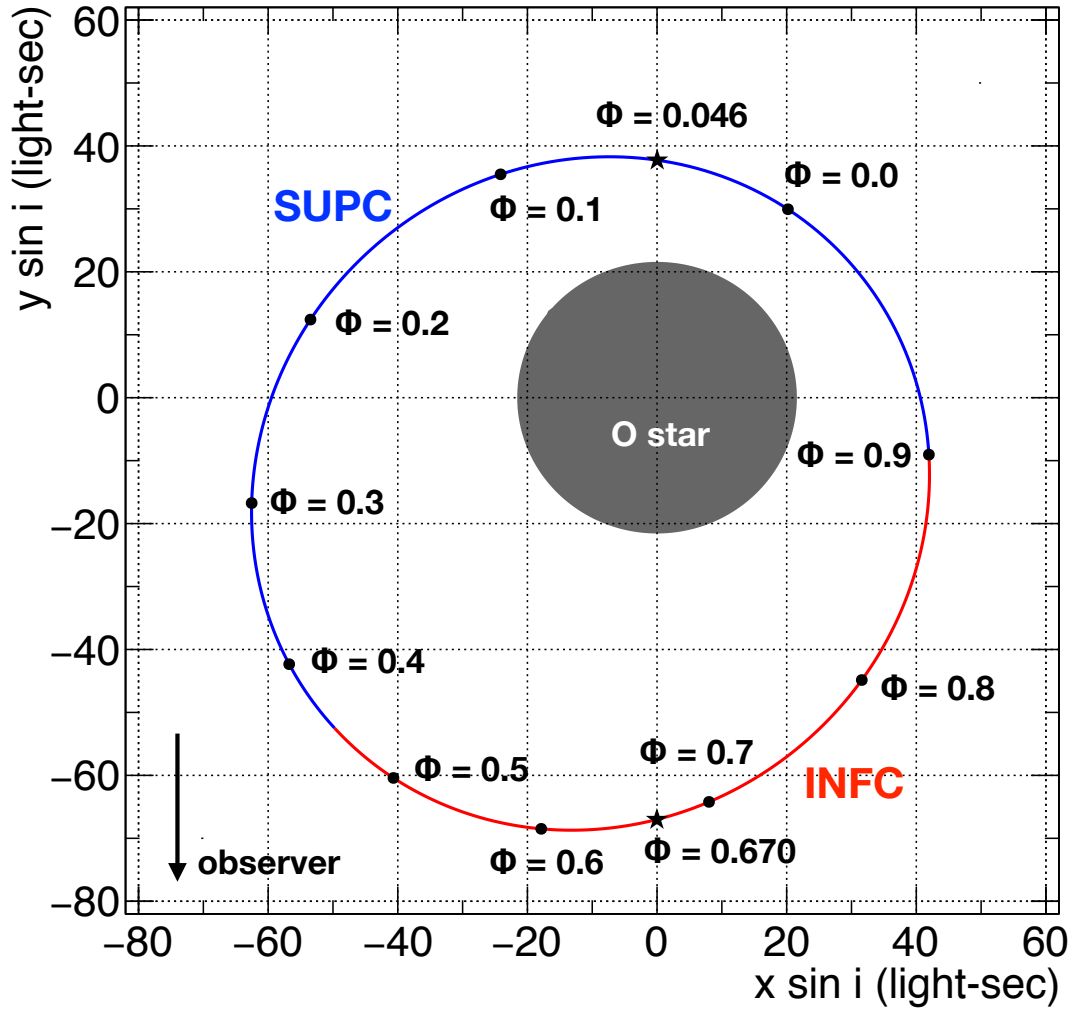
Figure 2.5: Orbital geometry of LS 5039, projected on the orbital plane. ϕ is the orbital phase and i is the inclination angle. $\phi = 0$ corresponds to the periastron of LS 5039. We adopted the orbital parameters obtained by Aragona et al. (2009). The compact star is the closest to the observer at $\phi = 0.670$ (inferior conjunction) and the farthest at $\phi = 0.046$ (superior conjunction). Here, the mass of the compact star is assumed to be 1.4 $M_\odot$. The mass and radius of the companion star are set to 2.9 $M_\odot$ and 9.3 $R_\odot$ (Casares et al., 2005).
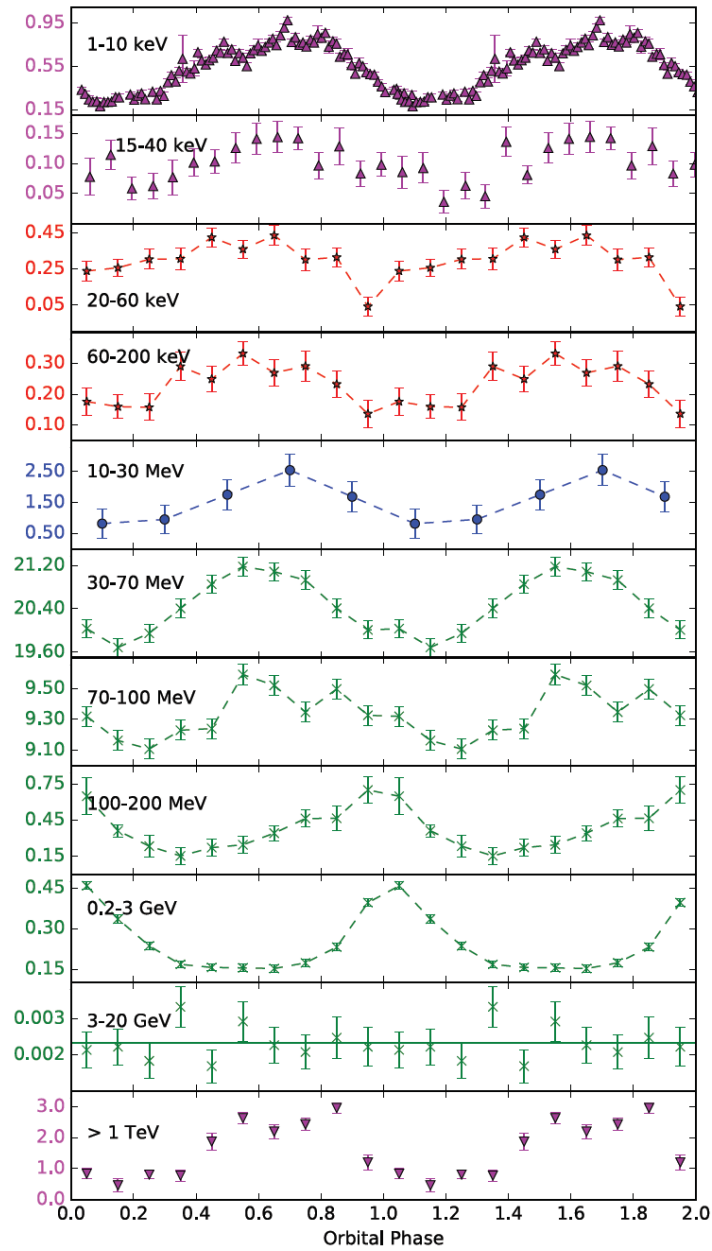
Figure 2.6: The dependence of the flux on the orbital phase (taken from Chang et al. 2016).
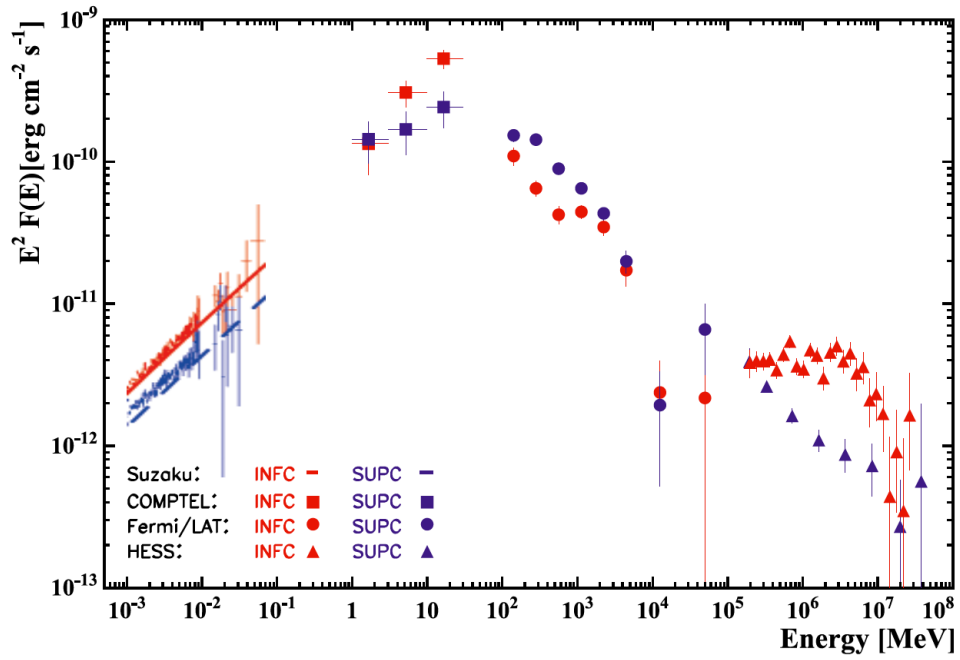
Figure 2.7: The spectral energy distribution of LS 5039 (Collmar & Zhang, 2014). The red points indicate the flux around the inferior conjunction ($0.45 < \phi < 0.9$). The blue points indicate the flux around the superior conjunction ($0.0 < \phi < 0.45, 0.9 < \phi < 1.0$). ϕ is the orbital phase of LS 5039.

Table 2.2: Orbital parameters obtained with optical observations

	Casares et al. (2005)	Aragona et al. (2009)	Sarty et al. (2011)
$P_{\rm orb}$ (day)	3.90603 ± 0.00017	3.90608 ± 0.00010	3.906
T_0 (HJD-245000)	1943.09 ± 0.10	2825.985 ± 0.053	5017.08 ± 0.06
e	0.35 ± 0.04	0.337 ± 0.036	0.24 ± 0.08
ω (deg.)	225.8 ± 3.3	236.0 ± 5.8	237.3 ± 21.8
$f(M)$ $(M_\odot)$	0.0053 ± 0.0009	0.00261 ± 0.00036	0.0049 ± 0.0006
$a_{\rm O} \sin i$ (light sec)	4.22 ± 0.23	3.33 ± 0.15	4.11 ± 0.35
$M_{\rm O}$ $(M_\odot)$	$22.9^{+3.4}_{-2.9}$	-	-

2.5.1 Radio band

High-resolution radio observations revealed the extented radio emission from LS 5039 by the VLBA and VLA (Paredes et al., 2000). The extend emission has the bipolar structure as shown in Figure 2.8. This feature was confirmed again with other radio observations (Paredes et al., 2002). The extend emission reached up to ~ 1000 AU ($\sim 10^{16}$ cm) from the center of LS 5039.

Virginia McSwain et al. (2011) performed the pulse search using radio observations. They aimed to identify the nature of the compact object in LS 5039 since the pulse detection is definitive evidence of a neutron star. However, the pulse was not detected between 4.1 and 14.5 μJy. It can be interpreted that the radio pulse emission is completely absorbed by the dense environment. In LS 5039, the optical depth of radio photons is very large ~ 100 even near the inferior conjunction where the absorption by the stellar wind from the companion star is the weakest.

Moldón et al. (2012) obtained the Galactic trajectory of LS 5039 and searched for their association *e.g.* supernova or an active site of star formation. They measured its proper motion as $\mu_\alpha \cos\delta \sim 7$ mas yr^{-1} and $\mu_\delta \sim 9$ mas yr^{-1}. They concluded that LS 5039 would have had to be formed in the Ser OB2 at 2.0 kpc if the age of the system is 1.0–1.2 Myr, or in the Sct OB3 at 1.5–2 kpc if the age is 0.1–0.2 Myr. Apart from LS 5039 by 20', there is a region named SNR G016.8 − 01.1. Although they discussed its association with LS 5039, Sun et al. (2011) noted that SNR G016.8-01.1 is likely a HII region rather than a supernova on the basis of polarization studies.
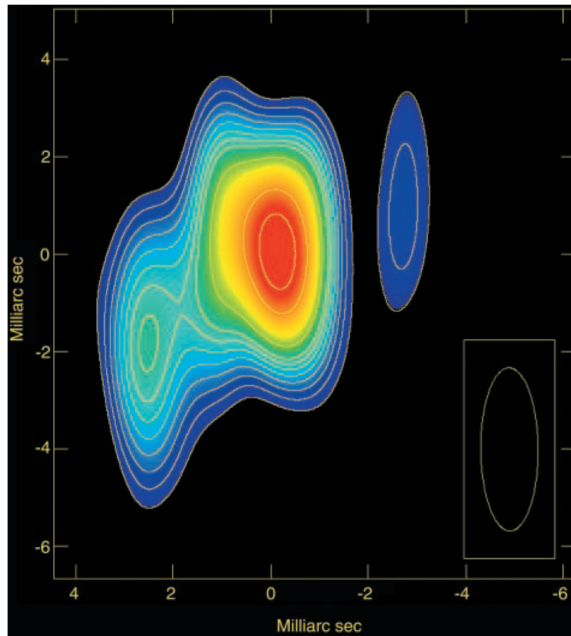
Figure 2.8: High-resolution radio map of LS 5039 obtained with the VLBA and the VLA (Paredes et al., 2000).

2.5.2   Optical band

The optical emission from LS 5039 is dominated by the O6.5 V(f) star. The luminosity and the temperature of the massive star are measured to be $\sim 7 \times 10^{38}$ erg s^{-1} and 39000 ± 1000 K, respectively (Casares et al., 2005). The system size is about $\sim$ 50 light-sec, though this depends on the mass of the compact object, as shown in Figure 2.9. Here, we used the observational parameters, shown in Table 2.2. The orbital parameters of LS 5039 were obtained using the narrow absorption lines of Balmer or He I/II from the companion star. Casares et al. (2005) suggests that the compact object in LS 5039 is a black hole, assuming pseudo-synchronization *i.e.* the companion star's rotational and orbital angular velocities are synchronized at periastron. However, this assumption can be valid only if the system's age is larger than a synchronization time-scale of $\sim$ 1 Myr. Moldón et al. (2012) reports that if LS 5039 was not formed near Ser OB2, then pseudo-synchronization is unlikely since the system is too young. The lower limit of the mass of the compact object was estimated as 1.5 M$_\odot$ (Casares et al., 2005) or 1.2 M$_\odot$ (Aragona et al., 2009) by using the upper limit on the inclination angle (Reig et al., 2003).
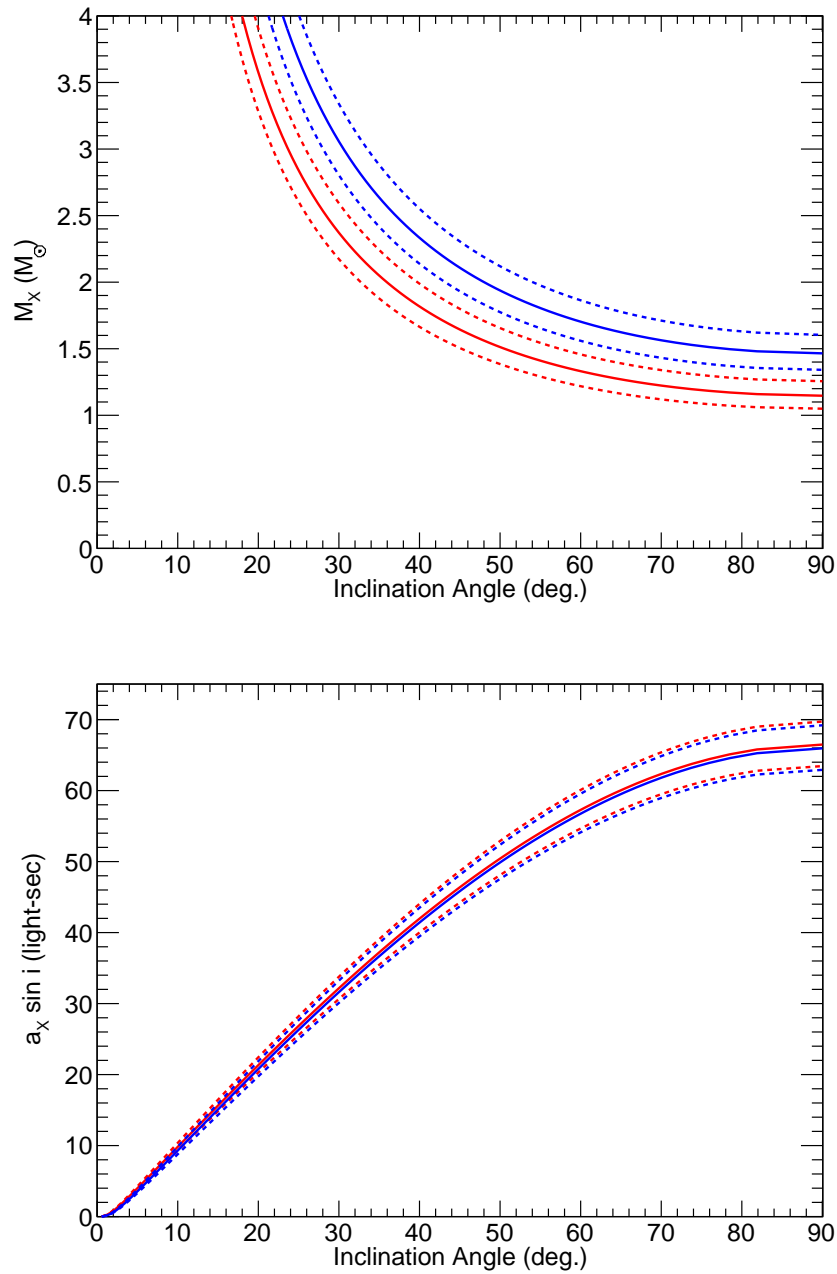
Figure 2.9: The system size of LS 5039. Top: The relation between M_X and the inclination angle. Bottom: The relation between $a_X \sin i$ and the inclination angle. The blue lines are based on the parameters from Casares et al. (2005). The red lines are based on the parameters from Aragona et al. (2009). The dot lines indicate 1-sigma confidence intervals.

2.5.3   X-ray band

Motivated by the detection of the orbital modulation in the TeV band, Takahashi et al. (2009) observed LS 5039 in X rays with *Suzaku* observatory for about 1.5 orbital periods. They found that the X-ray flux also depends on the orbital phase, and it is correlated with the TeV flux modulation. It was also reported that the hard X-ray spectrum with a photon index of ~ 1.5 is produced by adiabatic expansion in the emission region. Furthermore, they suggested that the acceleration in LS 5039 is extremely efficient, with an acceleration efficiency of $\eta \sim 1$ in order to achieve a short acceleration time which is faster than an adiabatic cooling time (we define η later.).

Kishishita et al. (2009) compared the *Suzaku* light curve with those of the previous observations made by *ASCA*, *XMM-Newton*, and *Chandra* as shown in Figure 2.10. They found that the modulation curves are very stable over a period of 8 years. Since unpredictable time variabilities are usually observed in accretion black hole binaries (Lewin & van der Klis, 2006), the clock-like behavior of LS 5039 favors the pulsar wind scenario rather than the microquasar model.

In the 25–200 keV band, Hoffmann et al. (2009) observed LS 5039 using the IBIS/ISGRI instrument on-board the INTEGRAL satellite. The orbital modulation was also detected in the hard X-ray band. However, they determined the flux for the inferior conjunction phase and set an upper limit for the inferior conjunction phase due to low photon statistics. Chang et al. (2016) analyzed data with better statistics using the IBIS, and detected LS 5039 in the inferior conjunction phase.

No X-ray eclipse allows the constraint on the inclination angle of the binary orbit. Since the eclipse is not detected in LS 5039, Reig et al. (2003) set an upper limit on the inclination angle i. They determined that $i < 66 \pm 2$ degrees. This constraint is useful in the spectral modeling because the inverse Compton emission strongly depends on the scattering angle of seed photons.

2.5.4   MeV gamma-ray band

1–30 MeV observations using COMPTEL/CGRO detected an unidentified source GRO J1823-12 (Collmar et al., 2000). It is located near $l/b = 17.5°/-0.5°$, which is spatially consistent with LS 5039. Strong et al. (2001) reported results of preliminary analyses on GRO J1823-12 between 1991 and 1997. Following the detections of the orbital modulation from X-ray to TeV band, Collmar & Zhang (2014) re-analyzed the COMPTEL/CGRO data, and found
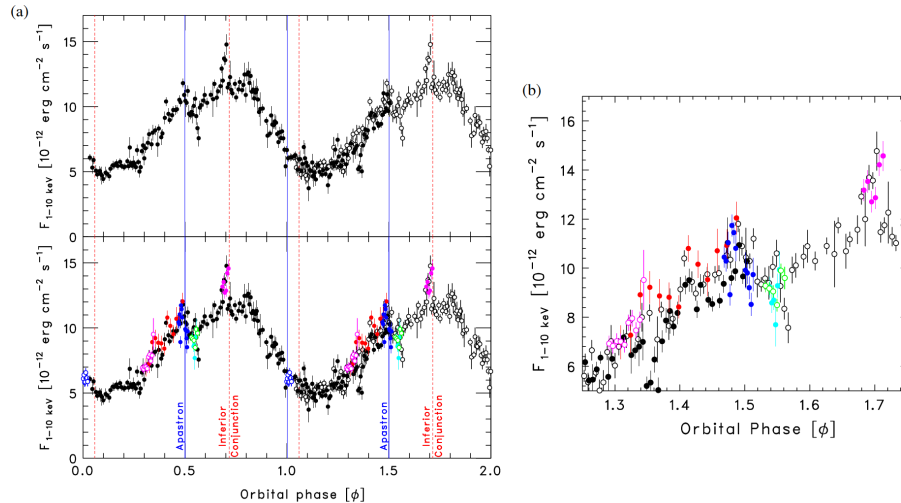
Figure 2.10: Orbital light curves of LS 5039 in the energy range of 1–10 keV (Kishishita et al., 2009). (a) the black points correspond to *Suzaku* XIS data with a bin of 2 ks. The colored points were obtained from past observations. The blue, cyan and green correspond to the *XMM-Newton* observations. The red and magenta correspond to the *ASCA* and *Chandra* observations respectively. (b) A closeup of the light curve between $1.2 < \phi < 1.8$.

evidence with 3σ significance: the MeV flux of GRO J1823-12 is modulated along the orbital phase of LS 5039. Furthermore, the orbital modulation is similar to those of LS 5039 in the X-ray and TeV band. Thus, they have concluded that GRO J1823-12 is the counterpart of LS 5039. The resulting spectrum shows dominant MeV gamma-ray emissions of LS 5039 (see Figure 2.7), and its bolometric luminosity was determined to be $\sim 10^{36}$ erg s^{-1}. Note that five gamma-ray sources detected by *Fermi* are located within the 3σ contour of the location of GRO J1823-12 since the angular resolution of COMPTEL/CGRO is $1.7°$–$4.4°$. The systematic uncertainty due to the contamination from these sources was not estimated in Collmar & Zhang (2014).

2.5.5 GeV gamma-ray band

The possible GeV emission from LS 5039 was discussed in Paredes et al. (2000), and the source was detected with *Fermi*/LAT. The Fermi LAT collaboration (2009) reported the early observation of LS 5039 in the 100 MeV - 300 GeV band. The spectrum was described by a cut-off powerlaw spectrum, which may indicate the magnetospheric emission from a pulsar. Furthermore, orbital modulation was also detected. Interestingly, the orbital modulation

is anti-correlated with those observed in the X-ray and TeV band. Hadasch et al. (2012) analyzed 3 years of observations by *Fermi*/LAT, and found that the emission in the 100 MeV – 300 GeV band is stable for ~ 3 years. In addition, they found that the GeV spectrum has a sign of a hump structure around 1 GeV. Chang et al. (2016) also analyzed the *Fermi*/LAT data above 30 MeV, and revealed that the orbital phase of the flux peak is shifted by a half of the orbital period from 10 MeV to 3 GeV.

2.5.6   TeV gamma-ray band

The H.E.S.S. telescope revealed gamma-ray emissions above 0.1 TeV from LS 5039 (Aharonian et al., 2005b). A deeper observation by HESS was carried out in order to probe the high-energy activity in LS 5039 (Aharonian et al., 2006b). It revealed that TeV gamma-ray flux depends on the orbital phase, which was the first time an orbital modulation in TeV band was detected. The modulation can be explained by a strong gamma-gamma absorption by UV photons which is emitted from the companion star. However, they also discussed that only the absorption effect cannot explain the spectral hardening. It implies that it is essential to consider other effects *e.g.* variations of the maximum accelerated energies with orbital phase, the angular dependence of the inverse Compton scattering, or possibilities of several spectral components.

2.6   Theoretical Models Proposed for LS 5039

So far, many theoretical models have been proposed to explain the unique properties of LS 5039. At an early stage, the microquasar model was intensively studied which was stimulated by several observational results which favor the existence of a black hole (Paredes et al., 2000; Casares et al., 2005). In addition, the variability in X-ray band was thought to be due to changes in the accretion rate along an eccentric orbit (Bosch-Ramon et al., 2005). In the leptonic jet model (Bosch-Ramon et al., 2006; Paredes et al., 2006; Khangulyan et al., 2008), the emissions from X-ray to MeV are explained by the synchrotron emission in the jet. Furthermore, the UV photons emitted from the companion star is up-scattered by the accelerated electrons. The GeV and TeV emissions are explained by the inverse Compton emission. Figure 2.11 shows the spectral model based on a cold matter dominated jet Paredes et al. (2006). The jet in this model is radiatively efficient $\sim 15\%$ and leptons are accelerated to TeV energies in the jet. Other scenarios based on the microquasar model were also discussed *e.g.* the hadronic model (Aharonian et al., 2006a) or a combination of Compton-scattered

stellar radiation and synchrotron self-Compton (Dermer & Böttcher, 2006).

The accreting neutron stars or black holes usually show short time flux variabilities with a time scale from seconds to hours (Lewin & van der Klis, 2006). Thus, the microquasar model predicts shorter time variability in addition to the flux modulation on the orbital phase. However, Kishishita et al. (2009) revealed that the X-ray flux depends only on the orbital phase, and it is remarkably stable for 8 years. This result is in contradiction with the microquasar model. Furthermore, the GeV spectrum obtained with *Fermi*/LAT is similar to the magnetosphere emission from pulsars. Thus, the pulsar wind model was studied more intensively than the microquasar model recently.

In the pulsar scenario, the shock is formed via interaction between the stellar winds of the O star and the relativistic pulsar winds as shown in Figure 2.13. Particles are then accelerated in the shock region, and produce the non-thermal radiation. Some hydrodynamical simulations suggest that the pulsar wind termination shock can be also formed in the opposite direction of the O star due to the orbital motion (Bosch-Ramon et al., 2012). In the shock far away from the companion star, UV photon density is low. Thus, it is an ideal region where the TeV gamma-rays are produced because the gamma-gamma absorption does not take place significantly due to the low UV photon density (Zabalza et al., 2013). Dubus et al. (2015) calculated the spectrum based on a relativistic hydrodynamical simulation. Figure 2.12 shows the resulting spectrum of LS 5039. Although it explains the GeV and TeV spectrum well, it can not reproduce the X-ray and MeV spectra with differences of factors of 2 and 10, respectively. In particular, the MeV emission is not satisfactorily explained by any theoretical model at this present time.

2.7   Physics of Particle Acceleration

The spectrum of LS 5039 has a peak value of around 100 MeV, and extends into the TeV band. This feature is completely different from thermal emissions. In order to produce the TeV gamma rays via the inverse Compton emission, there should be electrons whose energies are above TeV. Therefore, there should be some mechanisms to accelerate the charged particles to the TeV scale. Here, we briefly summarize the mechanisms of particle accelerations in astrophysics.

Generally, the acceleration of charged particles in an electric/magnetic field is described by

$$\frac{\mathrm{d}(\gamma m \boldsymbol{v})}{\mathrm{d}t} = q(\boldsymbol{E} + \boldsymbol{v} \times \boldsymbol{B}) \ . \tag{2.1}$$
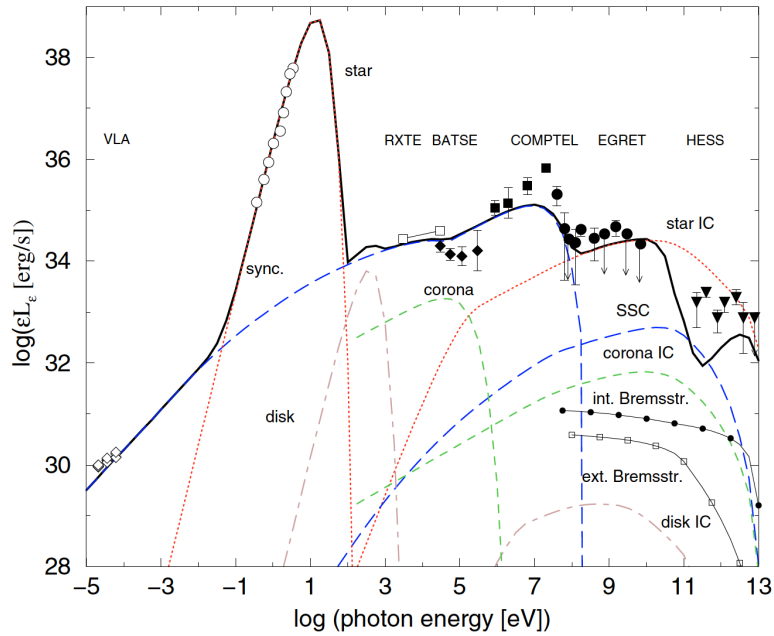
Figure 2.11: Spectral model based on the microquasar model (Paredes et al., 2006).
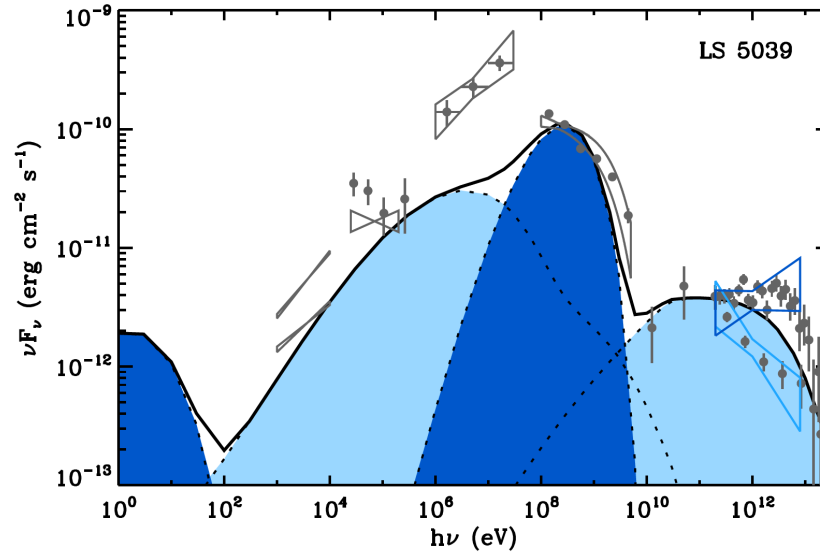
Figure 2.12: Spectral model based on the pulsar wind scenario (Dubus et al., 2015). The dark blue represents the synchrotron and inverse Compton contributions from the Maxwellian population of electrons formed at the shock. The light blue represents the contributions from the power-law population accelerated at the shock.
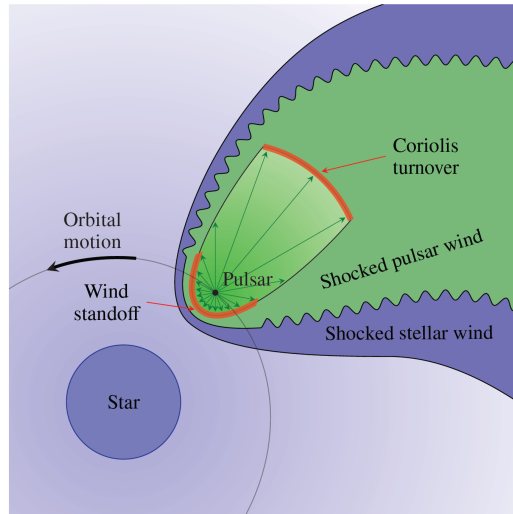
Figure 2.13: A sketch of shock formation in the pulsar wind model (Zabalza et al., 2013). Two important shock regions are highlighted. One is the termination shock between the pulsar and the companion star. The other shock is formed at the location where the ram pressures of the stellar wind owing to Coriolis forces and the pulsar wind are comparable with each other.

In order to treat the particle acceleration phenomenologically, it is useful to introduce the acceleration efficiency, η (Aharonian et al., 2002). It is defined as

$$\dot{E} = \frac{qBc}{\eta} \ , \tag{2.2}$$

where B/η is the projection of the electric field on the particle trajectory, that is, the effective acceleration electric field. It defines the acceleration time scale as

$$t_{\mathrm{acc}} \ = \ \frac{E}{\dot{E}} \tag{2.3}$$

$$= \ 0.11 \ [\mathrm{s}] \times \eta \left(\frac{B}{1 \ \mathrm{G}}\right)^{-1} \left(\frac{E}{1 \ \mathrm{TeV}}\right) \ . \tag{2.4}$$

In most of astrophysical environments, it is difficult to maintain static electric fields because they are screens out by the high electrical conductivity of ionized gases. Therefore, particles are accelerated by non-static electric fields or via stochastic processes. In both cases, Equation 2.2 is a useful representation for the particle accelerations in astrophysical context.

The energy of accelerated particles is limited by the size of the acceleration region R because the particle escapes from the acceleration region when its Larmor radius becomes

larger than R. Since the Larmor radius is defined as $E_{\max}/(qB)$, the electron energy is constrained as

$$E_{\mathrm{e}} < E_{\max} = qBR \ . \tag{2.5}$$

This constraint is called "Hillas criterion". The accelerated particles suffer from other physical processes *e.g.* radiative cooling. Such a process also limits the particle's energy. Therefore, in practice, the maximum electron energy can be smaller than the value in Equation 2.5.

2.7.1 Diffusive Shock Acceleration

The diffusive shock acceleration (DSA) was discovered in the late 1970s (Axford et al., 1977; Krymsky, 1977; Bell, 1978; Blandford & Ostriker, 1978) as an acceleration process in strong shock waves. Currently, the DSA is widely accepted as the standard acceleration mechanism because it successfully explains the energy distribution of the cosmic rays in a broad energy band. The DSA predicts the spectral index of the particle energy distribution as 2, which is consistent with those of many astrophysical objects. Furthermore, the spectral index does not depend on the detailed physical parameters of the shock region. Therefore, the DSA has been applied to many astrophysical environments *e.g.* supernova remnants and pulsar wind nebulae. Here, we describe the essence of the DSA briefly.

In the DSA, particles gain energy as it crosses the shock front and comes back many times. The particles obtain their energies proportional to their energy. The particle energy after k times of collision is described with a coefficient β as

$$E = E_0(1 + \beta)^k \ , \tag{2.6}$$

where E_0 is the initial energy of the particle. When the particle escapes from the acceleration region after a single collision with a probability of P, the total number of particles with energy E is

$$N_{>E} = N_0(1 - P)^k \ , \tag{2.7}$$

where N_0 is the number of particles at an initial moment. From Equation 2.6 and 2.7, the relation between $N_{>E}$ and E is given by

$$\frac{\ln\left(N_{>E}/N_0\right)}{\ln\left(E/E_0\right)} = \frac{\ln(1 - P)}{\ln(1 + \beta)} \tag{2.8}$$

$$N_{>E}/N_0 = (E/E_0)^{\ln(1-P)/\ln(1+\beta)} \ . \tag{2.9}$$

Since $N_{>E} = \int_E^\infty N(E)\mathrm{d}E$ the energy distribution of the accelerated particles is given by

$$N(E) \propto E^{-1-P/\beta} \ . \tag{2.10}$$

Here, we assumed that $P, \beta \ll 1$.

Next, we derive β and P in the DSA process. When the particles cross the shock front by angle θ which is the angle between the velocity of the particle and the normal vector of the shock plane, the particle gains energy at a rate of

$$\frac{\Delta E}{E} = 2 \left(\frac{V_1 - V_2}{c} \right) \cos\theta \ , \tag{2.11}$$

where V_1 and V_2 are the velocities of upstream/downstream flow respectively. Here we assumed that the particle is relativistic *i.e* $v = c$. Then, the coefficient β is calculated by averaging Equation 2.11 over θ such that

$$\beta = \left\langle \frac{\Delta E}{E} \right\rangle \tag{2.12}$$

$$= \frac{\int_0^{\pi/2} 2 \left(\frac{V_1 - V_2}{c} \right) \cos^2\theta \mathrm{d}(\cos\theta)}{\int_0^{\pi/2} \cos\theta \mathrm{d}(\cos\theta)} \tag{2.13}$$

$$= \frac{4}{3} \left(\frac{V_1 - V_2}{c} \right) \ . \tag{2.14}$$

The escape probability P is estimated simply by the ratio of the flux of the particles escaping with the downstream velocity to the flux of the particles entering the shock front. Hence

$$P = \frac{V_2}{c/4} \ . \tag{2.15}$$

From Equation 2.10, 2.14 and 2.15, the energy distribution is

$$N(E) \propto E^{-s}, \ s = \frac{V_1/V_2 + 2}{V_1/V_2 - 1} \ . \tag{2.16}$$

In shock regions, there is a relation between V_1 and V_2 given by the Rankine-Hugoniot equation (See Landau & Lifshitz 1987)

$$V_1/V_2 = \frac{(\gamma + 1)M_1^2}{(\gamma - 1)M_1^2 + 2} \ , \tag{2.17}$$

where γ is the heat capacity ratio, and M_1 is the Mach number of the upstream flow. In supernovae or pulsar wind nebulae, the shock velocity is considered to be much larger than the sound velocity ($M_1 \gg 1$). Thus, Equation 2.17 is valid in most of astrophysical environments. Finally, the energy distribution of the particle accelerated by the DSA process is

$$N(E) \propto E^{-2} \ . \tag{2.18}$$

Here we assumed non-relativistic gases in the flow ($\gamma = 5/3$).

Note that the above calculation above is only valid when the upstream flow is non-relativistic. In the relativistic case, the accelerated particle can be overtaken by the upstream flow if θ is large. This requires a more sophisticated treatment. The particle accelerations by a relativistic shock can be studied numerically, for example, by using particle-in-cell simulation (Sironi et al., 2015). They derived a characteristic energy spectral index of $\sim$ 2.2. Furthermore, the termination shock of pulsar wind nebulae is considered to be a good target for studying the relativistic shock because the pulsar wind has relativistic velocity. Atoyan & Aharonian (1996); Meyer et al. (2010) compared the spectrum observed from the Crab nebula with their synchrotron emission models, and estimated the injection index as 2.32 ± 0.01.

The acceleration time scale of the DSA process is estimated by Bednarz & Ostrowski (1996)

$$t_{acc} = \frac{3}{V_1 - V_2} \left(\frac{D_1}{V_1} - \frac{D_2}{V_2} \right) \tag{2.19}$$

$$= \frac{20D}{V_1^2} \tag{2.20}$$

where D is the diffusion coefficient. The fastest diffusion is achieved in the case of the Bohm limit $D(E) = r_g c/3$. Then the acceleration efficiency is

$$\eta \approx 6 \left(\frac{c}{V_1} \right)^2 \tag{2.21}$$

Therefore, even in extreme cases $V_1 \sim c$, it is difficult to reach η smaller than ~ 6.

2.7.2   Magnetic Reconnection Acceleration

Although the DSA process successfully explains a wide range of phenomena involving the particle accelerations, there are many other discussed proposed particle acceleration mechanisms. In some proposed acceleration processes, particles are accelerated along electric field lines. These processes are called "direct acceleration" in order to distinguish them from stochastical processes like the DSA. Here, we describe magnetic reconnection acceleration as a typical example of the direct acceleration.

The magnetic reconnection is a process in which the energy of the magnetic field in plasma is converted into the particle energy (Zenitani & Hoshino, 2001). Figure 2.15 shows a schematic picture of the magnetic reconnection. In some astrophysical environments, the
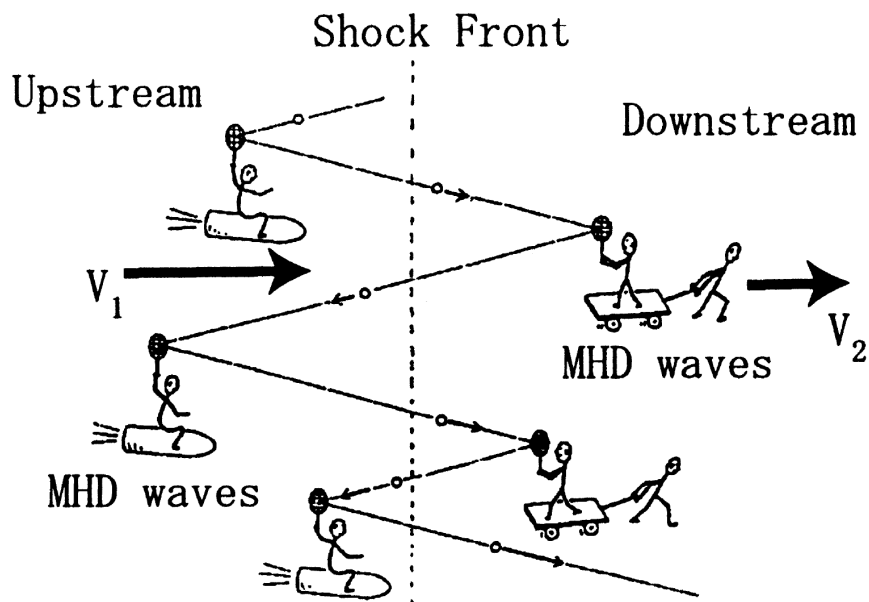
Figure 2.14: A sketch of the diffusive shock acceleration (Curtesy by M. Scholer).

magnetic reconnection has been considered intensively as a dominant process to produce non-thermal particles, for example, the heating process in the solar corona (Kopp & Pneuman, 1976) and the energy conversion of Poynting flux into particle energy in the pulsar wind (Lyubarsky & Kirk, 2001).

In order to explain the essence of the magnetic reconnection, we describe this acceleration process using a very simple approximation. Near the reconnection spot, particles are accelerated by electric field perpendicular to the reconnection plane (which is determined by directions of the magnetic field flow velocity)

$$\frac{\mathrm{d}\varepsilon}{\mathrm{d}t} \simeq qE_z c \; , \tag{2.22}$$

where ε is the particle energy and E_z is the strength of the acceleration electric field. The particles escape from the reconnection spot with a time scale of the same order of the gyro frequency. Hence

$$\frac{1}{N}\frac{\mathrm{d}N}{\mathrm{d}t} \simeq -\frac{qB_y}{mc\gamma} = \frac{qB_y c}{\varepsilon} \; , \tag{2.23}$$

where B_y is the strength of the reconnected magnetic field and N is the number of the accelerated particles. By combining Equation 2.22 and 2.23, we obtain the following equation

$$\frac{\mathrm{d}N}{\mathrm{d}\varepsilon} = -\frac{B_y}{E_z}\frac{N}{\varepsilon} \; . \tag{2.24}$$

Finally, by solving the above equation, the energy distribution is

$$N \quad \propto \quad \varepsilon^{-s}, \ s = B_y/E_z \ . \tag{2.25}$$

In the reconnection spot, the acceleration electric field is considered to be comparable with the magnetic field ($B_z \simeq E_y$). Therefore, the spectral index is ~ 1, which is smaller than that of the DSA. Furthermore, the acceleration efficiency η can be comparable to ~ 1 since the particles are accelerated by the electric field comparable to the magnetic field. Using a particle-in-cell simulation, Zenitani & Hoshino (2001) reported that the electric field is 0.3 times as large as the magnetic field.

In the magnetic reconnection, the particle with higher energy can be accelerated effectively compared with the DSA process. It is explained briefly as follows. The Larmor radius becomes larger as the energy of the charged particle becomes higher. As the particle acquires its energy, its trajectory becomes straighter. As a result, the particle with higher energy can stay in the acceleration region for a longer time, and gain more energy. This positive feedback achieves the efficient acceleration for higher energy.

In practice, the magnetic reconnection is much more complicated than what we described above. For example, the particle energy distribution depends on the structure of magnetic/electric fields. When the magnetic field close to the reconnection spot is described as

$$B_y(x) \propto |x|^p \frac{x}{|x|} \ , \tag{2.26}$$

the particle energy distribution becomes an exponential function or a powerlaw function if $p = 1$ or $p > 1$ respectively (Bulanov & Sasorov, 1976; Romanova & Lovelace, 1992).

As an example of magnetic reconnection in astrophysics, we explain reconnection events around the Earth. Figure 2.16 shows magnetic field lines around the Earth. Between the Sun and the Earth, a bow shock is formed due to interaction between solar winds and the magnetic field of the Earth. Then, the bow shock reconfigures the structure of the magnetic field. As a result, there are two spots where magnetic reconnection takes place. We show these spots as the red circles in Figure 2.16. One is located on the dayside of the Earth (A in the figure), and the other is located on the nightside of the Earth (B in the figure). In these spots, electrons are accelerated up to several keV (Øieroset et al., 2001). Then, they flow into the magnetic poles of the Earth along the magnetic field, which produces the aurora emission around the pole (Kivelson & Russell, 1995).
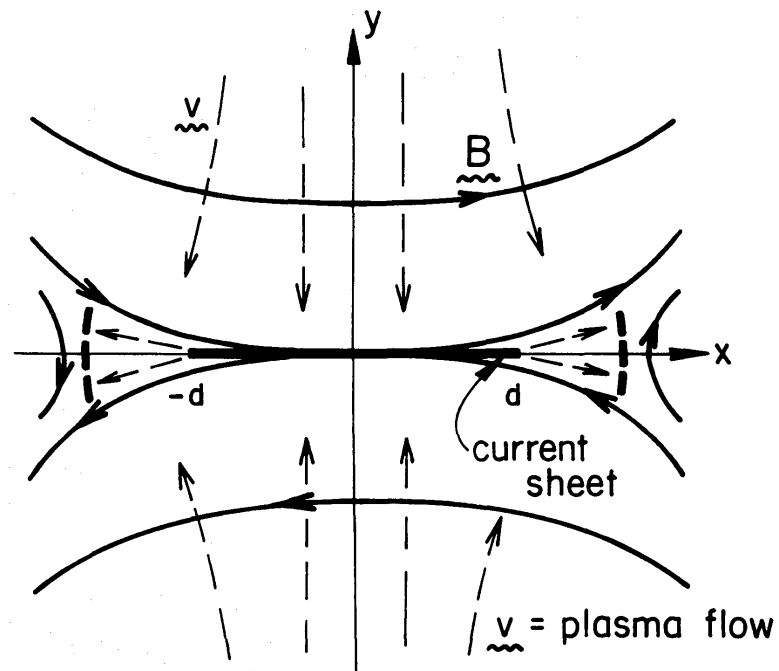
Figure 2.15: A sketch of the magnetic reconnection (taken from Romanova & Lovelace 1992). The charged particles flow into the reconnection spot from $y = \pm\infty$. They are accelerated around $(x, y) = (0, 0)$ by the induced electric fields, and leave the reconnection spot towards $x = \pm\infty$.
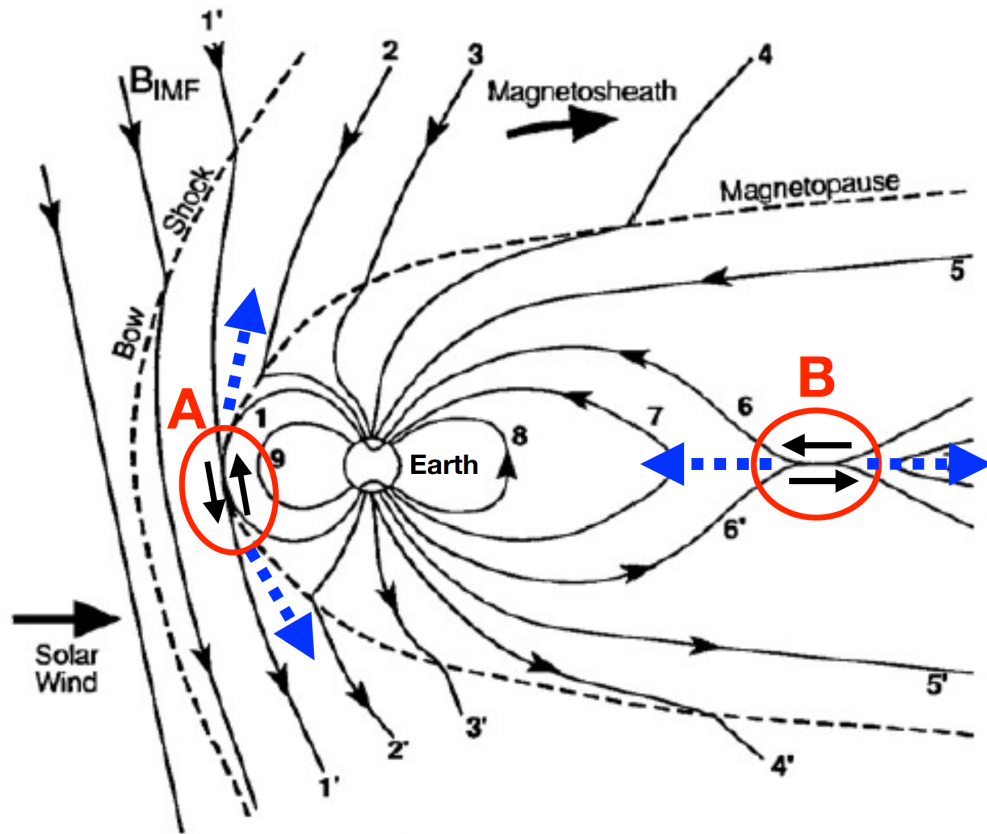
Figure 2.16: Solar wind-driven magnetic reconnection around the earth (taken from Kivelson & Russell 1995). The magnetic reconnection takes place at the spots surrounded by the red circles. In these spots, anti-parallel magnetic field lines are formed. Accelerated particles leave the reconnection spots forming a bipolar jet structure (the blue lines).

2.8 Radiative and Cooling Processes of Non-Thermal Particles

Non-thermal particles lose their energies and radiate gamma rays through several radiative processes. Therefore, the gamma-ray spectrum from astrophysical objects brings us information about the physical properties *i.e.* the magnetic field or the maximum electron energy. Here, we describe important processes related to the emission from LS 5039.

2.8.1 Synchrotron Radiation

Charged particles in magnetic fields are accelerated by the Lorentz force, which results in gamma-ray radiation. If the particles are relativistic, this radiation process is known as synchrotron radiation. Here, we summarize important features of synchrotron radiation (See for details in Rybicki & Lightman 1986).

The total power per frequency of synchrotron radiation by a single electron is

$$P(\omega) = \frac{\sqrt{3}q^3 B \sin\alpha}{2\pi m_e c^2} F\left(\frac{\omega}{\omega_c}\right) \, , \tag{2.27}$$

where

$$F(x) = x \int_x^\infty K_{5/3}(x')dx' \tag{2.28}$$

$$\hbar\omega_c = \frac{3}{4\pi} \frac{hqB \sin\alpha}{m_e c} \gamma^2 \, , \tag{2.29}$$

and $K_{5/3}(x)$ is the modified Bessel function of $5/3$ order and α is an angle between a pitch angle. The maximum of $F(x)$ is realized at $x = 0.29$. Thus, the typical energy of synchrotron radiation from an electron with an energy of E_e is

$$h\nu_{\text{sync}} = 19.2 \text{ keV} \times \left(\frac{B}{1 \text{ G}}\right) \left(\frac{E_e}{1 \text{ TeV}}\right)^2 \, . \tag{2.30}$$

In astrophysical environments, accelerated electrons are usually distributed with powerlaw distribution. Here, we describe the electron distribution as

$$N(E_e)dE_e \propto E_e^{-p}dE_e \, . \tag{2.31}$$

Then, the photon flux per energy of photon is

$$
\begin{aligned}
I(E_\gamma) &= \frac{1}{E_\gamma} \int P(\omega)N(E_e)dE_e & (2.32)\\
&\propto E_\gamma^{-(p+1)/2} \, . & (2.33)
\end{aligned}
$$

Hence, the photon index Γ of the synchrotron emission is

$$\Gamma = \frac{p+1}{2} \ . \tag{2.34}$$

Since the photon index can be measured from observations, it is a key parameter to investigate particle energy distributions.

Total power via synchrotron emission from a single electron with an energy of E_e is

$$\dot{\gamma}_{\text{sync}} = -\frac{1}{6\pi}\frac{\sigma_{\text{T}}B^2}{m_ec}\gamma^2 \tag{2.35}$$

$$= -\frac{4}{3}\frac{\sigma_{\text{T}}}{m_ec}U_{\text{B}}\gamma^2 \ , \tag{2.36}$$

where σ_{T} is the Thomson cross section and U_{B} is the energy density of the magnetic field. Then, the cooling time scale of the synchrotron emission is

$$t_{\text{sync}} = \frac{\gamma}{\dot{\gamma}_{\text{sync}}} \tag{2.37}$$

$$= 4.0 \times 10^2 \ [\text{s}] \times \left(\frac{B}{1\ \text{G}}\right)^{-2}\left(\frac{E_e}{1\ \text{TeV}}\right) \ . \tag{2.38}$$

In synchrotron radiation, $\gamma^{-2}\dot{\gamma}_{\text{sync}}$ is constant. On the other hand, in inverse Compton emission, $\gamma^{-2}\dot{\gamma}_{\text{IC}}$ decreases with electron energy when it is in the Klein-Nishina regime. Therefore, synchrotron cooling often determines the maximum energy of electrons. It is estimated by calculating the condition in which the acceleration time is the same as the synchrotron cooling time scale

$$-\dot{\gamma}_{\text{sync}} = \dot{\gamma}_{\text{acc}} \tag{2.39}$$

$$E_{\text{max}} = 59.6 \ \text{TeV} \times \left(\frac{B}{1\ \text{G}}\right)^{-1/2} \times \eta^{-1/2} \ . \tag{2.40}$$

The maximum electron energy determines the cut-off energy of the synchrotron spectrum. From Equation 2.30 and 2.40, it is

$$h\nu = 67 \ \text{MeV} \times \eta^{-1} \ . \tag{2.41}$$

The cut-off energy is solely determined by the acceleration efficiency. It does not depend on the strength of the magnetic field.

2.8.2   Inverse Compton Scattering

Compton scattering is a process in which a charged particle is scattered by a high-energy photon. After the scattering, the photon energy is

$$E_{\gamma}' = \frac{E_{\gamma}}{1 + \frac{E_{\gamma}}{m_ec^2}(1 - \cos\theta)} \ , \tag{2.42}$$

where θ is a scattering angle and E'_γ and E_γ is the photon energy after/before the scattering. In high energy astrophysics, the inverse process is often important *i.e.* low energy photons are scattered by accelerated particles. This process is known as inverse Compton scattering. The scattered gamma-ray energy can acquire energy of $\sim \gamma^2\varepsilon$, where γ is a Lorentz factor of the high energy particle and ε is the seed photon energy. If the particle energy is 1 TeV and the photon energy is 1 eV, then the scattered photon has an energy of ~ 1 TeV. Therefore, it is an efficient process to produce TeV gamma rays.

The cross section of inverse Compton scattering is described in a simple form within less than 10% accuracy (Coppi & Blandford, 1990)

$$\sigma_{\rm IC} = \frac{3\sigma_{\rm T}}{8\kappa_0}\left[\left(1 - \frac{2}{\kappa_0} - \frac{2}{\kappa_0^2}\right)\ln\left(1 + 2\kappa_0\right) + \frac{1}{2} + \frac{4}{\kappa_0} - \frac{1}{2(1 + 2\kappa_0)^2}\right] \tag{2.43}$$

$$\kappa_0 = \gamma\frac{\varepsilon}{m_ec^2} \ . \tag{2.44}$$

In the relativistic regime ($\kappa_0 \gg 1$) $\sigma_{\rm IC} \simeq (3/8)\sigma_{\rm T}\kappa_0^{-1}\ln(4\kappa_0)$, while in the non-relativistic regime ($\kappa_0 \ll 1$) $\sigma_{\rm IC} \simeq \sigma_{\rm T}(1 - \kappa_0)$. In the relativistic regime, the cross section significantly decreases.

When the photon energy in the rest frame of the particle is in Thomson scattering regime *i.e.* $\gamma\varepsilon \ll m_ec^2$, the total power via inverse Compton scattering from a single electron with an energy of E_e is

$$\dot{\gamma}_{\rm IC} = -\frac{4}{3}\frac{\sigma_{\rm T}}{m_ec}U_{\rm ph}\gamma^2 \ , \tag{2.45}$$

where $U_{\rm ph}$ is the photon energy density. In this case, the cooling time scale of inverse Compton scattering is derived as

$$t_{\rm IC} = 1.6 \times 10^{-1} \ [{\rm s}] \times \left(\frac{U_{\rm ph}}{100 \ {\rm erg} \ {\rm cm}^{-3}}\right)^{-1}\left(\frac{E_e}{1 \ {\rm TeV}}\right) \ . \tag{2.46}$$

When $\gamma\varepsilon$ starts to be comparable to m_ec^2, then cross section of inverse Compton scattering decreases. In LS 5039, the luminosity of the massive star is $\sim 7 \times 10^{38}$ erg s^{-1} with a temperature of 3.9×10^4 K (Casares et al., 2005). Thus, the compact object in LS 5039 is surrounded by UV photons which can be the seed photons of inverse Compton emission. The TeV gamma rays from LS 5039 is produced in the relativistic regime since $\kappa_0 \gg 1$. Therefore, the cooling time of inverse Compton emission is much longer than Equation 2.46. Khangulyan et al. (2008) approximated it as

$$t_{\rm IC} = 1.7 \times 10^2 \ [{\rm s}] \times \left(\frac{U_{\rm ph}}{100 \ {\rm erg} \ {\rm cm}^{-3}}\right)^{-1}\left(\frac{E_e}{1 \ {\rm TeV}}\right)^{0.7} \ . \tag{2.47}$$

2.8.3 Gamma-Gamma Absorption

Gamma-gamma absorption is a process in which two colliding photons are converted into an electron positron pair such that

$$\gamma + \gamma \longrightarrow e^+ + e^- \ . \tag{2.48}$$

From kinematics, this process can occur only under the condition that

$$\varepsilon_1 \varepsilon_2 (1 - \cos\theta) > (m_e c^2)^2 \ , \tag{2.49}$$

where $\varepsilon_{1,2}$ are the energy of colliding photons and θ is the colliding angle. Since LS 5039 harbors an O star with a temperature of 3.9×10^4 K, the threshold energy is calculated

$$\varepsilon \gtrsim 80 \ \text{GeV} \ . \tag{2.50}$$

Therefore, TeV gamma rays of LS 5039 are strongly absorbed by the UV photons emitted from the O star.

Within less than 3% accuracy (Aharonian, 2004), the cross section of gamma-gamma absorption is described by

$$\sigma_{\gamma\gamma} = \frac{3\sigma_T}{2s_0^2} \left[\left(s_0 + \frac{1}{2}\ln s_0 - \frac{1}{6} + \frac{1}{2s_0} \right) \ln\left(\sqrt{s_0} + \sqrt{s_0 - 1}\right) \right. \tag{2.51}$$
$$\left. - \left(s_0 + \frac{4}{9} - \frac{1}{9s_0} \right) \sqrt{1 - \frac{1}{s_0}} \right]$$

$$s_0 = \frac{\varepsilon_\gamma \varepsilon_0}{(m_e c^2)^2} \ , \tag{2.52}$$

where ε_γ and ε_0 are energies of a primary and a target photon, respectively. The maximum value of the cross section is about 0.2 σ_T which is achieved at $s_0 \simeq 3.5 - 4$.

Since the gamma-gamma absorption strongly depends on the colliding angle, the absorption effect varies with the orbital phase. Figure 2.17 shows the gamma-gamma absorption map of LS 5039 (Dubus, 2006). When the inclination angle is 90 degrees as shown in the figure, almost all of the 300 GeV gamma rays are absorbed around the inferior conjunction. It also depends on the inclination angle of the system and the location where gamma rays are produced. Figure 2.18 shows attenuation of gamma rays with different inclination angles. Here, gamma rays are assumed to be produced at the location of the compact star.

2.8.4 Adiabatic Cooling

When the acceleration/emission region is expanding, the accelerated particles lose their energy through adiabatic losses. Since LS 5039 is a compact system, the adiabatic cooling may have a non-negligible effect on the particle energy distribution.
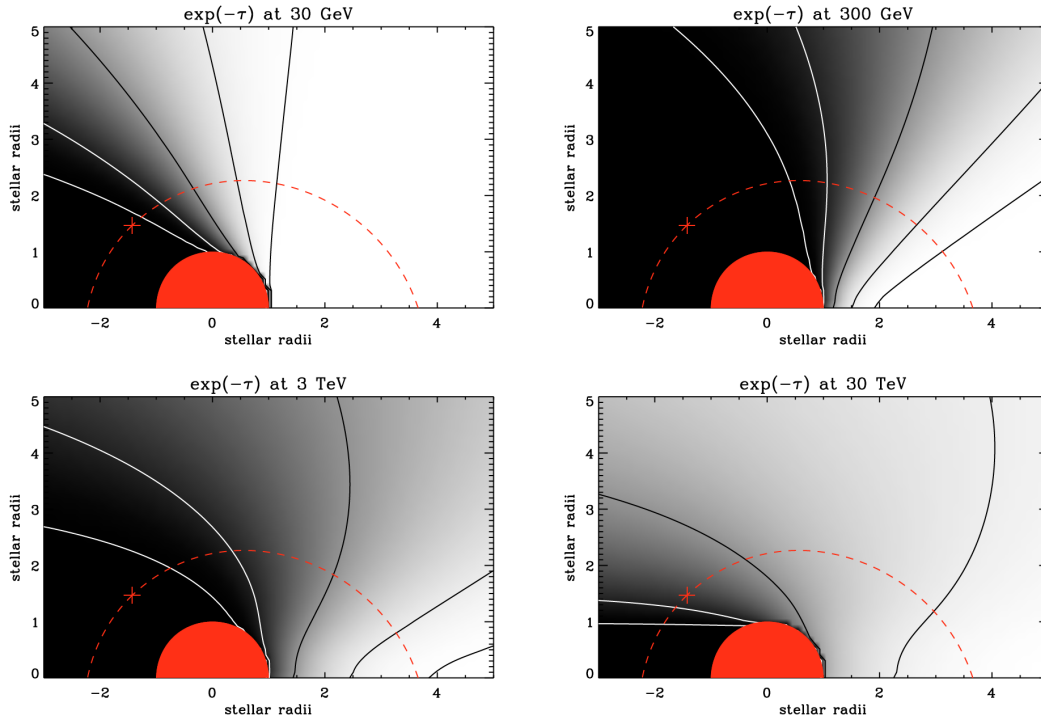
Figure 2.17: Gamma-gamma attenuation map around a massive star (Dubus, 2006). The grey-scale corresponds to the integrated absorption seen by a photon emitted at each location. An observer located at infinity is to the right. Solid lines are contours corresponding to 99%, 90%, 50%, 10% and 1% absorption. The star has a 10 R$_\odot$ radius and has an effective temperature of 40000 K. The orbit of LS 5039 is shown as a dotted red line.
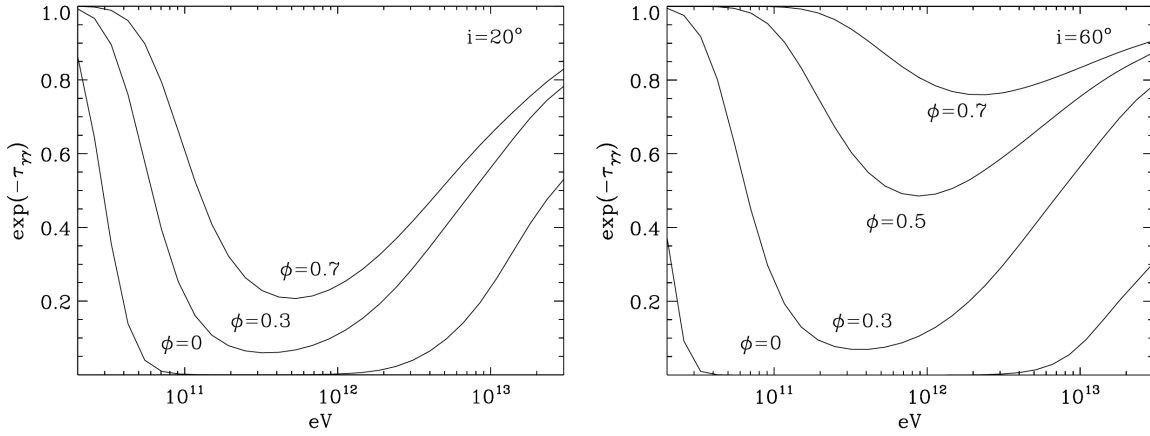
Figure 2.18: Gamma-ray attenuation in LS 5039 (Dubus, 2006). Here, it is assumed that gamma rays are emitted isotropically at the location of the compact object. i is the inclination angle. $i = 60$ and 20 degrees correspond to a canonical neutron star and a black hole of 4.5 $M_\odot$.

The internal energy $U = nVE$ decreases as the acceleration/emission region expands, where n, V are the density and volume of the expanding region and E is the particle energy. In adiabatic losses, the decrease of the internal energy is

$$dU = -p dV \; , \tag{2.53}$$

where p is the pressure of the expanding gas. In the relativistic case, $U = 3nkTV$ and $p = U/(3V)$ (Longair, 2011). Then

$$dU = nV dE = -\frac{1}{3}\frac{U}{V}dV \tag{2.54}$$

$$\frac{dE}{dt} = -\frac{1}{3}\frac{E}{V}\frac{dV}{dt} \; . \tag{2.55}$$

When the expansion is isotropic and relativistic, $dR/dt = c$. Hence, the adiabatic loss rate is

$$\frac{dV}{dt} = \frac{d}{dt}\left(\frac{4\pi}{3}\pi R^3\right) = 3\frac{cV}{R} \tag{2.56}$$

$$\frac{dE}{dt} = -\frac{cE}{R} \; . \tag{2.57}$$

The cooling rate is proportional to E while those of synchrotron and inverse Compton emission are proportional to square of E.

Since the system size of LS 5039 is ~ 50 light-sec, the typical cooling time due to adiabatic cooling is

$$t_{\mathrm{adia}} = 50.0 \ [\mathrm{s}] \times \left(\frac{R}{50 \ [\mathrm{light \ sec}]} \right) \ . \tag{2.58}$$

In LS 5039, it can be comparable to the time scale of the synchrotron and inverse Compton losses. Therefore, the adiabatic cooling can have an important impact on the formation of the particle energy distribution.

Chapter 3

Instrumentation

In this thesis, we observationally study the X-ray and GeV emission from LS 5039, utilizing three observatories, *Suzaku*, *NuSTAR* and *Fermi*. Here, we briefly overview the onboard instruments of each observatory.

3.1 The X-ray Observatory *Suzaku*

3.1.1 Overview

Suzaku, formerly named Astro-E2, is the fifth Japanese X-ray astronomy satellite (Mitsuda et al., 2007). It was launched on 2005 July 10 attached to the M-V launch vehicle from Uchinoura Space Center, a space launch facility of JAXA (Japan Aerospace Exporation Agency), and operated until 2015. The orbit of *Suzaku* is almost circular at 570 km altitude with an inclination angle of 31 degrees. Its orbital period is about 96 minutes.

The *Suzaku* consists of three co-aligned instruments of the X-ray observations (see Figure 3.1). The first instrument is the X-ray Imaging Spectrometer (XIS) consisting of four X-ray sensitive imaging CCD cameras. Each CCD camera has 1024×1024 pixels, with a pixel size of 24×24 μm. The size of the CCD is 25×25 mm^2, which covers a 17.8'×17.8' region of the sky. The three CCD cameras are front-illuminated CCDs covering the energy range of 0.4–12 keV, and the other CCD camera is a back-illuminated CCD, covering the energy range of 0.2–12 keV. Each camera is located in the focal plane of the X-ray Telescope (XRT). The XRT is a thin foil nested Wolter-I type telescope. Each nested shell is 152 μm thickness aluminum coated by a thin (> 1000 Å) gold layer. The angular resolutions of the XRT range from 1'.8 to 2'.3 (HPD), and the field of view is 17' at 1.5 keV and 13' at 8 keV.

The second instrument is the X-ray Spectrometer (XRS). It is the first X-ray microcalorime-

Table 3.1: Performance of *Suzaku* observatory (Mitsuda et al., 2007)

Instrument	Parameter	Value
XRT	Focal length	4.75 m
	Field of view	$17'$ at 1.5 keV
		$13'$ at 8 keV
	Angular resolution	$2'$ (HPD)
XIS	Field of view	$17.'8 \times 17.'8$
	Energy Range	0.2–12 keV
	Energy resolution	$\sim$130eV at 6 keV (FWHM)
	Effective area	330 cm^2 (FI), 370 cm^2 (BI) at 1.5 keV
HXD	Field of view	$4°.5 \times 4°.5$ ($>$ 100 keV)
		$34' \times 34'$ ($<$ 100 keV)
	Energy Range	10–600 keV
	– PIN	10–70 keV
	– GSO	40–600 keV
	Energy resolution (PIN)	$\sim$3.0 keV (FWHM)
	Energy resolution (GSO)	$7.6/\sqrt{E_\mathrm{MeV}}\%$ (FWHM)
	Effective area	$\sim$160cm^2 at 20 keV, $\sim$260cm^2 at 100 keV
	Time resolution	61μs

ter in orbit, and has a high energy resolution of $\sim$ 6 eV. However, due to the accidental evaporation of the liquid helium soon after the launch, it became impossible to cool down the XRS system. Thus, the XRS did not observe any astrophysical objects.

The Hard X-ray Detector (HXD) is a non-imaging collimated hard X-ray detector. It covers an energy range of 10–600 keV. A telescope which focuses hard X-ray was not available during the development of *Suzaku*. In order to achieve the high-sensitivity without the focusing optics, two new techniques were adopted for the HXD. One is Well-type active shield. The detector shielding is shaped like a well, and the main detectors, the silicon PIN diodes, are surrounded by the active shields. The second technique is a compound eye configuration. The main detector part of the HXD consists of 16 units. By placing the units in a matrix, the effective area of the HXD is increased. In addition to this, each unit can be used for the active shield of adjacent units.

The performance of *Suzaku* is summarized in Table 3.1. In this thesis, we analyzed the data taken by the HXD-PIN. In the following sections, we describe the details of the HXD.
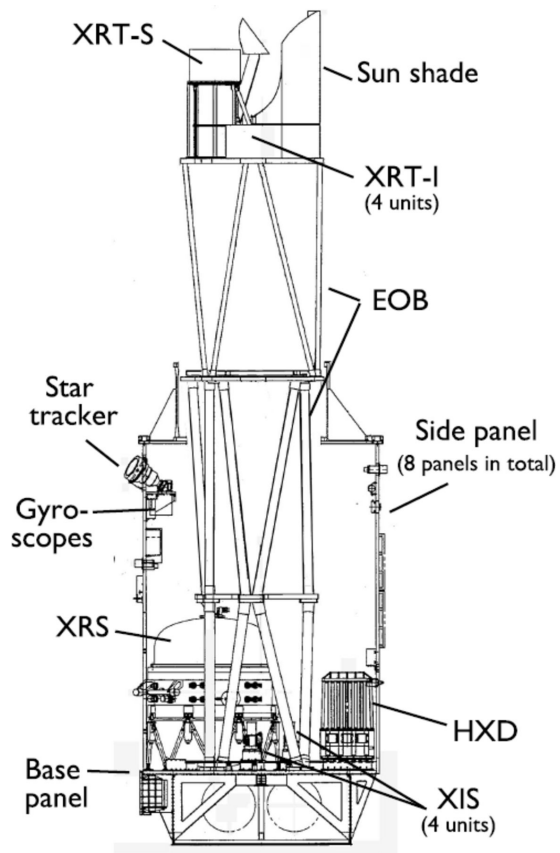
Figure 3.1: Left: A schematic of *Suzaku*, Right: A picture of HXD before installation.

3.1.2   HXD

The HXD was developed for the observation of hard X-rays from 10 keV to 600 keV using a non-imaging and collimated detector (Takahashi et al., 2007). Figure 3.2 shows a schematic of the HXD. The HXD consists of 32 modules; inner 16 are well-counters and the outer 20 are aniti-counters. The well-counter contains three materials for X-ray detection. The main detector is made of silicon PIN diodes with a thickness of 2 mm, which can detect the hard X-rays below $\sim$ 70 keV. Under the silicon PIN diodes, a gadolinium silicate crystal (GSO) detectors are assembled. The PIN and GSO detectors are located at the bottom of a well-shape bismuth germanate crystal (BGO) detector. Then, the main detector is surrounded by the well-shape active shield. This configuration is a key technique (Well-type active shield) to reduce the background level.

The GSO and BGO detectors are read out by a single photomultiplier. Since the two crystals have different decay times (GSO: 122 ns, BGO: 706 ns at -20 degree), the signals from both detectors can be distinguished (phoswich configuration). The well-counter units are arranged in a 4×4 matrix (the compound eye configuration). This configuration has two advantages. The first is that it increases the photon collection area, while the second is that a well-counter unit can also be used as an active shield for its neighboring well-counter units. The well-counter units are surrounded by 20 anti-coincidence counter unit consisting of BGO detectors.

In the hard X-ray band, one of the dominant background components is the cosmic X-ray background (CXB). In order to reduce the CXB, passive shields called "fine collimators", are inserted in the BGO well-type detector above the PIN diodes. The direction of incoming X-rays is constrained by the collimator in order to suppress the contamination from the CXB. The fine collimator is made of 50 μm thick phosphor bronze sheets which form an 8×8 square channels that are 3 mm in width and 300 mm in length. Below $\sim$ 100 keV, the fine collimator determines the field of view of the HXD as 34'×34'. Above 100 keV, the collimators become transparent to the X-rays, and the field of view increases to $4.5° \times 4.5°$ which is determined by the well shape of the BGO detector. The resulting effective areas of the PIN and BSO detectors are shown in Figure 3.3.

3.1.3   Background Model of HXD-PIN

The majority of the HXD background is caused by the non X-ray background (NXB), primary and secondary cosmic rays, atmospheric albedo neutrons, natural radioactive isotopes, and
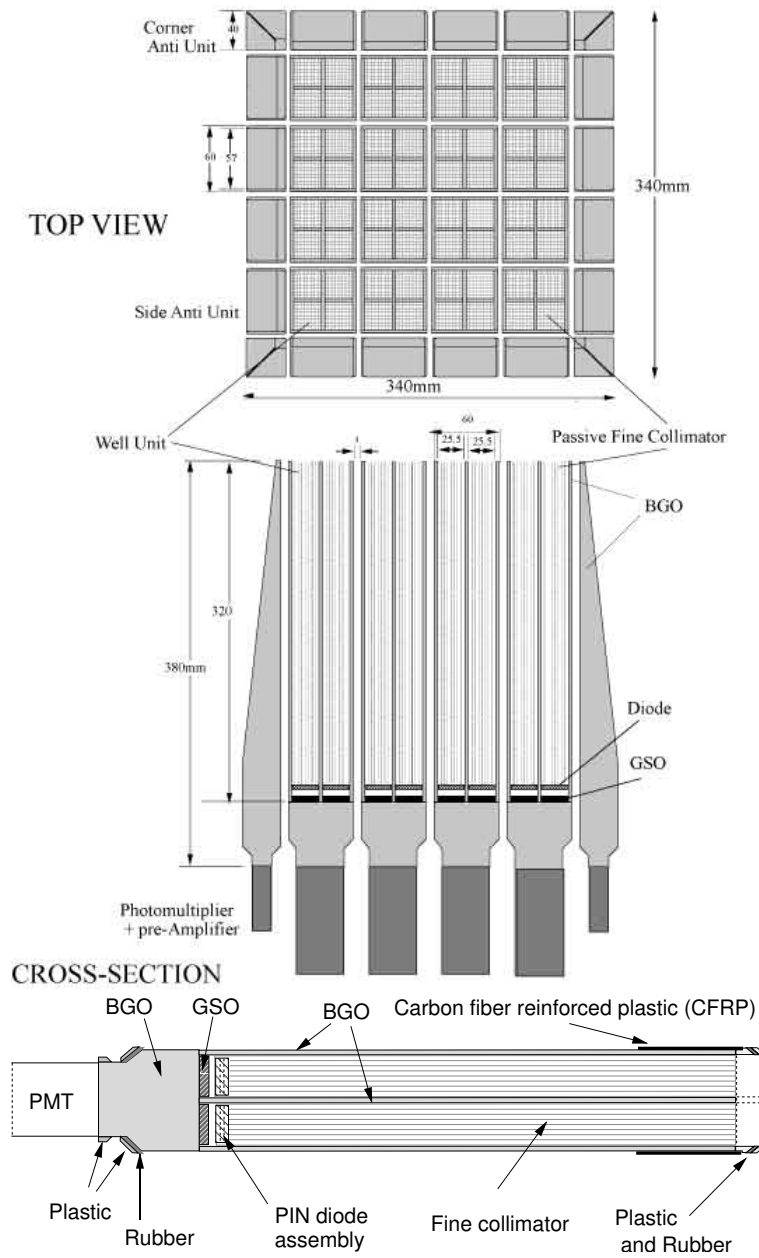
Figure 3.2: A schematic of HXD. Inner 16 modules are well-counters, and the outer 20 modules are anti-counters. The bottom figure is a schematic of the well-counter.
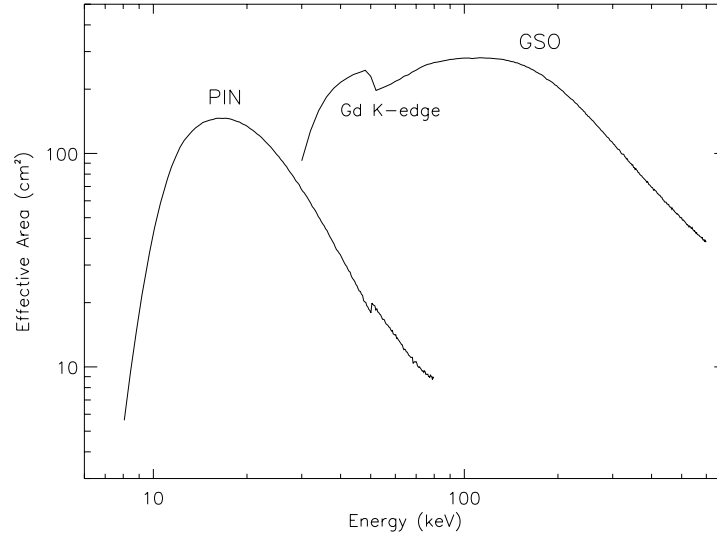
Figure 3.3: The effective area of the HXD detector, PIN and GSO.

SAA-induced radio isotopes. The SAA is the South Atlantic Anomaly (SAA) where the charged particles are trapped and concentrated by the magnetic field of the earth. In the observation of LS 5039, the NXB background is higher than the source flux by a factor of ~ 12. Since the count rate of the NXB depends on the flux of in-coming particles and the number of activated isotopes in the instrument, the background of the HXD varies strongly with time. The NXB background is mainly determined by two parameters: one is the geomagnetic cutoff rigidity, which determines the background effect due to primary cosmic rays and atmospheric neutrons. This background can be well tracked by PINUD which is the count rate of the upper discriminator signal of the PIN at a threshold energy of ~ 90 keV. Second is the exponential-decay components from the activated material by SAA protons. It can be monitored by the hit count of PINUD integrated during the SAA. Fukazawa et al. (2009) modeled the NXB background of HXD-PIN mainly using these two parameters. There are two available models based on different methods (`PINUDLCUNIT` and `LCFITDT`). In the latter one, the background light curve is modeled based on the additional parameters *e.g.* the 450-700 keV GSO count rate. In this thesis, we adopt the background model based on `LCFITDT`.

3.2 The X-ray Observatory *NuSTAR*

3.2.1 Overview

The *Nuclear Spectroscopic Telescope Array* (*NuSTAR*, Figure 3.4) is the first orbital mission of the observation using the hard X-ray focusing telescope and a solid state CdZnTe pixel detector. These new technologies enable hard X-ray observations with high sensitivity from 3 keV to 79 keV (see Figure 3.5 Left).

The *NuSTAR* observatory was launched on 2012 June 13 on a Pegasus XL vehicle. The launch site was the Reagan Test Site on the Kawajalein Atoll in the South Pacific in order to deploy it into a low-inclination angle ~ 6 degrees. The advantage of a low-inclination angle is that it can minimize the passage through the SAA. As a result, it suppresses the background due to the charged particles and the instrumental material activated by them. The altitude and the period of its orbit are from 610 to 650 km, and 97.126 minutes. The *NuSTAR* observatory has no consumables, thus the mission lifetime is determined by the decay of the orbit which is about 10 years. It consists of two co-aligned hard X-ray telescopes. The optics and the focal plane modules in each telescope are described in the following sections. The performance of *NuSTAR* is summarized in Table 3.2.

3.2.2 Optics

The two optics modules in *NuSTAR* contain 133 nested multilayer-coated grazing incidence shells in a conical approximation to a Wolter-I geometry. Each shell consists of 12 or 24 thin (0.2 mm) sheet glass segments. The optics are coated with depth-graded multi-layer structure designed to optimize the broadband energy response and FoV. The coating materials are Pt/C for the inner 89 shells and W/Si for the outer 44 shells.

Due to small graze angles of the optics, the image brightness gets darker when the photon enters off-axis. This effect becomes noticeable above 2'. By combining the reflectivity of the multilayers, which depends on the incoming angle and the energy of X-rays, the FoV of the optics is determined to be 10' at 10 keV and 6' at 68 keV. The point spread function of the optics is determined mainly by the figure errors in the substrates and in the mounting technique.

The focal length of the optics is 10.14 m. To achieve the large focal length, the optics and the focal plane modules are separated by a deployable mast. Thermal conditions which vary during the observations change the alignment of the optics and focal plane benches, resulting in a movement of the location of the optical axis. In order to correct this effect, each optics

Table 3.2: Performance of *NuSTAR* observatory (Harrison et al., 2013)

Parameter	Value
Energy range	$3 - 78.4$ keV
Angular resolution (HPD)	58"
Angular resolution (FWHM)	18"
FoV (50% resp.) at 10 keV	10'
FoV (50% resp.) at 68 keV	6'
Sensitivity ($6 - 10$ keV) [10^6 s, 3σ, $\Delta E/E = 0.5$]	2×10^{-15} erg cm^{-2} s^{-1}
Sensitivity ($10 - 30$ keV) [10^6 s, 3σ, $\Delta E/E = 0.5$]	1×10^{-14} erg cm^{-2} s^{-1}
Energy resolution (FWHM)	400 eV at 10 keV, 900 eV at 68 keV
Timing resolution	10 μs

or focal plane modules has a star tracker and two metrology laser units. The information from them is used to reconstruct the instantaneous alignment and pointing direction of the instrument.

3.2.3   Focal Plane

Each of the two focal plane modules consists of a solid state CdZnTe pixel detector. It is surrounded by a CsI anti-coincidence detector in order to identify background events. The focal plane modules are named FMPA and FMPB, and they consist of 2×2 array of detectors (see Figure 3.5 Right). A single array is a 32×32 pixel detector with a pixel size of 0.6 mm. The timing resolution of the detector is about 2 μs. However, it is found that the timing recorded on *NuSTAR* drifts depending on changing thermal conditions within the satellite. Due to this issue, the resulting timing resolution is about 10 μs. The pulse pile up does not occur until the source flux becomes larger than $\sim 10^5$ count s^{-1}. During the observation of LS 5039 we used in this thesis, the flux is much lower than this threshold. Therefore, the pile up effect is negligible in our analysis.

3.3   *Fermi* Gamma-ray Space Telescope

3.3.1   Overview

Fermi Gamma-ray Space Telescope is a mission designed for the all-sky survey in high energy gamma-rays. The telescope has two instruments; the Large Area Telescope (LAT, Figure 3.6)

Metrology
lasers

Deployed mast

Focal plane bench

Optics
modules

Instrument star tracker

Focal plane
detector
module (1 of 2)

Metrology
detector (1 of 2)

Mast canister
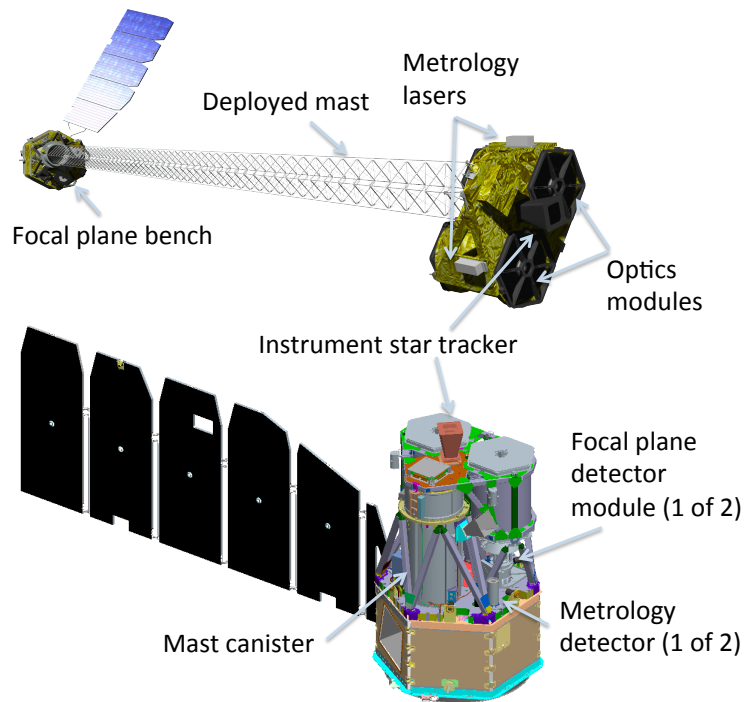
Figure 3.4: A schematic of *NuSTAR* observatory (Harrison et al., 2013)
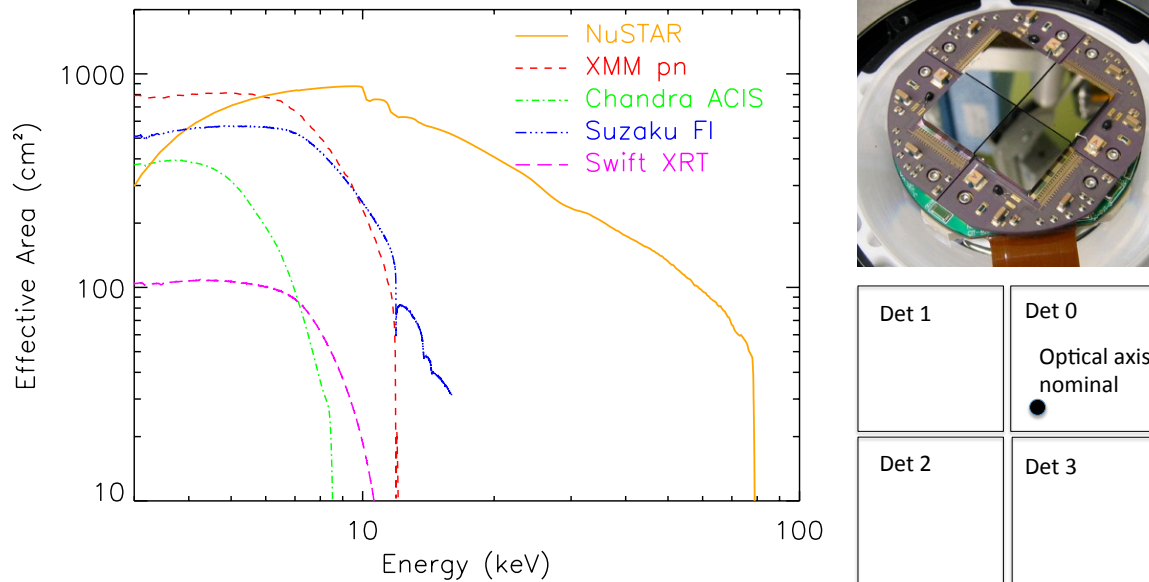
Figure 3.5: Left: Effective area of *NuSTAR* compared with the previous focusing X-ray telescopes. Right: A picture of the focal plane of *NuSTAR* (Harrison et al., 2013)

and the Gamma-ray Burst Monitor (GBM). The LAT is a wide field-of-view imaging telescope for the high energy gamma-rays from ~ 20 MeV to more than 300 GeV. The GBM consists of two types of detectors; sodium iodide (NaI) scintillators and cylindrical bismuth germanate (BGO) scintillators. The GBM is designed for detection and localization of the transient phenomena *e.g.* gamma-ray bursts, solar flares. It covers the energy range of ~ 150 keV to ~ 30 MeV.

The *Fermi* was launched in 2008 June 11 from Cape Canavera on a Delta II Heavy launch vehicle. The *Fermi* resides in a near circular orbit with an altitude of ~ 565 km, and with an inclination angle of $25.5°$. The orbital period is 96.5 minutes. While the mission design lifetime was determined to be for a minimum of 5 years, with a possible lifetime of 10 years, the *Fermi* is still being successfully operated over the mission lifetime.

While *Fermi* has several observing modes, it is operated in survey mode for most of the mission time (*e.g.* >80% of the observing time). In a standard survey mode, the uniform sky exposure is achieved about 3 hours. The dependence of the sensitivity on the observation time is shown in Figure 3.7. When *Fermi* is scanning through the SAA, the instruments lower the voltage on their photomultiplier tubes. Thus, *Fermi* does not take any scientific data in the SAA passage, which costs $\sim 15\%$ of the LAT's and GBM's potential observing time.

In the following sections, we describe details of the LAT and the data set which we analyzed in this thesis. The performance of the LAT is summarized in Table 3.3.

3.3.2 Large Area Telescope

The LAT is a pair-conversion telescope which measures the tracks of the electron and positron produced by the in-coming gamma-rays (Atwood et al., 2009). It consists of a 4×4 array of 16 modules. Each module is made up of a precision converter-tracker and calorimeter. The array of the modules is covered by a segmented anticoincidence detector in order to distinguish the background produced by charged particles such as those from primary cosmic rays.

Each converter-tracker has 18 XY tracker planes. Each plane has an array of two single-sided silicon strip tracking detectors (SSDs), in order to measure the direction of the charged particles. The single-sided silicon strip detector has 384 56-μm aluminum strips with 228 μm pitch. Its area and thickness are 8.95×8.95 cm^2 and 400 μm, respectively. The first 12 planes have tungsten plates 0.035 radiation lengths thick in front of the SSDs, and the next 4 planes have tungsten plates 0.18 radiation lengths thick. The last 2 planes do not have any converters. The design concept is that the incoming gamma-rays are converted into $e^- e^+$ pairs in the tungsten plates, and they are tracked by the SSDs.

Each calorimeter module has 96 CsI(Tl) crystals which have a volume of $2.7 \times 2.0 \times 32.6$ cm^3. They are used to measure the energy deposition due to the electromagnetic particle shower produced by the $e^- e^+$ pairs. In addition to this, it can image the shower development profile, which can be used as a background discriminator. The module array is covered by an anti-coincidence detector which consists of 89 plastic scintillator tiles. The efficiency of the charged particles is larger than 0.9997. By combining the other subsystems, more than 0.9999 ratio of incoming cosmic rays are identified.

3.3.3 Pass 8 Data

In this thesis, we analyze the newest released data set of *Fermi* which is named Pass 8 data (Bruel et al., 2018). Comparing the previous data set, the Pass 8 data provides a wider energy range and better energy measurements because of the improved event reconstruction. The effective area and the angular resolution of the Pass 8 data are shown in Figure 3.8.
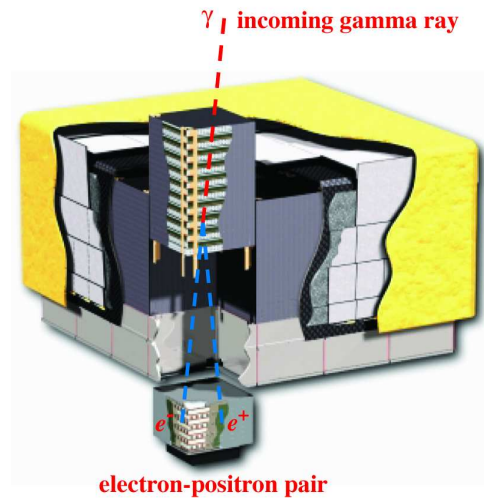
Figure 3.6: A schematic of the *Fermi* LAT (Atwood et al., 2009)
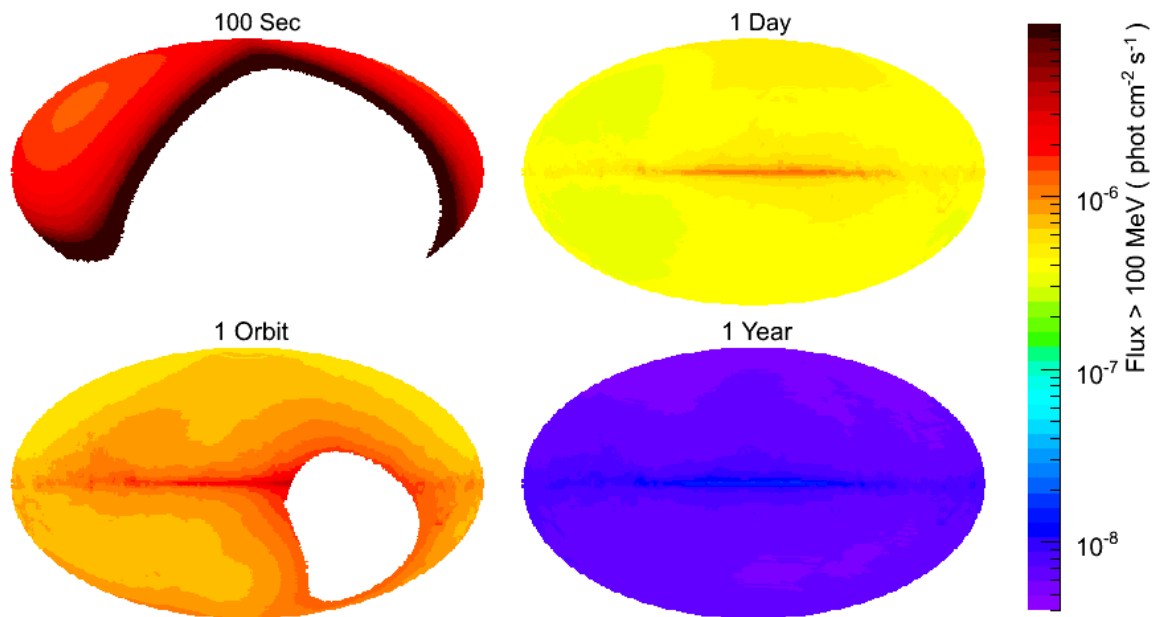
Figure 3.7: LAT source sensitivity for exposures on various timescales (Atwood et al., 2009)
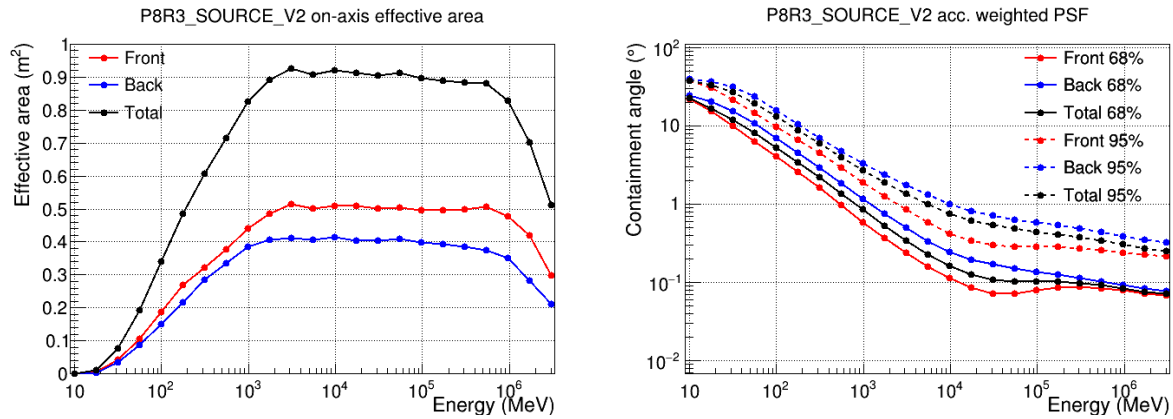
Figure 3.8: The effective area and the angular resolution of the Pass 8 data of *Fermi* LAT. These are taken from https://www.slac.stanford.edu/exp/glast/groups/canda/lat_Performance.htm

Table 3.3: Performance of *Fermi* LAT (Atwood et al., 2009)

Parameter	Value
Energy range	20 MeV – 300 GeV
Effective area at normal incidence	9,500 cm^2
Energy resolution (equivalent Gaussian 1σ):	
100 MeV – 1 GeV (on axis)	9%–15%
1 GeV – 10 GeV (on axis)	8%–9%
10 GeV – 300 GeV (on-axis)	8.5%–18%
Single photon angular resolution (space angle)	
on-axis, 68% containment radius:	
>10 GeV	$\leq 0.15°$
1 GeV	0.6°
100 MeV	3.5°
on-axis, 95% containment radius	$< 3 \times \theta_{68\%}$
off-axis containment radius at 55°	$< 1.7\times$ on-axis value
Field of View (FoV)	2.4 sr
Timing accuracy	< 10 μsec
Event readout time (dead time)	26.5 μsec

Chapter 4

Spectral Analysis in Hard X-rays

The X-ray emission from LS 5039 is considered to be synchrotron emission from the particle acceleration region. Thus, X-ray observations can give important information about the magnetic field and the electron energy distributions. In Takahashi et al. (2009) and Kishishita et al. (2009), LS 5039 was studied deeply in the X-ray band with a long observation time of ~ 500 ks. However, due to the large background of HXD, the spectrum above 10 keV is poorly determined. In order to investigate the spectrum above 10 keV accurately, we analyzed the *NuSTAR* data of LS 5039 with an exposure time of ~ 350 ks because *NuSTAR* achieves high signal-to-ratio in hard X-rays. Furthermore, we compared our result with the previous result, and discuss the time-variability of the X-ray emission.

4.1 *NuSTAR* Observation and Data Reduction

LS 5039 was observed with *NuSTAR* (OBSID: 30201034002) from 2016 September 1 to 5 for a gross exposure of 346 ks, which is roughly a full orbital period of LS 5039. The data reduction and analysis were performed by the Nuclear Spectroscopic Telescope Array data analysis software (`NuSTARDAS`) version 1.8.0, and `NuSTAR CALDB` version 20180312. Considering the angular resolution of 18 arcsec (FWHM), we extracted source events from a circular area centered at the source position with a radius of 30 arcsec.

During this observation, the solar coronal mass ejections (CME) was observed. The solar CME is a transient phenomenon in which a large amount of plasma ($> 10^{16}$ g) is released into the solar wind (Antiochos et al., 1999). It increases the background when the satellite gets close to the South Atlantic Anomaly (SAA) comparing with that when the solar CME does not occur. However, the standard *NuSTAR* data screening process does not consider

this phenomenon. Thus, when we adopt the standard process, the resulting light curve (see Figure 4.1 Top) shows a high count rate near SAA passage because the background due to the CME is not completely removed. Hence, we should apply more severe criteria for the selection of events near SAA. For this purpose, we used `nucalcsaa` which calculates the SAA passages on the basis of count rates of the high/low gain shield and the CZT detectors onboard. Since `nucalcsaa` provides 12 types of criteria *e.g.* which high/low-gain shield is used, or whether the count rate of CZT is considered for the calculation, we tested all of the parameter sets to the data, and compared the count rate lightcurves. In this chapter, we choose a parameter set (`saacalc=2 saamode=OPTIMIZED tentacle=yes`), which removes high background intervals completely and yields the maximum net exposure time (165 ks).
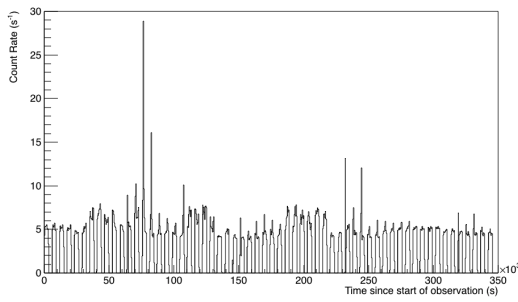
all region, w/standard process   source region, w/standard process
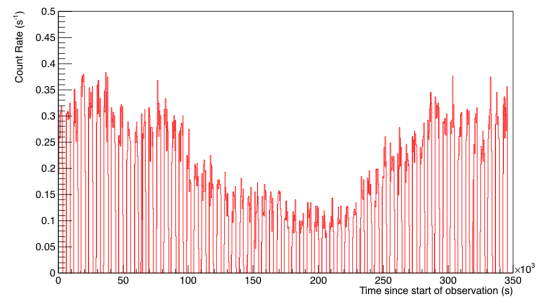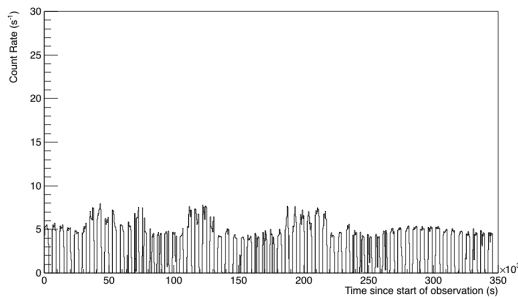
all region, w/`nucalcsaa`   source region, w/`nucalcsaa`
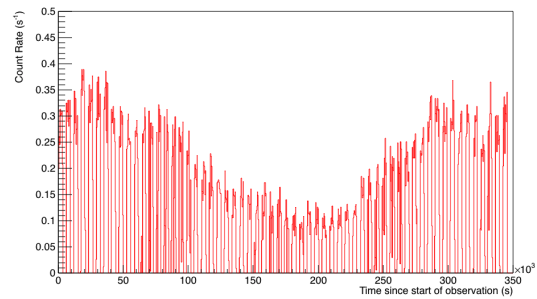
Figure 4.1: Count rate lightcurves of the *NuSTAR* observation. The count rate are obtained by using events of two detectors, namely, the FPMA and FPMB. The top figures show the lightcurves when we apply the standard data screening process. The bottom figures show the lightcurves when we calculate the SAA passage with `nucalcsaa` (`saacalc=2 saamode=OPTIMIZED tentacle=yes`).

4.2 Selection of Background Region

In the spectral analysis, we extract events in the source region as defined before. However, the background events also are included in the extracted events. The background are categorized into three types. One is the non X-ray background (NXB), the in-coming cosmic rays and the X-rays from the material around the detector and the detector itself activated by the cosmic rays. Second is the cosmic X-ray background (CXB), the subtropical X-ray emission from unresolved X-ray sources. The third is the galactic ridge X-ray emission, the emission from unresolved X-ray sources in the galactic plane. In this work, we extracted the events from the region as shown in Figure 4.2, and considered them as the sum of the three types of the background. The contribution of the background to the spectrum is estimated to be about 4 %. Furthermore, even if we choose smaller background regions, the best-fitting parameters in the spectral analysis do not change at all compared to statistical errors. Therefore, we ignored systematic errors due to the selection of the background region.
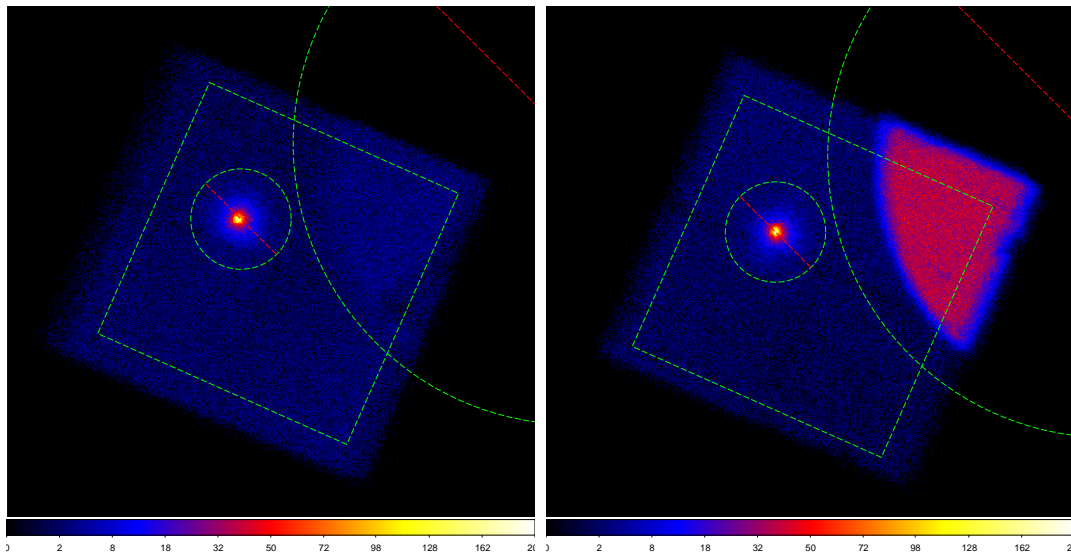
Figure 4.2: The background region selected in the spectral analysis of *NuSTAR*. The left and right images are obtained from FPMA and FPMB, respectively. The upper right region with high photon counts was produced by the stray light from a nearby bright X-ray source. This region is not used for the background estimation.

4.3   Spectral Analysis in $3 - 70$ keV

Since the X rays are absorbed by the interstellar medium and by the material in the observed system, the absorption effect should be considered in the spectral analysis, especially in the low energy band. The equivalent hydrogen column density can be determined by the low energy X-ray spectrum (< 1 keV). However, it is difficult to measure the column density from the *NuSTAR* data because the *NuSTAR* cannot observe X rays below 3 keV. Thus, in the spectral analysis, we utilized the column density measured by Kishishita et al. (2009). Although the column density varies depending on the orbital phase, we confirmed that the variability of the column density yields negligible systematic errors on the fitting parameters comparing with the statistical errors. Therefore, in the spectral analysis of *NuSTAR*, we fixed the column density n_{H} to 0.77×10^{21} cm^{-2}.

Figure 4.3 shows the spectrum of LS 5039 using all of the events of the *NuSTAR* data. It is described very well with a single powerlaw model with a photon index of 1.627 ± 0.010. The best-fitting parameters are shown in Table 4.1. In order to search for the thermal component, *e.g.* the emission from the surface of a neutron star, we added a single-temperature blackbody model into the spectrum model. However, no significant thermal component is detected. Figure 4.4 shows the upper limit of the flux of the blackbody component. The derived upper limit is 3σ upper limit, that is, the blackbody flux increases χ^2 by $+9.0$ from those derived using a single powerlaw component. Here, we assumed that the source distance is 2.5 kpc.

Next, in order to investigate the spectral change depending on the orbital phase, we analyzed the X-ray spectrum around the inferior/superior conjunction. We defined the orbital phase around inferior conjunction (INFC) as $0.45 < \phi < 0.9$, and superior conjunction (SUPC) as $0.0 < \phi < 0.45, 0.9 < \phi < 1.0$. The orbital phase is calculated using the orbital parameters obtained by Casares et al. (2005). Both spectra are described well again with a single powerlaw component as shown in Figure 4.5. In the SUPC spectrum, there is a sign of spectral hardening above 50 keV. In order to check this, we modeled the spectrum with $\mathtt{phabs} * (\mathtt{bknpowerlaw} + \mathtt{powerlaw})$. Although the number of free parameters are increased by three, the reduced chi-squared was improved by just 6.6, corresponding an F-test probability of $\sim 6\%$. Thus, the presence of a hard component above 50 keV is not statistically significant. Therefore, we conclude that the spectrum of LS 5039 is described well with a single powerlaw model in both INFC and SUPC.

Finally, in order to investigate the flux ratio between INFC and SUPC, we measured the X-ray flux in a narrow energy range in both spectra. Figure 4.6 shows the obtained fluxes and the flux ratio of the INFC/SUPC spectra. The flux ratio of INFC/SUPC is about 2 below
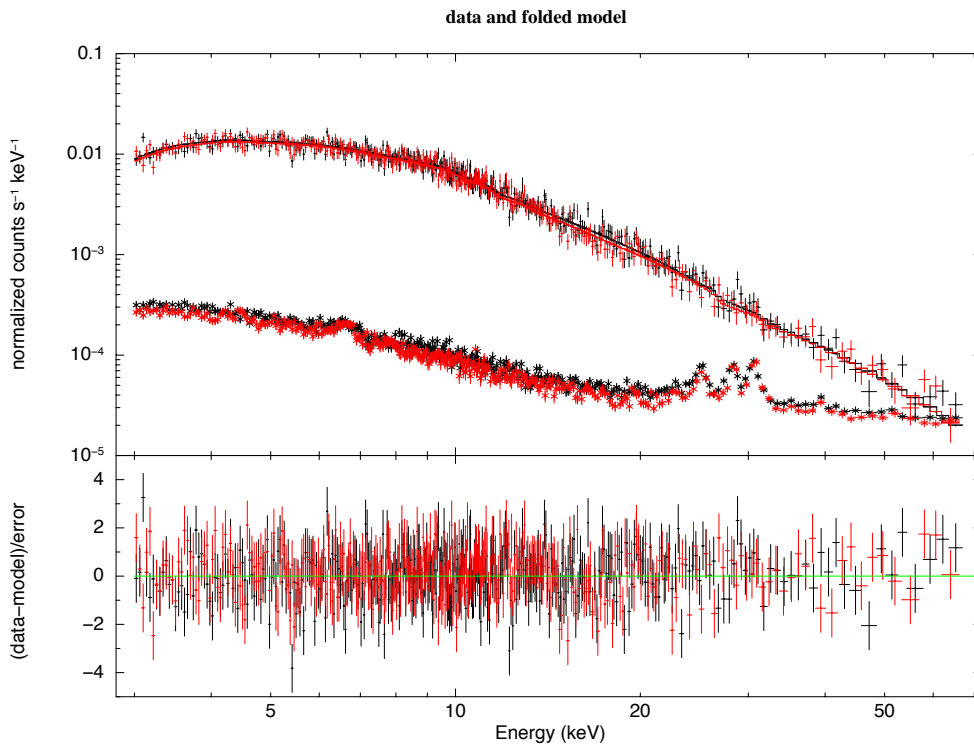
Figure 4.3: The phase-averaged spectrum of *NuSTAR*. The black/red lines correspond to FPMA/FPMB, respectively. The background spectra are shown below the background-included source spectra.
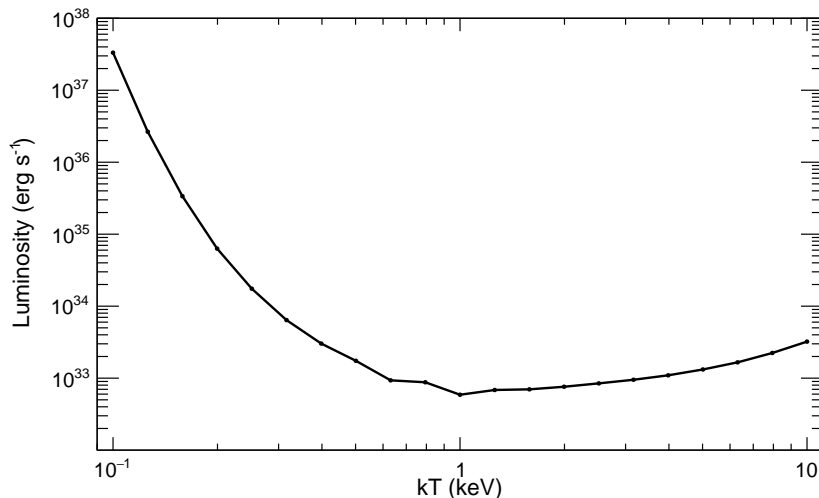
Figure 4.4: 3σ upper limit on the flux of the blackbody component in LS 5039.

Table 4.1: The best-fitting parameters obtained from 3–70 keV *NuSTAR* data. Errors correspond to $1\,\sigma$ confidence interval.

Orbital Phase	NuSTAR (3–70 keV)		
	Photon index	Flux (3–70 keV)	χ^2/dof
		$\times 10^{-11}$ erg cm^{-2} s^{-1}	
INFC	1.611 ± 0.012	3.19 ± 0.04	$514.6/526$
SUPC	1.639 ± 0.016	1.65 ± 0.03	$334.5/375$
All Phase	1.627 ± 0.010	2.34 ± 0.02	$676.0/677$

~ 30 keV. As the photon energy increases above 30 keV, the flux ratio becomes smaller.

4.4   Comparison with the *Suzaku* Result in 1–10 keV

In order to investigate the dependence of spectral parameters on the orbital phase, we divide the data into subsets corresponding to different orbital phases, and analyze the spectrum of each data. In addition to this, we compare our result with the previous works (Takahashi et al., 2009; Kishishita et al., 2009). They observed LS 5039 with the *Suzaku* from 2007 Sep 9 to 2007 Sep 15 (OBSID: 402015010). It covers about 1.5 orbital periods of LS 5039. Since they have analyzed the spectrum of 1–10 keV using *Suzaku* XIS, we focus on the spectrum

INFC   SUPC
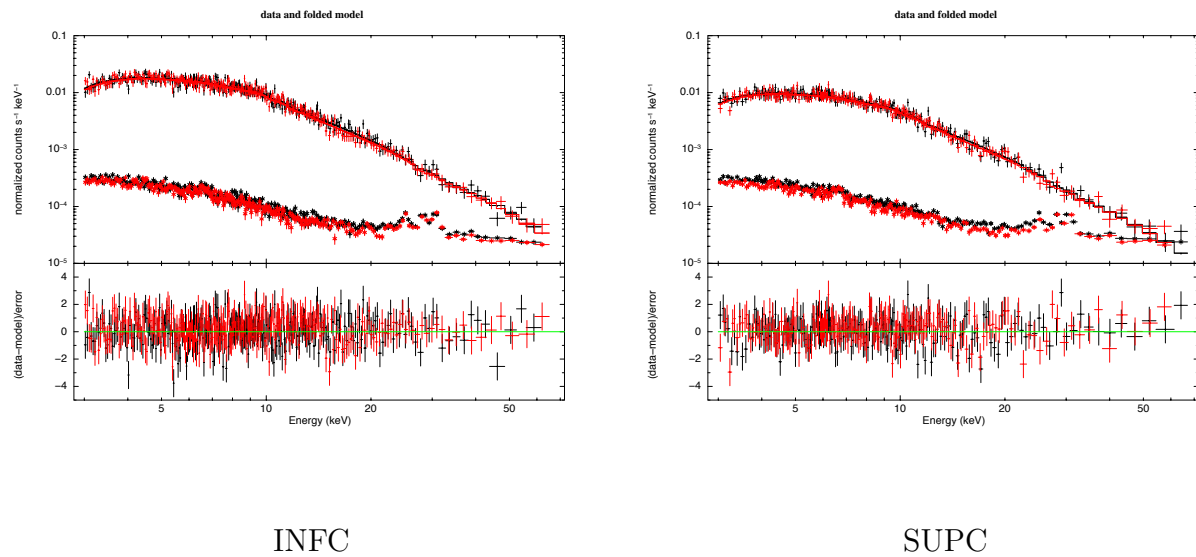
Figure 4.5: The *NuSTAR* spectra around the inferior conjunction and the superior conjunction.

of 3–10 keV.

First, we set the time duration of each subset to one-tenth of the orbital period. The obtained values are described in Table 4.2 and shown in Figure 4.7. The flux becomes a minimum between $\phi = 0.1$–0.2. The minimum flux is also achieved in the same phase in the previous work. Furthermore, the absolute value of the minimum flux is consistent with that by Takahashi et al. (2009). In contrast, the maximum flux obtained between $\phi = 0.6$–0.7 is higher than that obtained in the previous observation by ~ 10 %. As shown in Figure 4.7, the flux difference between the *NuSTAR* and the *Suzaku* is significant around INFC ($0.45 < \phi < 0.9$). We also investigate the change of the powerlaw index. The top of Figure 4.7 shows the photon index for different orbital phases. The photon index does not depend on the orbital phase, and the photon indices in INFC/SUPC are consistent with each other within the statistical errors. This is different from the previous result of the *Suzaku* observation. Furthermore, the photon index is higher than that of the previous observation by ~ 0.1 in all of the orbital phases.

In order to investigate short time variability, we also calculate the flux in 4 ks time interval. Here, again, we fit the spectrum in each interval with a single powerlaw component. Figure 4.8 shows the resulting light curve of the 3–10 keV flux. The flux changes gradually, and no flares are observed. Around $\phi = 0.8$, the light curve shows a local maximum, which was also observed by Kishishita et al. (2009). However, Figure 4.8 reveals no small spike which was observed at $\phi = 0.70$ by Kishishita et al. (2009). Considering that they discussed
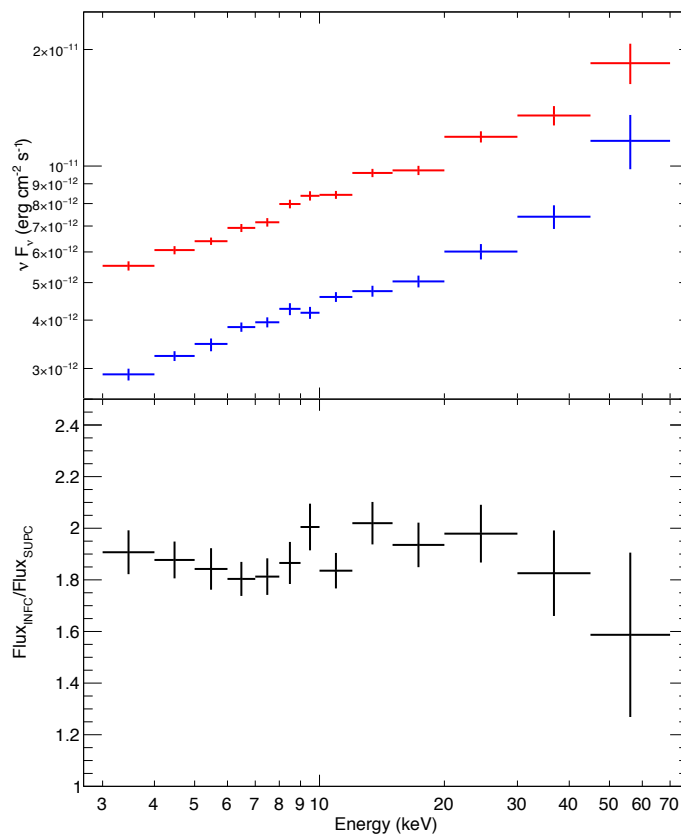
Figure 4.6: The flux ratio between INFC and SUPC in 3–70 keV. The red/blue points correspond to the flux in INFC/SUPC respectively.
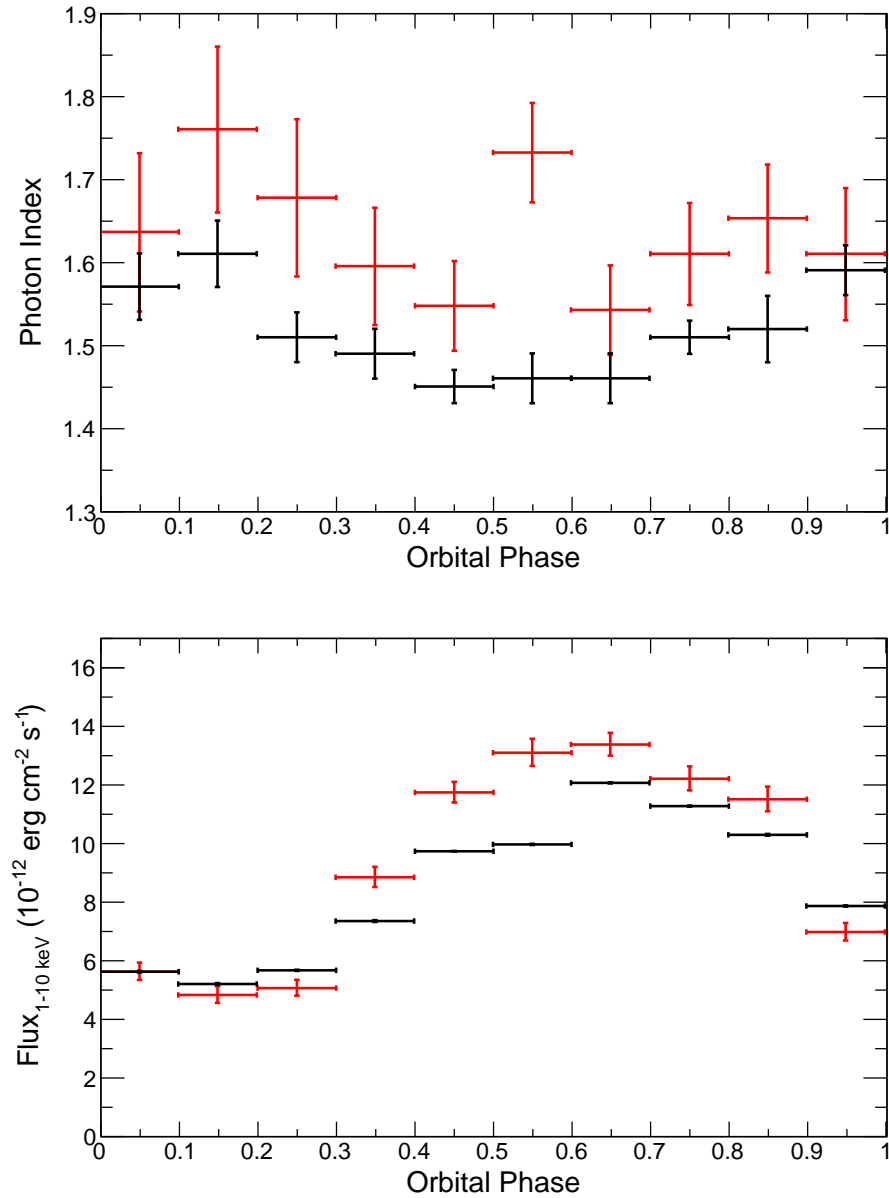
Figure 4.7: The dependence of the flux and the photon index on the orbital phase. The 3–10 keV *NuSTAR* data was analyzed. The red points are obtained from our analysis. The black points are taken from Kishishita et al. (2009)

Table 4.2: Results of spectral analysis in 3–10 keV. Errors correspond to 1 σ confidence interval.

	NuSTAR (3–10 keV)			Suzaku (1–10 keV, Kishishita et al. 2009)	
Orbital Phase	Photon index	Flux (1–10 keV)	χ^2/dof	Photon index	Flux (1–10 keV)
		$\times 10^{-12}$ erg cm^{-2} s^{-1}			$\times 10^{-12}$ erg cm^{-2} s^{-1}
INFC	1.61 ± 0.03	12.55 ± 0.19	311.1/317	1.48 ± 0.02	10.78 ± 0.05
SUPC	1.62 ± 0.03	6.77 ± 0.13	169.5/227	1.55 ± 0.02	6.72 ± 0.04
All Phase	1.62 ± 0.02	9.45 ± 0.11	341.5/346	1.51 ± 0.01	8.07 ± 0.03
0.0–0.1	$1.64^{+0.09}_{-0.10}$	$5.60^{+0.31}_{-0.28}$	36.2/40	1.57 ± 0.04	5.62 ± 0.03
0.1–0.2	1.76 ± 0.10	$4.81^{+0.30}_{-0.27}$	34.2/35	1.61 ± 0.04	5.18 ± 0.03
0.2–0.3	1.68 ± 0.09	$5.03^{+0.28}_{-0.26}$	40.4/37	1.51 ± 0.03	5.67 ± 0.02
0.3–0.4	1.60 ± 0.07	$8.82^{+0.36}_{-0.33}$	73.0/67	1.49 ± 0.03	7.34 ± 0.03
0.4–0.5	1.55 ± 0.05	$11.72^{+0.36}_{-0.34}$	104.9/98	1.45 ± 0.02	9.73 ± 0.01
0.5–0.6	1.73 ± 0.06	$13.07^{+0.47}_{-0.45}$	68.2/86	1.46 ± 0.03	9.95 ± 0.02
0.6–0.7	1.54 ± 0.05	$13.35^{+0.40}_{-0.38}$	97.0/106	1.46 ± 0.03	12.05 ± 0.02
0.7–0.8	1.61 ± 0.06	$12.18^{+0.42}_{-0.40}$	93.1/91	1.51 ± 0.02	11.27 ± 0.02
0.8–0.9	$1.65^{+0.06}_{-0.07}$	$11.47^{+0.43}_{-0.41}$	60.4/77	1.52 ± 0.04	10.29 ± 0.03
0.9–1.0	1.61 ± 0.08	$6.96^{+0.31}_{-0.29}$	63.4/59	1.59 ± 0.03	7.84 ± 0.02

that the spike in *Suzaku* lasts shorter than that observed by *Chandra* by $\Delta\phi \simeq 0.01$, such a fine structure in the light curve varies orbit-by-orbit.

4.5   Spectral Analysis of the *Suzaku* and *NuSTAR* in 10–30 keV

Owing to the high signal-to-noise ratio, we can investigate the flux dependence on the orbital phase above 10 keV. Here, we analyze the spectrum in 10–30 keV. Figure 4.9 shows the light curve of the flux and the photon index with a bin width of one-tenth of the orbital period. Table 4.4 describes the obtained spectral parameters. Similar to the analysis in 3–10 keV, the minimum and maximum of the flux achieve for ϕ between 0.1–0.2 and 0.6–0.7. Furthermore, the photon index does not show any significant variability. This is again similar to the result in the 3–10 keV range. Thus, the dependence of the emission on the orbital period does not change between 3–10 keV and 10–30 keV.

In addition, we analyzed the *Suzaku*-PIN data, and compared it to the result of the *NuSTAR*. The same data used by Takahashi et al. (2009); Kishishita et al. (2009) (OBSID:
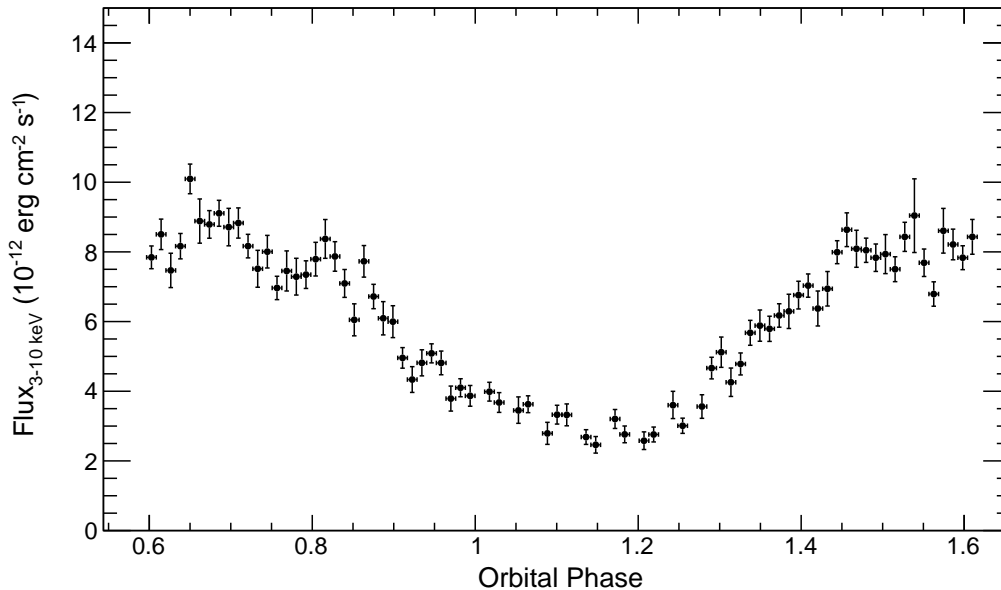
Figure 4.8: The orbital light curve in 3–10 keV using the *NuSTAR* data. The bin width of the light curve is 40 ks.

402015010) were analyzed, and they were screened with the standard pipeline software `SUZAKU AE pipeline` 1.1.0. The small number of events and the low signal-to-noise constrain the width of the orbital phase to 0.25 in the *Suzaku* PIN analysis. As the non X-ray background and the cosmic X-ray background, we used `LCFITDT` model provided by the *Suzaku* team (Fukazawa et al., 2009) and the model defined in Gruber et al. (1999). Since the HXD is a non-focusing detector, the contribution of the diffuse background emission of the HXD is larger than that of the *NuSTAR*. For the galactic ridge X-ray emission (GRXE), we used the same model estimated in Takahashi et al. (2009). Furthermore, in order to evaluate this GRXE estimation, we calculated the GRXE contribution to the PIN referring to Revnivtsev et al. (2006). On the basis of the intensity map in Revnivtsev et al. (2006), the GRXE intensity at a position of LS 5039 is estimated to be

$$I = 2.81 \times 10^{-11} \text{ erg s}^{-1}\text{cm}^{-2}\text{deg}^{-2} \ . \tag{4.1}$$

This is consistent with the estimation by Takahashi et al. (2009) to within 10%. In order to consider the uncertainty of the CXB and the GRXE model, we assumed that they had 10% systematic errors.

The results are shown as the black points in Figure 4.9, and the obtained parameters are

shown in Table 4.4. The 10–30 keV flux of *Suzaku* is higher than that of *NuSTAR*, by $\sim$ 25% around the INFC. Furthermore, the difference becomes much higher (by $\sim$69%) around SUPC. These results suggest that there is a variable spectral component above 10 keV. The error of photon index in *Suzaku* is too large, and thus, it is difficult to discuss whether the photon index is different between *Suzaku* and *NuSTAR*.

Note that the model of the GRXE affects the spectral analysis of the HXD-PIN data. For example, it is proposed that the GRXE has the cut-off feature around $\sim$30 keV (Krivonos et al., 2007). Figure 4.10 shows the result when we model the GRXE as `cutoffpl *` `highecut` with $E_0 = 30$ keV, $E_{\mathrm{cut}} = 35$ keV, $E_{\mathrm{fold}} = 20.0$ keV, $\Gamma = 1.90$. In this case, the measured photon index becomes smaller, and the flux becomes larger. As a result, the flux difference between *Suzaku* and *NuSTAR* becomes more obvious. However, when we analyzed the GRXE spectrum at $(l, b) = (28.46, -0.20)$, observed with HXD-PIN (OBSID: 500009020), the `cutoffpl * highecut` model was not statistically favored compared to a single powerlow model as shown in Figure 4.11.

Table 4.3: Results of the spectral analysis of 10–30 keV *NuSTAR* data.

Orbital Phase	NuSTAR (10–30 keV)		
	Photon index	Flux (10–30 keV) $\times 10^{-12}$ erg cm^{-2} s^{-1}	χ^2/dof
INFC	1.60 ± 0.05	11.31 ± 0.18	176.7/179
SUPC	1.69 ± 0.06	5.75 ± 0.12	143.9/123
All Phase	1.64 ± 0.04	8.26 ± 0.10	291.5/280
0.0–0.1	$1.62^{+0.19}_{-0.18}$	5.21 ± 0.3	10.6/16
0.1–0.2	$1.77^{+0.25}_{-0.24}$	$3.76^{+0.3}_{-0.29}$	9.8/12
0.2–0.3	$1.51^{+0.21}_{-0.20}$	4.26 ± 0.28	11.4/15
0.3–0.4	1.74 ± 0.15	7.38 ± 0.35	22.6/26
0.4–0.5	$1.62^{+0.11}_{-0.10}$	10.79 ± 0.37	55.3/45
0.5–0.6	$1.44^{+0.12}_{-0.11}$	10.71 ± 0.41	43.5/36
0.6–0.7	1.65 ± 0.09	12.57 ± 0.4	48.0/50
0.7–0.8	1.57 ± 0.11	11.49 ± 0.42	34.8/41
0.8–0.9	1.70 ± 0.13	$10.22^{+0.42}_{-0.41}$	38.4/35
0.9–1.0	1.96 ± 0.14	5.89 ± 0.27	20.2/25
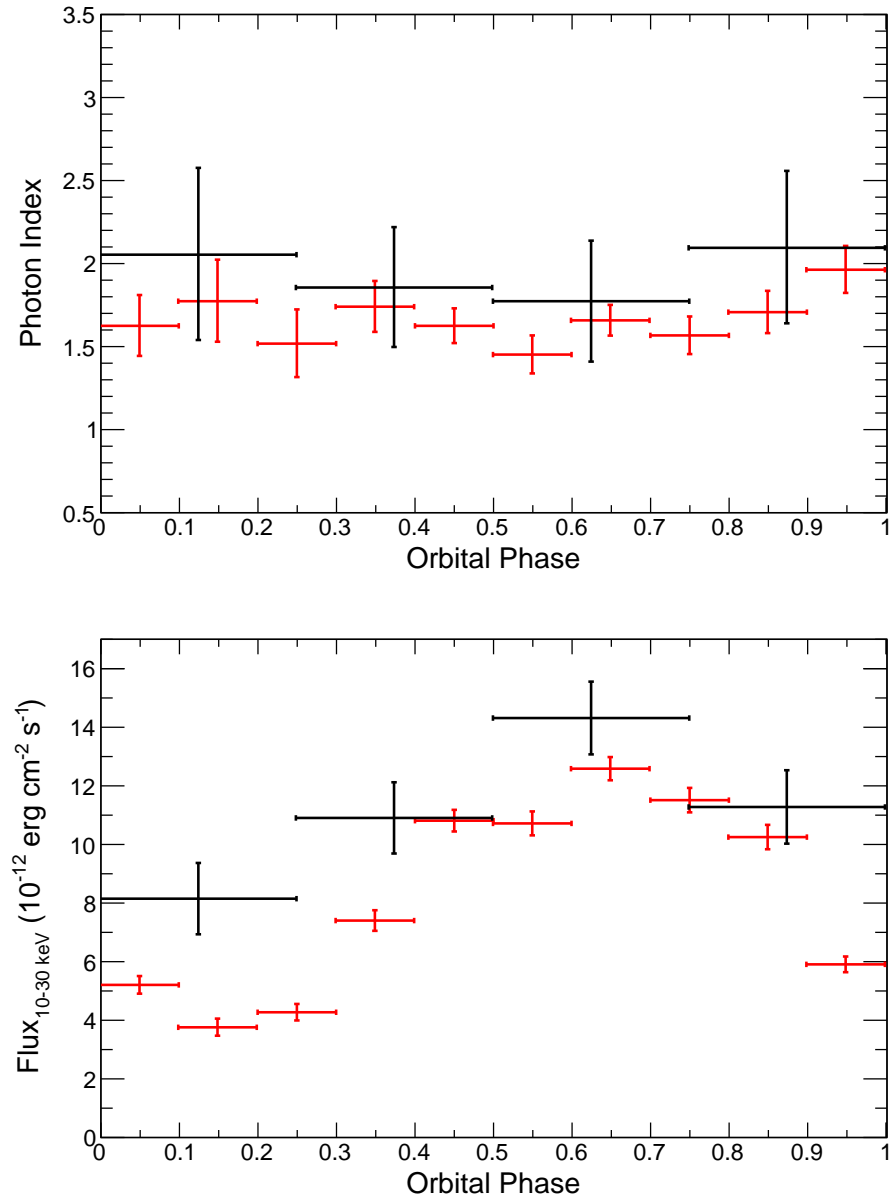
Figure 4.9: The dependence of the photon index (top) and the flux (bottom) on the orbital phase obtained from 10–30 keV *NuSTAR* data. The red points are obtained from our analysis. The black points are obtained from 10–30 keV HXD-PIN data.
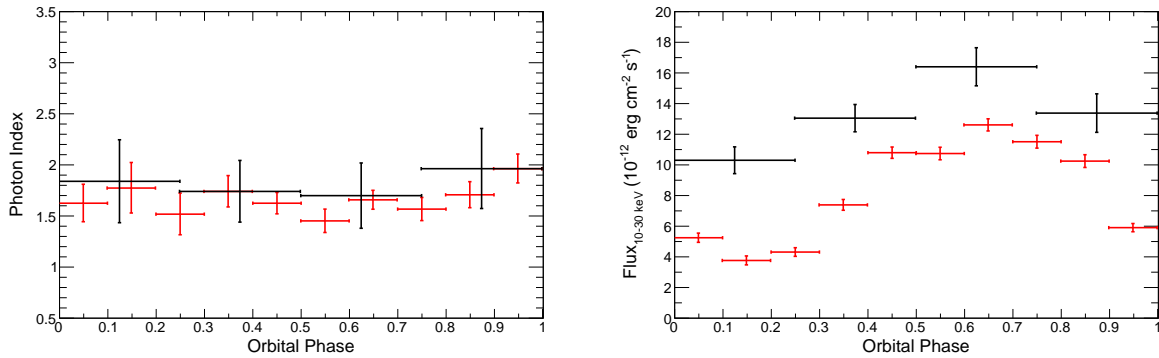
Figure 4.10: The same as Figure 4.9, but the GRXE is modeled as `cutoffpl * highecut` with $E_0 = 30$ keV, $E_{\text{cut}} = 35$ keV, $E_{\text{fold}} = 20.0$ keV, $\Gamma = 1.90$.
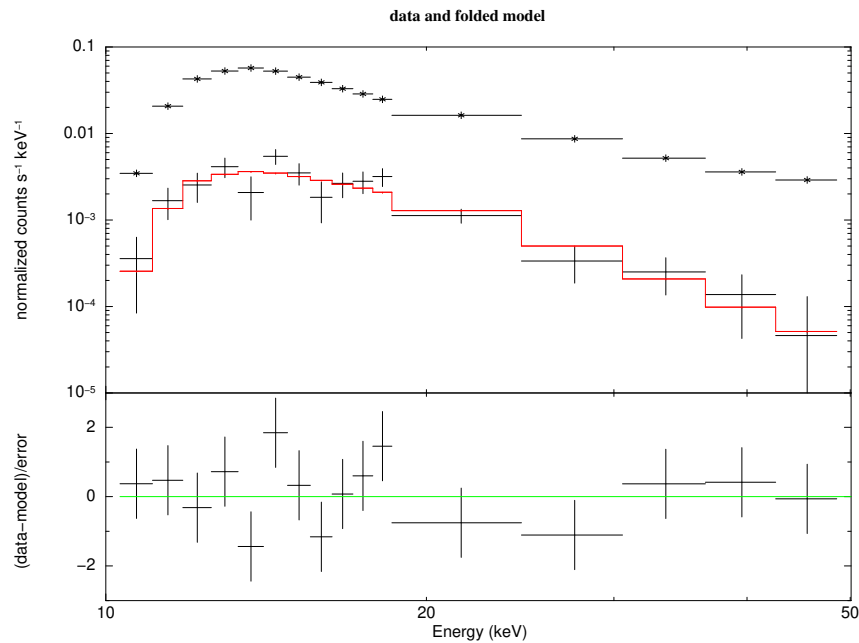
Figure 4.11: The spectrum of the GRXE at $(l, b) = (28.46, -0.20)$. The HXD/PIN data (OBSID: 500009020) was used. The top/bottom black points correspond to the background included/subtracted photon count rate. The red line represents the best-fitting model of a single powerlow.

Table 4.4: Results of the spectral analysis of 10–30 keV *Suzaku* HXD/PIN data.

Orbital Phase	Suzaku HXD/PIN (10–30 keV)		χ^2/dof
	Photon index	Flux (10–30 keV)	
		$\times 10^{-12}$ erg cm^{-2} s^{-1}	
INFC	1.67 ± 0.29	14.0 ± 1.2	7.7/6
SUPC	$2.56^{+0.40}_{-0.39}$	9.7 ± 1.2	8.0/6
All Phase	1.87 ± 0.21	10.7 ± 1.2	11.6/11
0.0–0.25	$2.05^{+0.52}_{-0.51}$	8.1 ± 1.2	8.4/6
0.25–0.5	1.85 ± 0.36	10.9 ± 1.2	6.1/6
0.5–0.75	1.77 ± 0.36	14.3 ± 1.2	6.1/6
0.75–1.0	$2.09^{+0.46}_{-0.45}$	11.3 ± 1.3	11.5/6

4.6 Summary

In this chapter, we analyzed the spectrum of LS 5039 using the *NuSTAR* data. Owing to the high signal-to-noise ratio, we found that the spectrum of LS 5039 is described well with a single powerlaw model below 70 keV. Comparing with the previous observation of *Suzaku*, the flux in the range of 3–10 keV varies by $\sim 10\%$ around the inferior conjunction. Furthermore, we did not find a small spike which is observed at $\phi = 0.70$ by Kishishita et al. (2009). These results suggest that the emission around the inferior conjunction varies slightly orbit-by-orbit. Additionally, we compare the *NuSTAR* and *Suzaku* spectrum in the range of 10–30 keV. Although the *Suzaku* result has large errors, the 10–30 keV flux of *Suzaku* is higher than that of *NuSTAR* by $\sim 25\%$ around the INFC and $\sim 69\%$ around SUPC. These results suggest that there is a variable spectral component above 10 keV.

Chapter 5

Pulse Search in Hard X-rays

Definitive and more direct evidence for the presence of a neutron star would be detection of periodically pulsed emission. Searches for pulsation from LS 5039 from radio (Virginia McSwain et al., 2011) to soft X-rays (Rea et al., 2011) have been unsuccessful so far, the fact of which is unsurprising, given that there is potentially strong absorption by stellar winds from the primary star. By contrast, higher energy photons, *i.e.* hard X-rays or GeV gamma-rays, penetrate dense stellar winds, and hence can be better probes in principle. In GeV gamma-rays, the data must be in practice accumulated over a time interval longer than the orbital period of the system due to the low photon count rates. Then, the timing information has to be corrected in good precision for the orbital Doppler effects to search for potential periodicity. The available orbital parameters acquired in the optical band (Casares et al., 2005; Aragona et al., 2009; Sarty et al., 2011; Caliandro et al., 2012) are, however, not sufficiently accurate for the required timing correction. Hence, GeV gamma-rays are unsuitable for the purpose, either. Accordingly, the hard X-ray band is the only promising energy band, considering that it requires a relatively short integration time, for which the orbital uncertainties are not critical. Here, we search the *Suzaku* and *NuSTAR* data for the hard X-ray pulsation.

5.1 Method of Pulse Search in Hard X-ray Data

If the compact object in LS 5039 is a pulsar with a mass of $1.4M_\odot$ and an intrinsic pulse period of P_{NS}, then its projected orbital radius is estimated to be ~ 50 light seconds. Thus, the individual pulses will undergo periodic delays/advances in their arrival times by ~ 50 s (see Figure 2.9 in Chapter 2), so they would be smeared out unless $P_{\mathrm{NS}} \gg 50$ s. The best way to treat the change of the arrival times would be to correct the photon arrival times

for the orbital motion of the pulsar. However, the orbital solutions currently available from optical observations (Casares et al., 2005; Aragona et al., 2009; Sarty et al., 2011) are not accurate enough for this purpose.

We thus search for pulsations, first without incorporating the orbital-motion corrections. The delays/advances translate into periodical variations in the line-of-sight velocity up to

$$\Delta v/c \sim 50 \text{ (sec)} \times 2\pi/P_{\text{orb}} = 0.001 \ . \tag{5.1}$$

Hence, the pulse period of a putative pulsar in LS 5039 should undergo Doppler modulations by $\pm 0.1\%$. Then, the simplest way to mitigate this effect is to divide the whole data into many subsets, each with a duration of ΔT which is short enough to satisfy

$$P_{\text{NS}}/\Delta T \lesssim 1 \times 10^{-3} \ . \tag{5.2}$$

Then, the Fourier frequency resolution $(1/\Delta T)$ becomes no higher than the intrinsic Doppler width $(\Delta v/(cP_{\text{NS}}))$. The power spectra calculated from individual subsets are merged incoherently into one averaged spectrum with improved statistics. In Figure 5.1, we demonstrate how the data division works in the Fourier analysis. We simulated the pulsation data with a pulse period of 5 s, and compared the Fourier power spectra with/without the data division. When we do not divide the data into subsets, the power spectrum shows a good timing resolution, but the binary motion smears the Fourier peal completely. On the other hand, when we divide the data into subsets, the Fourier analysis becomes no longer affected by the binary motion at the expense of the timing resolution.

5.2   Fourier Analysis of *Suzaku*

We applied Fourier analysis to the 10–30 keV HXD data. The photon count rate with the 10–30 keV *Suzaku* data is $81,522/500$ ks $\simeq 0.16$ photons/s, of which 90% is background as already stated. When choosing $\Delta T = P_0/1 \times 10^{-3} = 1 \times 10^3 P_0$, the number of source photons in each subset thus becomes $\sim 16 \times P_0(\text{sec})$. Requiring that each subset should include at least ~ 10 signal photons, we limit our pulsation search to $P_0 > 1$ s. Individual event arrival times were converted with the software `aebarycen` to those to be measured at the Solar system barycentre, using the Solar-system ephemeris JPL-DE200 and the source position of $(\alpha^{2000}, \delta^{2000}) = (18^{\text{h}}26^{\text{m}}15^{\text{s}}.06, -14°50'54''.31)$ as taken from the IRCS (Gaia Collaboration et al., 2018). Using a software `powspec` in the timing analysis software package `XRONOS` (Nasa High Energy Astrophysics Science Archive Research Center (Heasarc), 2014), we converted
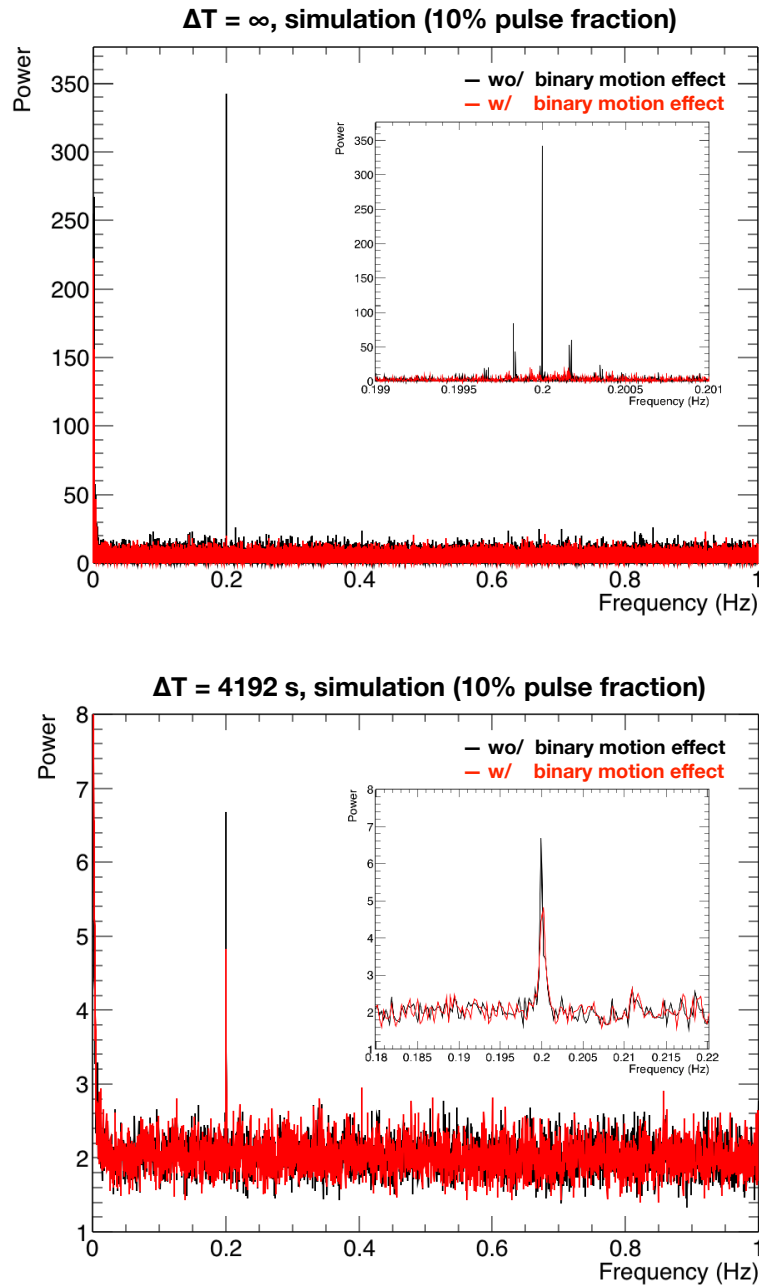
Figure 5.1: Merit of dividing data into subsets in Fourier analysis of compact binary data. We simulate the pulsation data with a period of 5 s. The number of photon counts and the observation time are the same as those of the 10–30 keV *Suzaku*/PIN data we analyzed. The pulse fraction was set to 10%. The black and red lines represent the Fourier spectrum without and with considering the orbital motion respectively. Top: the Fourier power spectrum without dividing data. Bottom: the Fourier power spectrum without dividing data ($\Delta T = 4192s$). We assumed that $P_{\rm orb} = 3.90608$ day, $a_{\rm x} \sin\theta = 50.0$ light sec, $e = 0.30$, $\omega = 56$ deg., and $\tau_0 = 0.0$.

the light curve in each subset, with a time bin width of 0.5 s, into a Fourier power spectrum covering a frequency range of $0.01 - 1.0$ Hz. Then, we derived an incoherently-average power spectrum, one for each value of ΔT from 4,096, 8,192 and 16,384 s.

Figure 5.2 shows the obtained power spectra. The result for $\Delta T = 8192$ s reveals a peak at $P_{NS} = 8.96$ s, where the power reaches 3.79 which is 6.6 σ above the average of 2.0. As we used 55 data subsets, each Fourier component in Figure 5.2 should obey a χ^2 distribution with 110 d.o.f, so that the local chance probability of the 8.96 s peak becomes 4.5×10^{-8}. Because we tested 8192 independent frequencies, the overall chance probability of the peak, considering the look-elsewhere effect, becomes $\mathcal{P}_{ch} = 4.5 \times 10^{-8} \times 8192 = 3.7 \times 10^{-4}$. To confirm this value, we performed a Monte-Carlo simulation. In a single trial, 8192 values were randomly sampled from a χ^2 distribution with 110 d.o.f., and their maximum was registered. Then, out of overall 100,000 trials, the registered maximum exceeded the observed one in 379 cases. This implies $\mathcal{P}_{ch} = 3.8 \times 10^{-4}$, which agrees well with the above value. Finally, when considering the number of ΔT tested, we obtain $\mathcal{P}_{ch} \sim 3.7 \times 10^{-4} \times 3 = 1.1 \times 10^{-3}$. Thus, we can claim a pulse detection with a confidence level close to 99.9%. The ratio $P_{NS}/\Delta T = 0.11\%$ is fully self-consistent within our framework.

5.3   Fourier Analysis of *NuSTAR*

We also analyze the 10–30 keV *NuSTAR* data. To correct arrival times of these events for their propagation within the Solar system and for the known clock drifts of *NuSTAR*, we employed `barycorr`, the *NuSTAR* clock correction file v079, and the Solar-system ephemeris JPL-DE405, and adopted the source position of $(\alpha^{2000}, \delta^{2000}) = (18^h 26^m 15^s.06, -14°50'54''.38)$ (IRCS). The slight difference in the two source positions between the *Suzaku* and *NuSTAR* analyses reflects the proper motion of LS 5039. The photon arrival times are accurate to 10 μs after these corrections. We extracted 10–30 keV events from an event accumulation radius of 30 arcsec around the source. The obtained total events are 12,014, of which about 4% is background. We performed the Fourier analysis using $\Delta T = 4,096$, 8,192, and 16,384 s. The results are shown in Figure 5.3, which revealed no significant peaks in the averaged power spectra. This is probably because the pulse fraction was considerably smaller at the epoch of the *NuSTAR* observation than that of *Suzaku* (see discussion later in this section) and partly because this method of analysis is still too crude.

In order to search for a weak pulsed signal, we adopt Z^2 statistics (de Jager et al., 1989), a method designed to search for periodic signals with unbinned likelihood evaluation. The
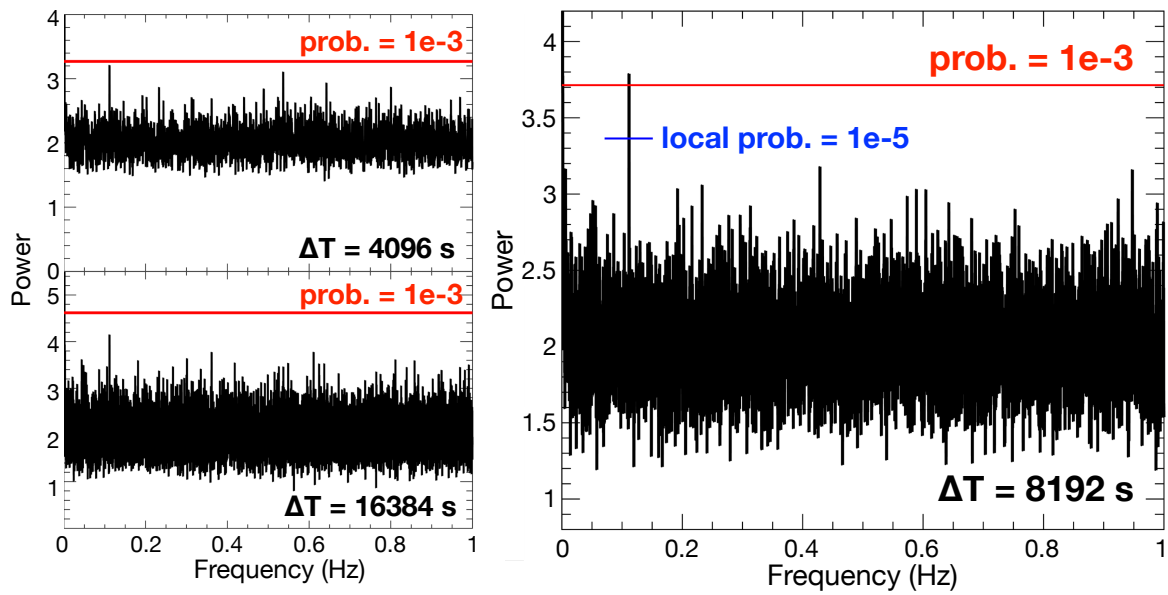
Figure 5.2: Evidence of the pulsation from LS 5039, where red lines indicate signal strengths that arise with a chance probability of 1.0×10^{-3} when considering the look-elsewhere effect. The blue line indicates the strength without considering that effect. Fourier analysis of the 10–30 keV *Suzaku* data in 2007 September. The data are divided into subsets with $\Delta T = $ 4096, 8192, and 16384 s, and the power spectra derived from individual subsets are averaged into a single Fourier power spectrum.

Z^2 statistics is defined as:

$$Z_m^2 = \frac{2}{N} \sum_{l=1}^{m} \left[\left(\sum_i^N \cos 2\pi l \frac{t_i}{P} \right)^2 + \left(\sum_i^N \sin 2\pi l \frac{t_i}{P} \right)^2 \right] \tag{5.3}$$

where t_i is the arrival time of the i-th photon, N is the number of total events, and P is the period to be investigated. When N is large, this statistics is proportional to the unbinned likelihood function (see mathematical details in Appendix A). We calculated Z^2 statistics, incorporating only the fundamental harmonic, over a range of $P = 7$–11 s (or 0.091–0.142 Hz), again for individual subsets of length ΔT, and incoherently stacked the results into a single Z^2 periodogram. Figure 5.4 shows the results with $\Delta T = 3000 - 12000$ s. Each result reveals a sign of periodicity at 9.046 s. When $\Delta T = 10,000$ s, the Z^2 analysis yielded a peak at $P_{\mathrm{NS}} = 9.046 \pm 0.009$ s; the quoted error reflects the orbital Doppler shifts, whereas the statistical error is much smaller.

The above Z^2 peak was evaluated with the Monte-Carlo method. In a single trial, we generated the entire subsets, each with the same photon counts and same observing windows as the actual data, but without any intrinsic periodicity. Each subset was Z^2-analyzed, and the results were stacked into a single periodgram in the same way as the actual data. Then maximum Z^2 was registered. Using 13216 fake data sets, the chance probability of this peak was calculated as 3.5×10^{-3}.

In Figure 5.5, we compare the Z^2 periodgrams using the 10–30 keV *Suzaku* and 10–30 keV *NuSTAR* data. The *Suzaku* periodgram was obtained by applying $\Delta T = 5000$ s, where the periodicity appears at $P_{\mathrm{NS}} = 8.960 \pm 0.009$ s. We identify the periodicity of very similar periods from two observations 9 years apart by two different satellites. Although it is essential that another observation reconfirms the pulse component with high significance, we found evidence that the compact object in LS 5039 is a neutron star with a spin period of $P_{\mathrm{NS}} \sim 9$ s and a period derivative of $\dot{P}_{\mathrm{NS}} \sim (9.046 \text{ s} - 8.960 \text{ s})/9 \text{ year} = 3 \times 10^{-10}$ s s^{-1}.

5.4   Correction for the orbital Doppler effects

Finally, to confirm that the pulsed emission really comes from the compact object in LS 5039, we repeated the Z^2 analysis separately using the entire *Suzaku* and *NuSTAR* data sets, subdividing neither of them, but incorporating corrections of the photon arrival times for the orbital motion. According to the optical information (Casares et al., 2005; Aragona et al., 2009; Sarty et al., 2011), we described the neutron star's orbit by an ellipse with five parameters: the projected semi-major axis ($a_{\mathrm{x}} \sin \theta$), orbital eccentricity $e \sim 0.3$, periastron
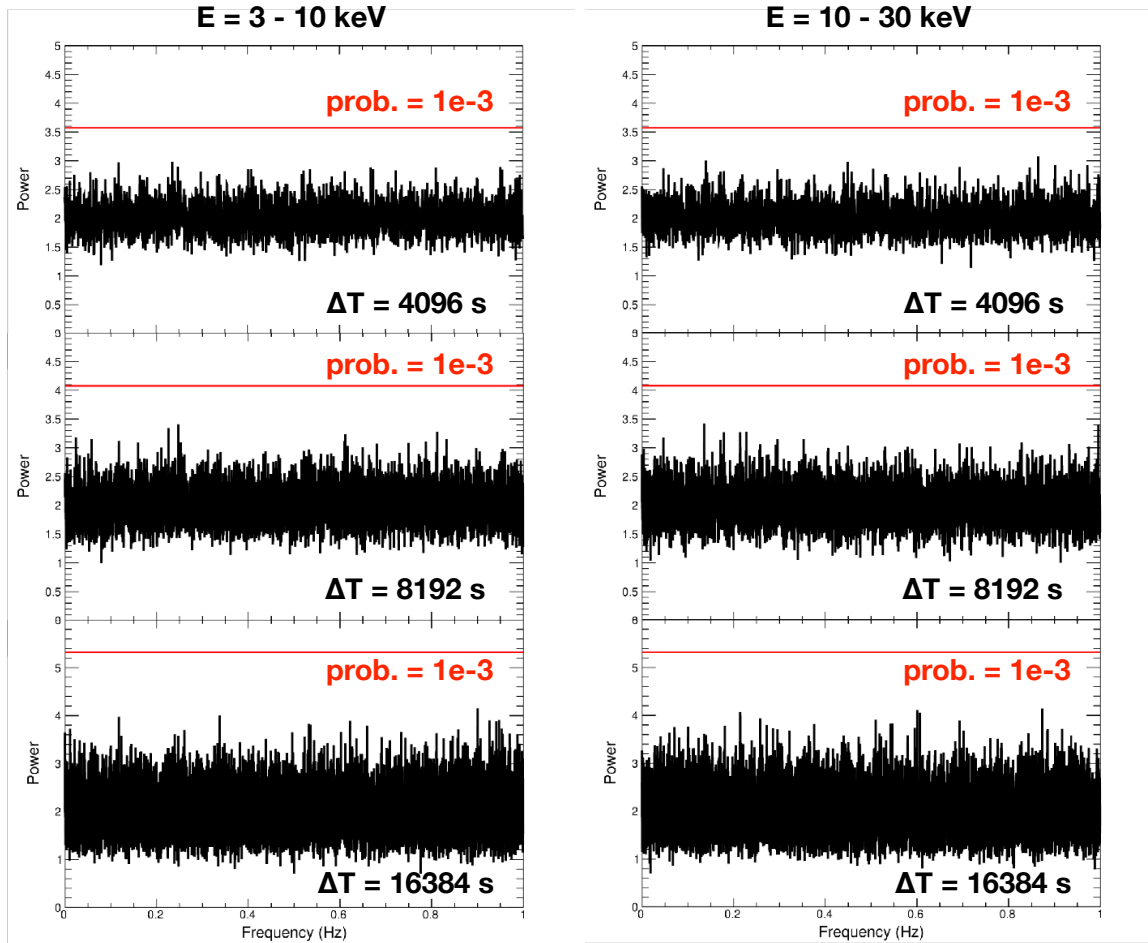
Figure 5.3: Fourier power spectrum using *NuSTAR* data, where red lines indicate signal strengths that arise with a chance probability of 1.0×10^{-3} when considering the look-elsewhere effect. The data is divided into subsets with $\Delta T = 4096$, 8192, and 16384 s. The left and right figures are obtained using 3–10 keV and 10–30 keV *NuSTAR* data respectively.

$\Delta = 3000$ s

$\Delta = 4000$ s

$\Delta = 5000$ s

$\Delta = 6000$ s

$\Delta = 7000$ s

$\Delta = 8000$ s

$\Delta = 9000$ s

$\Delta = 10000$ s

$\Delta = 11000$ s
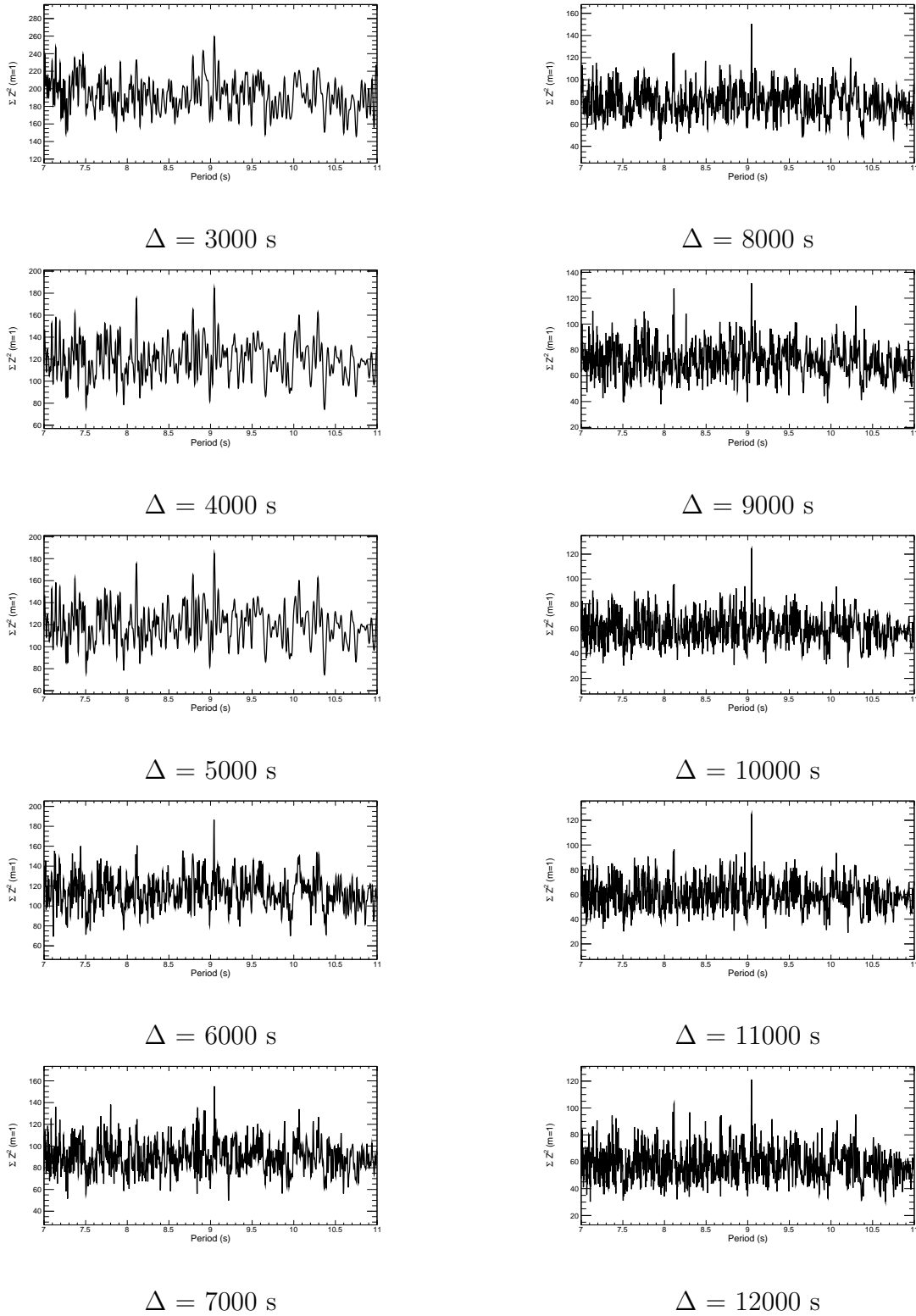
$\Delta = 12000$ s

Figure 5.4: Z^2 periodogram over $P = 7$–11 s using the 10–30 keV *NuSTAR* data. The results obtained from individual subsets are incoherently summed up. We adopt different time durations of each subset from 3000 s to 12000 s.
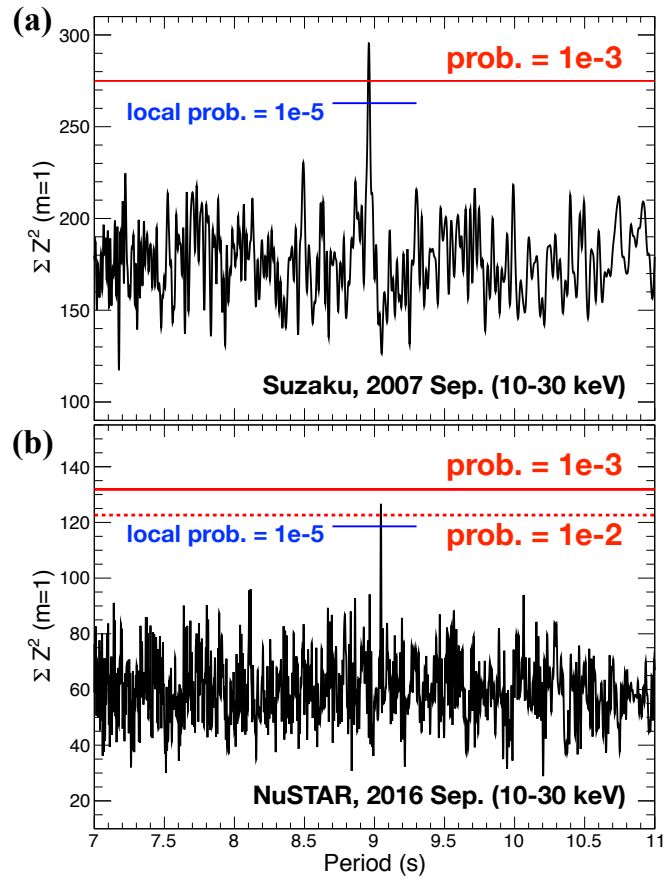
Figure 5.5: Z^2 periodgram in 10–30 keV, calculated over $P = 7$–11 s. The results obtained from individual subsets are incoherently summed up. Panel (a) shows the Suzaku data, which are divided into 86 subsets with $\Delta T = 5,000$s. Panel (b) shows the NuSTAR data for 30 subsets with $\Delta T = 10,000$ s.

argument $\omega \sim 55°$, initial orbital phase of the observation, and P_{orb} which was fixed at the optical value of 3.90608 days (Aragona et al., 2009). We first scanned the parameters and P_{NS} over the ranges given in Table 5.1. Then, starting from the sets of parameters that maximized Z^2 (separately for the two data sets), we repeated the parameter optimization using finer search steps. In this course, we allowed ω to vary over $45° - 65°$.

Table 5.1: Orbital parameter range searched in photon arrival time correction due to orbital motion.

parameter	min	max	step width	Aragona et al. (2009)	Sarty et al. (2011)
$a_{\mathrm{x}} \sin\theta$ [light sec.]	30.0	67.375	0.125	-	-
e	0.16	0.39	0.01	0.337 ± 0.036	0.24 ± 0.08
ω [deg.]	56		(fixed)*	56.0 ± 5.8	57.3 ± 21.8
τ_0 (*Suzaku*)**	-0.05	0.06875	0.00125	-0.022 ± 0.017	0.030 ± 0.07
τ_0 (*NuSTAR*)**	0.5	0.74875	0.00125	0.546 ± 0.034	0.615 ± 0.33
Orbital period [day]	3.90608		(fixed)	3.90608 ± 0.00010	3.906
P_{NS} [s] (*Suzaku*)	8.94	8.98	25 [μs]	-	-
P_{NS} [s] (*NuSTAR*)	9.025	9.065	25 [μs]	-	-

*: It was allowed to vary at later steps. See text.

**: The orbital phase at the time of the initial event in the data. The time of the initial event of *Suzaku* and *NuSTAR* is 54352.7163 and 57632.0952 (MJD TT) respectively.

Figure 5.6 shows the results of the orbital motion correction using 10–30 keV *Suzaku* data. Here, we adopt the maximum order m of the harmonics from 1 to 4. As m increases, a relatively large Z^2 value appears around $a_{\mathrm{x}} \sin\theta \sim 53$ light sec. The best-fitting values are described in Table 5.2. These parameters are more precise than those from the optical observations. Furthermore, we show the results using 10–30 keV *NuSTAR* data in Figure 5.7. However, in this case, the largest Z^2 values appear at different spots when m changes. In addition, the *Suzaku* and *NuSTAR* solutions using $m = 4$ actually agree only on ω though they should agree within errors on $a_{\mathrm{x}} \sin\theta$, e, and ω (Table 5.2). These problems with the present orbital parameters should be solved in future studies. A possible interpretation is some sporadic variations in the pulse properties. We discuss it in detail later.

Although the obtained orbital parameters are tentative, the *Suzaku* and *NuSTAR* pulse profiles shown in Figure 5.8, derived with the respective orbital solutions in Table 5.2, have similar three peaks with separations of ~ 0.25 pulse phases. This similarity may be caused by that *Suzaku* and *NuSTAR* observed the same phenomenon. The pulse fractions obtained

Table 5.2: Best-fitting values of the orbital parameters obtained from *Suzaku/NuSTAR* observations. Errors are in 90% confidence.

	$a_{\mathrm{x}} \sin\theta$ [light sec.]	e	τ_0	ω [deg.]	P_{NS} [s]	$Z^2(m=4)$
Suzaku	$53.05^{+0.70}_{-0.55}$	$0.278^{+0.014}_{-0.023}$	$0.067^{+0.009}_{-0.012}$	$54.6^{+5.1}_{-3.3}$	$8.95648(4)$	67.97
NuSTAR	$48.1^{+0.4}_{-0.4}$	$0.306^{+0.015}_{-0.013}$	$0.7285^{+0.0078}_{-0.0058}$	$56.8^{+2.3}_{-3.1}$	$9.05381(3)$	66.87

with *Suzaku* and *NuSTAR*, after background subtraction, are 0.68 ± 0.14 and 0.135 ± 0.043, respectively. The considerably lower pulse fraction with *NuSTAR* may explain why the *NuSTAR* data gave no evidence of periodicity via the Fourier analysis, and gave a somewhat higher $\mathcal{P}_{\mathrm{ch}}$ value via the Z^2 analysis, even though *NuSTAR* as a higher sensitivity than the *Suzaku* HXD. We also analyzed the 3–10 keV *NuSTAR* data using the parameters in Table 5.2, but found no periodic signals at the period with an upper-limit pulse fraction of 2.8% (99% confidence level). This suggests that the pulsation is detectable only in hard X-rays.

5.4.1   Possible Causes of the Lack of a Solution of the Orbital Parameters

We did not find a consistent solution of the orbital parameters when we applied the correction for the orbital motion to both *Suzaku* and *NuSTAR* data. A likely explanation is that the phases and/or shapes of the pulses are subject to gradual changes, which introduce additional modulations in the pulse arrival times. For example, some magnetars are known to undergo free precession (Makishima et al., 2014), possibly due to magnetic deformation. Note that magnetars are a class of neutron stars which have strong magnetic field $\sim 10^{15}$ G (see details in Chapter 8). The free precession modulates their hard X-ray pulse phases (though with a variable amplitude) at a period of several tens kiloseconds. If a neutron star in LS 5039 is also subject to a similar effect and if the pulse phase is modulated with a period which is comparable to or longer than P_{orb}, the two observations may have sampled different phases of the pulse-phase modulation. By further correcting the pulse arrival times for such effects, we expect that the two orbital solutions could be brought into a better agreement. This is a subject of future study.

5.4.2   Possibility of Contamination from Unrelated X-ray Sources

Since the HXD of Suzaku is a non-imaging collimated detector and has a relatively large field-of-view of $34' \times 34'$ at energies below 100 keV, there is a possibility that the detected

$$m = 1$$

$$m = 2$$

$$m = 3$$

$$m = 4$$
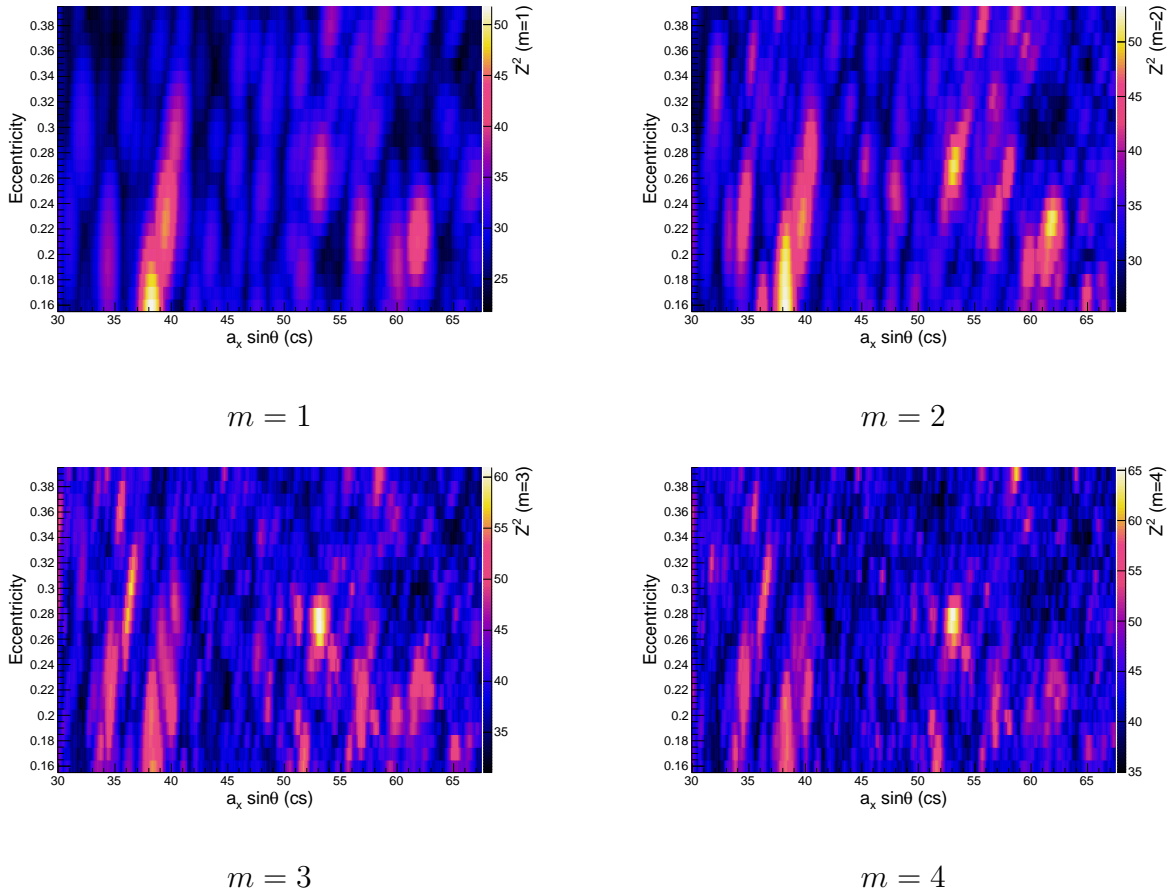
Figure 5.6: Z^2 statistics considering the orbital motion of LS 5039. The 10–30 *Suzaku* data were used. The colors indicate the Z^2 values after the orbital correction, shown on a plane of the projected orbital radius of the compact star (abscissa) and the orbital eccentricity (ordinate). m is the maximum order of the harmonics considered in the Z^2 statistics.

$$m = 1$$

$$m = 2$$

$$m = 3$$

$$m = 4$$
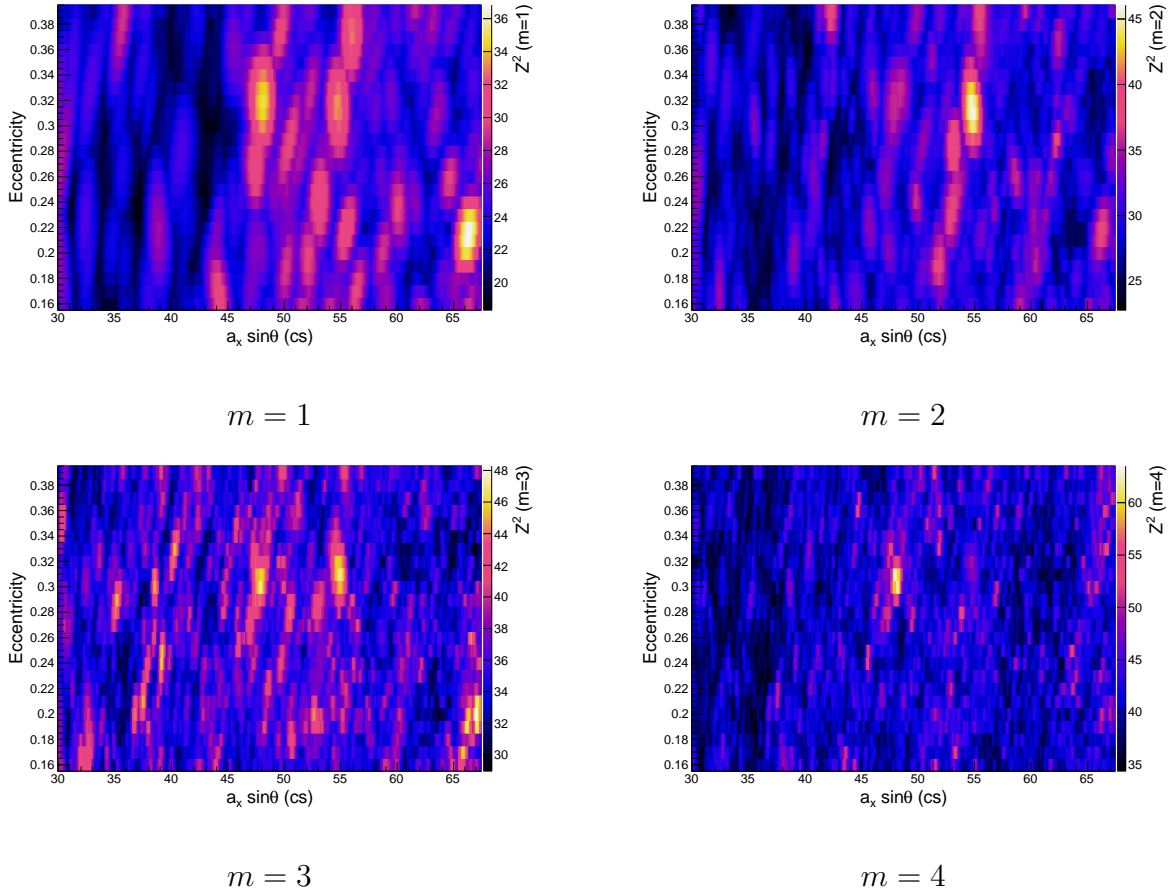
Figure 5.7: The same as Figure 5.6, but the 10–30 keV *NuSTAR* data were used.

(a)

(b)
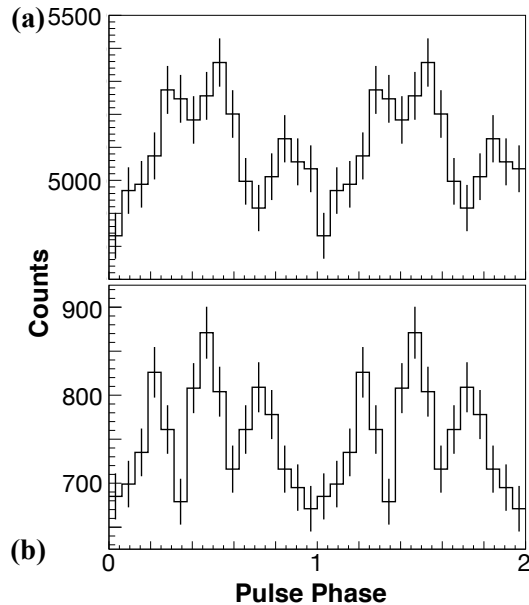
Figure 5.8:   The 10–30 keV folded pulse profiles from *Suzaku* (top) and *NuSTAR* (bottom), obtained using the best-estimated orbital parameters and optimum P_{NS} of the respective observations (Table 5.2).

pulsed emission originates from some unrelated source near or in the line of sight of LS 5039. Among catalogued celestial objects, the one nearest to LS 5039 is NVSS J182535−1455555 apart from LS 5039 by ~ 11 arcmin (Moldón et al., 2012). It is a radio source detected at 4.8 GHz (Condon et al., 1998), but is not catalogued as an X-ray emitter. Thus, it is unlikely to be a contamination source. Also, an isolated radio pulsar PSR J1825−1446 and a Wolf-Rayet star WR 115 (CXOU J182531.4−1444036) are at the edge of the HXD field-of-view. The spin period of PSR J1825−1446 is reported to be 0.28 s (Hobbs et al., 2004). As for WR 115, Chandra observations detected 780 s periodic signals and a hint of 5000 s periodicity (Muno et al., 2008). However, neither of the objects is reported to have a periodicity at ~ 9 s. Therefore, we conclude that the pulsed signal detected with the HXD is not due to contamination from nearby sources. This conclusion is strongly supported by the *NuSTAR* confirmation of the (presumably) same periodicity, in which the utilized data accumulation region of 30 arcsec in radius is much smaller than that of the HXD and hence excludes all the candidates above.

5.5 Summary

We searched hard X-ray data for the pulsed signal for the first time. In order to mitigate the Doppler effect due to the orbital motion, we divided the data into subsets with a time duration of 4196–16384 s, and calculated the power spectra calculated from individual subsets. Then, we merged them incoherently into one averaged spectrum with improved statistics. As a result, the *Suzaku* data revealed the periodic component of $P_{\mathrm{NS}} = 8.960 \pm 0.009$ s with a chance probability of $\mathcal{P}_{\mathrm{ch}} = 1.1 \times 10^{-3}$. Furthermore, the *NuSTAR* data shows a sign of the pulsation at $P_{\mathrm{NS}} = 9.046 \pm 0.009$ s. If we assume that these two peaks originate from the pulse emission, the compact object in LS 5039 is a neutron star with a spin period of $P_{\mathrm{NS}} \sim 9$ s and a period derivative of $\dot{P}_{\mathrm{NS}} \sim 3 \times 10^{-10}$ s s^{-1}. However, when we correct the photon time-of-arrival, considering the orbital motion, no consistent solution of orbital parameters are found from the *Suzaku* and *NuSTAR* data. In order to solve for the lack of a consistent orbital solution in the two observations, future work is needed *e.g.* an additional hard X-ray observation of LS 5039.

Chapter 6

Spectral Analysis in GeV gamma rays

LS 5039 is one of few binary systems detected in the GeV gamma-ray band. Due to its uniqueness, the GeV emission from LS 5039 has been studied in several works. The Fermi LAT collaboration (2009) reported the initial results of the *Fermi* LAT using 11 months worth of survey observations. They found that the spectrum followed a power law with an exponential cutoff with a cutoff at ~ 2.1 GeV and a photon index of ~ 1.9. Longer observations were analyzed by Hadasch et al. (2012), using 30 months worth of survey observations. Interestingly, they found that the INFC spectrum seems to have a hump around 2 GeV, which may indicate the existence of two spectral components in the GeV band. Furthermore, Chang et al. (2016) used ~ 7 years of observations, and reported that the orbital light curve in the 0.2–3 GeV band depends on the orbital phase which is different from that in the 3–20 GeV band. In this chapter, we analyze 11 years of *Fermi* data of LS 5039. Our aims are divided into two parts: (1) the detailed study of the GeV spectrum, especially, the hump at 2 GeV found by Hadasch et al. (2012); (2) the detailed study of the orbital phase dependence of the light curve.

6.1 *Fermi* Observation and Data Reduction

The data set used in this chapter spans from 2008 August 4 to 2019 September 21. It was reduced and analyzed using the *Fermi* Science Tools 1.0.10[1]. We used Reprocess Pass 8 data classified as event class "P8 source (`evclass=128`)" and event type "FRONT+BACK" (`evtype=3`)". In order to reduce the contamination due to Earth limb emission to the data, we selected events which were detected at a zenith angle less than 90 degrees. In the spec-

---

[1]Details of the Science Tools are described in https://github.com/fermi-lat/Fermitools-conda

tral analysis, the `P8R3_SOURCE_V2` instrument response functions were used. For the modeling of the Galactic diffuse emission and isotropic backgrounds, `gll_iem_v07.fits` and `iso_P8R3_SOURCE_V2_v1.txt`[2] were used.

6.2   Elimination of the Contamination from a Nearby Bright Pulsar

Since LS 5039 is located close to the Galactic plane, it is surrounded by many gamma-ray sources. There is an especially bright GeV pulsar PSR J1826-1256, apart from LS 5039 of $\sim$ 2 degrees. At 200 MeV, the flux of this pulsar is comparable to that of LS 5039. Considering that the point spread function of *Fermi* LAT is $\sim$ 3 degrees at 200 MeV, the gamma rays detected around the position of LS 5039 include those emitted from PSR J1826-1256. Thus, in order to eliminate this contamination, we discard the events whose arrival times are close to the peaks of the pulse emission of PSR J1826-1256 by following the previous analysis (The Fermi LAT collaboration, 2009; Hadasch et al., 2012). For this method, we need a pulse model parameters for PSR J1826-1256. However, the available parameters in Ray et al. (2011) are valid only from 2008 August to 2010 January. Therefore, we first calculate the pulse model parameters using the *Fermi* LAT data.

In the calculation of the pulse model parameters, we used the events which were detected in a circular region with a radius of 0.5 degrees centered at the location of PSR J1826-1256, (RA, DEC) = (18:26:08.53,-12:56:33.0). We constrained the gamma-ray energy to the range from 200 MeV to 1 TeV. The pulse profile is parameterized using three parameters; the frequency and the first and second derivative of the frequency. Since this pulse model cannot describe the pulse profile accurately, for more than about three years, we divided the data into subsets, and obtained the model parameters for every two years. The results are shown in Table 6.1. The pulse emission of PSR J1826-1256 has two sharp peaks, which is consistent with Ray et al. (2011). The calculation was done using the software which we developed for the pulse search using the Z^2 statistics discussed in Appendix A.

In the spectral analysis of LS 5039, we excluded the events which lie between $0.455 < \phi < 0.605$ or $0.925 < \phi < 1.075$, where ϕ is a pulse phase of PSR J1826-1256, defined in Figure 6.1. Figure 6.2 shows how the gamma-ray sky image is changed by excluding the pulse peak of PSR J1826-1256. By discarding these events, the exposure time of LS 5039

---

[2]These background models are available from the FSSC: https://fermi.gsfc.nasa.gov/ssc/data/access/lat/BackgroundModels.html

is reduced by 30%. To account for this, we multiplied a scaling factor (1/0.7) to the flux estimated from the binned likelihood analysis.

Table 6.1: The obtained parameters of the pulse timing model for PSR J1826-1256

Time Interval (s)	ephepoch (s)	f_0 (s^{-1})	f_1 ($\times 10^{-12}$ s^{-2})	f_2 ($\times 10^{-22}$ s^{-3})	ϕ at ephepoch
239557518–283456420	260314702.960	9.072468391(1)	−9.9967(2)	1.8(2)	0.0582
283456420–327355322	305989728.367	9.072012021(2)	−9.9850(2)	3.6(2)	0.1518
327355322–371254224	349374105.666	9.071579147(2)	−9.9709(2)	3.0(2)	0.9330
371254224–415153126	398186297.308	9.071118379(1)	−10.0086(3)	5.4(2)	0.0578
415153126–459052028	434432794.768	9.070755858(1)	−9.9965(2)	2.5(2)	0.0505
459052028–502950930	483220667.888	9.070268464(2)	−9.9826(2)	3.0(2)	0.4105
502950930–546849832	523881039.723	9.069862816(1)	−9.9708(2)	2.6(2)	0.5509
546849832–590748734	570655883.496	9.069406809(1)	−10.0025(2)	8.0(2)	0.0746

6.3   The Orbital Period of LS 5039

We measured the orbital period of LS 5039 by using the events which were detected in a circular region with 0.5 deg radius centered at the position of LS 5039. The gamma-ray energy was constrained in the range from 100 MeV to 1 TeV. In the Z^2 statistics only the first harmonics (m=1) was considered. We obtained an orbital period of

$$P_{\mathrm{orb}} = 3.90610 \pm 0.00012 \ (\mathrm{day}) \ , \tag{6.1}$$

as shown in Figure 6.3. It is consistent with the orbital period of 3.90608 ± 0.0001 day obtained by optical observations (Aragona et al., 2009).

6.4   Binned Likelihood Spectral Analysis

For the spectral parameters of LS 5039, the binned maximum likelihood method is used with `gtlike` of the *Fermi* Science Tools. In this method, we compare count maps obtained from the data with that predicted by the spectral model. Since the point spread functions of *Fermi* LAT strongly depends on the gamma-ray energy, the count maps are produced in different energy intervals. Even if the total photon counts are large, the count in each bin is small, which is characterized by the Poisson distribution and not a normal distribution. Therefore, it is favorable to use the likelihood function to treat the Poisson distribution properly.
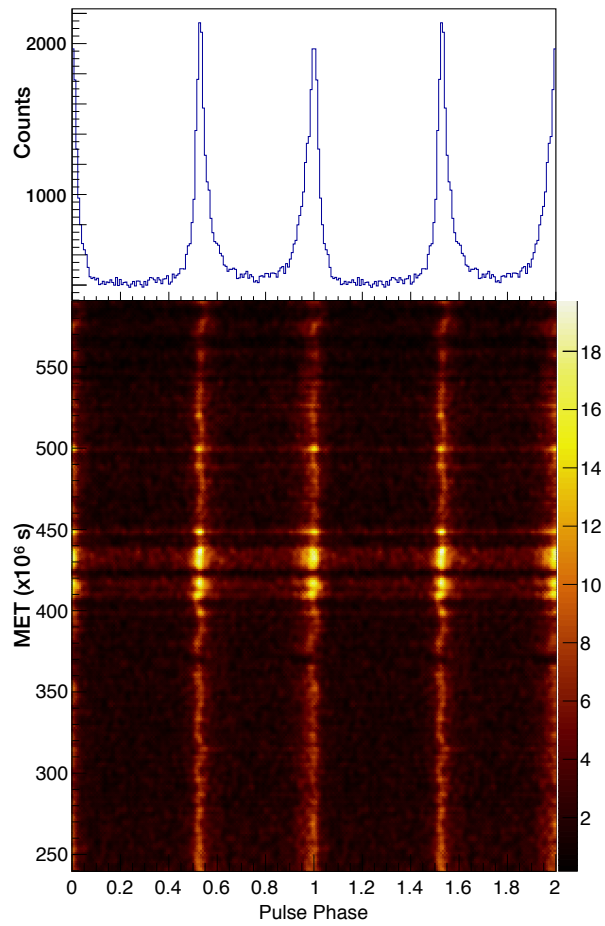
Figure 6.1: The pulse profile of PSR J1826-1256 in 11 years *Fermi* observation.
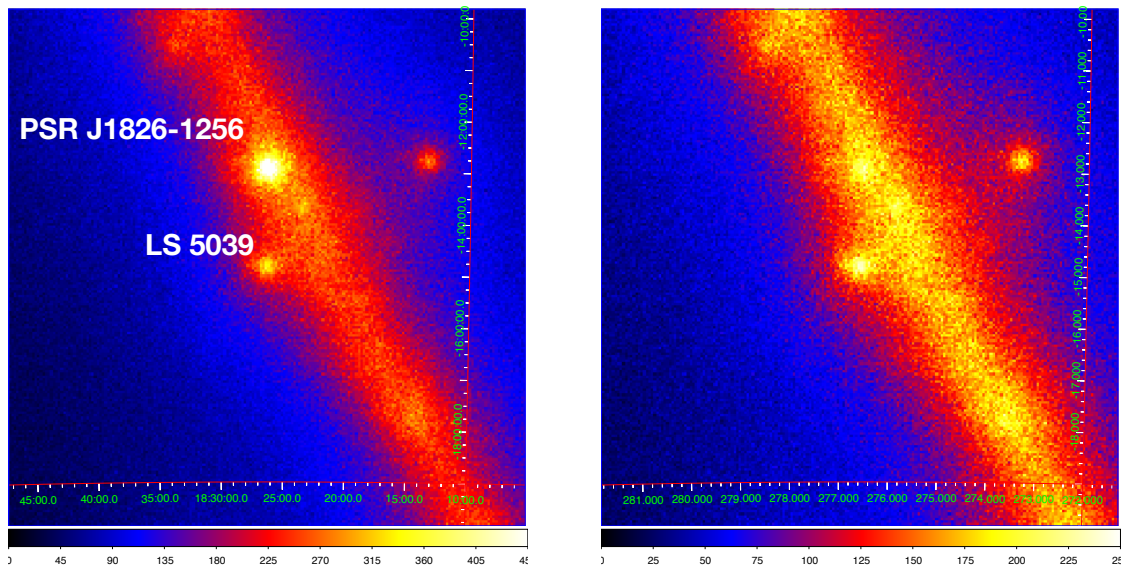
Figure 6.2: *Fermi* LAT images around LS 5039. The left figure is obtained using all of the 11 years of data from 30 MeV to 10 TeV. The right figure is the image after we exclude the events which correspond to the pulse peak of PSR J1826-1256 ($0.455 < \phi < 0.605$ or $0.925 < \phi < 1.075$).
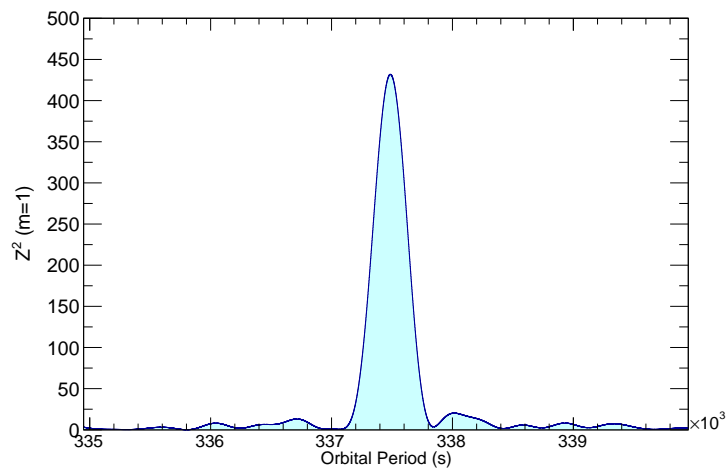
Figure 6.3: Z^2 periodram around a period of 3.9 days using the events within 0.5 deg radius centered at the position of LS 5039.

The likelihood function L is the product of the probabilities of observing the detected counts in each bin under a certain model. The best-fitting parameters are calculated as the parameter set which yields the maximum of L. Under the Poisson distribution, the probability p_i to detect n_i photons in i-th bin is calculated as:

$$p_i = m_i^{n_i} \frac{\exp{(-m_i)}}{n_i!} \ , \tag{6.2}$$

where m_i is the photon count in the i-th bin predicted by an assumed spectral model. By multiplying the p_i over all of the bins, the likelihood function is calculated as:

$$L = \exp{(-N_{\text{exp}})} \prod_i \frac{m_i^{n_i}}{n_i!} \ , \tag{6.3}$$

where N_{exp} is the total number of the events predicted from the assumed spectral model.

Source detection significance is evaluated with the Test Statistics (TS) defined as:

$$TS = -2 \ln{(L_0/L_1)} \ , \tag{6.4}$$

where L_0 is the likelihood for the model without the additional source, and L_1 is the likelihood for the model with the additional source. If the number of the photons is large, TS is expected to be asymptotically distributed with χ_1^2 under the null hypothesis from Wilks' Theorem (Mattox et al., 1996). Therefore, the significance is equal to $\sim (TS)^{0.5}$ σ. In general, if the number of additional parameters in the alternative hypothesis is m, TS is asymptotically distributed with χ_m^2.

In our analysis, the bin width of count maps is defined as 0.125 degrees in order to distinguish LS 5039 from the dim source 4FGL J1827-1445 separated by 0.31 degrees. Since the point spread function at 100 MeV is about 5 degrees, the size of the count maps is set to 10×10 degrees. The energy bins are defined by 6 bins every decade below 10 GeV and 3 bins every decade above 10 GeV . In order to consider the energy dependence of the point spread functions, we enabled the energy dissipation correction (`edisp=1`) in `gtlike`.

6.5   Pre-analysis for the Spectral Analysis

First, we modeled LS 5039 with a powerlaw with an exponential cutoff. Furthermore, we included all sources within 18° of the ROI center listed in the 4FGL catalog (The Fermi-LAT collaboration, 2019). Their spectral models are the same as described in the catalog. As for the sources within 5° of the ROI center and with TS values larger than 9.0, their spectral parameters are set free. We also set the normalization and the photon index of the Galactic

diffuse model free. After the spectral fitting, we compared the difference between the count map and the best-fitting model. We found a few bins which show relatively large values of the difference. Figure 6.4 is a histogram of the difference of event counts in each bin. In order to investigate the origin of them, we extracted four bins in which the differences are larger than 100 counts, and added the spectral model described by LogParabola function locating the center of each bin. The four spots are shown as the green circles in Figure 6.4. After applying the spectral fitting, 3 in 4 sources yielded large TS values as shown in Table 6.2. These TS values correspond to more than 5σ significance, which we conclude that the large differences in these three bins are due to point sources that were not listed in the 4FGL catalog. As for the spot where the TS value is not high, the difference is probably due to statistical fluctuations. Thus, we added the three sources in the spectral model.
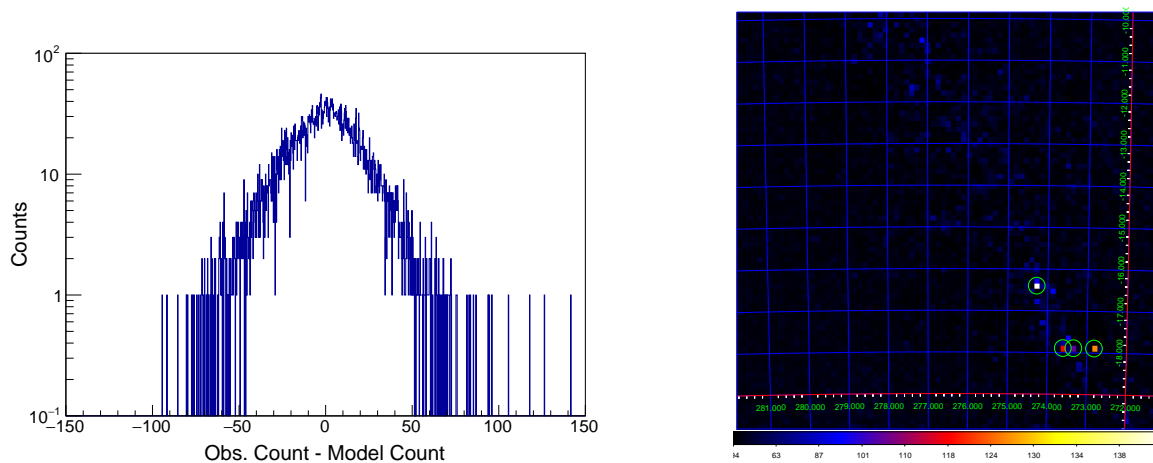
Figure 6.4: The difference between event counts in each bin using the 4FGL catalog. The left is a histogram of the difference. The right is a map of the difference in each bin. The green circles are the spots where the differences are larger than 100.0.

Table 6.2: List of added point sources

RA	DEC	TS value
274.28	-16.40	138.3
273.606	-17.89	82.9
273.34	-17.89	40.0

In order to check the accuracy of the fitting result, we calculate the ratio of the observed counts to the model prediction in each energy bin as shown in Figure 6.5. The derived ratios

lie between -0.05 to 0.05. These deviations are thought to be produced by the uncertainties of the effective area and the point spread function of *Fermi* LAT because they have $\sim 3\%$ and $\sim 5\%$ uncertainties from 100 MeV to 100 GeV[3]. In order to consider these systematic uncertainties, we assumed that the flux in each energy bin has 5% systematic error. The systematic uncertainties are estimated as the following. This is called the "bracketing Aeff method". In this method, we change the effective area by multiplying it by $1 \pm \epsilon$ below a certain energy E and by multiplying it by $1.0 \mp \epsilon$ above E, and obtained the best-fitting parameters. Systematic errors are estimated by determining how much the parameter values are changed. We set ϵ as 0.05 and E as the cutoff energy of the exponential-cutoff powerlaw.
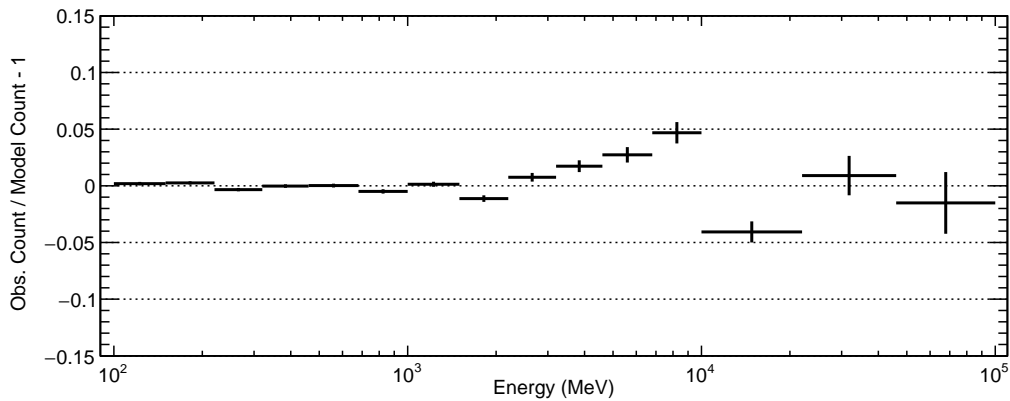
Figure 6.5: The ratio between the observed counts and the best-fitting model predictions in each energy bin.

6.6   Spectrum of LS 5039 in the GeV gamma-ray band

Figure 6.6 shows the resulting spectrum of LS 5039. It is described well with a single exponential-cutoff powerlaw. The best-fitting parameters using 100 MeV–10GeV gamma rays are described in Table 6.3. The photon index and the cutoff energy were ~ 2.4 and ~ 8.0 GeV.

Next, we analyzed the spectrum around the inferior conjunction (INFC) and the superior conjunction (SUPC). Following on from the previous chapter, the INFC and the SUPC are defined between $0.45 < \phi < 0.9$ and $0.0 < \phi < 0.45, 0.9 < \phi < 1.0$, where ϕ is the orbital phase of LS 5039. We adopted the orbital period of 3.90608 days (Aragona et al., 2009) and

---

[3]Details are described in https://fermi.gsfc.nasa.gov/ssc/data/analysis/LAT_caveats.html

$T_0 = 2455017.08$ (HJD) (Sarty et al., 2011). The spectra of INFC and SUPC are shown at the bottom of Figure 6.6. The SUPC spectrum is well described by a single exponential-cutoff powerlaw. On the other hand, the INFC spectrum shows a hump structure around a few GeV. Although this spectral feature was mentioned in Hadasch et al. (2012), they modeled the spectrum with a single exponential-cutoff powerlaw. Here, we modeled it with a sum of a exponential-cutoff powerlaw and a simple powerlaw. Table 6.3 describes the best-fitting parameters. The two-component model improves the TS value by ~ 1500 when comparing it with the single exponential-cutoff powerlaw model. Thus, the two-component model is significantly favored. The powerlaw component with a photon index of ~ 3.6 is dominant below ~ 400 GeV. Above 400 GeV, a new spectral component becomes dominant. It has a photon index of ~ 1.3 and a cutoff energy of ~ 1.9 GeV.

Table 6.3: Best-fitting parameters of the GeV spectra. The first and second errors correspond to 1σ statistical errors and systematic errors.

Phase	Photon Index	Cutoff Energy GeV	Flux at 1 GeV $\times 10^{-11}$ cm^{-2} s^{-1} MeV^{-1}	TS value
All Phase	$2.442 \pm 0.008 \pm 0.007$	$8.0 \pm 0.5 \pm 0.3$	$3.49 \pm 0.04 \pm 0.19$	11511
SUPC	$2.370 \pm 0.009 \pm 0.028$	$4.4 \pm 0.2 \pm 0.5$	$4.82 \pm 0.06 \pm 0.30$	9003
INFC[1]	$2.38 \pm 0.02 \pm 0.02$	$11.6 \pm 1.7 \pm 0.8$	$2.56 \pm 0.05 \pm 0.15$	2883
INFC[2]	$1.29 \pm 0.04 \pm 0.53$	$1.87 \pm 0.06 \pm 0.38$	$3.62 \pm 0.12 \pm 0.56$	4410
	$3.57 \pm 0.02 \pm 0.37$	$-$	$0.31 \pm 0.01 \,^{+0.32}_{-0.19}$	

[1]: the spectrum is modeled with a single exponential cutoff powerlaw.

[2]: the spectrum is modeled with sum of a single exponential cutoff powerlaw and a simple powerlaw.

6.7 Dependence of the Flux on the Orbital Phase

We analyzed the spectrum of LS 5039 by dividing the data into subsets with an interval of $\Delta\phi = 0.1$. The resulting spectrums are showin in Figure 6.7. The flux is highest around $\phi \sim 0.0$, where the compact object is closest to the companion star. As ϕ gets closer to $\phi \sim 0.5$, the flux gets lower especially in the low energy band, and the spectrum becomes harder.

Figure 6.8 shows the orbital light curves in different energy intervals. From 100 MeV to
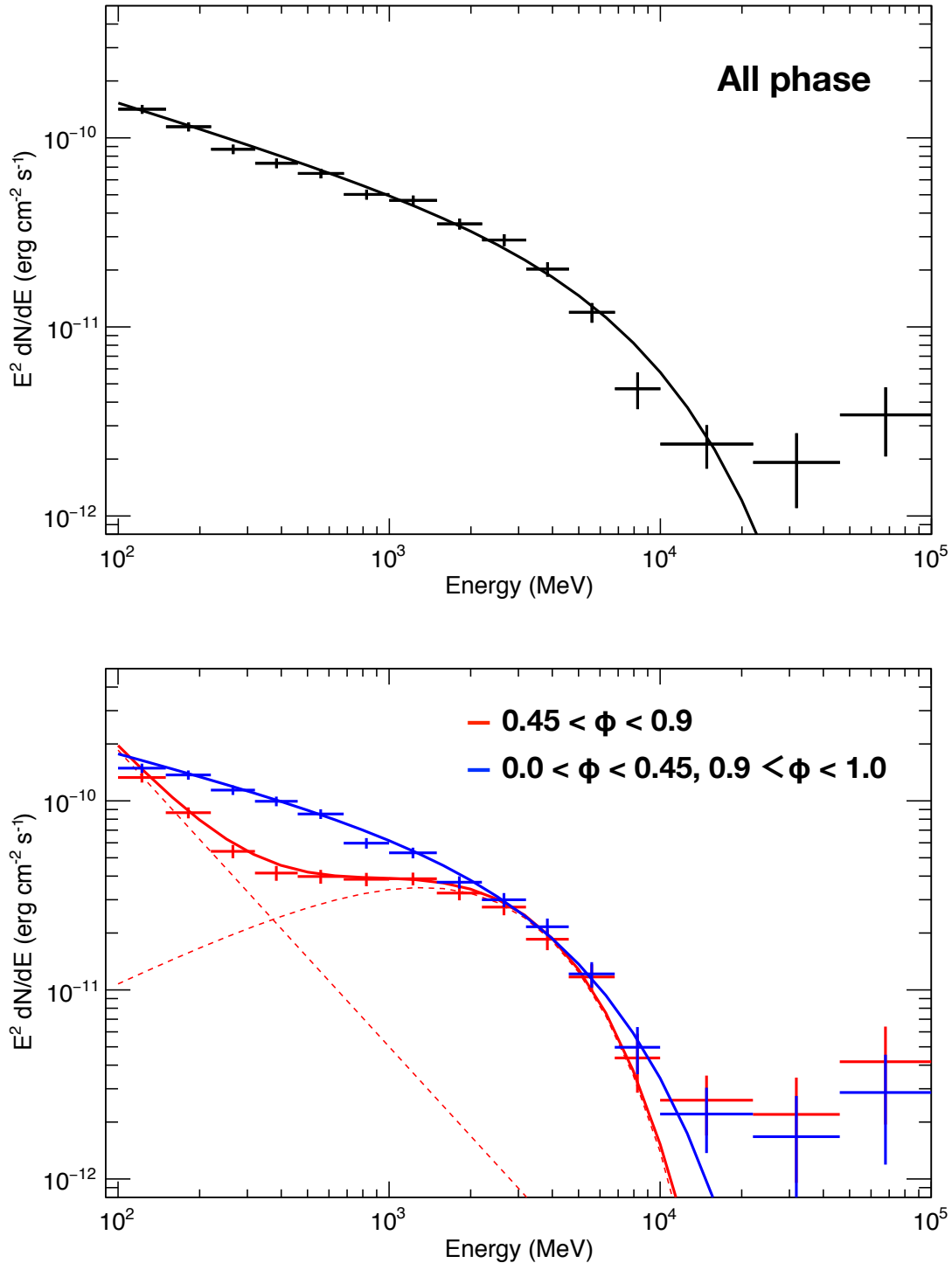
Figure 6.6: GeV spectra of LS 5039. The top figure is the averaged spectrum over all of the orbital phase. The bottom figure shows the spectra dividing the data into two intervals of the orbital phase. The red and blue lines represent the INFC and the SUPC, respectively.

1 GeV, the light curves have a strong peak around $\phi \sim 0.0$. The phase of the minimum flux is shifted from $\phi \sim 0.3$ at 100–220 MeV to $\phi \sim 0.8$ at 460–1000 MeV. Above 1 GeV, the orbital modulation becomes considerably weak. In order to evaluate the transition of the orbital modulation, we calculate the ratio from $(F_{\max} - F_{\min})$ to $(F_{\max} + F_{\min})$, where $F_{\max}$ and $F_{\min}$ are the maximum and minimum flux in the light curves, respectively. This value is interpreted as the fraction of the variable component over the total flux. Figure 6.9 shows the significant decrease of the ratio around 1 GeV. While the fraction of the variable component is $\sim 60\%$ around 300 MeV, it decreases to $\sim 20\%$ in 1–5 GeV. Considering the spectral change at around 1 GeV (Figure 6.6), this result supports the hypothesis that the spectral components below 1 GeV and above 1 GeV are different from each other.

6.8 Search for Time Variability

The stability of the emission can provide important information on the physical mechanism of the emission. Since the cooling time of accelerated particles in LS 5039 is much shorter than the orbital period, the flux variability is considered to reflect the stability of the acceleration process in LS 5039. Here, we search for the time variability of the emission by studying the light curve of LS 5039.

6.8.1 1 year intervals

First, we investigate the flux variability with a time scale of one year. When the observation period is changed, other sources may change their fluxes. Furthermore, in *Fermi* LAT, the effective exposure time at each sky location changes non-uniformly. This can affect the flux estimation. In order to consider these systematics, we calculate the flux of LS 5039 in different ways: (1) only the spectral parameters of LS 5039 are set free. Those of other sources are fixed to the best-fitting parameters obtained with 11 year observations.; (2) the same analysis as the spectral analysis of 11 year observations.; (3) the same as (2), but the spectral parameters of the Galactic diffuse emission are fixed.; (4) the same as (3), but the spectral parameters except for the normalization are fixed. The spectral parameters of LS 5039 are set free.

Figure 6.10 shows the resulting light curves. The flux points in the 100–220 MeV light curve have a large deviation in 2019. Since the flux in this interval is changed dramatically depending on the different protocols, the large derivation is due to the systematics rather than a flare-like activity by LS 5039. Hereafter, we ignore this time interval. As shown in
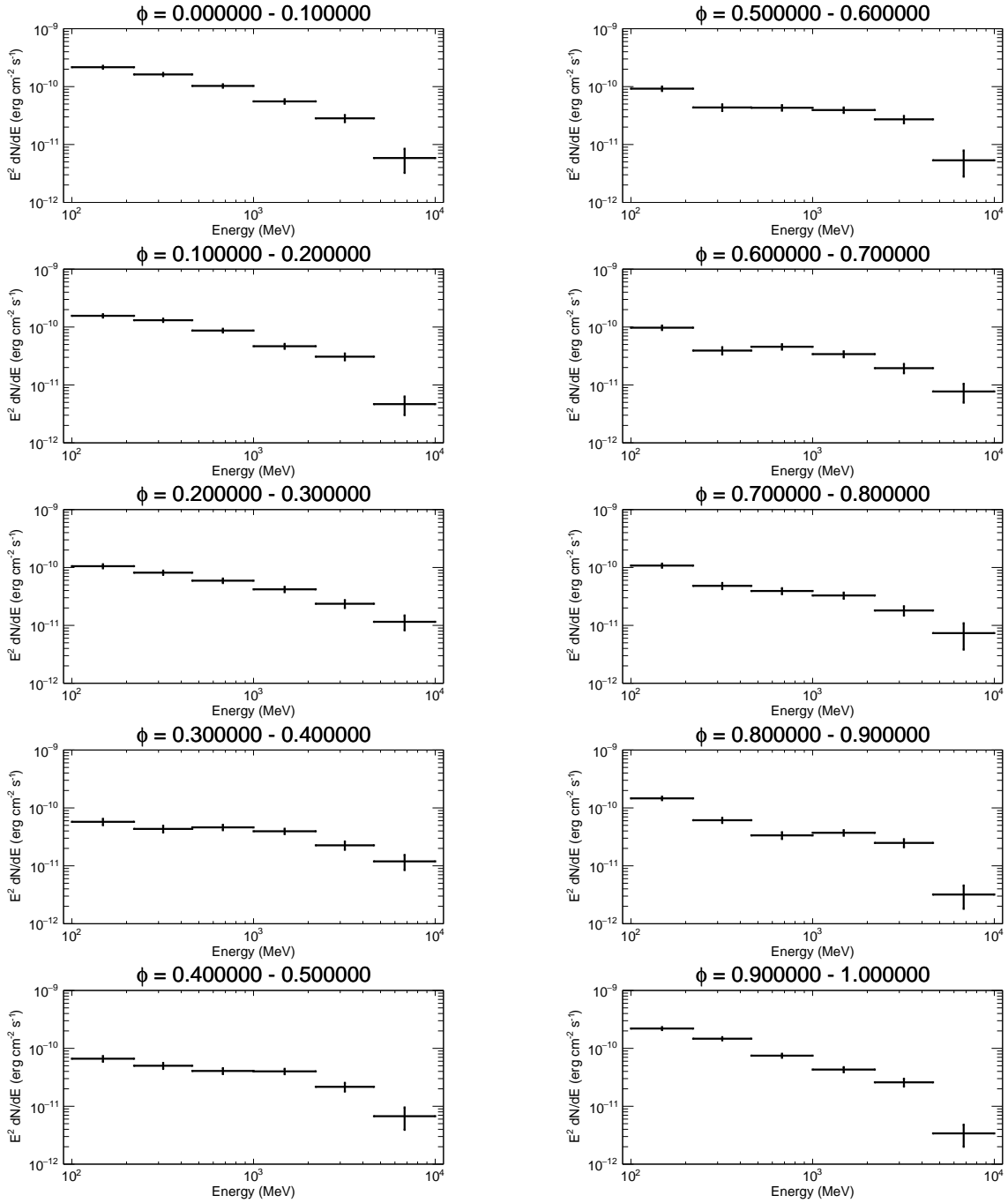
Figure 6.7: The spectra of LS 5039 in different orbital phase intervals.
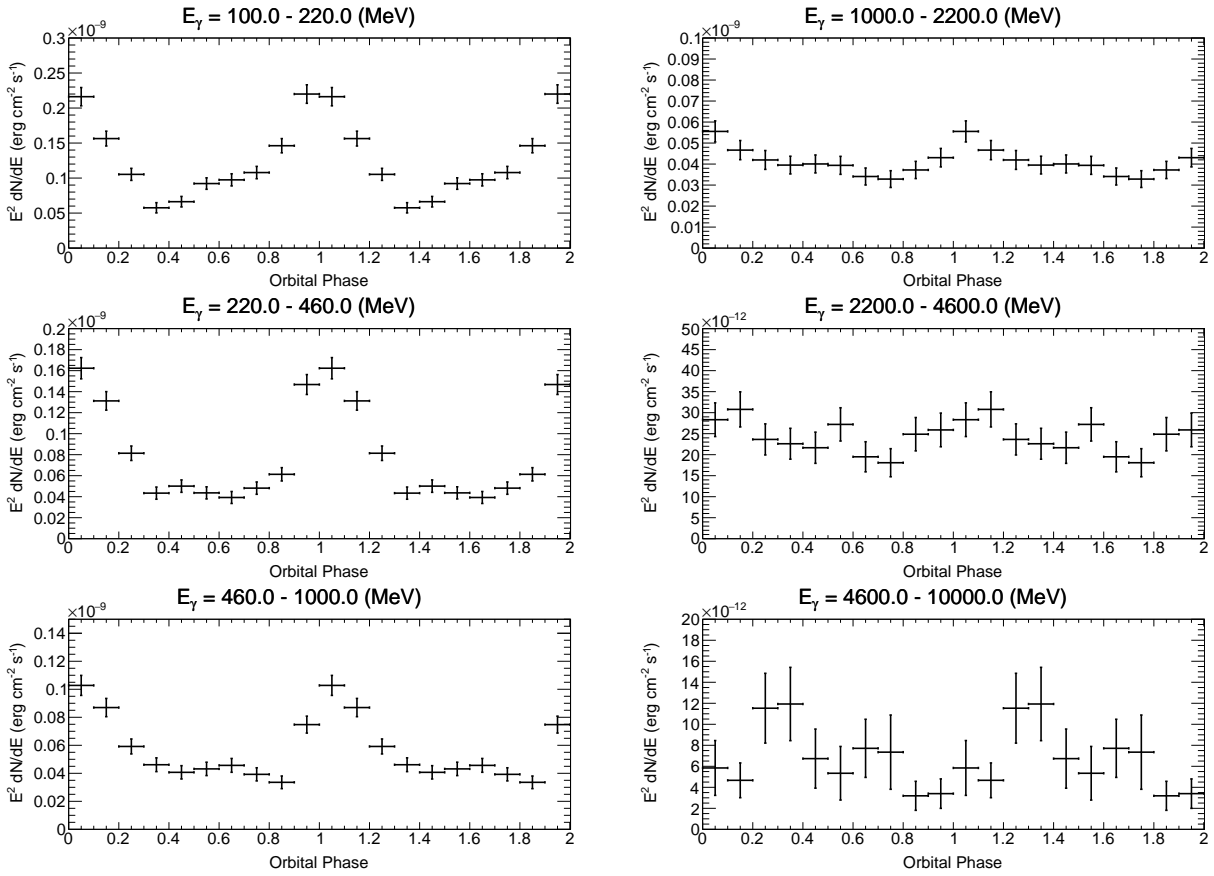
Figure 6.8: The orbital light curve in different energy intervals.
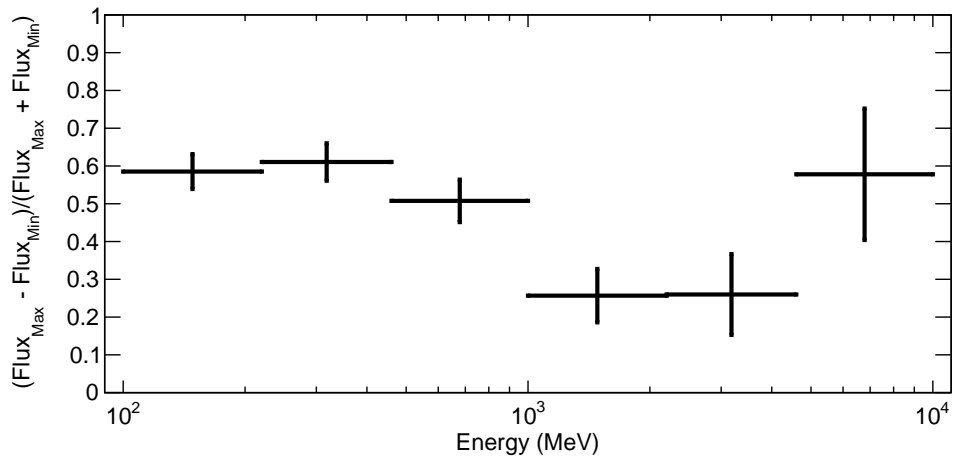
Figure 6.9: The flux ratio of the variable component to the total. Here we calculated $(F_{max} - F_{min})$ to $(F_{max} + F_{min})$; F_{max} and F_{min} are the maximum and minimum flux in the light curves of Figure 6.8.

Figure 6.10, there is no flaring activities. The fluxes between 100–220 MeV and 220 MeV–4.6 GeV are stable with deviations of $\sim 30\%$ and $\sim 20\%$ respectively. Above 4.6 GeV, it seems that flux is gradually decreasing. However, since the difference between the minimum and the averaged fluxes is just 1.4 σ, the flux decrease is not statistically significant.
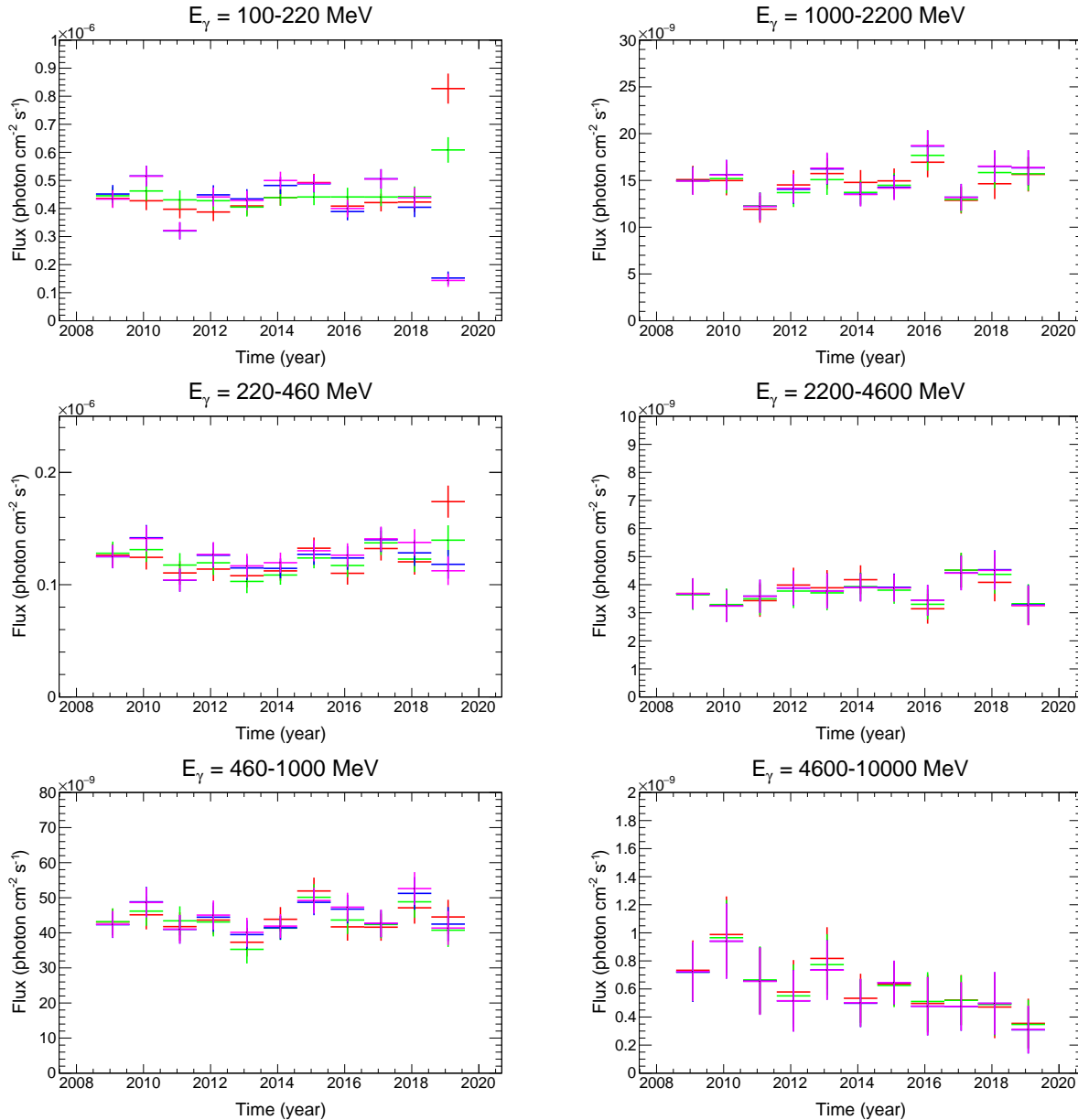
Figure 6.10: The light curve of LS 5039 with a bin width of 1 year. The different colors corresponds to the different spectral fittings. The red, magenta, blue and green points are obtained with the different protocols (1), (2), (3) and (4) described in the text.

6.8.2 1 month intervals

In order to investigate shorter time variabilities, we analyzed the spectrum every month. Here, we ignore the data after 2018 August 5 since the results have large systematic errors as shown in Figure 6.10. We enlarged the energy intervals (100–460 MeV, 460 MeV–2.2 GeV and 2.2–10 GeV). In 2.2–10 GeV, we analyze the spectrum every 4 months because the photon counts are small. In this analysis, only the spectral parameters of LS 5039 are set free. Those of other sources are fixed to the best-fitting parameters obtained with 11 year of observations. The obtained light curves are shown in Figure 6.11. In all cases, there are no time intervals when the flux is higher than the average by more than 3σ fluctuation. Therefore, the flux of LS 5039 is found to be stable over 100 MeV–10 GeV with a time scale of one month.

6.9 Summary

We analyzed 11 year of observations by *Fermi* LAT. The spectrum averaged over the orbital phase is well described with a single cut-off powerlaw component. Furthermore, the spectrum around INFC shows a prominent hump at around 1 GeV. It is described well with two components; a powerlaw with a photon index of ~ 3.6, and an exponential cutoff powerlaw with a photon index and a cutoff energy of ~ 1.3 and ~ 1.9 GeV, respectively. We analyzed the dependence of the flux on the orbital phase. While the fraction of the variable component is $\sim 60\%$ at around 300 MeV, it decreases to $\sim 20\%$ from 1 GeV to 5 GeV. On the basis of these results, we conclude that there are two spectral components in the GeV band. Finally, we searched for time variability, and found that the flux of LS 5039 is stable across the energy band in both 1-month and 1-year time scales.
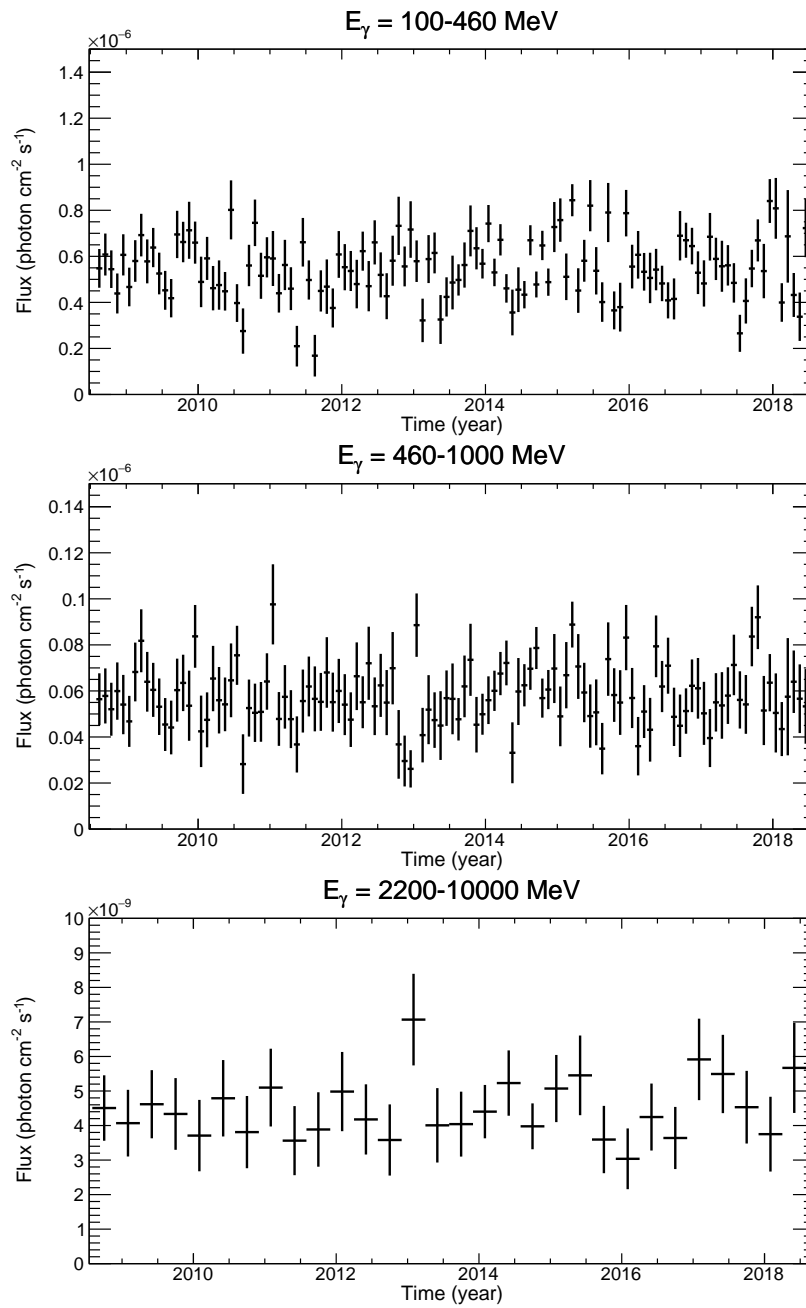
Figure 6.11: The light curve of LS 5039 with a bin width of 1 month. From 2.2–10 GeV, the bin width is enlarged to 4 months since the photon counts are small.

Chapter 7

Spectral Modeling and Comparison with the Observed Spectrum

In the previous chapters, we analyzed the X-ray and GeV gamma-ray spectra of LS 5039 using the *NuSTAR* and *Fermi* observations. In order to interpret these spectra, we developed a spectral model of LS 5039 from the X-ray to TeV band. Considering that neither the pulsar wind model or the microquasar model has failed to explain its spectrum, the spectral model is described with several basic parameters without assuming specific conditions *e.g.* the nature of the compact object. By comparing the model with the observed spectrum, we constrain the physical parameters of LS 5039 and derive properties of spectral components.

7.1   Purpose and Method of Spectral Modeling

Using the result of the spectral analysis in Chapter 4 and 6, we obtained the spectral energy distribution (SED) of LS 5039 as shown in Figure 7.1. Owing to the *NuSTAR*'s high sensitivity and the large statistics of 11 years of the *Fermi* data, the spectral shape from 10 keV to 70 keV and from 100 MeV to 100 GeV is obtained with smaller errors than those in the previous SED (see Figure 2.7 in Chapter 2). The spectrum around 10 MeV connects that around 100 MeV smoothly, and there is a hump structure around 300 MeV. This indicates that the spectral component around 10 MeV extends to $\sim$ 300 MeV, and then drops with a sharp spectral cutoff. On the other hand, the relation between the X-ray and MeV gamma-ray components is not obvious. While the X-ray spectrum seems to connect the MeV gamma-ray spectrum for the inferior conjunction, the X-ray spectrum for the superior conjunction seems to become hard above 30 keV. Thus, on the basis of the spectral shape

alone, it is difficult to conclude whether the origin of the X-ray component is the same for the MeV gamma-ray component.

In order to answer this question, we developed a spectral model and compare it with the observed spectrum of LS 5039. Our strategy is the following:

1. In the spectral modeling, we do not assume specific conditions *i.e.* the nature of the compact object and detail geometry of the emission region of LS 5039. Instead, we develop a spectral model that is described by basic physical parameters of an emission region and particle acceleration, for example, the size of and the magnetic field in an emission region.

   Our aim is to allow for a wide range of physical parameters by minimizing assumptions of the spectral modeling. Although many detailed spectra models have been developed by assuming the pulsar wind model (*e.g* Dubus et al. 2015; Takata et al. 2014) or the microquasar model (*e.g* Khangulyan et al. 2008; Paredes et al. 2006), so far no model explains the MeV component successfully. This suggests that there is an acceleration/emission mechanism that is not described by either models. The spectral model without specific assumptions can allow us to test physical parameters which are not achieved in previous models. Hereafter, we refer to our model as the general spectral model.

2. We search for physical parameters of the general spectral model which produce a SED consistent with the observed one. Here we assume the following assumptions:

   (a) The X-ray spectrum is produced by synchrotron emission.

   (b) Electrons of the synchrotron emission are accelerated by the diffusive shock acceleration.

   (c) Electrons also produce GeV/TeV gamma rays via inverse Compton scattering with UV photons which are emitted from the companion O star.

   We derive physical parameters which satisfy the following conditions:

   (a) The flux and the photon index of the X-ray synchrotron spectrum is consistent with those observed by the *NuSTAR*.

   (b) The flux of the corresponding inverse Compton emission is lower than that observed by the *Fermi*.

   As a result, we constrain parameter space of the general spectral model.

3. Finally, we check whether the constrained parameter space contains any parameter set which explains the X-ray and MeV spectra as a single spectral component.

Hereafter, we describe details of the general spectral model and the results of the spectral comparison.
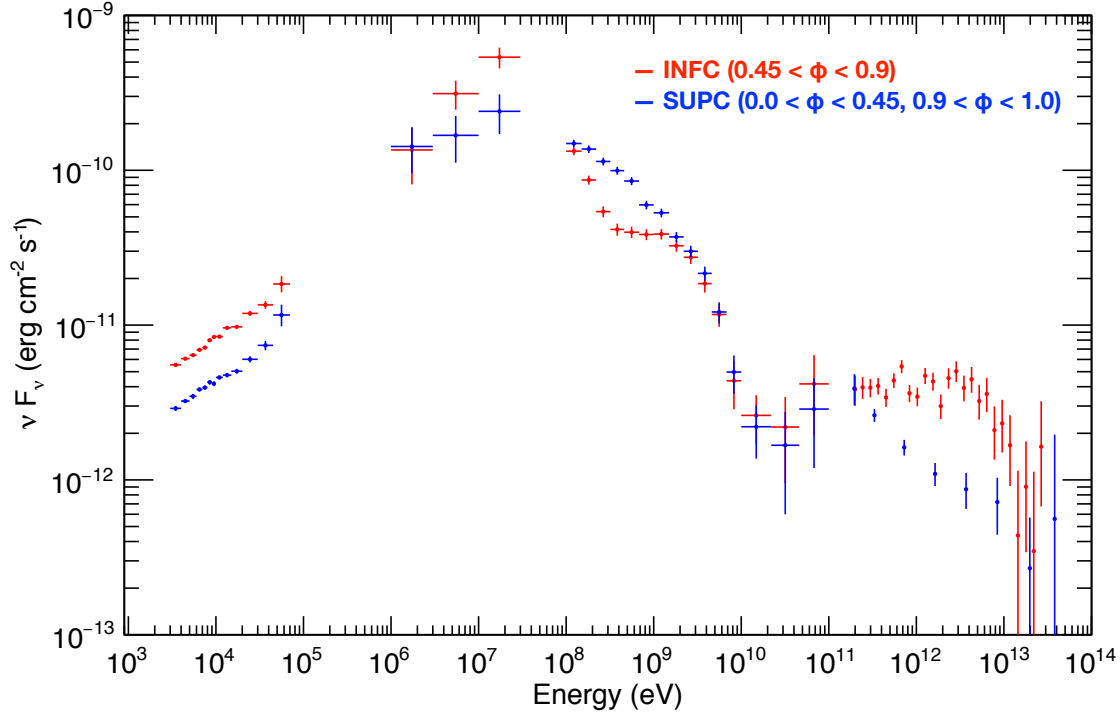
Figure 7.1: The spectral energy distribution of LS 5039. The red and blue points correspond to the flux levels around the inferior conjunction ($0.45 < \phi < 0.9$) and the superior conjunction ($0.0 < \phi < 0.45$, $0.9 < \phi < 1.0$). The flux points in 10^3–10^5 eV and 10^8–10^{11} eV are obtained in this work. The MeV and TeV gamma-ray spectra are taken from Collmar & Zhang (2014) and Aharonian et al. (2006b), respectively.

7.2 Development of the General Spectral Model

In order to describe the general spectral model without specific geometrical assumptions, we assume homogeneous physical conditions *i.e.* the magnetic field and the density of seed photons are constant in the emission region which is expanding uniformly. By particle acceleration in LS 5039, accelerated electrons are injected into the emission region. The injected

electron energy spectrum is assumed to be a powerlaw function. Considering cooling of the accelerated electrons, we consider three processes, synchrotron radiation, inverse Compton and adiabatic losses which are considered to be main cooling processes in LS 5039 (Dubus et al., 2015; Takata et al., 2014; Khangulyan et al., 2008; Paredes et al., 2006). Thus, our model is described with nine parameters as summarized in Table 7.1. In the following two sections, we explain the details of the spectral calculation.

Table 7.1: Parameters of the general spectral model

Parameter	Description
R_{acc} (light sec)	the size of the acceleration region
B (G)	the strength of the magnetic field in the acceleration region
D_{acc} (light sec)	the distance between the companion star and the acceleration region
θ_{IC} (degree)	the scattering angle of the seed photons in the inverse Compton scattering
η	the acceleration efficiency
s	the spectral index of the injection electron energy distribution ($Q(\gamma) \propto \gamma^{-s}$)
$kT_{\star}$	the surface temperature of the companion star. We fix it to 3.3 eV (Casares et al., 2005).
$R_{\star}$	the radius of the companion star. We fix it to 9.3 $R_{\odot}$ (Casares et al., 2005).
Norm	the normalization of the model spectrum

7.2.1   Spectrum Calculation

For the calculation of the spectrum, we use `Naima`, a Python package for computation of non-thermal radiation from relativistic particle populations (Zabalza, 2015). `Naima` includes non-thermal radiative models of the synchrotron, inverse Compton, bremsstrahlung, and neutral pion decay processes. `Naima` calculates the inverse Compton spectra by using the analytical approximations derived by Khangulyan et al. (2014). It calculates the synchrotron spectra based on the parametrization of the emissivity function in random magnetic fields derived by Aharonian et al. (2010). All of the models allow the use of an arbitrary shape of the particle energy distribution. We first compute the electron energy distribution, and input the distribution into `Naima` and compute the synchrotron and inverse Compton spectra. In the following section, we describe the computation of the electron distribution.

7.2.2 Electron Energy Distribution

In order to calculate the radiation spectrum, the electron energy distribution should be first determined. When the physical parameters do not have spatial dependence, the time evolution of the electron energy distribution $n(t, \gamma)$ is described by the following equation (Ginzburg & Syrovatskii, 1964)

$$\frac{\partial n(t, \gamma)}{\partial t} + \frac{\partial \dot{\gamma}(\gamma) n(t, \gamma)}{\partial \gamma} + \frac{n(t, \gamma)}{T_{\text{esc}}} = Q(t, \gamma) , \tag{7.1}$$

where γ is the Lorentz factor of the electron and T_{esc} is the escape time of the electron from the acceleration region; $\dot{\gamma}(\gamma)$ is the cooling rate of the electron, and $Q(t, \gamma)$ is the injection electron spectrum. Since the cooling and acceleration time scales in LS 5039 are much shorter than the orbital period of ~ 4 days, the electron energy distribution can be described by a steady-state solution of Equation 7.1. Then, it is derived as

$$n(\gamma) = \frac{1}{|\dot{\gamma}(\gamma)|} \int_{\gamma}^{\infty} Q(\gamma') e^{-\tau_c(\gamma, \gamma')/T_{esc}} \mathrm{d}\gamma' , \tag{7.2}$$

where τ_c is defined as

$$\tau_c(\gamma, \gamma') = \int_{\gamma}^{\gamma'} \frac{\mathrm{d}\gamma''}{|\dot{\gamma}(\gamma'')|} . \tag{7.3}$$

$\tau_c(\gamma, \gamma')$ is the time which it takes to cool an electron from the Lorentz factor of γ' to γ. When electron escape is negligible ($\tau_c(\gamma, \gamma') \ll T_{\text{esc}}$), $n(\gamma)$ is described as

$$n(\gamma) = \frac{1}{|\dot{\gamma}(\gamma)|} \int_{\gamma}^{\infty} Q(\gamma') \mathrm{d}\gamma' . \tag{7.4}$$

For diffusion escape in the Bohm limit, the escape time scale is estimated as

$$T_{\text{esc}} \sim \frac{3R_{\text{acc}}^2}{r_{\text{L}} c} = 7 \times 10^2 \, [s] \times \left(\frac{R_{\text{acc}}}{5 \, [\text{light sec}]} \right) \left(\frac{B}{1 \, [\text{G}]} \right) \left(\frac{\gamma m_e c^2}{1 \, [\text{TeV}]} \right) , \tag{7.5}$$

where R_{acc} is the size of the acceleration size and r_{L} is the Larmor radius. This is much larger than the adiabatic cooling time scale (~ 1 s) estimated using the X-ray modulation of LS 5039 (Takahashi et al., 2009). Therefore, it is valid to assume $\tau_c(\gamma, \gamma') \ll T_{esc}$ in our case. In Equation 7.4, the energy distribution is determined by only two functions, $Q(\gamma)$ and $\dot{\gamma}(\gamma)$. Next we explain how to calculate these two functions.

Injection Electron Spectrum $Q(\gamma)$

We assume that the injection electron spectrum is described by a powerlaw function

$$Q(\gamma) = \begin{cases} \gamma^{-s} & (\gamma < \gamma_{\text{max}}) \\ 0 & (\gamma > \gamma_{\text{max}}) , \end{cases} \tag{7.6}$$

where $\gamma_{\max}$ is the maximum energy of the accelerated electron, defined as

$$\gamma_{\max} = 1.16 \times 10^8 \times \left(\frac{B}{1 \text{ G}} \right)^{-0.5} \eta^{-0.5} , \tag{7.7}$$

where η is the acceleration efficiency. It is determined by the condition in which the acceleration time is equal to the synchrotron cooling time.

Electron Cooling Rate $\dot{\gamma}(\gamma)$

We describe the cooling rate $\dot{\gamma}(\gamma)$ as a sum of three processes, synchrotron, inverse Compton and adiabatic cooling:

$$\dot{\gamma}(\gamma) = \dot{\gamma}_{\text{IC}} + \dot{\gamma}_{\text{sync}} + \dot{\gamma}_{\text{ad}} . \tag{7.8}$$

The cooling rate is due to inverse Compton emission and depends on the energy distribution of seed photons. In LS 5039, the companion O star emits UV photons, and they are dominant seed photons for inverse Compton emission, Thus, we assume that the energy distribution of the seed photons is described by a Maxwellian with a temperature of 3.3 eV (Casares et al., 2005). We adopted a simple analytical approximation for the inverse Compton cooling rate (Khangulyan et al., 2014) given by

$$\dot{\gamma}_{\text{IC}} = \frac{2r_0^2 m_e^3 c^4 \kappa (kT_\star/m_e c^2)^2}{\pi \hbar^3} F \left(\frac{4\gamma kT_\star}{m_e c^2} \right) , \quad \kappa = \left(\frac{R_\star}{2D_{\text{acc}}} \right)^2 , \tag{7.9}$$

where r_0 is the classical electron radius and $T_\star, R_\star$ are the temperature and the radius of the companion star respectively; D_{acc} is the distance between the acceleration region and the companion star; $F(u)$ is a function described by

$$F(u) = \frac{c_{\text{iso}} u \log(1 + 0.722 u/c_{\text{iso}})}{1 + c_{\text{iso}} u/0.822} \left(\frac{1 + a_{\text{iso}} u^{\alpha_{\text{iso}}}}{1 + b_{\text{iso}} u^{\beta_{\text{iso}}}} \right)^{-1} \tag{7.10}$$

$$\alpha_{\text{iso}} = 0.682, \beta_{\text{iso}} = 1.281, a_{\text{iso}} = -0.362, b_{\text{iso}} = 0.826, c_{\text{iso}} = 5.68. \tag{7.11}$$

This approximation provides $\sim 1\%$ accuracy over a wide energy range which is accurate enough for our calculation.

The synchrotron cooling rate is determined by two parameters B, γ such that

$$\dot{\gamma}_{\text{sync}} = \frac{1}{6\pi} \frac{\sigma_T B^2}{m_e c} \gamma^2 . \tag{7.12}$$

We describe the cooling rate of adiabatic losses as shown in Equation 2.57

$$\dot{\gamma}_{\text{ad}} = \frac{c}{R_{\text{acc}}} \gamma . \tag{7.13}$$

Here, we assume that the emission region expands relativistically.

7.3 Dependence of the spectrum on the physical parameters

Before we compare the spectral model with the observed spectrum, we investigate how the model spectrum depends on the parameters in Table 7.1. In later sections, we interpret the spectrum of LS 5039 on the basis of the basic features we explain in this section.

The first three parameters in Table 7.1, R_{acc}, B, and D_{acc}, have a strong impact on the spectral shape because they determine the cooling rate of adiabatic losses, synchrotron radiation and inverse Compton emission. Since the cooling rate of each process has a different dependence on electron energy, the electron energy distribution changes significantly depending on which process is dominant. To understand this feature in more detail, it is helpful to divide the problem into two cases: (1) when the inverse Compton cooling for GeV electrons is dominant over the adiabatic losses in a wide energy range; (2) when the adiabatic losses is dominant over the inverse Compton cooling in an entire energy range. In the next two subsections (7.3.1, 7.3.2), we adopt the following numerical values for the model parameters: $D_{\mathrm{acc}} = 50$ light-sec, $\theta_{\mathrm{IC}} = 90$ degrees, $\eta = 1$ and $s = 2$.

7.3.1 Case 1: inverse Compton cooling is dominant

If the cooling rate due to inverse Compton emission is larger than that due to adiabatic losses in a wide energy range, then the spectrum is determined by the balance between synchrotron radiation and inverse Compton emission. When $D_{\mathrm{acc}} = 50$ light sec, it is achieved if R_{acc} is larger than ~ 10 light sec. As one example, we show the cooling rate of each process and the resulting electron energy distribution when $R_{\mathrm{acc}} = 1000$ light-sec in Figure 7.2. In this figure, we assumed different strengths of the magnetic field (1, 10, 100 G).

When the energy density of the magnetic field is comparable or larger than that of the seed photon ($B = 100$ G, the blue lines in Figure 7.2), the cooling rate is proportional to E_e^2 in all energy range. If the cooling rate and the injection electron spectrum are proportional to E_e^a and E_e^{-s} respectively, Equation 7.4 derives the electron distribution proportional to E_e^{1-a-s}. Since $a = 2$ and $s = 2$ here, the electron energy distribution is proportional to E_e^{-3}. Then, from Equation 2.34, the photon index of the synchrotron spectrum is determined as 2. Figure 7.3 shows the resulting synchrotron and the inverse Compton spectra. In this case, we observe a flat X-ray spectrum in the spectral energy distribution.

On the other hand, when the magnetic field is weak, the synchrotron spectrum becomes hard (see the red line in Figure 7.3). This is explained by the following: In this case, when

electron energy is small, inverse Compton cooling is dominant over synchrotron cooling. However, when electron energy is very high, synchrotron cooling becomes dominant because the Klein-Nishina effect reduces the cross section of inverse Compton scattering. In Figure 7.2, when $B = 1$ G, the Klein-Nishina effect becomes important at $E_1 \simeq 10^{10}$ eV, and above $E_2 \simeq 10^{13}$ eV synchrotron cooling becomes dominant. When electron energy is between E_1 and E_2 (the transition region from synchrotron cooling to inverse Compton cooling), the cooling rate is less dependent on the electron energy. It results in hard electron distribution in this energy range as shown in Figure 7.2 to the right. Consequently, the X-ray synchrotron spectrum also becomes hard. Hereafter, we refer to this effect as the Klein-Nishina hardening.

We measured the photon index in X-ray band as ~ 1.6 using the *NuSTAR* observation. In order to explain this value, the Klein-Nishina hardening should take place if the inverse Compton cooling is dominant over the adiabatic cooling.

7.3.2   Case 2: adiabatic losses are dominant

When the emission region becomes small, adiabatic losses become dominant. In this case, the electron energy distribution is determined by the balance between adiabatic losses and synchrotron cooling. As an example, Figure 7.4 shows the cooling rate of each process and the resulting electron energy distribution when $R_{\mathrm{acc}} = 1.0$ light-sec. When synchrotron cooling is dominant, the electron energy distribution is proportional to E_e^{-3} since $a = 2$ and $s = 2$ here. On the other hand, when adiabatic losses are dominant, the electron energy distribution is proportional to E_e^{-2} because the adiabatic cooling rate is proportional to E_e^1. In Figure 7.4 to the right, we see that the electron distribution becomes soft as the synchrotron cooling becomes dominant. From Equation 2.34, the photon index of the synchrotron spectrum is 2.0 when synchrotron cooling is dominant, while it is 1.5 when adiabatic losses are dominant. As shown in Figure 7.5, the synchrotron spectrum becomes harder when the magnetic field is weaker. This is because the adiabatic losses become dominant up to higher electron energy in weaker magnetic field. Therefore, in this case, considering the observed photon index of ~ 1.6, the adiabatic losses should dominate over the synchrotron cooling in order to make a hard synchrotron spectrum.
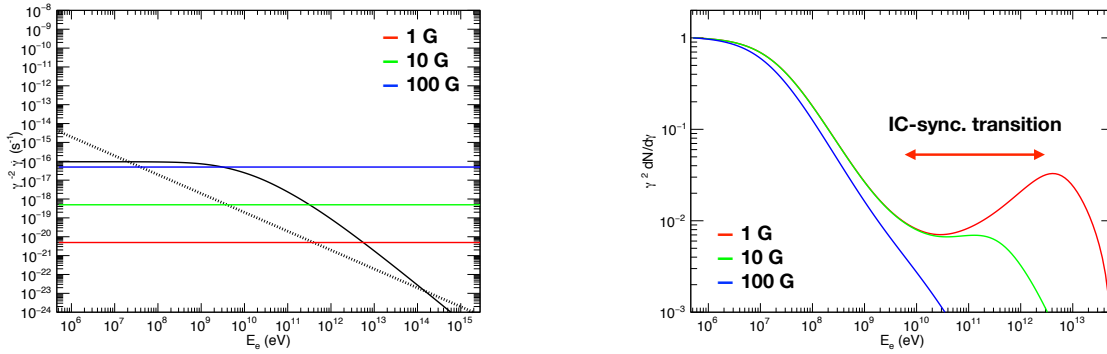
Figure 7.2: The cooling rate and the electron energy distribution for the case of dominant inverse Compton losses ($R_{\mathrm{acc}} = 1000$ light-sec). Left: the cooling rates for each process. The black solid and dotted lines are those of the inverse Compton and the adiabatic cooling, respectively. The colored lines are for the synchrotron cooling. Right: the electron energy distribution. The colored lines (red, green, blue) correspond to the magnetic field of 1, 10, 100 G respectively.
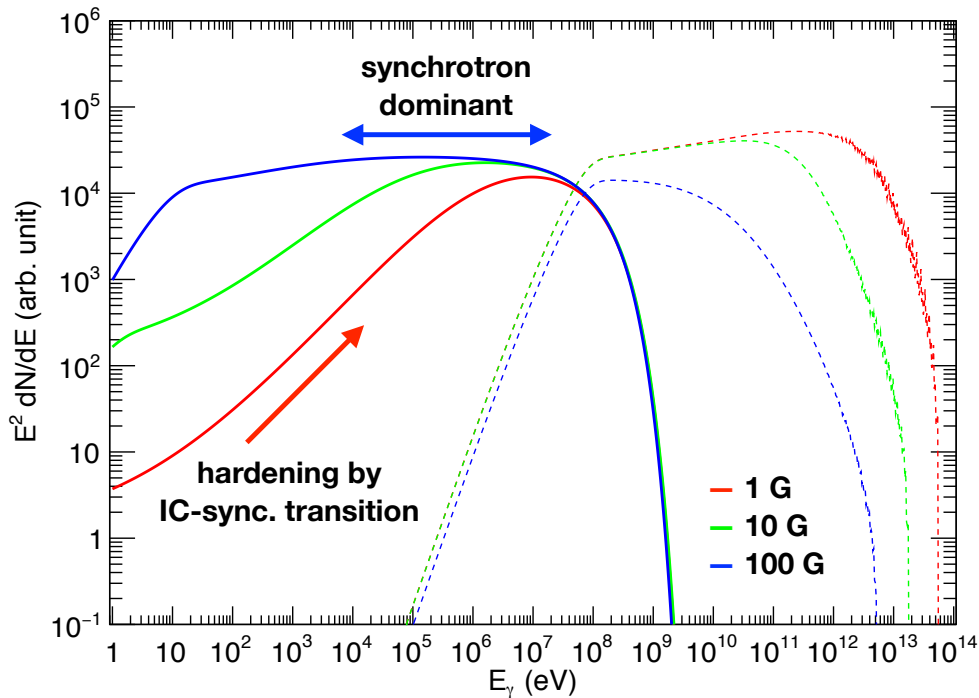
Figure 7.3: The resulting spectra under the same assumption of Figure 7.2. The solid and dashed lines represent the spectra of the synchrotron and the inverse Compton components, respectively.
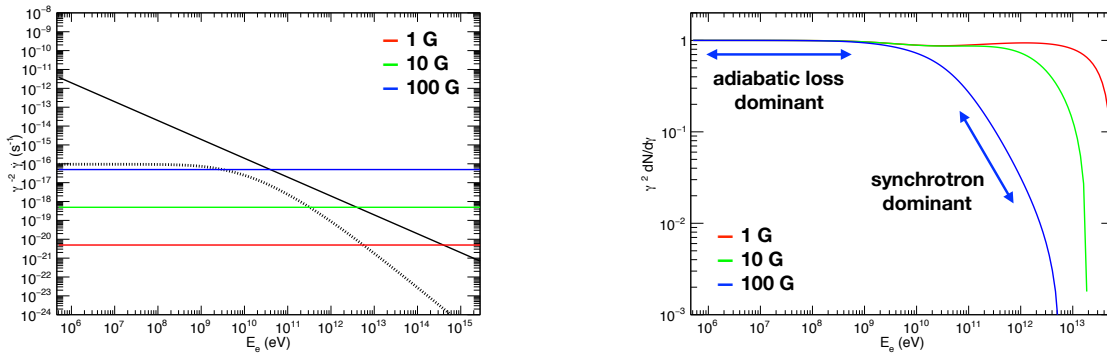
Figure 7.4: The cooling rate and the electron energy distribution for the case of dominant adiabatic losses ($R_{\mathrm{acc}} = 1.0$ light-sec). Left: the cooling rates for each process. The black solid and dotted lines are those of the inverse Compton and the adiabatic cooling respectively. The colored lines are for the synchrotron cooling. Right: the electron energy distribution. The colored lines (red, green, blue) correspond to the magnetic field of 1, 10, 100 G respectively.
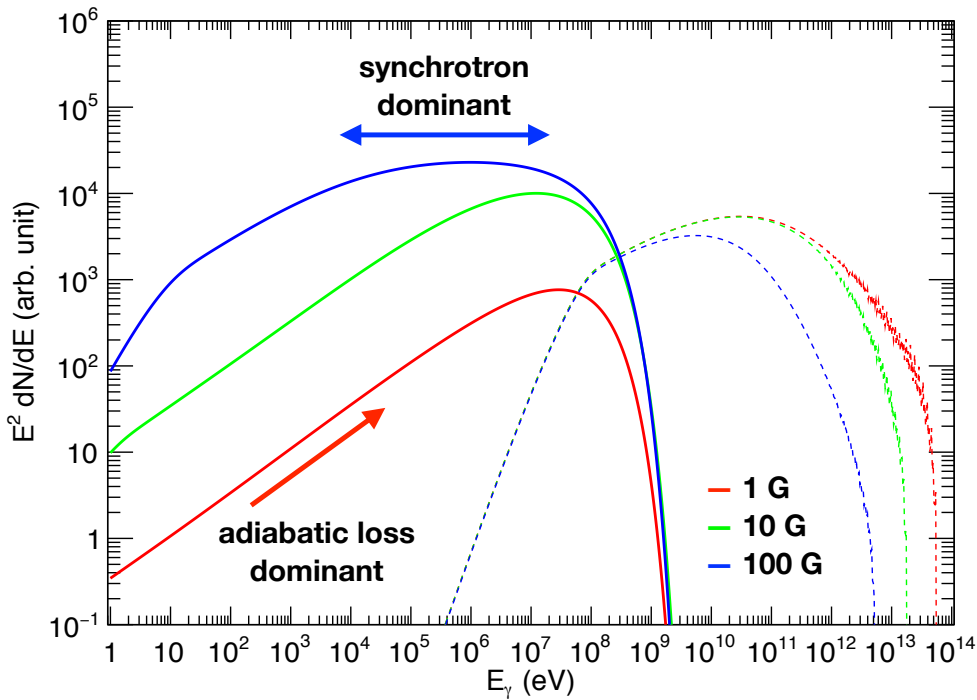
Figure 7.5: The resulting spectra under the same assumption of Figure 7.4. The solid and dashed lines represent the spectra of the synchrotron and the inverse Compton components, respectively.

7.4 Constraint on Physical Parameters in the Shock Region

As discussed above, in order to explain the hard X-ray spectrum of LS 5039, the synchrotron cooling should be dominated by adiabatic cooling or inverse Compton cooling. This indicates that very strong magnetic field is not favorable. Furthermore, we can use the flux of inverse Compton emission to constrain physical properties, especially, the strength of a magnetic field. If the magnetic field is too weak, the flux of the resulting inverse Compton emission would be much larger than those of synchrotron radiation, which is inconsistent with the observed spectrum in the GeV band. Therefore, very weak magnetic fields can also be rejected. In this section, on the basis of these two conditions, we put quantitative constraints on the physical parameters of the emission region using the general spectral model.

7.4.1 Conditions that spectral model must satisfy

First we explain how to constrain the parameters by using inverse Compton emission. Here we use the ratio of νF_ν in the X-ray band to that in the GeV band. The condition is that the ratio calculated from the model spectrum should be higher than the observed value. Since the inverse Compton spectrum in the GeV/TeV band can be affected by gamma-gamma absorption, care must be taken when treating the flux of inverse Compton emission. In order to minimize the absorption effect, we use the observed spectrum around the inferior conjunction. Since observers see the compact star in front of the companion star, gamma-ray photons interact with fewer seed photons around the inferior conjunction. Second, we use the flux at gamma-ray energy less than 20 GeV at least because the absorption does not occur if gamma rays have energies less than a kinematic threshold. The threshold energy is given as:

$$E_\gamma = \frac{2(m_e c^2)^2}{E_{\text{seed}}(1 - \cos\theta_{\text{IC}})} \ , \tag{7.14}$$

where E_{seed} is the seed photon energy. The optical observation measured the temperature of the companion star as $T_\star = 39000 \pm 1000$ K (Casares et al., 2005). By applying $E_{\text{seed}} = kT_\star = 3.3$ eV and $\theta_{\text{IC}} = 180$ degrees, we obtain the threshold as $E_\gamma < 150$ GeV. However, when the seed photons are distributed with the Planck distribution, high energy photons in the Wien tail absorb gamma rays whose energies are lower than 150 GeV. Dubus (2006) calculated the optical depth of the absorption by the black-body photons in LS 5039. They assumed that they are produced isotropically near the compact star. When the gamma-ray energy is at 20 GeV and the orbital phase is from $0.5 < \phi < 1.0$, at most 1% of the gamma rays

are absorbed (see Figure 2.18 in Chapter 2). Furthermore, the *Fermi* observation revealed that the flux in 1–5 GeV is nearly independent of the orbital motion. Since gamma-gamma absorption depends strongly on the orbital phase, this observational result also supports that gamma-gamma absorption does not take place below 5 GeV. Therefore, we use the flux at ~ 5 GeV for the constraint on the physical parameters. We refer to the flux at 10.9 keV as the flux of synchrotron radiation. Table 7.2 shows the observed fluxes which we use for the constraint.

Table 7.2: The ratio of νF_ν of X-ray to that of GeV gamma ray. We calculated the ratio using the result of the *NuSTAR* and *Fermi* observations.

$\nu F_\nu(E_X)$ at $E_X = 10.9$ keV	$\nu F_\nu(E_{\mathrm{GeV}})$ at $E_{\mathrm{GeV}} = 5.59$ GeV	$\nu F_\nu(E_X)/\nu F_\nu(E_{\mathrm{GeV}})$	
		$1\,\sigma$	$2\,\sigma$
$8.43 \pm 0.20 \times 10^{-12}$ erg cm^{-2} s^{-1}	$1.17 \pm 0.20 \times 10^{-11}$ erg cm^{-2} s^{-1}	> 0.60	> 0.51

Second, we explain how to constrain the parameters by using the X-ray spectrum. As discussed above, the photon index ~ 1.6 in the X-ray band is explained by the Klein-Nishina hardening or adiabatic losses. Thus, we search for a physical parameter which produces the photon index in the X-ray band consistent with the observed value. The minimum and maximum photon indices around the inferior conjunction ($0.45 < \phi < 0.9$) were obtained as 1.54 ± 0.05 and 1.73 ± 0.06 , respectively (see Table 4.2). Considering the errors, we set the condition as that the photon index Γ in the 3–10 keV calculated from a model spectrum satisfies:

$$1.49 \quad < \Gamma < 1.79 \ (1\sigma \text{ interval}) \tag{7.15}$$

$$\text{or} \quad 1.44 \quad < \Gamma < 1.85 \ (2\sigma \text{ interval}) \ . \tag{7.16}$$

7.4.2 Range of the Model Parameters

We calculate the model spectrum using the general spectrum model we developed in Section 7.2. The general spectrum model requires 9 parameters as described in Table 7.1. Then, we obtained parameter sets of R_{acc} and B which satisfy the two conditions described in Table 7.5, Equation 7.15. The search ranges of R_{acc} and B are set from 10^{-1} to 10^3 light sec and 10^{-1} to 10^3 G, respectively.

As for D_{acc}, we consider different values, 25, 50, 100 and 150 light sec since we do not know where the emission region is in the binary system. The minimum value (25 light sec) corresponds to the binary separation when the compact is a black hole with a mass of 4 $M_\odot$ (see Figure 2.9). If the compact star is a neutron star with a mass of 1.5 $M_\odot$, the separation becomes $\sim$ 50 light sec. Furthermore, there is a possibility that gamma rays are produced with larger D_{acc}. For example, the pulsar wind model predicts that a termination shock is formed in the opposite direction from the companion star (Bosch-Ramon et al., 2012). The distance between this shock and the pulsar is estimated as the same order of the orbital radius (Bosch-Ramon & Barkov, 2011; Zabalza et al., 2013). Considering this possibility, we include $D_{\mathrm{acc}} = 100, 150$ light sec.

θ_{IC} is set to 25 degrees because of the following reason. The flux of inverse Compton emission depends on the scattering angle θ_{IC} of seed photons. As θ_{IC} decreases, the flux of inverse Compton emission also decreases. Here we find parameter sets which produce the νF_ν ratio of synchrotron radiation to inverse Compton emission larger than the value in Table 7.2. Thus, the most robust constraint when θ_{IC} is the minimum. Reig et al. (2003) derived the upper limit of the inclination angle i as $i < 66 \pm 2$ degrees, which constrains that θ_{IC} is larger than 24 ± 2 degrees. Hence, we assume that $\theta_{\mathrm{IC}} = 25$ degrees.

Here, we assume that electrons are accelerated by the diffusive shock acceleration (DSA). Thus, we constrain the spectral index of the injection electron spectrum s from 2.0 to 2.4 because of the following reasons. When the shock velocity is non-relativistic, the accelerated electron spectrum in the DSA is predicted as a powerlaw with a spectral index of 2. On the other hand, when the shock velocity is relativistic, the spectral index can be larger than 2. For example, the spectral index is reported as 2.32 ± 0.01 in the Crab nebula which is considered to have a relativistic termination shock.(Meyer et al., 2010). Therefore, we determine the maximum value of s as 2.4, since it is significantly larger than the observed value.

The acceleration efficiency η determines the maximum energy of accelerated electrons. Then, the spectral peak of synchrotron emission is derived as shown in Equation 2.41. When η is smaller, the spectral peak becomes higher, which yields a harder X-ray spectrum. Since we constrain the physical parameters by using the small photon index in the X-ray band, the most robust constraint is derived when η is the minimum. Thus, we set η to 1.0. Summarizing above, the range of the model parameters is shown in Table 7.3. Note that we do not have to determine the normalization factor because the values (the photon index, the $\nu F \nu$ ratio) in the two conditions are intensive variables.

Table 7.3: Parameter range of the general spectral model

Parameter	Description
R_{acc} (light sec)	$10^{-1} - 10^3$
B (G)	$10^{-1} - 10^3$
D_{acc} (light sec)	25, 50, 100, 150
θ_{IC} (degree)	25
η	1.0
s	2.0–2.4
$kT_\star$ (eV)	3.3
$R_\star$ ($R_\odot$)	9.3

7.4.3   Results

Figure 7.6 shows the result of the constraint on R_{acc} and B. Here D_{acc} is set to 50 light sec. When the magnetic field is strong ~ 100 G, a small acceleration region is required in order to explain the hard X-ray spectrum by adiabatic losses (see Section 7.3.2). When the magnetic field becomes weak, the hard X-ray spectrum can be generated by the Klein-Nishina hardening (see Section 7.3.1). Thus large acceleration region is also accepted. Furthermore, if the magnetic field is too weak, inverse Compton emission is too strong to explain the observed GeV spectrum. This determines the boundary line for low magnetic fields in Figure 7.6. When we exclude very small acceleration region ($R_{\mathrm{acc}} < 0.1$ light sec), the magnetic field is constrained as 1.4 G $< B < 1.5 \times 10^2$ G.

Figure 7.7 shows the accepted parameter regions assuming different values of $D_{\mathrm{acc}} = 25, 50, 100$ and 150 light sec. As the acceleration region gets farther from the companion star, the seed photon density becomes smaller. It reduces the flux of inverse Compton emission. Thus, a weaker magnetic field is accepted since the $\nu F \nu$ flux ratio becomes larger. Furthermore, when the seed photon density becomes smaller, Klein-Nishina effect stops at weaker magnetic field. Then, the hard X-ray spectrum can be produced by adiabatic losses. As a result, as D_{acc} becomes larger, the constraint from the photon index in hard X-rays becomes more severe. When we exclude very small acceleration region ($R_{\mathrm{acc}} < 0.1$ light sec), the magnetic field are constrained as 4.3 G $< B < 1.5 \times 10^2$ G and 2.7×10^{-1} G $< B < 1.5 \times 10^2$ G if $D_{\mathrm{acc}} = 25$ and 150 light sec respectively.
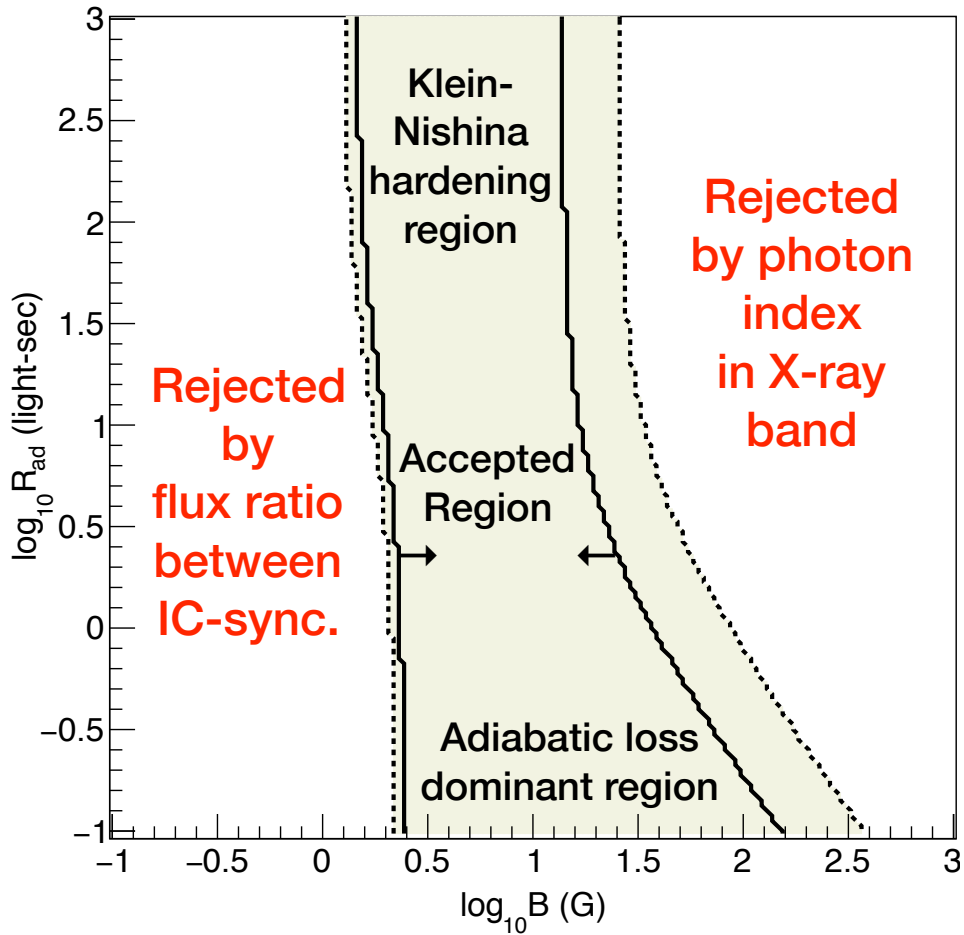
Figure 7.6: The accepted physical parameters. Here, we assumed $D_{\mathrm{acc}} = 50$ light sec. The white solid and dashed lines are obtained by using the 1σ and 2σ values respectively, described in Table 7.5, Equation 7.15.
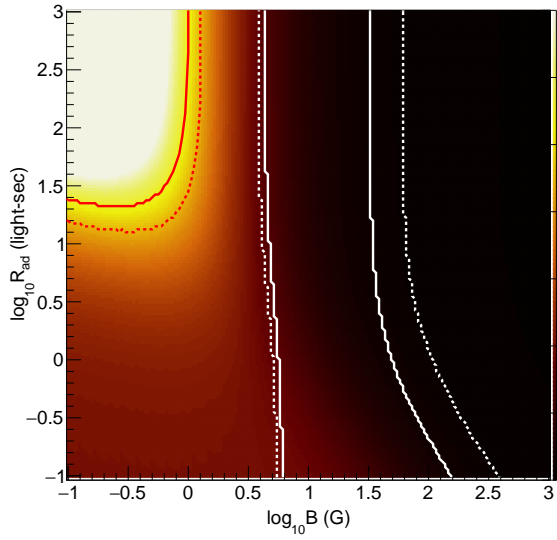
$D_{\mathrm{acc}} = 25$ light sec $D_{\mathrm{acc}} = 50$ light sec
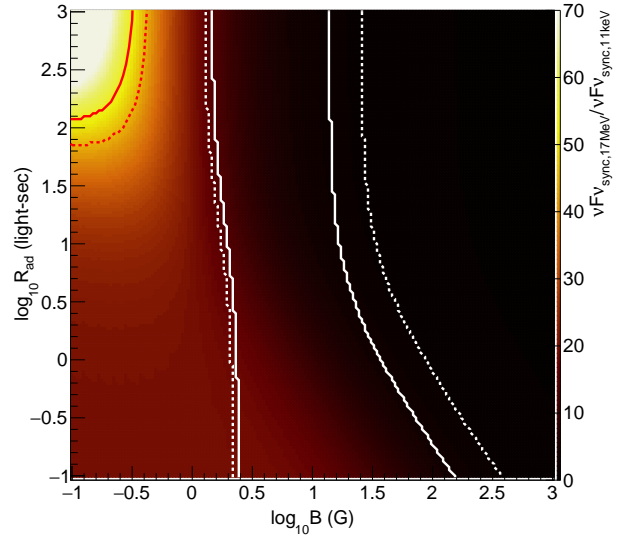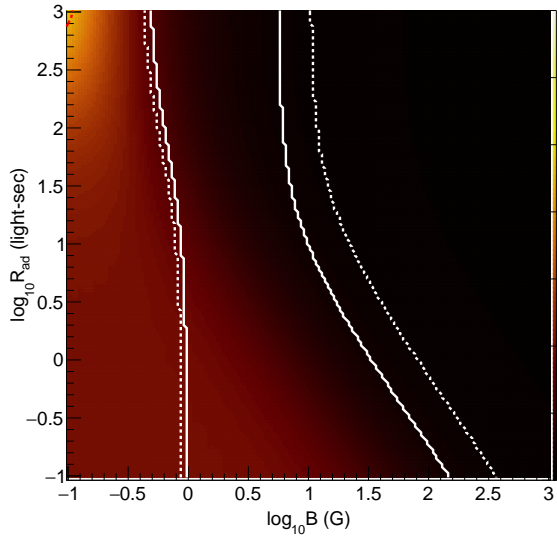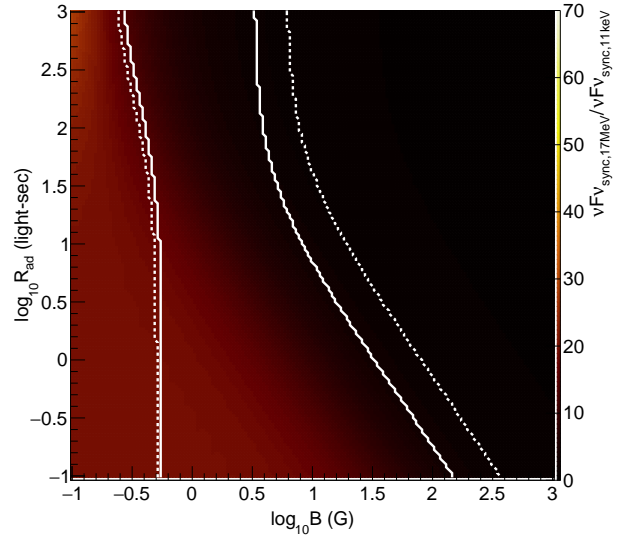
$D_{\mathrm{acc}} = 100$ light sec $D_{\mathrm{acc}} = 150$ light sec

Figure 7.7: The accepted physical parameters applying different values of D_{acc}. The white solid and dashed lines are obtained using 1σ and 2σ values respectively, described in Table 7.5, Equation 7.15. The red solid and dashed lines represent the parameter regions where the flux ratio of MeV gamma-ray band to X-ray band is larger than 1σ and 2σ values described in Table 7.4. The color contour represents the flux ratio between the MeV band and X-ray band at each parameter set.

7.5 Requirement for the MeV gamma-ray emission

7.5.1 Difficulty of the same origin of the X-ray and MeV gamma-ray emissions

The primary motivation of this chapter is to investigate whether the origin of the X-ray emission is the same as that of MeV gamma rays. Since we constrained the magnetic field and the size of the emission region (Figure 7.7), we check whether there are any parameter set which satisfies the constraint and explains the X-ray and MeV emission simultaneously. From observations, the emission in the MeV band is much larger than that in the X-ray band by a factor of ~ 60. Considering the errors, the $\nu F\nu$ ratio between the X-ray and MeV band is derived as described in Table 7.4. We refer to the $\nu F\nu$ at $E_{\mathrm{X}} = 10.9$ keV and at $E_{\mathrm{MeV}} = 17.3$ MeV. The ratios predicted from the model spectra are shown in Figure 7.7. The observed ratio can be explained when the parameter set is in the region surrounded by the red lines. Regardless of D_{acc}, all parameter sets which explain the MeV/X-ray flux ratio are rejected by the two observational conditions (Table 7.5, Equation 7.15).

Qualitatively, we describe the reason why it is difficult to explain the X-ray and MeV spectrum as a single spectral component as follows. When adiabatic losses are dominant, the hardest photon index is $\simeq 1.5$. In this case, the largest $\nu F\nu$ ratio between the X-ray and MeV band is calculated as $(10 \mathrm{~MeV}/10 \mathrm{~keV})^{0.5} = 32$, which is much smaller than the observed value (Table 7.4). On the other hand, when inverse Compton losses are dominant, the hard X-ray spectrum can be explained by the Klein-Nishina hardening. Then, it requires the weak magnetic field as discussed in Section 7.3.1. When the magnetic field is weak, inverse Compton emission dominates over synchrotron radiation. However, weak magnetic fields are excluded by $\nu F\nu$ ratio between the X-ray and GeV band. Therefore, in either case, it is difficult to explain the X-ray and MeV spectrum as a single spectral component.

In order to verify the robustness of our result, we investigate how the constrained parameter region changes when we loosen the condition on the $\nu F\nu$ ratio between the X-ray and GeV band. We use the flux at $E_{\mathrm{GeV}} = 1.22$ GeV as the flux of inverse Compton emission. The condition on the ratio is shown in Table 7.5. Figure 7.8 shows the resulting constrained regions with $E_{\mathrm{GeV}} = 1.22$ GeV. The smaller E_{GeV} makes the lower limit of the magnetic field smaller. However, even if we decrease the reference energy E_{GeV}, the region surrounded by the red lines are outside of the constrained parameter region. Thus, again, it is difficult to explain the X-ray and MeV emission simultaneously. Furthermore, in this constraint, we assumed the most efficient acceleration ($\eta = 1.0$). This assumption makes the peak energy

of the synchrotron the highest, resulting in the largest MeV gamma-ray emission. Thus, if we assume a larger value of η, it becomes more difficult to explain the strong MeV emission. Note that η is considered to be larger than ~ 6 in the diffusive shock acceleration. Therefore, we conclude that the origin of the MeV gamma-ray emission is different from that of the X-ray emission.

Table 7.4: The ratio of νF_ν of MeV gamma ray to that of X ray. We set $E_X = 10.9$ keV and $E_{MeV} = 17.3$ MeV, and calculated the ratio using the result of the *NuSTAR* and *COMPTEL* observation (Collmar & Zhang, 2014).

$\nu F_\nu(E_{MeV})$ at $E_{MeV} = 17.3$ MeV	$\nu F_\nu(E_{MeV})/\nu F_\nu(E_X)$	
	$1\,\sigma$	$2\,\sigma$
$5.38 \pm 0.83 \times 10^{-10}$ erg cm^{-2} s^{-1}	> 54.0	> 44.2

Table 7.5: The ratio of νF_ν of X ray to that of GeV gamma ray. We set $E_X = 10.9$ keV, and calculated the ratio using the result of the *NuSTAR* and *Fermi* observation.

E_{GeV} (GeV)	$\nu F_\nu(E_X)/\nu F_\nu(E_{GeV})$	
	$1\,\sigma$	$2\,\sigma$
1.22	> 0.197	> 0.180

7.5.2   Physical properties of MeV gamma-ray emitters in LS 5039

Here we discuss the origin of the MeV emission. Since the MeV gamma-ray emission in LS 5039 is dominant over the other emissions from X rays to TeV gamma rays, it is natural to consider that the MeV gamma rays are produced by an efficient radiative process, that is synchrotron radiation or the inverse Compton emission. By focusing these two possibilities, we investigate physical properties of the emission region where the MeV gamma rays are produced.

When we interpret that the MeV emission is produce by synchrotron radiation, the acceleration efficiency η is estimated by the spectral peak, because η determines the synchrotron peak as ~ 60 MeV $\times \eta^{-1}$ (see Equation 2.41). It is observed at ~ 30 MeV, as shown in
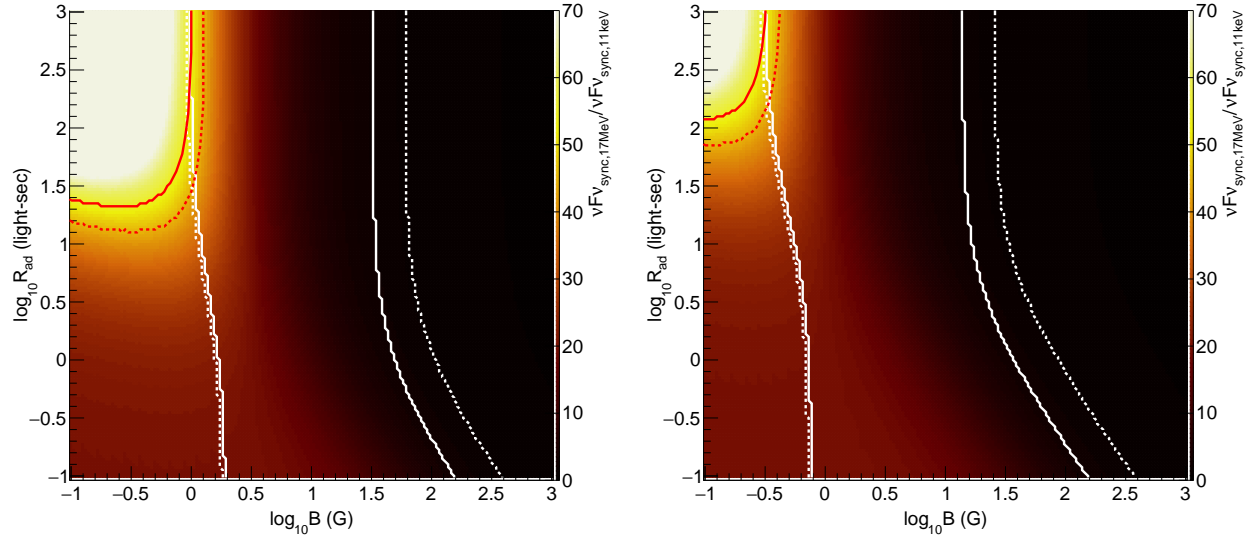
$D_{\mathrm{acc}} = 25$ light sec

$D_{\mathrm{acc}} = 50$ light sec
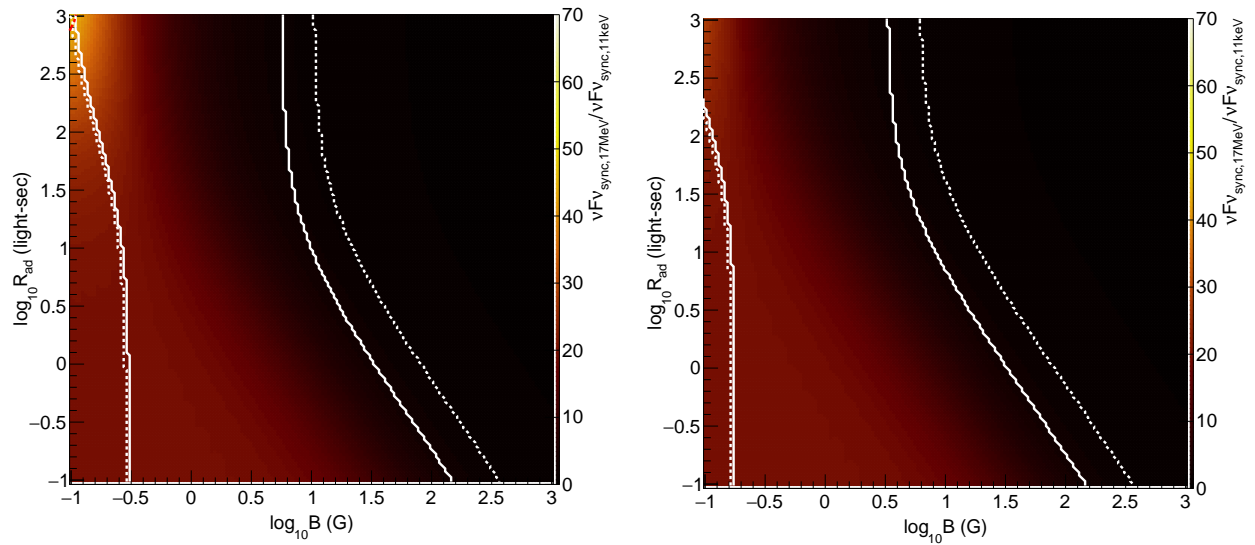
$D_{\mathrm{acc}} = 100$ light sec

$D_{\mathrm{acc}} = 150$ light sec

Figure 7.8: The accepted physical parameters using the flux at 1.22 GeV. Other parameters are the same as those adopted in Figure 7.7.

Figure 7.1. Hence, η is given by

$$67 \text{ MeV} \quad \times \quad \eta^{-1} \simeq 30 \text{ MeV} \tag{7.17}$$

$$\eta \quad \simeq \quad 2 \tag{7.18}$$

Moreover, since the spectral component for the MeV emission should have X-ray flux which is lower than the observed value, its photon index in the X-ray band is smaller than ~ 1.6. As discussed before, a hard synchrotron spectrum with a photon index of ~ 1.6 is produced via adiabatic losses or by Klein-Nishina hardening. Therefore, the MeV gamma-ray emission is produced in a region where adiabatic losses are dominant or the Klein-Nishina hardening takes place.

Figure 7.9 shows synchrotron spectra when adiabatic losses are dominant. In order to make adiabatic losses significant, a small emission region is needed. Here, we assume that $R_{\text{acc}} = 10^{-6}$ light sec, $\eta = 2.0$, $B = 1000$ G and different values of the index s of the injection electron spectrum. When the index s is equal to 2.0 (see the blue line in the figure), it is difficult to explain the observed spectrum because the MeV component has too large flux in the X-ray band. In order to make the model spectrum consistent with the observed X-ray and MeV spectra, a smaller value of s is required. When $s = 1$ (see the red line in the figure), the model spectrum explains the observation very well. Such a small value of s can be achieved in direct acceleration processes *e.g.* the magnetic reconnection. On the other hand, the injection index is larger than ~ 2 in the stochastic acceleration process *e.g.* Fermi acceleration. Thus, this scenario favors a direct acceleration process for the production of the MeV gamma rays.

Next, we consider the Klein-Nishina hardening. The Klein-Nishina hardening takes place when the inverse Compton cooling dominant over the synchrotron cooling in the low energy band, where the magnetic field should be weak (see Section 7.3.1 and Figure 7.3). Figure 7.10 shows the synchrotron spectra when the Klein-Nishina hardening occurs. We assume that $R_{\text{acc}} = 10^3$ light sec, $\eta = 2.0$, $\theta_{\text{IC}} = 25$ degrees for different values of the magnetic field B. Here, we assume the hard injection spectrum ($s = 1$) to make the hard spectrum easily. The synchrotron spectrum with $B = 0.1$ G is consistent with the observation in the X-ray band (see the red line in the figure). However, the flux of inverse Compton emission is significantly larger by more than two orders of magnitude than the observation. Even if considering gamma-gamma absorption, it is difficult to explain the observed spectrum. Dubus (2006) shows the gamma-gamma absorption can decrease the 10 TeV flux by 90% at most (Figure 2.18). When we explain the MeV emission by the Klein-Nishina hardening, a small

magnetic field is required to make a hard synchrotron spectrum. However it overestimates the inverse Compton emission. Therefore, this scenario is unlikely.

Finally, we consider inverse Compton emission for the MeV emission. In order to produce 30 MeV gamma rays with seed photons with an energy of 3.3 eV, the energy of electrons which scatter the seed photons should be a few GeV. The GeV electrons might be produced in the shock acceleration. Sironi & Spitkovsky (2009, 2011) reported that the Maxwellian-like electron population is formed together with the powerlaw component using particle-in-cell simulations. However, this scenario can be rejected by the flux dependence on the orbital phase. In inverse Compton emission, the flux is maximized when the scattering angle is the largest, which implies that the maximum of MeV emission is achieved around the inferior conjunction. On the other hand, Collmar & Zhang (2014) reported that it is achieved around the superior conjunction. In order to solve this inconsistency, we need an electron injection spectrum that is unnaturally tuned to make the orbital dependence consistent with the observation.

Summarizing above; we conclude that the MeV spectral component is a synchrotron spectrum hardened by adiabatic losses. By comparing the model spectra with the observation, a very hard injection spectrum ($s \sim 1$) is required. It suggests that particles are accelerated via a direct acceleration process. In order to make the adiabatic-loss dominant spectrum, the hardening by adiabatic losses should take place up to the spectral peak ~ 30 MeV. This condition is described as

$$19.2 \text{ keV} \times \left(\frac{B}{1 \text{ G}} \right) \left(\frac{E_e}{1 \text{ TeV}} \right)^2 \gtrsim 30 \text{ MeV} , \tag{7.19}$$

where E_e is defined by

$$\dot{\gamma}_{\text{adia}}(E_e) = \dot{\gamma}_{\text{sync}}(E_e) . \tag{7.20}$$

Note that the left term in Equation 7.19 is a peak energy of synchrotron radiation from a single electron (Equation 2.30). As a result, we obtain

$$R_{\text{acc}} < 10 \text{ [light sec]} \times \left(\frac{B}{1 \text{ G}} \right)^{-2/3} \tag{7.21}$$

Therefore, a small acceleration region is favored for the MeV gamma-ray emitter. Furthermore, the magnetic field should be larger than few gauss at least to make inverse Compton emission consistent with observation.
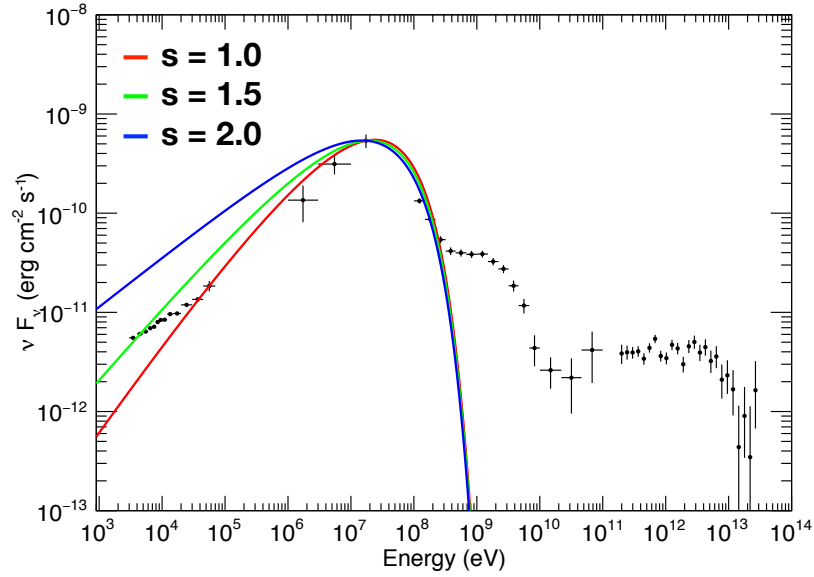
Figure 7.9: Synchrotron spectra when the adiabatic losses are dominant. The injection spectral index s varies from 1.0 to 2.0. We assume that $R_{acc} = 10^{-6}$ light sec, $\eta = 2.0$, $B = 1000$ G. Each spectrum is normalized at 17.3 MeV.
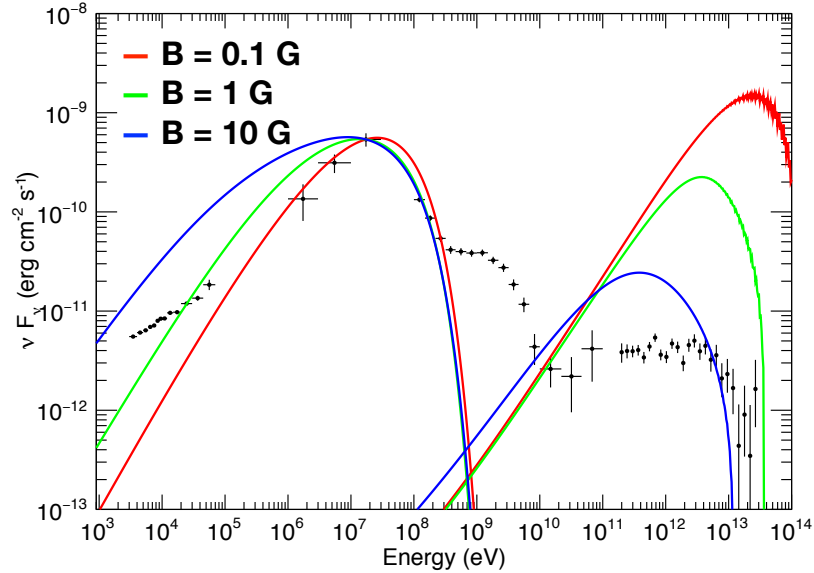
Figure 7.10: Synchrotron/inverse-Compton spectra when the Klein-Nishina hardening occurs. The magnetic field B varies from 0.1 to 10 G. We assume that $R_{acc} = 10^3$ light sec, $\eta = 2.0$, $s = 1$ and $\theta_{IC} = 25$ degrees. Each spectrum is normalized at 17.3 MeV.

7.6 No Relation between X-ray and GeV gamma-ray emissions

We find that the origin of particles which produce the GeV emission is different from that for the X-ray emission. If these origins are the same, the GeV emission has to be produced via inverse Compton emission because its energy is higher than the maximum energy (~ 100 MeV) of synchrotron radiation. The energy of the electrons producing the GeV emission $\gamma_{\mathrm{G}} m_e c^2$ is estimated to be

$$\gamma_{\mathrm{G}}^2 \times 10 \text{ [eV]} \simeq 5 \text{ [GeV]} \tag{7.22}$$

$$\gamma_{\mathrm{G}} m_e c^2 = \left(\frac{5 \text{ [GeV]}}{10 \text{ [eV]}}\right)^{0.5} \times m_e c^2 \simeq 10 \text{ [GeV]} \tag{7.23}$$

If electrons of 10 GeV emit 1–10 keV photon via the synchrotron radiation, the strength of the magnetic field should be

$$B_{\mathrm{acc}} > 1 \text{ G} \times \left(\frac{10 \text{ keV}}{19.2 \text{ keV}}\right) \left(\frac{10 \text{ [GeV]}}{1 \text{ [TeV]}}\right)^{-2} \simeq 500 \text{ G} \tag{7.24}$$

However, in this case, the total power of synchrotron radiation in the X-ray band is much larger by ~ 20 than that of inverse Compton emission in the GeV band. Figure 7.11 shows the model spectra with $B_{acc} = 500$ G. These are completely inconsistent with the observed spectrum, especially, in the X-ray band. Furthermore, the orbital light curves in the X-ray and GeV band are very different from each other. This also supports different origins of the X-ray and GeV gamma-ray emissions. Therefore, we conclude that the GeV emission is not related to the X-ray emission. In the same way, we can explain that the GeV emission is not related to the MeV emission neither.

7.7 Summary

In this chapter, we investigated whether the origin of the X-ray component is the same as the MeV gamma-ray component. To answer this question, we first developed a spectral model (the general spectral model) that is described by basic physical parameters as shown in Table 7.1. Here we minimized assumptions in the spectral modeling in order to allow for physical parameters that are not considered in previous models. We searched for the model parameters which produce spectra consistent with observation. By using the photon index in the X-ray band and the $\nu F \nu$ ratio between in the X-ray and the GeV band, we put constraints
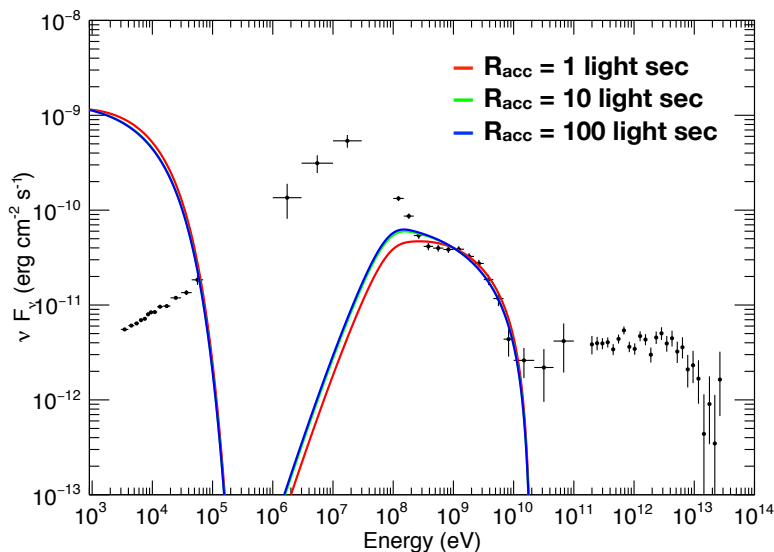
Figure 7.11: Attempts to explain the X-ray and the GeV emission from a single emission region. R_{acc} varies from 1 light sec to 100 light sec. We assume that $B = 500$ G, $\eta = 10000.0$, $s = 2$, $D_{\mathrm{acc}} = 50$ light sec and $\theta_{\mathrm{IC}} = 90$ degrees. Each spectrum is normalized at 1 GeV.

on the magnetic field and the size of the emission region. When the emission region is separated from the companion star by 50 light sec, the magnetic field is constrained between 1.4 G $< B <$ 150 G. Finally, we found that none of the parameter sets in the accepted region can explain the X-ray and MeV spectra simultaneously. Therefore, we conclude that the MeV gamma-ray component has a different spectral origin from the X-ray component.

The MeV spectral component is explained only as a synchrotron spectrum that is hardened by adiabatic losses. By comparing the observed spectrum, we obtained physical properties of a region where the MeV gamma-ray are produced:

1. The injection electron spectrum is very hard with a spectral index $s \sim 1$.

2. The acceleration is very efficient with $\eta \sim 2$.

3. The magnetic field is larger than few gauss at least.

4. A small emission region is required. Its size should satisfy Equation 7.21.

These requirements suggest that a direct acceleration takes place in LS 5039. Finally, we found that the GeV emission is not related to the X-ray emission. Therefore, LS 5039 has at least three spectral components which are produced in different regions.

Chapter 8

Discussion

In this chapter, we propose a new interpretation of the high-energy emission from LS 5039; the compact object in LS 5039 is a neutron star with strong magnetic field of $\sim 10^{15}$ G, and gamma rays are produced via interactions between the strong magnetic field and stellar winds from the companion O star. Hereafter, we refer to this hypothesis as the "magnetar binary hypothesis". On the basis of the hard X-ray pulse period and its derivative, we explain why such a strong-magnetized neutron star is required. Next, we describe how the magnetar binary hypothesis explains the spectral components of LS 5039 from the X-ray to TeV band. A noteworthy feature of this hypothesis is that it can naturally explain the origin of the MeV emission as magnetic reconnection in the magnetosphere of the magnetar. Finally, we propose a broadband spectral model from the X-ray to TeV band and a plausible mechanism which causes efficient magnetic reconnection.

8.1 Energy Source of the Emission of LS 5039

In Chapter 5, we found the evidence of hard X-ray pulsation in LS 5039 using the *Suzaku* and the *NuSTAR*. If the reported periodic signals originate from a pulsar, the compact object in LS 5039 is a neutron star with a spin period of $P_{\mathrm{NS}} \sim 9$ s and a period derivative of $\dot{P}_{\mathrm{NS}} \sim 3 \times 10^{-10}$ s s^{-1}. These two values are crucial to answer a fundamental question: what is the energy source that powers this unusual object? In order to explain the non-thermal luminosity from LS 5039, an energy supply of 10^{36} erg s^{-1} is required (Collmar & Zhang, 2014). Given that LS 5039 consists of a pulsar (a magnetized neutron star) and a massive star, four types of energy source are considered as a candidate:

1. rotational energy of the pulsar

2. gravitational energy due to mass accretion

3. stellar winds from the massive star

4. magnetic energy of the pulsar.

Here, assuming that LS 5039 contains a neutron star with the obtained P_{NS} and its derivative $\dot{P}_{\mathrm{NS}}$, we discuss in detail the maximum amount of energy which each of the four categories can supply, and explain that only magnetic energy of the pulsar can explain the luminosity of LS 5039.

8.1.1   Rotation-powered pulsar scenario

In this scenario, the rotational energy loss of the neutron star is converted to the radiation energy of the system (Ghosh, 2007). From the measured pulse period P_{NS} and its time derivative $\dot{P}_{\mathrm{NS}}$ of LS 5039, the luminosity L_{SD} due to spin-down energy loss of the neutron star is estimated to be

$$L_{\mathrm{SD}} = \frac{(2\pi)^2 I \dot{P}_{\mathrm{NS}}}{P_{\mathrm{NS}}^3} \sim 10^{34} \,\mathrm{erg\ s^{-1}}\,, \tag{8.1}$$

where $I \sim 10^{45}\,\mathrm{g\,cm^2}$ is a canonical value of the moment of inertia of the neutron star. This value is about two orders of magnitude lower than the requirement. Although the unknown equation of state for the super dense matter inside a neutron star does not allow us to obtain the precise value for I, this uncertainty can alter I only by a factor of ~ 2 at most (Worley et al., 2008). Hence, P_{NS} is too long for this object to be a rotation-powered pulsar. Therefore, this scenario is excluded unequivocally.

8.1.2   Accreting pulsar scenario

Here we consider that the neutron star in LS 5039 is an accreting pulsar. In this scenario, the neutron star gravitationally captures a fraction of stellar winds from the massive star. The captured matter, falling onto the neutron star, releases its gravitational energy, and a significant fraction of the output is converted into radiation (Ghosh, 2007). Since the luminosity available in this way can reach $\sim 10^{35}$ erg s^{-1} (so-called Eddington limit), this option is energetically feasible. However, the measured positive $\dot{P}$ does not support this scenario, given that accreting pulsars usually spin up as a result of the infalling matter always bringing in some angular momentum. In addition, the radiation spectra of accreting pulsars are distinct from that of LS 5039; the former is thermal and is limited to energies

below a few hundred keV, never extending to the MeV range as in the latter. Therefore, this scenario is also excluded.

Strictly speaking, an accreting pulsar can spin down, when the accretion rate decreases and the Alfvén radius becomes larger than the co-rotation radius (see Section 2.1 in Chapter 2). Since the change of the accretion rate is unstable, the luminosity of these accreting pulsars also varies with time. It changes by a factor of ~ 4 with a time scale of one year (Yatabe et al., 2018). This feature is quite different from the observational results of LS 5039 since in Chapter 4 we found that the luminosity in 3–10 keV varies by just $\sim 10\%$ in 8 years. Moreover, the $\dot{P}$ of these accreting pulsars varies following the change in the luminosity. In the accreting pulsar X Persei, $\dot{P}$ changes from -1.5×10^{-8} s s^{-1} to 0.5×10^{-8} s s^{-1} (Yatabe et al., 2018). If we measure the spin period of LS 5039 again and confirm that $\dot{P}$ is stable, we can reject definitively the possibility that the neutron star in LS 5039 is an accreting pulsar which spins down.

8.1.3 Kinetic energy of stellar winds

Even when the mass accretion is somehow hampered, some energy is still available when the stellar winds hit the pulsar's magnetosphere. Assuming that the massive star launches isotropic stellar winds with a velocity $v_{\rm w}$ at a mass-loss rate $\dot{M}_{\rm w}$, the kinetic energy $L_{\rm w}$ of the stellar winds which interact with the pulsar's magnetosphere is calculated as

$$
\begin{aligned}
L_{\rm w} &\sim \frac{1}{2}\dot{M}_{\rm w}v_{\rm w}^2 \times \frac{\pi R_{\rm A}^2}{4\pi D_{\rm sep}^2} \\
&= 6 \times 10^{31} \times \left(\frac{\dot{M}_{\rm w}}{10^{-6}M_\odot\ {\rm yr}^{-1}}\right)\left(\frac{v_{\rm w}}{2000\ {\rm km/s}}\right)^2\left(\frac{R_{\rm A}}{2\times 10^{10}\ {\rm cm}}\right)^2\left(\frac{D_{\rm sep}}{50\ {\rm light\ sec}}\right)^{-2}\ {\rm erg\ s}^{-1}
\end{aligned}
\tag{8.2}
$$

where $D_{\rm sep}$ is the binary separation and $R_{\rm A}$ is the Alfvén radius (see below). Note that $10^{-6}M_\odot\ {\rm yr}^{-1}$ is the upper limit of the mass loss rate of the wind reported in an optical observation (Casares et al., 2005). Again, this is orders of magnitude too low to explain the bolometric luminosity of LS 5039.

8.1.4 Magnetar binary hypothesis

The remaining possibility is that the magnetic field of the neutron star is the energy source of the emission of LS 5039 in a similar way as magnetars. Magnetars are neutron stars with ultra-strong magnetic field of $\sim 10^{15}$ G, which is higher by two orders of magnitude or more than those of ordinary neutron stars including pulsars (Thompson & Duncan, 1993).

Their emission, mostly in soft to hard X-rays, is thought to be produced by dissipation of their huge magnetic energy, although details of the magnetic-field dissipation are yet to be clarified. Assuming that the pulsar in LS 5039 is powered by the magnetic-field dissipation in the same way as magnetars, we can estimate the energy release rate L_{BF} as

$$L_{\mathrm{BF}} = \frac{B_{\mathrm{NS}}^2 R_{\mathrm{NS}}^3}{6\tau} \sim 10^{37} \times \left(\frac{B_{\mathrm{NS}}}{10^{15}\ \mathrm{G}}\right)^2 \left(\frac{R_{\mathrm{NS}}}{10\ \mathrm{km}}\right)^3 \left(\frac{\tau}{500\ \mathrm{yr}}\right)^{-1}\ \mathrm{erg\ s}^{-1}, \qquad (8.3)$$

where R_{NS} and B_{NS} are the radius and surface magnetic field of the pulsar, respectively; $\tau = P_{\mathrm{NS}}/(2\dot{P}_{\mathrm{NS}}) \sim 500\,\mathrm{yr}$ is the characteristic age of the neutron star in LS 5039 (Shapiro & Teukolsky, 1983). Accordingly, the energy balance of LS 5039 can be explained if $B_{\mathrm{NS}} \gtrsim 3 \times 10^{14}\,\mathrm{G}$. Since this is a typical value of a magnetar and all the other energy-source candidates have been rejected, the neutron in LS 5039 is inferred to be a magnetar. The detected $\sim 9\,\mathrm{s}$ pulsation period also supports this hypothesis, because it falls in the observed period range of magnetars of 2–11 s (Enoto et al., 2010). Therefore, we propose a new hypothesis that the compact object in LS 5039 is a magnetar with magnetic field of $\sim 10^{15}$ G. Hereafter we refer to this as "magnetar binary hypothesis". Since so far magnetars are observed only as isolated objects, this is the first time a binary system which contains a magnetar has been discovered.

The luminosity of 10^{36} ergs^{-1} is somewhat higher than the typical value of isolated magnetars of $\sim 10^{35}$ ergs^{-1}. This fact suggests that the magnetic-energy dissipation in LS 5039 proceeds faster than in isolated magnetars. We explain later that the dissipation process can be enhanced by interactions with the stellar winds. From the following section, we discuss the mechanism of the high-energy emission of LS 5039 assuming the magnetar binary hypothesis.

8.2   X-ray Emission in the Magnetar Binary Hypothesis; Shock Acceleration

We cannot apply the shock formation mechanism of the pulsar wind model to our hypothesis directly because of the following reasons. In the pulsar wind model, the X-ray emission of LS 5039 is explained as synchrotron emission from electrons accelerated in a shock which is formed by interactions between the strong pulsar winds and the stellar winds. However, currently there is no observational evidence that a magnetar has strong pulsar winds although extended emissions which might be made by the winds are reported from a few magnetars (Reynolds et al., 2017).

Even if the magnetar in LS 5039 has no stellar winds, a shock can be formed because the magnetic field pressure is high enough to halt the stellar winds. They are terminated at the Alfvén radius R_A, where the magnetic pressure of the neutron star P_B becomes comparable to the ram pressure of the material around the source P_w. P_B and P_w are described as

$$P_\mathrm{B} = \frac{1}{8\pi} B_\mathrm{NS}^2 \left(\frac{R_\mathrm{NS}}{R_\mathrm{A}} \right)^6 \tag{8.4}$$

$$P_\mathrm{w} = \frac{\dot{M}_\mathrm{w} v_\mathrm{w}}{4\pi D_\mathrm{sep}^2} . \tag{8.5}$$

Here the magnetic field is assumed to be bipolar. This is valid only when R_A is smaller than the radius of the light cylinder of the neutron star (Ghosh, 2007). From $P_\mathrm{B} = P_\mathrm{w}$, we obtain R_A as

$$R_\mathrm{A} = \left(\frac{B_\mathrm{NS} R_\mathrm{NS}^3 D_\mathrm{sep}}{\sqrt{2 \dot{M}_\mathrm{w} v_\mathrm{w}}} \right)^{1/3}$$

$$\sim 2 \times 10^{10} \ \mathrm{cm} \tag{8.6}$$

$$\times \left(\frac{B_\mathrm{NS}}{10^{15} \ \mathrm{G}} \right)^{1/3} \left(\frac{\dot{M}_\mathrm{w}}{10^{-6} M_\odot \ \mathrm{yr}^{-1}} \right)^{-1/6} \left(\frac{v_\mathrm{w}}{2000 \ \mathrm{km \ s}^{-1}} \right)^{-1/6} \left(\frac{D_\mathrm{sep}}{50 \ \mathrm{light \ sec}} \right)^{1/3} .$$

Since the radius of the light cylinder R_lc is calculated as $c P_\mathrm{NS}/(2\pi) \simeq 4 \times 10^{10}$ cm, it is valid to assume the bipolar magnetic field. In this way, the magnetar binary hypothesis predicts that a shock is formed apart from the neutron star by ~ 1.0 light sec. In more detail, the deformation of the bipolar magnetic field by the external pressure should be considered, which is a future study. Note that the size of the shock would be smaller than that of the pulsar wind model since the pulsar wind model predicts that the shock is apart from the neutron star by ~ 10 light sec (Takata et al., 2014; Dubus et al., 2015).

In order to make particle acceleration in the shock, at least the matters in the stellar winds should be halted by the magnetic pressure before they are captured by the gravity of the compact star. If they are captured by the gravity, they should be located at the position where their gravitational energies are larger than their kinetic energy. The radius of the gravitational capture region, so-called the Bondi-Hoyle capture radius, is calculated as

$$R_\mathrm{B} = \frac{2GM_\mathrm{NS}}{v_\mathrm{w}^2} \sim 1 \times 10^{10} \times \left(\frac{v_\mathrm{w}}{2000 \ \mathrm{km \, s}^{-1}} \right)^{-2} \ \mathrm{cm} \tag{8.7}$$

When $B_\mathrm{NS} \gtrsim 10^{14}$ G, the Alfvén radius R_A is larger than R_B. Therefore, a magnetic field of $B_\mathrm{NS} \gtrsim 10^{14}$ G can prevent the accretion, which satisfies the condition for particle acceleration.

In this scenario, the shock is formed apart from a neutron star by ~ 1 light sec. By assuming the dipole magnetic field, its strength in the shock region is estimated as

$$B_{\mathrm{sh}} = 37 \text{ G} \times \left(\frac{R_{\mathrm{A}}}{1 \text{ light sec}}\right)^{-3} \left(\frac{R_{\mathrm{NS}}}{10 \text{ km}}\right)^{3} . \tag{8.8}$$

This satisfies the constraints we obtained in the previous chapter. The size of the shock is also accepted if it is comparable to the separation between the shock and the neutron star. Therefore, we propose that the X-ray emission of LS 5039 is produced by non-thermal electrons in the shock which is formed by interaction between the magnetar's strong magnetic field and the stellar wind.

The orbital modulation of the X-ray emission would be explained by the Doppler boosting due to the velocity of accelerated materials in the shock. In the pulsar wind model, this Doppler boosting explains the modulation very well (Takata et al., 2014; Dubus et al., 2015). Though the mechanism of the shock formation in the magnetar binary hypothesis is different from that in the pulsar wind model, the shock itself is similar to that in pulsar wind model. Therefore, the orbital modulation of the X-ray emission would be explained in the same way as the pulsar wind model.

8.3 MeV gamma-ray Emission in the Magnetar Binary Hypothesis; Magnetic Reconnection

8.3.1 Requirement of magnetic reconnection in LS 5039

In the previous chapter, we found that the MeV spectral component should have a different origin from the X-ray component. By assuming this, the acceleration process for the MeV emission should satisfy the following conditions:

1. The energy distribution of injection electrons has a hard spectrum with a spectral index of $s \sim 1$.

2. The acceleration is very efficient with η of ~ 2.5.

3. The magnetic field B should be larger than a few G at least.

4. The size of the acceleration site should be smaller than 10 [light sec] $\times (B/1 \text{ G})^{-2/3}$.

Such a hard injection and a high efficiency are difficult to be achieved with the diffusive shock acceleration since it predicts $s \sim 2$ and $\eta \gtrsim 6$. Therefore, these conditions suggest that a direct acceleration takes place in LS 5039 for the MeV emission.

The most plausible process is magnetic reconnection because it achieves both the small acceleration region and the strong magnetic field easily. In order to supply the energy of the magnetic reconnection, a stable magnetic field is required since the magnetic energy is converted into kinetic energy of accelerated electrons in the reconnection. Thus, the neutron star is favored for a compact star in LS 5039. Since LS 5039 was discovered in 1971 (Stephenson & Sanduleak, 1971) and its age is larger than ~ 50 years at least, we can estimate the minimum magnetic field B_{NS} of the neutron star. Then the total magnetic energy stored in the neutron star should be larger than the energy released so far:

$$\frac{4\pi R_{\mathrm{NS}}^3}{3} \times \frac{B_{\mathrm{NS}}^2}{8\pi} \; > \; 1 \times 10^{36} \text{ erg s}^{-1} \times 50 \text{ yr} \tag{8.9}$$

$$B_{\mathrm{NS}} \; > \; 10^{14} \text{ G} . \tag{8.10}$$

Here, we assumed that $R_{\mathrm{NS}} = 10$ km. The essence of our discussion is: If we assume that the energy of the direct acceleration is supplied by the electromagnetic field of the compact star, then a strong magnetic field is required. Thus this constraint remains valid even if the acceleration is not the magnetic reconnection. Therefore, the hard spectrum in the MeV band also suggests that the compact object in LS 5039 is a magnetar with a magnetic field of $\sim 10^{14-15}$ G. On the basis of these arguments, we propose that magnetic reconnection takes place using magnetic energy of a magnetar in LS 5039 and the MeV emission is produced via synchrotron radiation from accelerated particle in the reconnection region.

8.3.2 Physical properties of the magnetic reconnection region

By using observed values, we can estimate the magnetic field and the size in the reconnection region. When the magnetic reconnection occurs at the distance of D_{rc} from the neutron star, we can obtain its luminosity L_{rc} as

$$L_{\mathrm{rc}} = \kappa \times \frac{B_{\mathrm{rc}}^2}{8\pi} \times 4\pi D_{\mathrm{rc}}^2 c . \tag{8.11}$$

where κ is the efficiency of the energy release of the magnetic reconnection and B_{rc} is the magnetic field in the reconnection region. Since L_{rc} is measured as $\sim 10^{36}$ erg s^{-1}, we obtain the following equation

$$\kappa \left(\frac{B_{\mathrm{rc}}}{1 \text{ G}}\right)^2 \left(\frac{D_{\mathrm{rc}}}{1 \text{ light sec}}\right)^2 = 7.4 \times 10^4 . \tag{8.12}$$

Since the reconnection process is a direct acceleration, the maximum energy E_{max} of the accelerated electrons is considered proportional to the size of the reconnection spot. When we define the size as $f \times D_{\mathrm{rc}}$, then the maximum energy is derived as

$$
\begin{aligned}
E_{\mathrm{max}} &\simeq q B_{\mathrm{rc}} f D_{\mathrm{rc}} & (8.13)\\
&= 9.0 \ [\mathrm{TeV}] \times f \left(\frac{B_{\mathrm{rc}}}{1 \ \mathrm{G}}\right) \left(\frac{D_{\mathrm{rc}}}{1 \ \mathrm{light \ sec}}\right) . & (8.14)
\end{aligned}
$$

Then, from Equation 2.30, the peak energy of the synchrotron radiation is calculated as

$$
E_{\mathrm{sync}} = 1.6 \ [\mathrm{MeV}] \times f^2 \left(\frac{B_{\mathrm{rc}}}{1 \ \mathrm{G}}\right)^3 \left(\frac{D_{\mathrm{rc}}}{1 \ \mathrm{light \ sec}}\right)^2 . \tag{8.15}
$$

Since it is observed as $E_{\mathrm{sync}} \simeq 20$ MeV (see Figure 7.1), we obtain the following relation

$$
f^2 \left(\frac{B_{\mathrm{rc}}}{1 \ \mathrm{G}}\right)^3 \left(\frac{D_{\mathrm{rc}}}{1 \ \mathrm{light \ sec}}\right)^2 = 1.3 \times 10 . \tag{8.16}
$$

Finally, we estimate the magnetic field in the reconnection region by assuming a dipole magnetic field

$$
\begin{aligned}
B_{\mathrm{rc}} &= B_{\mathrm{NS}} \left(\frac{R_{\mathrm{NS}}}{D_{\mathrm{rc}}}\right)^3 & (8.17)\\
&= 37 \ [\mathrm{G}] \times \left(\frac{B_{\mathrm{NS}}}{10^{15} \ \mathrm{G}}\right)^3 \left(\frac{D_{\mathrm{rc}}}{1 \ \mathrm{light \ sec}}\right)^{-3} & (8.18)
\end{aligned}
$$

By solving three equations (Equation 8.12, 8.16 and 8.17), the physical parameters are estimated as:

$$
B_{\mathrm{rc}} = 7.4 \times 10^2 \ [\mathrm{G}] \times \kappa^{-3/4} \left(\frac{B_{\mathrm{NS}}}{10^{15} \ \mathrm{G}}\right)^{-1/2} \tag{8.19}
$$

$$
D_{\mathrm{rc}} = 3.7 \times 10^{-1} \ [\mathrm{light \ sec}] \times \kappa^{1/4} \left(\frac{B_{\mathrm{NS}}}{10^{15} \ \mathrm{G}}\right)^{1/2} \tag{8.20}
$$

$$
f = 4.9 \times 10^{-4} \times \kappa^{7/8} \left(\frac{B_{\mathrm{NS}}}{10^{15} \ \mathrm{G}}\right)^{1/4} \tag{8.21}
$$

$$
E_{\mathrm{max}} = 1.2 \ [\mathrm{TeV}] \times \kappa^{3/8} \left(\frac{B_{\mathrm{NS}}}{10^{15} \ \mathrm{G}}\right)^{1/4} . \tag{8.22}
$$

From them, we obtain two interesting features. First, the magnetic field in the reconnection region must be larger than $\sim 10^3$ G. This satisfies the condition obtained from the observed spectrum. The second feature is that the reconnection spot should be located at $D_{\mathrm{rc}} < 3.7 \times 10^{-1}$ light sec. Since the shock region is apart from the magnetar by ~ 1 light sec, this feature indicates that magnetic reconnection takes place closer to the magnetar than the

shock acceleration does. As the location of acceleration/radiation process becomes closer to the neutron star, its rotation would affect the process more. Thus, we propose that the MeV emission is pulsed. Since the spectrum of the MeV component is very hard, it is reasonable that the pulse fraction is larger in the hard X-ray band than in the soft X-ray band. This can explain why we detected the pulsation only in the hard X-ray band.

8.3.3 Stability of the reconnection spot

The accelerated elections via the magnetic reconnection would form charge current. Then, the current would produce the magnetic field due to electromagnetic induction. If the induced magnetic field is very strong, it might violate the global magnetic field from the neutron star, which suppresses the efficient reconnection process. Thus, here we estimate the strength of the induced magnetic field. By assuming that the total area of the magnetic reconnection spot is the same as $\kappa \times 4\pi R_{\mathrm{rc}}^2$, the charged current i per unit area and per unit time is given as

$$i \;=\; \frac{L_{\mathrm{rc}}/E_{\mathrm{max}}}{\kappa \times 4\pi D_{\mathrm{rc}}^2} \tag{8.23}$$

$$=\; 6.1 \times 10^{12} \ [\mathrm{cm}^{-2} \ \mathrm{s}^{-1}] \times \kappa^{-1} f^{-1} \left(\frac{B_{\mathrm{rc}}}{1 \ \mathrm{G}}\right)^{-1} \left(\frac{D_{\mathrm{rc}}}{1 \ \mathrm{light \ sec}}\right)^{-3}. \tag{8.24}$$

Then, the current I in a single reconnection spot is

$$I \;=\; i \times q_e \times 4\pi f^2 D_{\mathrm{rc}}^2 \tag{8.25}$$

$$=\; 1.1 \times 10^{16} \ [\mathrm{A}] \times \kappa^{-1} f \left(\frac{B_{\mathrm{rc}}}{1 \ \mathrm{G}}\right)^{-1} \left(\frac{D_{\mathrm{rc}}}{1 \ \mathrm{light \ sec}}\right)^{-1}. \tag{8.26}$$

Finally, the induced magnetic field B_{induced} is calculated by Ampère's circuital law

$$B_{\mathrm{induced}} \;=\; \frac{\mu I}{2\pi f R_{rc}} \tag{8.27}$$

$$=\; 7.3 \times 10^2 \ [\mathrm{G}] \times \kappa^{-3/4} \left(\frac{B_{NS}}{10^{15} \ \mathrm{G}}\right)^{-1/2} \tag{8.28}$$

$$=\; B_{\mathrm{rc}} \tag{8.29}$$

This result implies that the reconnection process can produce the magnetic field comparable to the global field of the neutron star. This means that the magnetic reconnection in the neutron star magnetosphere would be spatially unstable *i.e.* the reconnection spots move sporadically. This could explain the lack of a consistent solution of the orbital parameters in the hard X-ray pulse search using the *Suzaku* and *NuSTAR*.

If the total area of the reconnection region $\sim \kappa \times 4\pi R_{\mathrm{rc}}^2$ is smaller than the surface area $4\pi R_{rc}^2$, the process will not change the global structure of the magnetic field *i.e.* the dipole magnetic field assumption is valid. Therefore, κ should be much smaller than 1. If $\kappa = 10^{-2}$, then the size of a single reconnection spot is just ~ 300 m (see Equation 8.19).

8.4 GeV gamma-ray Emission in the Magnetar Binary Hypothesis; Curvature Radiation

8.4.1 Curvature Radiation by Electrons Accelerated by Magnetic Reconnection

Here, we discuss the origin of the GeV emission from LS 5039. In the previous chapter, we explained that the GeV spectral component has a different origin from the X-ray and the MeV component. Furthermore, in Chapter 6 found that the flux in 1–5 GeV is nearly independent of the orbital phase. The flux modulation in this energy range, defined as $(F_{\max} - F_{\min})/(F_{\max} + F_{\min})$ was derived as 10–20%. Therefore, the GeV component should not be affected by the physical parameters related to the binary motion *e.g.* the binary separation.

We propose that the GeV emission is produced via the curvature radiation. The curvature radiation is a radiation process when a charged particle moves along a curved magnetic field line (Gil et al., 2004). This process is similar to synchrotron radiation, but its spectral peak is higher that of synchrotron radiation. In pulsars, the curvature radiation is usually observed in the GeV band (Wang et al., 2010), It is thought that the curvature radiation takes place in a pulsar's magnetosphere. If a similar process takes place in LS 5039, it would explain the stable GeV emission as long as the binary motion does not affect the curvature radius of the pulsar's magnetosphere.

The typical gamma-ray energy from the curvature radiation is derived as (Takata et al., 2014)

$$
\begin{aligned}
E_{\mathrm{cuv}} &= \frac{3}{2}\frac{\hbar\gamma^3 c}{R_{\mathrm{cuv}}} & (8.30)\\
&= 5.2 \text{ MeV} \times \xi^{-1}\left(\frac{P_{\mathrm{NS}}}{9 \text{ s}}\right)^{-1}\left(\frac{E_e}{10 \text{ TeV}}\right)^3, & (8.31)
\end{aligned}
$$

where R_{cuv} is the curvature radius of the magnetic field line and P_{NS} is a spin period of the neutron star, and ξ is the ratio of R_{cuv} to the radius of the light cylinder ($R_{\mathrm{cuv}} = $

$\xi \frac{cP_{\mathrm{NS}}}{2\pi}$). In Chapter 6, we measured the cutoff energy of the GeV spectrum around the inferior conjunction as $1.87 \pm 0.06 \pm 0.38$ GeV. In order to make E_{cuv} comparable to this observed value, ξ should be $\sim 3 \times 10^2$. This indicates that the curvature radiation takes place apart from the neutron star by $D_{\mathrm{cuv}} \sim 4 \times 10^{-3}$ light sec if R_{cuv} is comparable to D_{cuv}.

We propose that the curvature radiation is produced by electrons accelerated in reconnection spots close to the magnetar. Figure 8.1 shows a schematic of this scenario. In the reconnection spots, accelerated particles lose most of their energy via the synchrotron radiation. However, if the accelerated particle has a very small pitch angle *i.e.* its initial velocity is parallel to the magnetic field, then it can survive from the synchrotron radiation and move along the magnetic field lines in the magnetosphere. Then, GeV gamma rays are produced via curvature radiation.

A drawback is that this scenario seems to predict the correlation between the MeV and the GeV emission, while the observations have shown that their flux dependences on the orbital phase are very different from each other. This would be explained by considering the geometrical effect. Since the MeV gamma rays are produced in a small region and electrons are accelerated along the magnetic field, the flux of the MeV gamma rays is affected by the Doppler boosting, which makes the flux modulation depending on the orbital phase. On the other hand, the GeV gamma rays are produced by moving along the magnetic field lines. Then, as shown in Figure 8.1, the curvature radiation can be more isotropic than the MeV gamma-ray emission. This is consistent with the observational result that the flux in 1–5 GeV is nearly independent of the orbital phase.

8.4.2 Other Possibilities

Here we discuss several scenarios which have been proposed for the GeV emission. Takata et al. (2014) proposed that the GeV component is the outer gap emission in the pulsar magnetosphere (Cheng et al., 1986). In this scenario, particles are accelerated in a region where the charge density changes sign near the light cylinder. However, since it is located close to the light cylinder, Equation 8.30 yields the typical gamma-ray energy in the MeV band. Thus, it is difficult to explain the GeV emission. In addition, it is well known that the particles can be accelerated near the magnetic pole of the neutron star because the low change density is also achieved there (the polar cap model, Daugherty & Harding 1982). However, in this case, GeV gamma rays would be completely absorbed by the strong magnetic field via the electron-positron pair production ($\gamma B \rightarrow e^- e^+$, Erber 1966).
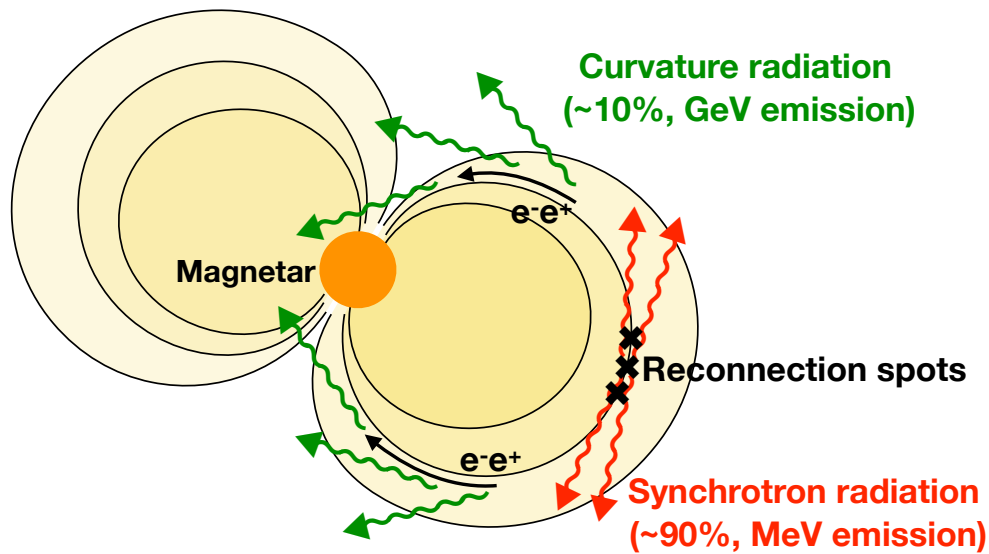
Figure 8.1: A schematic of the radiation process for the MeV and GeV gamma rays.

Dubus et al. (2015) proposed that the GeV emission is produced by electrons distributed with a narrow Maxwellian in the shock region. This scenario is supported by some particle-in-cell simulations (Sironi & Spitkovsky, 2009, 2011) which show that the relativistic shock produces the Maxwellian-distributed electrons in addition to powerlaw-distributed electrons. In this scenario, the GeV gamma rays are produced via inverse Compton scattering by the Maxwellian-distributed electrons. However, Dubus et al. (2015) predicts that the GeV flux varies significantly following the orbital phase because the inverse Compton emission and the amount of the Maxwellian-distributed electrons depend on the orbital phase strongly. Consequently, the predicted light curve is inconsistent with that obtained with the *Fermi*.

GeV electrons might be produced when TeV gamma rays are converted into electron-positron pairs via gamma-gamma absorption. Then, they would emit the GeV gamma rays via inverse Compton scattering. In order to explain the GeV emission of LS 5039 in this scenario, at least 90% of the TeV gamma rays should be absorbed because the flux of the GeV component is larger by ~ 10 than that of the TeV component. However, such a strong absorption is difficult to achieve in LS 5039 (Dubus, 2006). In addition, GeV gamma rays might be produced via pion decay process. The stellar winds from the companion star may supply protons to the shock region. However, the cooling time is estimated as $\sim 10^5$ s (Aharonian, 2004), which is too long to explain the observed spectrum.

8.5 TeV gamma-ray Emission in the Magnetar Binary Hypothesis; Magnetic Reconnection Driven Jet

Here we discuss the origin of the TeV gamma-ray emission by referring to the previous works. So far, two scenarios have been proposed for the TeV gamma-ray emission:

1. The Coriolis shock in the pulsar wind model (Bosch-Ramon et al., 2012; Takata et al., 2014; Dubus et al., 2015); A shock is formed at the location where the ram pressures of the stellar wind owing to Coriolis forces and the pulsar wind are comparable with each other (see Figure 2.13).

2. The jet-like structure in the microquasar model (Bosch-Ramon et al., 2006; Paredes et al., 2006; Khangulyan et al., 2008).

Two scenarios have two common features: (1) TeV gamma rays are produced via inverse Compton scattering; (2) The emission region is located apart from the companion star by $\gtrsim 100$ light sec. The second condition is required from the TeV gamma-ray observation (Aharonian et al., 2006b). This is because if the emission region is close to the companion star, the UV photons from it would strongly absorb the TeV gamma rays and makes the TeV spectrum inconsistent with the observation (Khangulyan et al., 2008). Hereafter we consider the two scenarios assuming the existence of a magnetar in LS 5039.

First we consider the Coriolis shock scenario. As mentioned above, currently there is no strong evidence that a magnetar has a strong pulsar wind. Without a strong wind, it is difficult to form the Coriolis shock in the magnetar binary hypothesis. The Coriolis shock might be formed by the balance between the magnetic field pressure and the ram pressure of the stellar winds accelerated by the Coriolis forces. Following Bosch-Ramon et al. (2012), the location of the Coriolis shock can be estimated as

$$\frac{B_{\rm NS}^2}{8\pi} \frac{R_{\rm NS}^6}{R_{\rm lc}^4} \frac{1}{x^2} = \frac{\dot{M}_{\rm w}}{4\pi (x + D_{\rm sep})^2 v_{\rm w}} \left(\frac{4\pi}{P_{\rm orb}}\right)^2 x^2 \;, \tag{8.32}$$

where $R_{\rm lc}$ is the radius of the light cylinder and x is the distance between the Coriolis shock and the magnetar. As a result, x is obtained as ~ 6 light sec. Thus, the Coriolis shock formed by the magnetic pressure is very close to the magnetar. Since the binary separation is about 50 light sec, the Coriolis shock is located apart from the companion star by ~ 50 light sec, which is too close to avoid gamma-gamma absorption. Therefore, the Coriolis shock in the magnetar binary hypothesis cannot satisfy the requirement from the TeV observation.

Second we consider the TeV emission from a jet. It is discussed that particles in a jet launched from a black hole are accelerated by magnetic reconnection. For example, De Gouveia Dal Pino et al. (2016) suggests that anti-parallel magnetic field lines can be formed between the black hole and the accretion disk. This scenario seems to be favored because it may explain magnetic reconnection in LS 5039 simultaneously. However, to begin with, it is difficult to consider a jet that is considered in accreting systems because the accretion does not occur in the magnetar binary hypothesis as discussed above. Interestingly, several works suggest that a jet-like structure is formed purely by magnetic reconnection. Clausen-Brown & Lyutikov (2012) predicts that in a pulsar wind nebula there are unaligned small jets driven by magnetic reconnection. Moreover, a jet-like outflow can be also formed in the magnetosphere of the Earth (Dai et al., 2015). In the reconnection spot on the dayside of the Earth (see (A) in Figure 2.16), a bipolar jet is formed perpendicular to the orbital plane. If LS 5039 has a configuration of magnetic field lines similar to Figure 2.16, LS 5039 would have a jet driven by purely magnetic reconnection. In this sense, we refer to it as the magnetic reconnection driven jet. Furthermore, the existence of a jet-like outflow is favored since the radio emission of LS 5039 has a bipolar structure (Paredes et al., 2000). Therefore, we propose that LS 5039 has a relativistic outflow driven by magnetic reconnection. In the following section, we discuss details of a plausible configuration of magnetic field lines which can launch the magnetic reconnection driven jet.

In order to explain the TeV emission by inverse Compton scattering of the stellar UV photons, accelerated electrons should have an energy of few tens TeV (Khangulyan et al., 2008). In our estimation, the maximum energy of accelerated electrons in the reconnection region is less than ~ 1 TeV (see Equation 8.19). This discrepancy would be solved when we consider multiple accelerations in the reconnection region. By using particle-in-cell simulations, Sironi & Spitkovsky (2014) demonstrates that a chain of magnetic reconnection spots are formed in magnetic reconnection process. Furthermore, they also predict that the plasmoid instability produces smaller reconnection spots which are also chained with each other. Thus, a reconnection spot in LS 5039 would be surrounded by other reconnection spots. If an electron accelerated in a single reconnection spot enters into another reconnection spot, its energy is increased again. By repeating this re-acceleration process, the maximum energy of accelerated electrons would reach at few tens TeV.

8.6 Broadband Spectral Model of the Magnetar Binary Hypothesis

In this chapter, we propose the magnetar binary hypothesis; the compact object in LS 5039 is a magnetar with a magnetic field of $\sim 10^{15}$ G. On the basis of this hypothesis, we propose the origins of the high-energy emission of LS 5039 from the X-ray to TeV band. Summarizing above, they are explained as:

1. X-rays are produced in the shock region at Alfvén radius ~ 1.0 light sec. The shock is located inside the magnetosphere of the magnetar. The size and magnetic field of the emission region are few light sec and $30 - 100$ G, respectively.

2. MeV gamma rays are produced via magnetic reconnection near the magnetar. The magnetic field is larger than $\sim 10^3$ G. The reconnection spots are located within 0.4 light sec from the magnetar.

3. About 10% of electrons which are accelerated in the reconnection spots enter into the magnetosphere of the magnetar. These electrons emit GeV gamma rays via curvature radiation.

4. TeV gamma rays are produced via inverse Compton scattering in a relativistic outflow driven by magnetic reconnection.

On the basis of these statements, we propose a spectral model using the general spectral model developed in the previous chapter. Following the physical parameters of the emission regions we explained above, we define the parameters of the spectral model as shown in Table 8.1. Since the general spectral model does not contain curvature radiation, the GeV gamma-ray component is modeled by an exponential cutoff powerlow function. Figure 8.2 shows the comparison between the observed spectra and the spectral model. The model explains the observation very well from the X-ray to TeV band.

Note that the flux of the reconnection component in the soft X-ray band might be overestimated because we do not consider synchrotron self absorption and escape of electrons from small acceleration spots. These effects may make the MeV spectral component harder in the low energy band. Although there is a discrepancy of the spectrum around the superior conjunction in the TeV band, it can be improved by considering gamma-gamma absorption. As discussed above, in order to understand the dependence of the flux on the orbital phase, the Doppler boosting should be considered. Here the ratio of the normalization between the

inferior/superior conjunction ($\mathrm{Norm_{INFC}/Norm_{SUPC}}$ in Table 8.1) reflects the boosting effect approximately, but it is still crude. In addition, we fixed the scattering angle which varies with the orbital phase. Future work is needed to consider these effects.

Table 8.1: Parameters adopted in Figure 8.2.

	Shock	Jet	Reconnection
R_{acc} (light sec)	5.0	100.0	10^{-6}
B (G)	50.0	0.1	2×10^{4}
D_{acc} (light sec)	50.0	100.0	50.0
η	10.0	10.0*	2.5
s	2.4	2.0	1.0
$\mathrm{Norm_{INFC}/Norm_{SUPC}}$	1.66	4.0	2.0

*: In the general spectral model, it is assumed that the emission and acceleration take place in the same region. However, in our scenario the maximum energy in the jet is determined by the reconnection region. Thus, η for the jet spectrum does not mean the acceleration efficiency. It is a parameter which determines the maximum energy of electrons injected into the jet. From Equation 7.7, this value corresponds to the maximum energy of 60 TeV here.

8.7   A Plausible Configuration of Magnetic Field Lines in LS 5039

To explain the spectral origins simultaneously, we propose a plausible configuration of magnetic field lines in LS 5039 on the analogy of that around the Earth. Figure 8.3 shows the configuration that we propose. In this scenario, the high-energy emission is explained as follows: When strong stellar winds interact with magnetic fields of the magnetar in LS 5039, a shock is formed at Alfvén radius (the blue region in the figure). Then, the shock formation reconfigures the structure of the magnetic fields of the magnetar. The structure of global magnetic field lines is determined as they connect smoothly with the magnetic field lines from the magnetar. In the figure, the direction of the magnetic field lines around the shock region is upward. However, since the magnetar's dipolar magnetic field line is closed inside the light cylinder of the magnetar, it has an opposite direction from that of the global magnetic field on the orbital plane. Therefore, in a certain region between the magnetar and the shock, the direction of the magnetar's dipolar magnetic field is anti-parallel to that of the global mag-
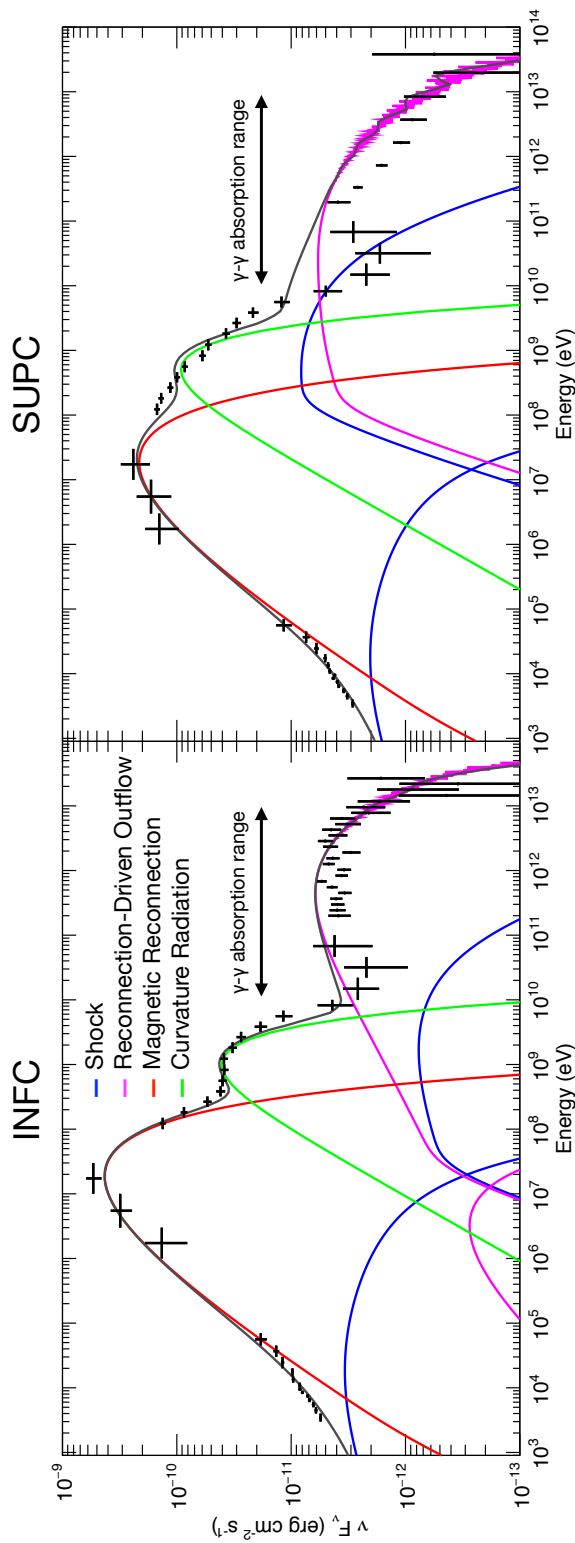
Figure 8.2: The spectrum model for LS 5039 under the magnetar binary hypothesis. The spectral components for the shock, the outflow and the magnetic reconnection are modeled with the general spectral model developed in the previous chapter. The adopted parameters are defined in Table 8.1. The GeV components are model with an exponential cutoff powerlow function with a photon index of 1.0. The cutoff energy is defined as 1 GeV in the INFC and 0.5 GeV in the SUPC. The scattering angle is set to 45 degrees in the INFC and 135 degrees in the SUPC.

netic field. In this region (the red crosses in Figure 8.3 bottom), magnetic reconnection takes place efficiently because a set of anti-parallel magnetic field lines is an ideal configuration for magnetic reconnection. This is perfectly consistent with what we have discussed above; the reconnection spots should be located closer to the magnetar than the shock does.

In the reconnection spots, electrons are accelerated efficiently, and they emit MeV gamma rays via synchrotron radiation. A fraction of accelerated electrons leave the reconnection spot before they lose their energies via synchrotron radiation. Some of them move along magnetic field lines of the magnetar's magnetosphere, and produce GeV gamma rays via curvature radiation. Remaining electrons leave the reconnection region along open magnetic field lines, which forms a relativistic outflow. Since the reconnection spots are smaller than ~ 50 km at least (see Equation 8.19), the root of the outflow is also very small. Furthermore, the trajectory of the outflow is aligned along the strong magnetic field lines. Thus, the outflow would have a bipolar jet-like structure. In this way, LS 5039 has a jet purely driven by magnetic reconnection. Finally, electrons in the jet produce TeV gamma rays via inverse Compton scattering using UV stellar photons as seed photons.

Note that this scenario might have an issue from an energetic point of view. In Figure 8.3, the energy source of the X-ray emission in the shock seems to be kinetic energy of the stellar winds. However, it is estimated to be $\sim 10^{31}$ erg s^{-1} (see Equation 8.2), which is too small to explain the observed X-ray luminosity of $\sim 10^{34}$ erg s^{-1}. We believe that there are two possibilities which can explain this difficulty: One is the energy of the magnetic field in the shock, which is estimated to be $\sim 10^{34}$ erg s^{-1}. If it is efficiently converted to the radiation energy in some way, the X-ray luminosity might be explained. The second is that X rays are produced near the magnetar rather than in the shock. For example, electrons in the magnetosphere might emit X-ray photons via synchrotron radiation in addition to GeV gamma rays via curvature radiation. Furthermore, if the energy source of the magnetic reconnection is the magnetar's magnetic energy as discussed before, there should be Poynting flux from the magnetar towords the reconnection spots. However, the details of this energy transfer are not clear at this moment. A possibility is that a twisted magnetosphere is formed around the magnetar. Future work is needed to investigate these issues.
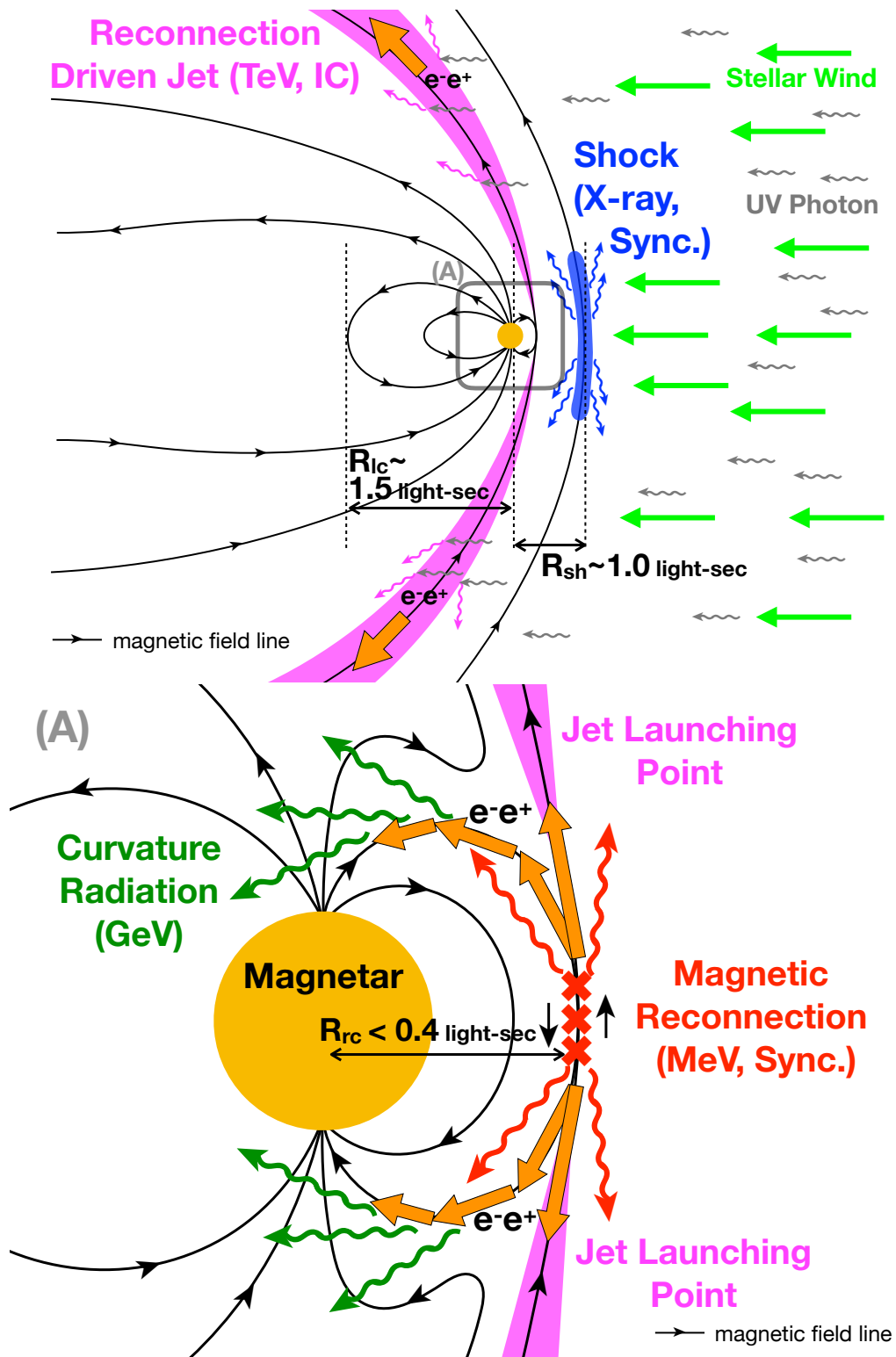
Figure 8.3: A schematic of the magnetar binary hypothesis for LS 5039.

8.8   Possibility of Magnetic Reconnection in Other Gamma-ray Binary Systems

Here we describe that the proposed mechanism which triggers magnetic reconnection in LS 5039 can be applied to other gamma-ray binary systems. The two gamma-ray binary systems, LS I+61°303 and PSR B1259-63 are discussed here. In either case, by considering the structure of magnetic field lines around the neutron star, we can explain the high-energy emission from these system qualitatively. Although more detailed study is needed, the magnetic reconnection process which we proposed for LS 5039 might be realized in other high-energy gamma-ray sources.

8.8.1   LS I+61°303

LS I+61°303 is another bright gamma-ray binary system in the Galaxy. Similar to that of LS 5039, its spectrum is peaked at 10–100 MeV (see Figure 2.3 Left). However, differently from LS 5039, its emission is not stable. Hadasch et al. (2012) reported that the averaged flux in the GeV band changed by $\sim 30\%$ in 2009 Marth. The orbital light curve was also changed after that. Furthermore, it is reported that the peak in the X-ray orbital light curve varies from $\phi = 0.4$ to $\phi = 0.8$ depending on cycle (Paredes et al., 1997; Torres et al., 2010; Li et al., 2011; Chernyakova et al., 2012).

Torres et al. (2012) suggested that LS I+61°303 contains a magnetar on the basis of a short X-ray burst detected from this system. Although X-ray bursts are usually observed from LS I+61°303, the detected short burst was very different from them because its time duration was ~ 0.3 s while those of the usual bursts are few ks. Since isolated magnetars often show similar short bursts with a time duration of $\sim$0.01–0.2 s (e.g. Rea et al. 2009), they proposed that the observed short burst is a burst from a magnetar in LS I+61°303.

If LS I+61°303 really contains a magnetar, its time-variability can be interpreted by the change of the structure of magnetic field lines near the magnetar as shown in Figure 8.4. Since LS I+61°303 has a massive star which emits strong stellar winds, the shock would be formed near the magnetar by interaction of the ram pressure of the stellar winds and the magnetic pressure of the magnetar. If the shock is located inside the light cylinder (see Figure 8.4 Top), the reconnection spots are formed in the same way as discussed above. Then, its spectrum would be similar to that LS 5039. However, if the shock is located outside the light cylinder (see Figure 8.4 Bottom), the reconnection spots would not be formed because outside the light cylinder the magnetic field from the magnetar should be open, otherwise the

velocity of the magnetic field is larger than speed of light. Then, its emission from the MeV to TeV band would be decreased dramatically. In LS I+61°303, we propose that the location of the shock region fluctuates sporadically. As the shock region crosses the light cylinder, the high-energy emission changes dramatically. The change of the shock location would be caused by decay of the magnetar's magnetic field or the change of the amount of in-coming stellar winds since the location is determined by interaction between these two components.
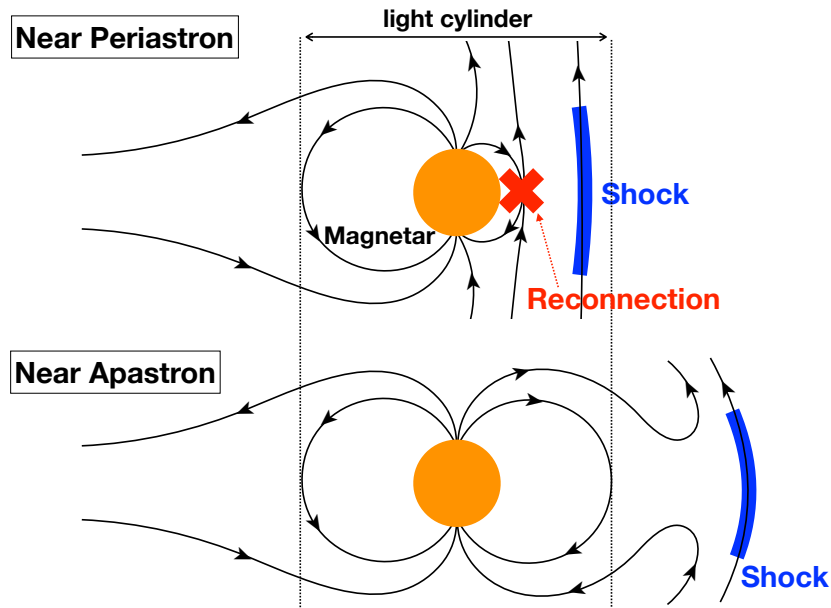
Figure 8.4: A possible scenario of magnetic reconnection in LS I+61°303.

8.8.2   PSR B1259-63

PSR B1259-63 is a gamma-ray binary system consisting of a Be star and a milli second pulsar with a period of $P_{\rm p} \sim 48$ ms (Johnston et al., 1992). So far strong gamma-ray emissions have been observed around the periastron passage (Aharonian et al., 2005a). This is interpreted as that shock acceleration takes place when the pulsar penetrates the dense environment formed by the outflowing material from the Be star. Interestingly, Abdo et al. (2011) observed the strong GeV emission from PSR B1259-63 ~ 30 days after the periastron. During the flare, its bolometric luminosity is observed as $\sim 8 \times 10^{35}$ erg s^{-1}, which is comparable to the spin down luminosity of the milli second pulsar (8.3×10^{35} erg s^{-1}). However several theoretical explanations are proposed (Bogovalov et al., 2008; Dubus et al., 2010), currently the mechanism, region and energy source of the GeV flare are still unclear.

Here we propose that the GeV flare of PSR B1259-63 is also explained by magnetic reconnection near the neutron star. The proposed scenario goes as follows. At periastron, the pulsar winds from the pulsar collide with the surrounding dense material, and the shock is formed. Since the light cylinder of the pulsar is small with a radius of $cP_{\mathrm{p}}/(2\pi) = 7.6 \times 10^{-3}$ light sec, the shock is formed outside the light cylinder. Due to the shock formation, the magnetic field lines between the shock and the light cylinder would be distorted as shown in Figure 8.5 Top. As PSR B1259-63 leaves from the dense region, the shock becomes further away from the pulsar. Then, the distorted magnetic field lines start to return to the original. At a point in time, anti-parallel magnetic field lines are formed near the light cylinder as shown in the bottom of Figure 8.5. Then, the magnetic reconnection takes place, which would produce strong MeV emission. The energy E_{B} of the magnetic field at the light cylinder is estimated as

$$E_{\mathrm{B}} = 5.4 \times 10^{36} \text{ erg s}^{-1} \times \left(\frac{B}{10^{12} \text{ G}}\right)^2 \left(\frac{R_{\mathrm{NS}}}{10 \text{ km}}\right)^{-4} \left(\frac{P_{\mathrm{p}}}{48 \text{ ms}}\right)^6 , \qquad (8.33)$$

where B and R_{NS} are the magnetic field and the radius of the pulsar. If $\sim 10\%$ of this magnetic energy is converted into the radiation energy, the bolometric luminosity of the GeV flare of PSR B1259-63 can be explained.
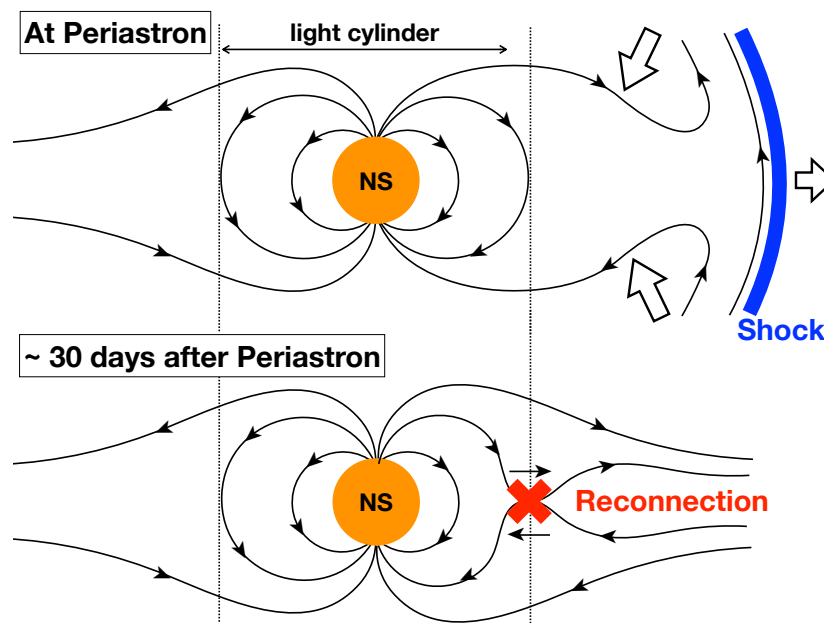
Figure 8.5: A possible scenario of magnetic reconnection in PSR B1259-63.

8.9 Future Prospects

8.9.1 Detailed study of the pulsation from LS 5039

In this chapter, we proposed a hypothesis: the energy source of the high-energy emission of LS 5039 is supplied by the strong magnetic field of a magnetar in LS 5039, on the basis of the evidence of the hard X-ray pulsation. In order to confirm this hypothesis, it is crucial to detect the pulsation again using another hard X-ray observations since the confidence level of the detected pulsation is still $\sim 3\sigma$. Needless to say, another independent pulse detection would strengthen the magnetar binary hypothesis.

The magnetar binary hypothesis predicts that the MeV emission is produced closer to a magnetar than the X-ray emission is. Since a region closer to a neutron star will be affected by its rotation, it is natural to interpret that the detected hard X-ray pulsation originates from the MeV spectral component. Thus, gamma-ray emission from the reconnection spots should be pulsed. We propose two possibilities for the pulsation mechanism of the MeV emission as shown in Figure 8.6. First is that the reconnection spot moves spatially as the magnetar rotates (see the top in the figure). The periodical motion of the reconnection spot might produce a pulsation signal. The other is that the reconnection takes place periodically (see the bottom in the figure). Since the rotational axis and the magnetic axis are not aligned, the magnetar's bipolar magnetic field can be anti-parallel to the global magnetic field only in certain rotational phases. If magnetic reconnection takes place only in these phases, the synchrotron emission would be pulsed. In either case, the pulsed signal is produced in the magnetosphere of the magnetar, not on the surface. Thus, we consider that the pulsed signal reflects the properties of the magnetosphere. If the reconnection changes the structure of the magnetosphere, the pulsed signal might be modulated. In Chapter 5, no consistent solution for orbital parameters was found from the hard X-ray pulsation of the *Suzaku* and *NuSTAR*. The modulation by the changes of the magnetosphere structure may explain the lack of the solution for orbital parameters.

Since most of the MeV gamma rays are predicted to be produced in the reconnection spots, we would observe strong pulsed signal in the MeV band. Future MeV gamma-ray missions *e.g.* AMEGO (McEnery et al., 2019), e-ASTROGAM (De Angelis et al., 2017), GRAMS (Aramaki et al., 2020) and SMILE (Takada et al., 2011) will successfully detect the MeV gamma-ray pulsation from LS 5039.
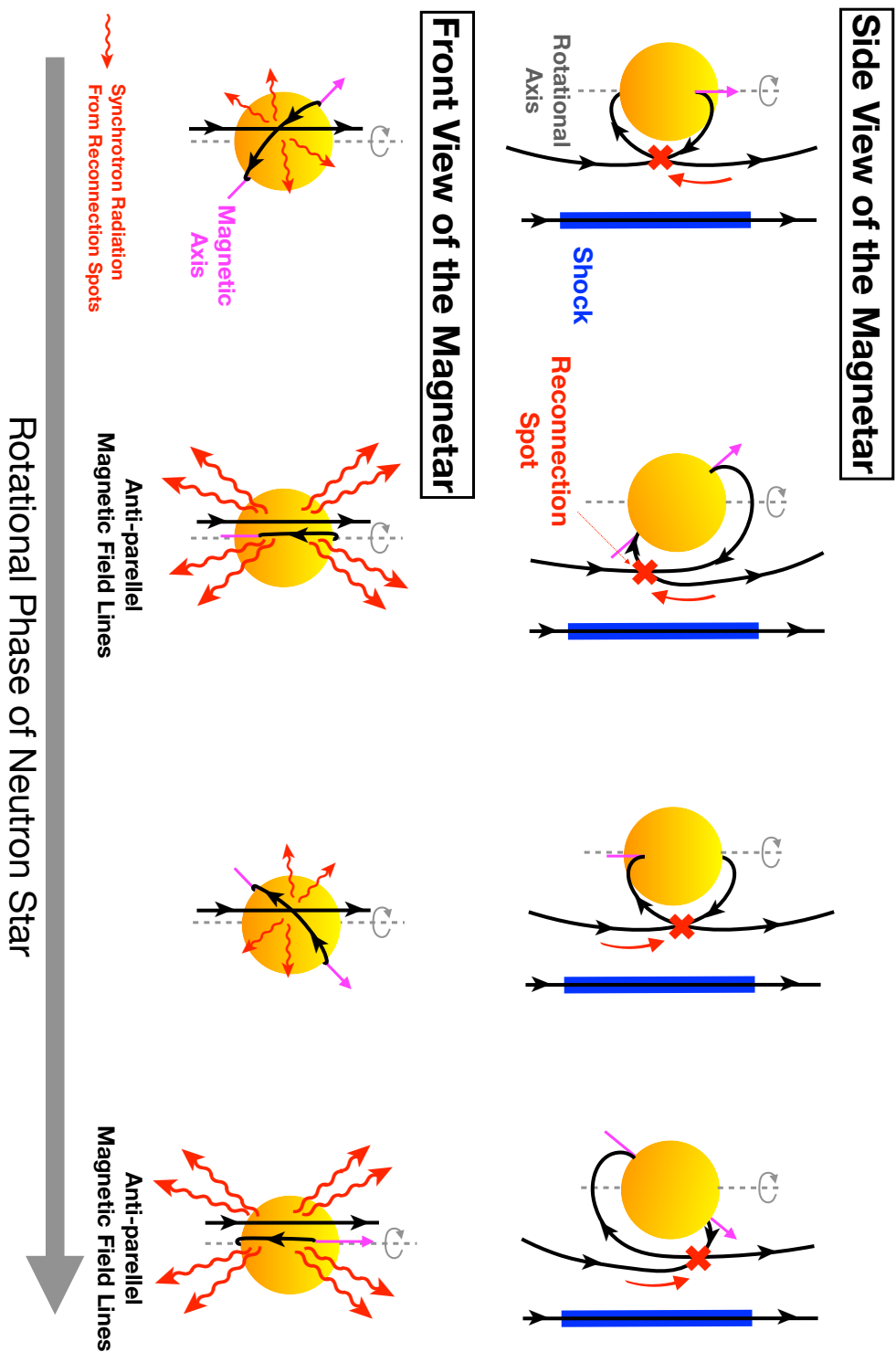
Figure 8.6: Pulsation Mechanism of LS 5039 in the hard X-ray band

8.9.2 Study of the structure of the magnetic field in magnetar binary systems

In order to achieve an efficient and stable magnetic reconnection process in this source, we proposed that the magnetic field lines are configured by the shock formation as shown in Figure 8.3. By considering the direction of the magnetar's bipolar magnetic field and the global magnetic field, we explained how these magnetic field lines are formed qualitatively. In order to understand this process in detail, it is essential to calculate quantitatively the structure of the magnetic field in a binary system containing a magnetar and a massive star with strong stellar winds. If a theoretical study reproduces stable anti-parallel magnetic lines in the magnetosphere, our hypothesis would be strengthened.

8.9.3 Detailed spectral modeling of magnetar binary systems

In this thesis, we reproduced the spectrum of LS 5039 using the general spectral model we developed in the previous chapter. However, the following points are not considered in our calculation:

1. gamma-gamma absorption

2. synchrotron self absorption for the MeV emission

3. escape of electrons from the reconnection spots

4. the Doppler boosting of outflowing material in acceleration regions

5. detailed modeling of curvature radiation

6. dependence of the scattering angle of the inverse Compton emission on the orbital phase

7. dependence of the binary separation on the orbital phase

Considering these effects precisely, we need to understand the acceleration/emission mechanisms in LS 5039 in more detail *e.g.* the maximum energy of electrons which are accelerated in the reconnection spots, the curvature radius of the magnetic field lines on which the GeV gamma rays are produced. In order to tackle these problems, we need to study details of the following processes in the future:

1. magnetic reconnection in strong magnetic field

2. shock acceleration by interaction between magnetic pressure and ram pressure

3. a formation of magnetic reconnection driven jet.

8.9.4 Other Subjects

Where was the magnetar in LS 5039 born?

By following Equation 8.9, the age of the magnetar in LS 5039 is estimated as

$$T_{\mathrm{NS}} \simeq 5.2 \times 10^3 \mathrm{\ yr} \times \left(\frac{B_{\mathrm{NS}}}{10^{15} \mathrm{\ G}} \right)^2 \ , \tag{8.34}$$

which indicates that the magnetar in LS 5039 is a very young system. Therefore, it can be considered that a supernova remnant associated with the magnetar is located near LS 5039. The only possible association is SNR G016.8-01.1, which is a diffuse emission region located from LS 5039 apart from LS 5039 by 2'. Considering the proper motion, LS 5039 can be associated with it if $T_{\mathrm{NS}} \sim 10^5$ yr which corresponds to $B_{\mathrm{NS}} \sim 4.5 \times 10^{15}$ G (Moldón et al., 2012). However, Sun et al. (2011) claimed that SNR G016.8-01.1 is likely a HII region rather than a supernova. A further study is needed to conclude this association.

What makes LS 5039 different from Isolated Magnetars?

Isolated magnetars have blackbody emissions with a temperature of ~ 0.5 keV in the X-ray band, and their luminosities are typically $\sim 10^{35}$ erg s^{-1} although the radiation mechanism is still unclear (Enoto et al., 2010). On the other hand, we did not find any blackbody emission from LS 5039, and obtained 3σ upper limit on the flux as 2×10^{33} erg s^{-1} at a temperature of 0.5 keV (see Figure 4.4). Thus, the radiation mechanism of isolated magnetars would be different from that of LS 5039. This suggests that isolated magnetars are heated externally because an obvious difference between them is the structure of magnetic field lines in the magnetosphere. It is plausible that the magnetic poles of an isolated magnetar are heated by high-energy electrons moving along the magnetic field lines. Since there are no strong stellar winds around isolated magnetars, the curvature radius of the magnetic field lines would be much larger than LS 5039. Thus, electrons in an isolated magnetar can reach to the magnetic pole before they lose their energy through curvature radiation.

Chapter 9

Conclusion

In this thesis, we studied the gamma-ray binary LS 5039 in both hard X-ray and GeV band. In the hard X-ray band, In Chapter 4, we analyzed the spectrum of LS 5039 from 3 keV to 70 keV with *NuSTAR* observatory. The hard X-ray spectrum was found to be described well with a single powerlaw model below 70 keV. By comparing with the previous observation with *Suzaku*, we found that the flux in 3–10 keV varies by $\sim 10\%$ around the inferior conjunction. In addition, a small spike observed at $\phi = 0.70$ in the previous observations was not found in the *NuSTAR* observation. These results suggest that the emission around the inferior conjunction varies slightly orbit-by-orbit. Furthermore, we found that 10–30 keV flux varies by $\sim 25\%$ around the INFC and by $\sim 69\%$ around SUPC comparing with the har X-ray observation with *Suzaku*. This suggests that there is a variable emission component above 10 keV.

In Chapter 5, we searched hard X-ray data for the pulsed signal for the first time. From *Suzaku*/HXD data, Fourier analysis arranged to mitigate the Doppler effect due to the orbital motion revealed the periodic component of $P = 8.960 \pm 0.009$ s with a chance probability of $\mathcal{P}_{\mathrm{ch}} = 1.1 \times 10^{-3}$. The *NuSTAR* data also shows a sign of the pulsation at $P = 9.046 \pm 0.009$ s. These two peaks are evidence that LS 5039 contains a neutron star with a spin period of $P_{\mathrm{NS}} \sim 9$ s and a period derivative of $\dot{P}_{\mathrm{NS}} \sim 3 \times 10^{-10}$ s s^{-1}. However, when we corrected the photon time-of-arrival considering the orbital motion, no consistent solution was found from the *Suzaku* and *NuSTAR* data.

In order to study the GeV gamma-ray emission, we analyzed 11 year observations of *Fermi* LAT. The spectrum averaged over the orbital phase was found to be well described with a single cut-off powerlaw component. On the other hand, the spectrum around INFC shows a hump around 1 GeV clearly, and it is described well with two components; a powerlaw

with a photon index of ~ 3.6, and an exponential cutoff powerlaw with a photon index and a cutoff energy of ~ 1.3 and ~ 1.9 GeV respectively. Furthermore, the dependence of the flux on the orbital phase varies with the gamma-ray energy. While the fraction of a variable component is $\sim 60\%$ around 300 MeV, it is decreased to $\sim 20\%$ from 1 GeV to 5 GeV. Thus, we concluded that there are two spectral components in the GeV band. We also investigated the long-term variability, and revealed that the GeV gamma-ray flux of LS 5039 is stable in both 1-month and 1-year time scales.

In order to interpret the multi-band spectrum of LS 5039, we constructed a spectral model with assuming the minimum assumptions, and compared the observed spectra with the model prediction. Using the photon index in the X-ray band and the flux ratio of X-rays to GeV gamma-rays, we obtained constraints on the magnetic field in the X-ray emission region. When the acceleration region is apart from the companion star by 50 light sec, it is constrained as 1.4 G $< B < 150$ G. Moreover, we found that LS 5039 has at least three spectral components which are produced in different acceleration regions; especially the X-ray and MeV spectra cannot be explained as a single spectral component. The MeV spectral component is explained only if it is the synchrotron spectrum hardened by both adiabatic losses and the very hard injection spectrum with a spectral index of $s \sim 1$. It suggests that a direct acceleration takes place in LS 5039.

On the basis of the pulse period obtained in hard X-ray timing analysis, we proposed a new hypothesis for LS 5039: the compact star in LS 5039 is a magnetar with a strong magnetic field of $\sim 10^{15}$G and its magnetic energy is the dominant energy source for non-thermal activity of LS 5039. In this scenario, the very hard injection electron spectrum for the MeV gamma-ray emission is naturally interpreted as the magnetic reconnection near the magnetar. Then, we interpret the origin of the high-energy emission from LS 5039 as follows:

- X-rays are produced in the shock located at Alfvén radius ~ 1.0 light sec. The size and magnetic field of the emission region are a few light sec and $30 - 100$ G, respectively.

- MeV gamma rays are produced via magnetic reconnection near the magnetar. The reconnection spots are located apart from the magnetar by less than 0.4 light sec.

- Electrons which are accelerated in the reconnection spots produce GeV gamma rays via curvature radiation in the magnetar's magnetosphere.

- TeV gamma rays are produced via inverse Compton emission in a relativistic outflow driven by magnetic reconnection.

Finally, on the analogy of magnetic field lines around the Earth, we proposed a plausible configuration of magnetic field lines in LS 5039 which can explain the spectral origins simultaneously.

Appendix A

Z^2 statistics

Z^2 statistics are statistics used in periodic signal search with time-series data. When a periodic signal is modeled by

$$\sum_{l=1}^{l=m} \left(a_l \cos 2\pi l \frac{t}{P} + b_l \sin 2\pi l \frac{t}{P} \right) \tag{A.1}$$

Z^2 statistics are defined as

$$Z_m^2 = \frac{2}{N} \sum_{l=1}^{l=m} \left(\left(\sum_i \cos 2\pi l \frac{t_i}{P} \right)^2 + \left(\sum_i \sin 2\pi l \frac{t_i}{P} \right)^2 \right) , \tag{A.2}$$

where t_i is a time of each event and N is the total event number and P is the period of the signal. In this section, we prove the following formula, which is a relation between Z^2 statistics and the likelihood functions

$$Z_m^2 \simeq 2 \log L(\boldsymbol{t}; a_1, ..., a_m, b_1, ..., b_m, P) \tag{A.3}$$

$\log L(\boldsymbol{t}; a_1, ..., a_m, b_1, ..., b_m, P)$ is a likehood function defined as

$$\log L(\boldsymbol{t}; a_1, ..., a_m, b_1, ..., b_m, P) = \sum_i \log \left(1 + \sum_{l=1}^{l=m} \left(a_l \cos 2\pi l \frac{t_i}{P} + b_l \sin 2\pi l \frac{t_i}{P} \right) \right) . \tag{A.4}$$

A.1 Likelihood Analysis in Time Series Analysis

A.1.1 Analysis with a Binned Light Curve

Here, we consider an time series analysis using a binned light curve. We define the following parameters as:

n_i: the number of photons detected in the i-th bin.

λ_i: the number of photons predicted by a model.

In X-ray or gamma-ray astronomy, the time of events is usually recorded event-by-event. In this case, a binned light curve can be produced from the event data by assuming the bin width of the light curve. When the number of photons in each bin is small, it is Poisson-distributed:

$$n_i \sim Poisson(\lambda_i) \tag{A.5}$$

The probability of detecting x events when it is Poisson-distributed with an expected value λ is

$$Poisson(x; \lambda) = \frac{\lambda^x e^{-\lambda}}{x!} \tag{A.6}$$

Therefore, the likelihood is given by

$$
\begin{aligned}
L(\boldsymbol{n}; \boldsymbol{\lambda}) &= \exp\left(-\sum_i \lambda_i\right) \prod_i \left(\frac{\lambda_i^{n_i}}{n_i!}\right) \tag{A.7} \\
&= \exp\left(-N_{\text{exp}}\right) \prod_i \left(\frac{\lambda_i^{n_i}}{n_i!}\right), \tag{A.8}
\end{aligned}
$$

where we define N_{exp} as:

$$N_{\text{exp}} = \sum_i \lambda_i . \tag{A.9}$$

A.1.2 Analysis without a Binned Light Curve

When a binned light curve is used and the number of events is small, the bin width of the light curve should be narrow. Otherwise, it is difficult to test models because the bin width loses timing information. Since the estimation could depend on the bin width, the best way is to set it at an infinitely small value. In this case, we do not lose any amount of timing information.

When the bin width Δt is very small, the number of photons in each bin is 0 or 1. In an instrument such as a radiation detector, we define Δt smaller or comparable to the timing resolution of the detector. We assume $f(t)$, which is a model function that calculates the number of photons per unit time. Then, we derive the following equation:

$$\frac{\lambda_i^{n_i}}{n_i!} = \begin{cases} 1 & (n_i = 0) \\ f(t_i)\Delta t & (n_i = 1) . \end{cases} \tag{A.10}$$

Hence, the likelihood function in Equation A.7 is deformed into the following:

$$L(\boldsymbol{n}; \boldsymbol{\lambda}) = \exp\left(-N_{\text{exp}}\right) \prod_{i \ where \ n_i=1} f(t_i)\Delta t \tag{A.11}$$

Since Δt is smaller or comparable to the timing resolution, t_i can be interpreted as the time when the i-th event was detected. Therefore, the likelihood function is derived without using the binned light curve. Here, we refer to this likelihood function as the unbinned likelihood function.

A.2 Periodic Signal Search with the Unbinned Likelihood Function

Here we assume that the time series data are generated from a periodic signal. In the simplest case, the number of photons per unit time is modeled as:

$$f(t) = A\left(1 + a\cos 2\pi\frac{t}{P} + b\sin 2\pi\frac{t}{P}\right) . \tag{A.12}$$

We insert this equation into Equation A.11. When we define T_{obs} as the exposure time of the data, N_{exp} is equal to AT_{obs}. Then, the unbinned likelihood function in Equation A.11 is deformed into the following:

$$L(\boldsymbol{n}; \boldsymbol{\lambda}) = \exp\left(-AT_{\text{obs}}\right) A^{N_{\text{obs}}} \times (\Delta t)^{N_{\text{obs}}} \times \prod_i \left(1 + a\cos 2\pi\frac{t_i}{P} + b\sin 2\pi\frac{t_i}{P}\right) \tag{A.13}$$

where N_{obs} is the total number of detected events.

In the likelihood analysis, values of the parameters in a model are estimated as the parameter set which maximizes the likelihood function. The first term in Equation A.13 is maximized when:

$$A = \frac{N_{obs}}{T_{obs}} . \tag{A.14}$$

The second term does not depend on the parameters. The third term is the only term which depends on the amplitude and period of the signal. Therefore, we can estimate the parameters by maximizing the third term in Equation A.13.

In general, when we model the number of photons per unit time as:

$$f(t) = A\left(1 + \sum_{l=1}^{l=m}\left(a_l\cos 2\pi l\frac{t}{P} + b_l\sin 2\pi l\frac{t}{P}\right)\right) , \tag{A.15}$$

the parameters are estimated by maximizing the following equation:

$$\log L(\boldsymbol{t}; a_1, ..., a_m, b_1, ..., b_m, P) = \sum_i \log \left(1 + \sum_{l=1}^{l=m} \left(a_l \cos 2\pi l \frac{t_i}{P} + b_l \sin 2\pi l \frac{t_i}{P} \right) \right) \quad \text{(A.16)}$$

A.3 Relation between the Unbinned Likelihood Function and Z^2 statistics

For simplicity, we model the periodic signal only with a first harmonics as described in Equation A.12. The parameter set which maximizes the unbinned likelihood function is obtained by solving the following equation:

$$\frac{\partial \log L(\boldsymbol{t}; a, b, P)}{\partial a} = \frac{\partial \log L(\boldsymbol{t}; a, b, P)}{\partial b} = 0 \ . \quad \text{(A.17)}$$

It is transformed into the following:

$$\frac{\partial \log L(\boldsymbol{t}; a, b, P)}{\partial a} = \sum_i \frac{\cos 2\pi \frac{t_i}{P}}{1 + a \cos 2\pi \frac{t_i}{P} + b \sin 2\pi \frac{t_i}{P}} \quad \text{(A.18)}$$

$$\simeq \sum_i \left(\cos 2\pi \frac{t_i}{P} - \frac{a}{2} \left(1 + \cos 4\pi \frac{t_i}{P} \right) - b \cos 2\pi \frac{t_i}{P} \sin 2\pi \frac{t_i}{P} \right) \text{(A.19)}$$

When we assume that the amplitudes a, b are small, Equation A.17 and A.18 yields the following

$$a \simeq \frac{2}{N_{obs}} \sum_i \cos 2\pi \frac{t}{P}_i \ . \quad \text{(A.20)}$$

In a similar way, b is derived as

$$b \simeq \frac{2}{N_{obs}} \sum_i \sin 2\pi \frac{t}{P}_i \ . \quad \text{(A.21)}$$

We expand Equation A.16 as the following:

$$\log L(\boldsymbol{t}; a, b, P) = \sum_i \sum_{n=1}^{\infty} \frac{(-1)^{n-1} \left(a \cos 2\pi \frac{t_i}{P} + b \sin 2\pi \frac{t_i}{P} \right)^n}{n} \quad \text{(A.22)}$$

$$= \sum_{n=1}^{\infty} \frac{(-1)^{n-1}}{n} F_n \ , \quad \text{(A.23)}$$

where we define F_n as:

$$F_n = \sum_i \left(a \cos 2\pi \frac{t_i}{P} + b \sin 2\pi \frac{t_i}{P} \right)^n \ . \quad \text{(A.24)}$$

Then, F_1 is equal to the Z^2 statistics considering only first harmonics (see Equation A.2).

$$F_1 = \sum_i \left(a \cos 2\pi \frac{t_i}{P} + b \sin 2\pi \frac{t_i}{P} \right) \tag{A.25}$$

$$= \frac{N_{\text{obs}}}{2} \left(a^2 + b^2 \right) \tag{A.26}$$

$$= \frac{2}{N_{\text{obs}}} \left(\left(\sum_i \cos 2\pi \frac{t_i}{P} \right)^2 + \left(\sum_i \sin 2\pi \frac{t_i}{P} \right)^2 \right) , \tag{A.27}$$

F_2 is transformed to

$$F_2 = a^2 \sum_i \cos^2 2\pi \frac{t_i}{P} + b^2 \sum_i \sin^2 2\pi \frac{t_i}{P} + 2ab \sum_i \cos 2\pi \frac{t_i}{P} \sin 2\pi \frac{t_i}{P} \tag{A.28}$$

$$= a^2 \sum_i \frac{1}{2} \left(1 + \cos 4\pi \frac{t_i}{P} \right) + b^2 \sum_i \frac{1}{2} \left(1 - \cos 4\pi \frac{t_i}{P} \right) + ab \sum_i \sin 4\pi \frac{t_i}{P} \tag{A.29}$$

$$= \frac{N_{\text{obs}}}{2} \left(a^2 + b^2 \right) + (\text{a quadratic equation with } a, b) \times O \left(\sum_i \exp \left(4\pi i \frac{t_i}{P} \right) \right) \tag{A.30}$$

In a similar way, we can transform F_n into a simple form. When n is odd, F_n is described as (an equation of n-th degree with a, b) $\times O \left(\sum_i \exp(in2\pi \frac{t_i}{P}) \right)$, while when n is even, F_n is described as (an equation of n-th degree with a, b) $\times O \left(N_{\text{obs}} \right)$ When a, b are small, $\frac{N_{\text{obs}}}{2} \left(a^2 + b^2 \right)$ dominates over other terms. Therefore, we derived the relation between the unbinned likelihood function and Z^2 statistics:

$$\log L(\boldsymbol{t}; a, b, P) \simeq \frac{N_{\text{obs}}}{2} \left(a^2 + b^2 \right) - \frac{N_{\text{obs}}}{4} \left(a^2 + b^2 \right) \tag{A.31}$$

$$= \frac{N_{\text{obs}}}{4} \left(a^2 + b^2 \right) \tag{A.32}$$

$$= \frac{1}{2} Z_1^2 . \tag{A.33}$$

In general, when the periodic signal is modelled by as:

$$f(t) = A \left(1 + \sum_{l=1}^{l=m} \left(a_l \cos 2\pi l \frac{t}{P} + b_l \sin 2\pi l \frac{t}{P} \right) \right) , \tag{A.34}$$

the following equation holds:

$$\log L(\boldsymbol{t}; a_1, ..., a_m, b_1, ..., b_m, P) \simeq \frac{1}{2} Z_m^2 \tag{A.35}$$

A.4   Hypothesis Testing with Z^2 Statistics

A.4.1   Likelihood Ratio Test

The likelihood ratio test is a hypothesis test which helps to decide the best model between two nested models H_1 and H_2. When H_1 is nested in H_2, H_1 and H_2 are called as the null hypothesis and the alternative hypothesis. For example, when we search for a periodic signal modeled as Equation A.12, H_1 is defined as $a = 0, b = 0$. When the likelihood functions for the two models are defined, we calculate the maximum value L^* of each likelihood function by sweeping its parameter space. Then the following test statistics are used

$$\Delta D_{1,2} = -2 \times (\log L_1^* - \log L_2^*) \ . \tag{A.36}$$

In a periodic signal search, Equation A.16 yields $\log L_1^* = 0$. Therefore, from Equation A.35, $Z^2(l = m)$ is equal to $\Delta D_{1,2}$.

When the period is fixed, $Z^2(l = m)$ is distributed following χ^2 distribution with $2l$ degrees of freedom, if the null hypothesis is true. When the period is not fixed, it is not χ^2-distributed due to the looking-elsewhere effect. Therefore, the significance should be calculated on the basis of other methods *i.e.* Monte Calro calculations.

A.4.2   Error Estimation

When the null hypothesis is rejected in the likelihood ratio test, we estimate the parameters in the alternative hypothesis. A likelihood function for the null hypothesis is described as:

$$\log L(\boldsymbol{\theta}) = \log L^* - \frac{Q(\boldsymbol{\theta})}{2} \ , \tag{A.37}$$

where $\boldsymbol{\theta}$ is true values and $\log L^*$ is the maximum value of the likelihood function.

The confidence region of parameters in a model is estimated by solving $Q(\boldsymbol{\theta}) < Q_\gamma$. When we assume $\boldsymbol{\theta}^*$ is the true parameters, $Q(\boldsymbol{\theta}^*)$ is distributed with n degrees of freedom, where n is the number of free parameters. When $n = 1$, the relation between the confidence level and Q_γ is derived as described in Table A.1. Therefore, from Equation A.35, a 1 sigma confidence region on a single parameter is calculated as the parameter region where $Z^2(m = 1) < Z^{2*}(m = 1) - 1$. $Z^{2*}(m = 1)$ is the maximum value of Z^2 statistics.

confidence level	Q_γ
0.683	1.0
0.90	2.705
0.95	3.841
0.954	4.0

Table A.1: Relation between confidence level and Q_γ.

A.5 A Validation Using Simulation Data

We proved the following fomula:

$$\log L(\boldsymbol{t}; a_1, ..., a_m, b_1, ..., b_m, P) \simeq \frac{1}{2} Z_m^2 \ . \tag{A.38}$$

Here, we generate time series data assuming a periodic signal, and calculate Z^2 statistics and a likelihood function using the data. The periodic signal has a frequency of 1 Hz with a pulse profile as shown in Figure A.1.
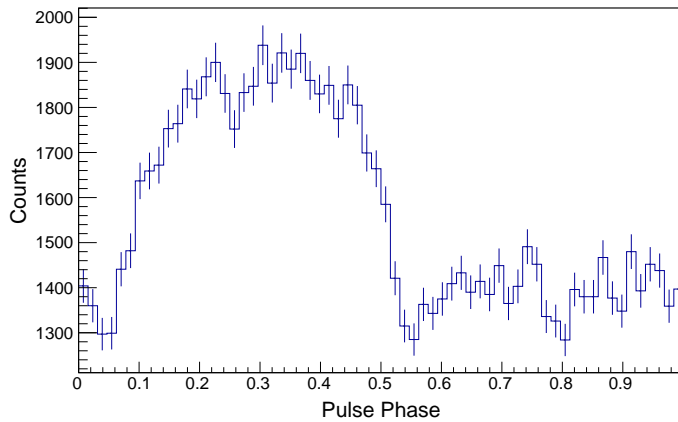
Figure A.1: The pulse profile in the simulation data.

Figure A.2 shows the results of the calculation. Here we calculated the data with the number of events $N = 50, 100, 200, 500, 1000, 2000$. The red lines correspond to Z^2 statistics, and the blue lines correspond to the likelihood function multiplied by two. In all cases, the two values are almost the same. In this thesis, the number of events is basically larger than ~ 50. Therefore, it is valid to treat Z^2 statistics as the likelihood function multiplied by two.
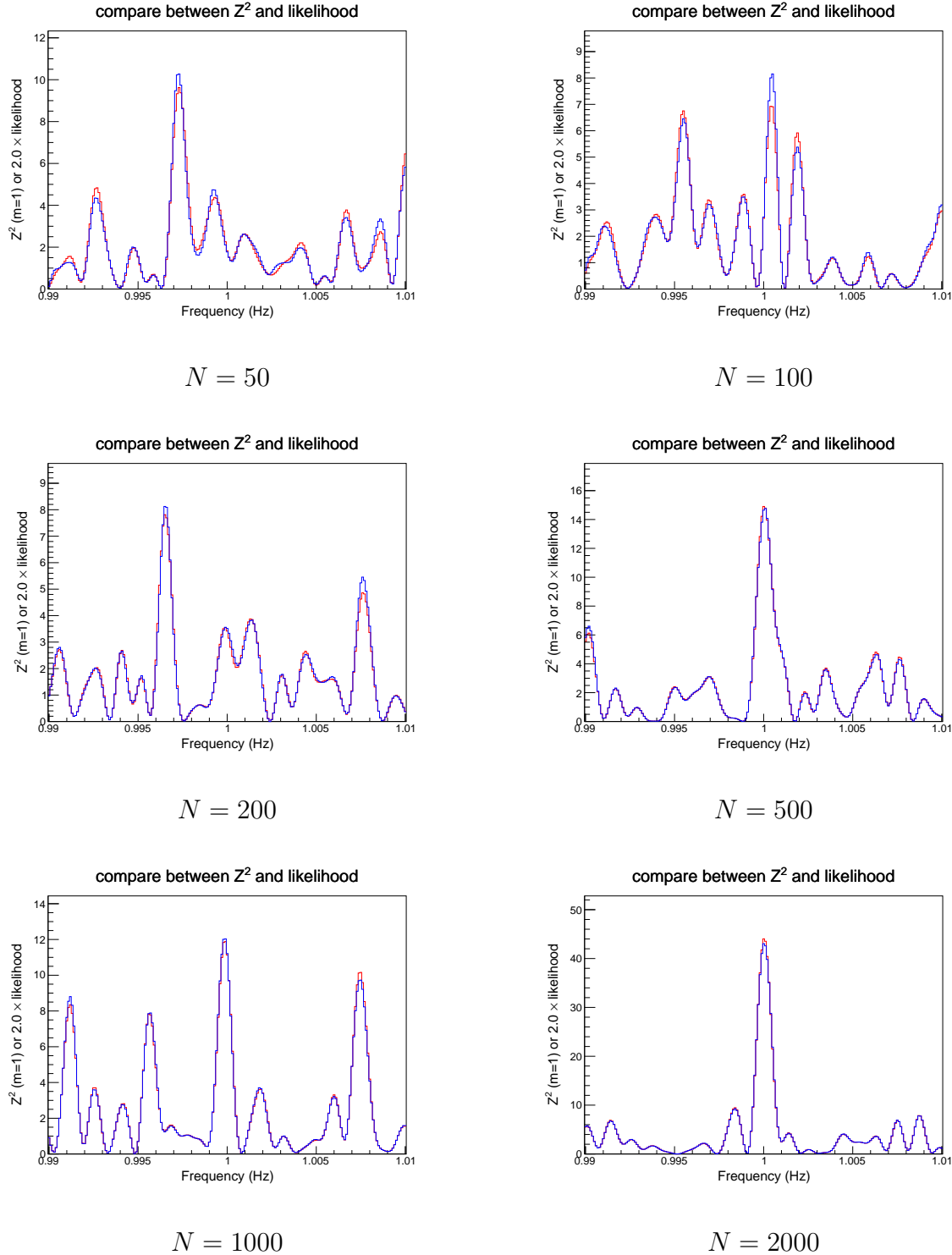
Figure A.2: Comparison between Z^2 statistics and likelihood functions using the simulation data. Here we consider only the first harmonics. The red lines correspond to Z^2 statistics, and the blue lines correspond to the likelihood function multiplied by two. N is the number of events in each simulation data.

Bibliography

Abdo, A. A., et al. 2011, The Astrophysical Journal, 736, L11

Aharonian, F., Anchordoqui, L., Khangulyan, D., & Montaruli, T. 2006a, in Journal of Physics Conference Series, Vol. 39, Journal of Physics Conference Series, 408–415

Aharonian, F., et al. 2005a, Astronomy and Astrophysics, 442, 1

—. 2005b, Science, 309, 746

—. 2006b, Astronomy and Astrophysics, 460, 743

Aharonian, F. A. 2004, Very high energy cosmic gamma radiation : a crucial window on the extreme Universe

Aharonian, F. A., Belyanin, A. A., Derishev, E. V., Kocharovsky, V. V., & Kocharovsky, V. V. 2002, Physical Review D, 66, 023005

Aharonian, F. A., Kelner, S. R., & Prosekin, A. Y. 2010, Physical Review D, 82, 043002

Antiochos, S. K., DeVore, C. R., & Klimchuk, J. A. 1999, Astrophysical Journal, 510, 485

Aragona, C., McSwain, M. V., Grundstrom, E. D., Marsh, A. N., Roettenbacher, R. M., Hessler, K. M., Boyajian, T. S., & Ray, P. S. 2009, Astrophysical Journal, 698, 514

Aramaki, T., Adrian, P. O. H., Karagiorgi, G., & Odaka, H. 2020, Astroparticle Physics, 114, 107

Atoyan, A. M., & Aharonian, F. A. 1996, Mon. Not. R. Astron. Soc., 278, 525

Atwood, W. B., et al. 2009, Astrophysical Journal, 697, 1071

Axford, W. I., Leer, E., & Skadron, G. 1977, in International Cosmic Ray Conference, Vol. 11, International Cosmic Ray Conference, 132

Becker, P. A., & Wolff, M. T. 2007, Astrophysical Journal, 654, 435

Becker, P. A., & Wolff, M. T. 2007, The Astrophysical Journal, 654, 435

Bednarz, J., & Ostrowski, M. 1996, Mon. Not. R. Astron. Soc., 283, 447

Bell, A. R. 1978, Mon. Not. R. Astron. Soc., 182, 147

Bignami, G. F., et al. 1975, Space Science Instrumentation, 1, 245

Blandford, R. D., & Ostriker, J. P. 1978, Astrophys. J. Letters, 221, L29

Bogovalov, S. V., Khangulyan, D. V., Koldoba, A. V., Ustyugova, G. V., & Aharonian, F. A.
    2008, Mon. Not. R. Astron. Soc., 387, 63

Bosch-Ramon, V., & Barkov, M. V. 2011, Astronomy and Astrophysics, 535, A20

Bosch-Ramon, V., Barkov, M. V., Khangulyan, D., & Perucho, M. 2012, Astronomy and
    Astrophysics, 544, A59

Bosch-Ramon, V., Paredes, J. M., Ribó, M., Miller, J. M., Reig, P., & Martí, J. 2005,
    Astrophysical Journal, 628, 388

Bosch-Ramon, V., Romero, G. E., & Paredes, J. M. 2006, Astronomy and Astrophysics, 447,
    263

Bruel, P., Burnett, T. H., Digel, S. W., Johannesson, G., Omodei, N., & Wood, M. 2018,
    arXiv e-prints, arXiv:1810.11394

Bulanov, S. V., & Sasorov, P. V. 1976, Soviet Astronomy, 19, 464

Caliandro, G. A., Torres, D. F., & Rea, N. 2012, Mon. Not. R. Astr. Soc., 427, 2251

Camilo, F., et al. 2009, Astrophysical Journal, 705, 1

Casares, J., Ribo, M., Ribas, I., Paredes, J. M., Marti, J., & Herrero, A. 2005, Mon. Not. R.
    Astr. Soc., 364, 899

Casares, J., Ribó, M., Ribas, I., Paredes, J. M., Vilardell, F., & Negueruela, I. 2012, Mon.
    Not. R. Astron. Soc., 421, 1103

Chakrabarty, D., et al. 1993, Astrophys. J. Letters, 403, L33

Chang, Z., Zhang, S., Ji, L., Chen, Y. P., Kretschmar, P., Kuulkers, E., Collmar, W., & Liu, C. Z. 2016, Mon. Not. R. Astron. Soc., 463, 495

Cheng, K. S., Ho, C., & Ruderman, M. 1986, Astrophysical Journal, 300, 500

Chernyakova, M., Neronov, A., Molkov, S., Malyshev, D., Lutovinov, A., & Pooley, G. 2012, Astrophys. J. Letters, 747, L29

Church, M. J., Gibiec, A., & Bałucińska-Church, M. 2014, Mon. Not. R. Astron. Soc., 438, 2784

Clausen-Brown, E., & Lyutikov, M. 2012, Mon. Not. R. Astron. Soc., 426, 1374

Collmar, W., Schönfelder, V., Strong, A. W., Bloemen, H., Hermsen, W., McConnell, M., Ryan, J., & Bennett, K. 2000, in American Institute of Physics Conference Series, Vol. 510, American Institute of Physics Conference Series, ed. M. L. McConnell & J. M. Ryan, 591–595

Collmar, W., & Zhang, S. 2014, Astronomy and Astrophysics, 565, A38

Condon, J. J., Cotton, W. D., Greisen, E. W., Yin, Q. F., Perley, R. A., Taylor, G. B., & Broderick, J. J. 1998, The Astronomical Journal, 115, 1693

Coppi, P. S., & Blandford, R. D. 1990, Mon. Not. R. Astron. Soc., 245, 453

Corbet, R. H. D., et al. 2016, The Astrophysical Journal, 829, 105

Corbet, R. H. D., et al. 2019, arXiv e-prints, arXiv:1908.10764

Dai, L., Wang, C., Angelopoulos, V., & Glassmeier, K. H. 2015, Annales Geophysicae, 33, 1147

Daugherty, J. K., & Harding, A. K. 1982, Astrophysical Journal, 252, 337

De Angelis, A., et al. 2017, Experimental Astronomy, 44, 25

De Gouveia Dal Pino, E., del Valle, M. V., Kadowaki, L., Khiali, B., Kowal, G., Mizuno, Y., & Singh, C. B. 2016, in Frontier Research in Astrophysics II (FRAPWS2016), 56

de Jager, O. C., Raubenheimer, B. C., & Swanepoel, J. W. H. 1989, Astronomy and Astrophysics, 221, 180

Dermer, C. D., & Böttcher, M. 2006, Astrophysical Journal, 643, 1081

Dubus, G. 2006, Astronomy and Astrophysics, 451, 9

Dubus, G., Cerutti, B., & Henri, G. 2010, Astronomy and Astrophysics, 516, A18

Dubus, G., Lamberts, A., & Fromang, S. 2015, Astronomy and Astrophysics, 581, A27

Enoto, T., Nakazawa, K., Makishima, K., Rea, N., Hurley, K., & Shibata, S. 2010, Astrophys. J. Letters, 722, L162

Erber, T. 1966, Reviews of Modern Physics, 38, 626

Fabbiano, G. 2006, Annual Review of Astronomy & Astrophysics, 44, 323

Fermi LAT Collaboration et al. 2012, Science, 335, 189

Frail, D. A., & Hjellming, R. M. 1991, Astronomical Journal, 101, 2126

Fukazawa, Y., et al. 2009, Publications of the Astronomical Society of Japan, 61, S17

Gaia Collaboration et al. 2018, Astronomy and Astrophysics, 616, A1

Ghosh, P. 2007, Rotation and Accretion Powered Pulsars, Vol. 10

Gil, J., Lyubarsky, Y., & Melikidze, G. I. 2004, Astrophysical Journal, 600, 872

Ginzburg, V. L., & Syrovatskii, S. I. 1964, The Origin of Cosmic Rays (Oxford : Pergamon Press)

Gregory, P. C. 2002, Astrophysical Journal, 575, 427

Gregory, P. C., & Taylor, A. R. 1978, Nature, 272, 704

Grimm, H. J., Gilfanov, M., & Sunyaev, R. 2002, Astronomy and Astrophysics, 391, 923

Gruber, D. E., Matteson, J. L., Peterson, L. E., & Jung, G. V. 1999, Astrophysical Journal, 520, 124

Hadasch, D., et al. 2012, Astrophysical Journal, 749, 54

Harrison, F. A., et al. 2013, Astrophysical Journal, 770, 103

Hartman, R. C., et al. 1999, The Astrophysical Journal Supplement Series, 123, 79

Ho, W. C. G., Ng, C. Y., Lyne, A. G., Stappers, B. W., Coe, M. J., Halpern, J. P., Johnson, T. J., & Steele, I. A. 2017, Mon. Not. R. Astron. Soc., 464, 1211

Hobbs, G., Lyne, A. G., Kramer, M., Martin, C. E., & Jordan, C. 2004, Mon. Not. R. Astr. Soc., 353, 1311

Hoffmann, A. D., Klochkov, D., Santangelo, A., Horns, D., Segreto, A., Staubert, R., & Pühlhofer, G. 2009, Astronomy and Astrophysics, 494, L37

Johnston, S., Manchester, R. N., Lyne, A. G., Bailes, M., Kaspi, V. M., Qiao, G., & D'Amico, N. 1992, Astrophys. J. Letters, 387, L37

Johnston, S., Manchester, R. N., Lyne, A. G., Nicastro, L., & Spyromilio, J. 1994, Mon. Not. R. Astron. Soc., 268, 430

Khangulyan, D., Aharonian, F., & Bosch-Ramon, V. 2008, Mon. Not. R. Astr. Soc., 383, 467

Khangulyan, D., Aharonian, F. A., & Kelner, S. R. 2014, Astrophysical Journal, 783, 100

Kiminki, D. C., Kobulnicky, H. A., Vargas Álvarez, C. A., Alexander, M. J., & Lundquist, M. J. 2015, Astrophysical Journal, 811, 85

Kishishita, T., Tanaka, T., Uchiyama, Y., & Takahashi, T. 2009, Astrophysical Journal, 697, L1

Kivelson, M. G., & Russell, C. T. 1995, Introduction to Space Physics

Kopp, R. A., & Pneuman, G. W. 1976, Solar Physics, 50, 85

Krivonos, R., Revnivtsev, M., Churazov, E., Sazonov, S., Grebenev, S., & Sunyaev, R. 2007, Astronomy and Astrophysics, 463, 957

Krymsky, G. F. 1977, Dokl. Akad. Nauk SSSR, 234, 1306

Lamers, H. J. G. L. M. 1981, Astrophysical Journal, 245, 593

Lamers, H. J. G. L. M., & Leitherer, C. 1993, Astrophysical Journal, 412, 771

Landau, L. D., & Lifshitz, E. M. 1987, Fluid Mechanics

Lewin, W. H. G., & van der Klis, M. 2006, Compact Stellar X-ray Sources, Vol. 39

Li, J., Torres, D. F., Zhang, S., Hadasch, D., Rea, N., Caliandro, G. A., Chen, Y., & Wang, J. 2011, The Astrophysical Journal, 744, L13

Liu, Q. Z., van Paradijs, J., & van den Heuvel, E. P. J. 2006, Astronomy and Astrophysics, 455, 1165

—. 2007, Astronomy and Astrophysics, 469, 807

Longair, M. S. 2011, High Energy Astrophysics

Lyubarsky, Y., & Kirk, J. G. 2001, Astrophysical Journal, 547, 437

Makishima, K., Enoto, T., Hiraga, J., Nakano, T., Nakazawa, K., Sakurai, S., Sasano, M., & Murakami, H. 2014, Physical Review Letters, 112

Massey, P., & Thompson, A. B. 1991, Astronomical Journal, 101, 1408

Mattox, J. R., et al. 1996, Astrophysical Journal, 461, 396

McEnery, J., et al. 2019, arXiv e-prints, arXiv:1907.07558

McSwain, M. V., Gies, D. R., Riddle, R. L., Wang, Z., & Wingert, D. W. 2001, Astrophys. J. Letters, 558, L43

Meyer, M., Horns, D., & Zechlin, H. S. 2010, Astronomy and Astrophysics, 523, A2

Miller-Jones, J. C. A., et al. 2018, Mon. Not. R. Astron. Soc., 479, 4849

Mirabel, I. F. 2012, Science, 335, 175

Mitsuda, K., et al. 2007, Publications of the Astronomical Society of Japan, 59, S1

Moldón, J., Ribó, M., Paredes, J. M., Brisken, W., Dhawan, V., Kramer, M., Lyne, A. G., & Stappers, B. W. 2012, Astronomy and Astrophysics, 543, A26

Moritani, Y., Kawano, T., Chimasu, S., Kawachi, A., Takahashi, H., Takata, J., & Carciofi, A. C. 2018, Publications of the Astronomical Society of Japan, 70, 61

Motch, C., Guillout, P., Haberl, F., Pakull, M., Pietsch, W., & Reinsch, K. 1997, Astronomy and Astrophysics, 318, 111

Muno, M. P., Gaensler, B. M., Nechita, A., Miller, J. M., & Slane, P. O. 2008, Astrophysical Journal, 680, 639

Napoli, V. J., McSwain, M. V., Marsh Boyer, A. N., & Roettenbacher, R. M. 2011, Publications of the Astronomical Society of the Pacific, 123, 1262

Narayan, R., & Yi, I. 1995, Astrophysical Journal, 452, 710

Nasa High Energy Astrophysics Science Archive Research Center (Heasarc). 2014, HEAsoft: Unified Release of FTOOLS and XANADU

Negueruela, I., Ribó, M., Herrero, A., Lorenzo, J., Khangulyan, D., & Aharonian, F. A. 2011, Astrophys. J. Letters, 732, L11

Øieroset, M., Phan, T. D., Fujimoto, M., Lin, R. P., & Lepping, R. P. 2001, Nature, 412, 414

Paredes, J. M., Bosch-Ramon, V., & Romero, G. E. 2006, Astronomy and Astrophysics, 451, 259

Paredes, J. M., Marti, J., Peracaula, M., & Ribo, M. 1997, Astronomy and Astrophysics, 320, L25

Paredes, J. M., Martí, J., Ribó, M., & Massi, M. 2000, Science, 288, 2340

Paredes, J. M., Ribó, M., Ros, E., Martí, J., & Massi, M. 2002, Astronomy and Astrophysics, 393, L99

Ray, P. S., et al. 2011, The Astrophysical Journal Supplement Series, 194, 17

Rea, N., Torres, D. F., Caliandro, G. A., Hadasch, D., van der Klis, M., Jonker, P. G., Méndez, M., & Sierpowska-Bartosik, A. 2011, Mon. Not. R. Astr. Soc., 416, 1514

Rea, N., et al. 2009, Monthly Notices of the Royal Astronomical Society, 396, 2419

Reig, P., Ribó, M., Paredes, J. M., & Martí, J. 2003, Astronomy and Astrophysics, 405, 285

Revnivtsev, M., Sazonov, S., Gilfanov, M., Churazov, E., & Sunyaev, R. 2006, Astronomy and Astrophysics, 452, 169

Reynolds, S. P., Pavlov, G. G., Kargaltsev, O., Klingler, N., Renaud, M., & Mereghetti, S. 2017, Space Science Reviews, 207, 175

Romanova, M. M., & Lovelace, R. V. E. 1992, Astronomy and Astrophysics, 262, 26

Rybicki, G. B., & Lightman, A. P. 1986, Radiative Processes in Astrophysics

Sarty, G. E., et al. 2011, Monthly Notices of the Royal Astronomical Society, 411, 1293

Scarsi, L., et al. 1977, in ESA Special Publication, Vol. 124, Recent Advances in Gamma-Ray Astronomy, ed. R. D. Wills & B. Battrick, 3

Schönfelder, V., et al. 2000, Astronomy and Astrophysics Supplement, 143, 145

Shakura, N. I., & Sunyaev, R. A. 1973, Astronomy and Astrophysics, 500, 33

Shapiro, S. L., & Teukolsky, S. A. 1983, Black holes, white dwarfs, and neutron stars : the physics of compact objects

Sironi, L., Keshet, U., & Lemoine, M. 2015, Space Science Reviews, 191, 519

Sironi, L., & Spitkovsky, A. 2009, The Astrophysical Journal, 698, 1523

—. 2011, The Astrophysical Journal, 741, 39

Sironi, L., & Spitkovsky, A. 2014, Astrophys. J. Letters, 783, L21

Stephenson, C. B., & Sanduleak, N. 1971, Luminous stars in the Southern Milky Way (Publication of the Warner and Swasey Observatory)

Strong, A. W., et al. 2001, in American Institute of Physics Conference Series, Vol. 587, Gamma 2001: Gamma-Ray Astrophysics, ed. S. Ritz, N. Gehrels, & C. R. Shrader, 21–25

Sun, X. H., Reich, P., Reich, W., Xiao, L., Gao, X. Y., & Han, J. L. 2011, Astronomy and Astrophysics, 536, A83

Takada, A., et al. 2011, in ESA Special Publication, Vol. 700, 20th Symposium on European Rocket and Balloon Programmes and Related Research, ed. L. Ouwehand, 567–571

Takahashi, T., et al. 2007, Publications of the Astronomical Society of Japan, 59, S35

—. 2009, Astrophysical Journal, 697, 592

Takata, J., Leung, G. C. K., Tam, P. H. T., Kong, A. K. H., Hui, C. Y., & Cheng, K. S. 2014, Astrophysical Journal, 790, 18

The Fermi LAT collaboration. 2009, The Astrophysical Journal, 706, L56

The Fermi-LAT collaboration. 2019, arXiv e-prints, arXiv:1902.10045

Thompson, C., & Duncan, R. C. 1993, Astrophysical Journal, 408, 194

Torres, D. F., Rea, N., Esposito, P., Li, J., Chen, Y., & Zhang, S. 2012, Astrophysical Journal, 744, 106

Torres, D. F., et al. 2010, The Astrophysical Journal, 719, L104

van Soelen, B., Komin, N., Kniazev, A., & Väisänen, P. 2019, Mon. Not. R. Astron. Soc., 484, 4347

Virginia McSwain, M., Ray, P. S., Ransom, S. M., Roberts, M. S. E., Dougherty, S. M., & Pooley, G. G. 2011, Astrophysical Journal, 738, 105

Wang, Y., Takata, J., & Cheng, K. S. 2010, Astrophysical Journal, 720, 178

Wolff, M. T., et al. 2016, The Astrophysical Journal, 831, 194

Worley, A., Krastev, P. G., & Li, B.-A. 2008, The Astrophysical Journal, 685, 390

Yatabe, F., Makishima, K., Mihara, T., Nakajima, M., Sugizaki, M., Kitamoto, S., Yoshida, Y., & Takagi, T. 2018, Publications of the Astronomical Society of Japan, 70, 89

Yuan, F., & Narayan, R. 2014, Annual Review of Astronomy & Astrophysics, 52, 529

Zabalza, V. 2015, Proc. of International Cosmic Ray Conference 2015, 922

Zabalza, V., Bosch-Ramon, V., Aharonian, F., & Khangulyan, D. 2013, Astronomy and Astrophysics, 551, A17

Zdziarski, A. A., & Gierliński, M. 2004, Progress of Theoretical Physics Supplement, 155, 99

Zdziarski, A. A., Neronov, A., & Chernyakova, M. 2010, Mon. Not. R. Astron. Soc., 403, 1873

Zenitani, S., & Hoshino, M. 2001, Astrophys. J. Letters, 562, L63

Acknowledgement

I would like to express the deepest appreciation to my supervisor Prof. T. Takahashi who guided and encouraged me throughout the five years of my graduate course. He provided me a lot of exciting experiences in the academic field and beyond it. I learned from him how it is important *not to stop questioning* and to keep curiosity alive. I also deeply appreciate Prof. K. Makishima for introducing me this work and his helpful support on this thesis. I learned from him how it is important to be brave when building up a new hypothesis. I gratefully thank Dr. D. Khangulyan for all the fruitful discussions and his productive advice through this project. I learned from him how it is important to acquire basics of physics when testing the new hypothesis. I would like to thank Dr. T. Enoto for giving me kind advice on the data analysis of the X-ray observations. I also thank Mr. T. Matsumoto for his contribution to the timing analysis of the *Suzaku* observation. I wish to thank Dr. S. Ikeda and Dr. M. Morii for helpful discussions about the statistical aspects of timing analysis on X-ray data. I would like to thank Prof. F. Aharonian for stimulating discussions during my stay in Max-Planck-Institut für Kernphysik. I also wish to thank Prof. P. Coppi for giving me advice on my thesis when I stayed in Yale University. I thank Dr. T. Mizuno and Dr. Y. Tanaka for giving me advice on the data analysis of *Fermi* LAT. I would like to thank Dr. H. Odaka for a lot of discussions and kind advice during my graduate course. Special thanks to Dr. P. Caradonna for correcting the English grammar in this thesis. I thank Mr. K. Mine and Mr. S. Nagasawa for their helps on the *Fermi* data analysis and checking the sentences on this thesis. I also wish to thank Mr. R. Tomaru, who is my great colleague through the five years. I would like to express my gratitude to all the people of Takahashi group and all the people I worked with in this five years. Finally, I thank my family for their continuous support and encouragement.